The evaluation of sintering as a potential cause of duct blockages for a submerged arc furnace applied in silicomanganese production

By

Martin Sitefane

A dissertation submitted to the School of Chemical and Metallurgical Engineering at the University of the Witwatersrand, Johannesburg, in partial fulfilment of the degree master of science in engineering

October 2020

SUMMARY

A study was undertaken to evaluate sintering as a potential cause of duct blockage for a submerged arc furnace applied in silicomanganese production. Within the broader aim of the study, four research questions were of principal interest. The research questions were as follows:

- Is there a potential for dust to sinter in the off-gas duct?
- If so, what mechanism of sintering is applicable, under the given conditions?
- Does the firing temperature have an effect on sinter formation and the compressive strength of the dust, given a fixed PSD?
- Does PSD have an effect on sinter formation and the compressive strength of the dust, given a fixed firing temperature?

In order to address the aforementioned research questions, several plant-based, laboratory-based, and desktop-based activities were undertaken. The activities were divided into five chronological stages as follows:

- Stage 1: Smelter based activities – entailed the collection of dust samples from the three streams in the baghouse and the measurement of the furnace duct temperatures. From this exercise, a total of 505 kg of dust across the three streams was collected. The duct temperature was found to vary between 600–1300°C.
- Stage 2: Laboratory dust samples preparations – entailed sample preparation, and PSD and chemical characterisation of each dust stream.
- Stage 3: Laboratory pellet-pressing and firing tests – entailed the pressing of pellets at a pressure of 5 MPa pressure, followed by oven drying, and then firing in a muffle furnace at 600–1300°C (the measured duct temperature) in an air atmosphere. For each temperature and dust stream, forty one pellets were fired.
- Stage 4: Fired dust examination: the fired pellets were examined for sintering using observations of their: physical appearance, compressive strength, bulk chemistry, bulk phase chemical composition.
- Stage 5: Chemical thermodynamic evaluation: thermodynamic calculations were performed using FactSage^{TM}, to determine the amount of liquid formed from bulk mixtures, as well phases that were observed to have sintered together.

Following the testwork, the following research outcomes were found:

- There was sound evidence of sintering in the off-gas duct of the smelter in question.
- Both solid- and liquid-state sintering were observed. The former was more localised–observed only in some areas in the sample–and most prominent at firing temperatures of 600–900°C. The latter was observed between 600–1100°C; it was prevalent at 1100°C–where long networks of sintered materials were observed.
- The firing temperature was found to have an effect on sinter formation and the compressive strength.
- The PSD was also found to have an effect on sinter formation and the compressive strength of the formed sinters.

TABLE OF CONTENTS

LIST OF FIGURES

LIST OF TABLES

ACKNOWLEDGMENTS

1 INTRODUCTION

The section introduces the project by providing the background to the project; the problem statement - formulated in-line with the identified problem; the four key research questions that this study aims to address; the aims and as well as the corresponding objectives of the study; At the end of this section, a dissertation outline that highlights the main emphasis of each chapter, is given.

1.1 Background

During a two-day furnace off-gas duct excavation (from the 19th to 20th July 2018) at a silicomanganese-producing (SiMn) smelter in South Africa, it was observed that a large section of the off-gas duct had been heavily blocked by what appeared to be dust forming part of the off-gas stream. Following engagements with operational personnel at the smelter about this observation, it surfaced that blockages in the ducts were a regular, though undesirable occurrence. Until that point, neither the mechanism of blockages, nor the solution to this problem were fully understood. Figure 1 shows two pictures of the blocked duct taken during the excavation.

Figure 1: Top view photographic image showing blocked section of the off-gas duct (the two photographs were taken on the 19 July 2018, i.e., the first day of the excavation)
(D = diameter)

The information provided by the engineering personnel, who are amongst other things tasked with managing the off-gas ducts, revealed that typically the smelter reacts to duct blockages in two ways:

- *Approach 1: 'Short shutdowns'* – The first approach is to employ external contractors during 8-hour shutdowns, about every 2 to 3 months, to clear as much as they can. The difficulty with this approach, apart from other challenges, is that there is limited time for the activity. Furthermore the furnace is normally too hot, and therefore unsafe, to enable complete clearance of the blockages. According to the engineering personnel, this type of intervention is very often ineffective.
- *Approach 2: 'Long shutdowns'* – The second approach is to employ external contractors during the yearly planned 10-to-21-day shutdown to clear the blockage completely.

The problem with both of the aforementioned blockage clearance approaches is that they adversely affect certain spheres of operation, during normal production and during annual

shutdowns. The affected spheres of operation, as discussed with the operating and engineering personnel, are summarised in Table 1.

Table 1: Spheres of operation adversely affected by duct blockages during normal smelting operations and during blockage clearance on shutdowns

During normal smelting operations	During blockage clearance on shutdowns
Operations	Maintenance cost
Health	Time
Safety	Infrastructure (refractory and duct shell)
Environment	Safety
Operating cost	

Given that smelter personnel do not fully understand the mechanism of blockage (although from experience and general smelting consensus dust settling followed by sintering is suspected), no working solution to the problem has been devised.

To this end, it is proposed that an investigation be conducted to study the cause of dust blockages, specifically evaluating for this dissertation the possibility of sintering as a cause of blockages in the ducts (sintering was identified as it seemed most plausible based on the information gathered from smelter personnel). Outside of sintering, intense foaming has been documented in literature as a possible cause of duct blockage for open bath furnaces (Jordan, 2011). However, since a submerged arc furnace technology utilising a semi-open roof is in view in this dissertation, and the fact that the production superintendent did not report any incident of foaming up to the ducts, this possibility was discounted. Furthermore, it was acknowledge that the duct design may have contribute to the observed duct blockages; however, because blockages were observed in different areas around the duct (areas had different designs), its effect was unlikely to be a sufficient condition. As a result, both foaming and duct design were discounted as part of the scope of this dissertation.

In broad terms, sintering may occur either when solids interact to form new compounds (i.e., solid-state sintering with no melting taking place), or as a result of partial liquid formation, which causes individual particles to agglomerate (i.e., liquid-state sintering where some form of melting takes place) (German, 1996; Leriche et al., 2017). In some textbooks, viscous sintering is also mentioned whereby a viscous (glassy) phase under capillary forces induces sintering (Rahaman, 2003), usually in silicate systems (Kingery et al., 1960). For the purpose of this study, a clear distinction between liquid-phase and viscous-phase sintering will not be made as this will require additional assessments that go beyond the scope of the study. Instead, sintering will be evaluated with respect to the two general categories, solid state and liquid state.

It should also be noted that according to smelter personnel such a study has never been undertaken at the smelter; thus, the information gathered will be invaluable, either in eliminating sintering as an explanation for the observed duct blockages, or in validating sintering, at least in part, as a contributor to the observed duct blockages. The information gathered from this investigation is expected to go a long way in facilitating the thinking around designing a future solution that will have beneficial consequences, such as reducing the risks to the safety and health of workers, eliminating risks to the environmental, protecting the

refractory and shell from damage, saving on time spent unblocking the duct, and ultimately saving on smelter maintenance costs.

To this end then, the duct blockage will be examined by making observations of the blockages inside the ducts during shutdown periods (i.e., smelter based work). Also, laboratory-scale controlled tests will be conducted in such a way as to simulate the conditions in the duct to see if sintering occurs.

1.2 Problem statement

The smelter in question is important in that it is the largest producer of SiMn in Africa (Steenkamp et al., 2018). Its process entails smelting of various manganese-bearing ore types in the presence of reductants and fluxes to produce a saleable SiMn alloy product. The business model follows a low-margin, high-volume approach (Steenkamp et al., 2018). This means that typically the SiMn alloy market price is very close to the production cost, and hence maximisation of profit depends strongly on the units of SiMn produced daily, weighed against the production cost. For this reason, the smelter aims to maximise furnace availability (i.e., with limited breakdowns and process complications), whilst minimising the costs related to furnace repairs and maintenance in order to maintain good and sustainable profit margins.

For a substantial period of time, the smelter has been experiencing recurring furnace off-gas-duct blockages. The problem is caused by dust in the off-gas stream. A blockage triggers a series of other problems both during furnace operation and during shutdown. These problems have an adverse effect on safety, health, the environment, furnace up-time, refractory and shell integrity, furnace availability, operations, and ultimately profit maximisation. The smelter is thus seeking a solution to the problem, but acknowledges that a proper understanding of the cause is a crucial fundamental first step in formulating a viable solution.

Several personnel at the smelter have proposed explanations for the likely cause of duct blockages (all without empirical evidence to back up their claims); interestingly, all of them implicated sintering of dust to some degree. Whilst the cause, and therefore explanation, is inferred from the observation of blockage, the cause as premise has not been confirmed empirically, and thus no informed solution has been proffered to date. The proposed investigation will focuses on evaluating dust sintering as a possible cause of duct blockage. Sintering can be influenced by a host of factors such as temperature, particle size distribution (PSD), residence time, gas flow rate, and gas composition (Kingery, W.D. et al., 1960; Rahaman, 2003); but for the purposes of this study, only the effects of temperature and PSD will be examined. As mentioned by the aforementioned citations, this can be done by keeping all the other factors constant throughout the investigation. Several ordinary assumptions, which are explained later, were made in the process.

It is believed that the information gained from this investigation will be invaluable in establishing or disproving sintering as a contributor to duct blockages under the given conditions. The study will also provide valuable insights into the type of sintering observed (i.e., whether liquid- or solid-state sintering occurs), if sintering is established as a cause. In the long run, this study will provide a foundation for the future development of solutions that address the problem of duct blockages more comprehensively. This foundation could provide significant benefits not only to the smelter in question, but also to other pyrometallurgical processes that experience similar difficulties.

1.3   Research questions

This study is structured to answer the following questions:

- Is there a potential for dust to sinter in the off-gas duct?
- If so, what mechanism of sintering would be applicable under the given conditions - i.e., solid- or liquid-state sintering?
- Given a fixed PSD, does the firing temperature have an effect on sinter formation as well as the compressive strength of the dust? (Note, the definition of PSD in this project is based on the inherent difference in absolute particle sizes of the three dust streams. For example, a coarse PSD means that the dust is made out of predominantly coarse particles)
- Given a fixed firing temperature, does PSD have an effect on sinter formation and the compressive strength of the dust?

1.4   Research aims

The aim of the project is two-fold:

(1) To establish if the dust produced at a SiMn smelter does in fact sinter.
(2) To explore the thesis that dust sintering may be contributing significantly to observed duct blockages.

1.5   Research objectives

Pursuant on these aims, the study has several objectives:

- To determine the maximum and minimum duct temperatures by optical pyrometry and thermocouple measurements. These temperatures are used for the laboratory firing tests.
- To collect plant-based dust samples from each of the streams for use in the laboratory tests
- To determine for each stream the phase-chemical composition of the sampled dust. This is done by means of inductively coupled Plasma – optical emission spectrometry (ICP-OES), carrier-gas hot extraction (LECO), Inductively Coupled Plasma – Mass Spectrometry (ICP-MS), X-ray diffractometry (XRD), and Scanning Electron Microscopy combined with Energy Dispersive Spectroscopy (SEM-EDS). These analytical techniques are used to describe the dust samples, which can then be compared with the fired samples as part of the sintering evaluation.
- To measure by sieve analysis the PSD of the dust samples. This helps differentiate the dust streams according to particle size. The streams are classified as fine, intermediate, or coarse size.
- To determine the mechanism of sintering in those instances where sintering is observed. Sintering is assessed mainly by SEM-EDS. Micrographs generated by SEM are evaluated for solid-state and liquid-state sintering. EDS point analyses on SEM micrographs, along with equilibrium thermodynamics calculations in FactSage help in assessing whether observed sintered phases are liquid or solid at the firing temperature. This in turn helps in classifying the sintering observed. XRD supplements SEM by identifying the phases associated with sintering.
- To determine the effect of a change in firing temperature on sinter formation and sinter strength for dusts of similar PSD. This is determined qualitatively by SEM micrographs and quantitatively by compression strength tests.

To determine the effect of PSD on sinter formation and strength at comparable temperatures. Similar to the effect of temperature, SEM and compression strength tests are used to determine this effect.

1.6 Dissertation outline

This dissertation is structured as follows:

- Chapter 1 introduces the project by contextualising it and arguing the need for a study of this nature.
- Chapter 2 provides a review of the literature covering the major themes relevant to this study.
- Chapter 3 outlines the sampling and test procedure followed, both at the smelter and in the laboratory, to investigate the problem.
- Chapter 4 presents and discusses the findings of the entire project.
- Key findings that relate specifically to the research questions are discussed further in Chapter 5.
- Chapter 6 draws conclusions and offers recommendations after evaluation of the findings.

2   LITERATURE REVIEW

This section discusses the major themes that are most relevant to this dissertation. The bulk of the literature review was gathered by evaluating the available literature. A small portion of the literature e.g. smelter layout and the negative impacts of duct blockage on smelter operations, was gathered directly from the smelter personnel during numerous visits as well as email interactions over a period of two years. The main themes that are covered in the literature review are as follows:

- Smelter overview
- Sintering overview
- Manganese furnace-dust characterisation
- Chemical thermodynamics evaluations
- Sampling and statistics

2.1   Smelter overview

The smelter overview looks at the general description of the smelters SiMn production process, as well as information related to duct blockage.

2.1.1   General overview of the smelter

The smelter in question applies open submerged arc furnace technology for the production of SiMn (Steenkamp et al., 2018). The process entails charging into the furnace cold mixtures of several manganese ores, carbon reductants, and fluxes. The products are a SiMn alloy, slag, and dust-laden off-gas.

The off-gas passes through three stages of dust recovery (see Figure 2). There are three units in total. They are arranged such that the coarse dust, labelled stream 1, is recovered first (by the spark trap), the intermediately sized dust (stream 2) is recovered next by two cyclones, and the fine dust (stream 3) is finally recovered by the baghouse and collected in the silo. According to smelter personnel, the reason for this arrangement is that potential damage, caused by impact and abrasion when coarse and intermediate dust comes into contact with downstream units, is reduced. Damage to the bag filters stationed in the baghouse compartments is particularly severe. Figure 3 shows photographs of some of the actual units appearing in Figure 2. It should be noted that all dust samples used for laboratory test work were collected directly from these units over a period of three months. The procedure followed is discussed in section 3.1.1 and Appendix A.
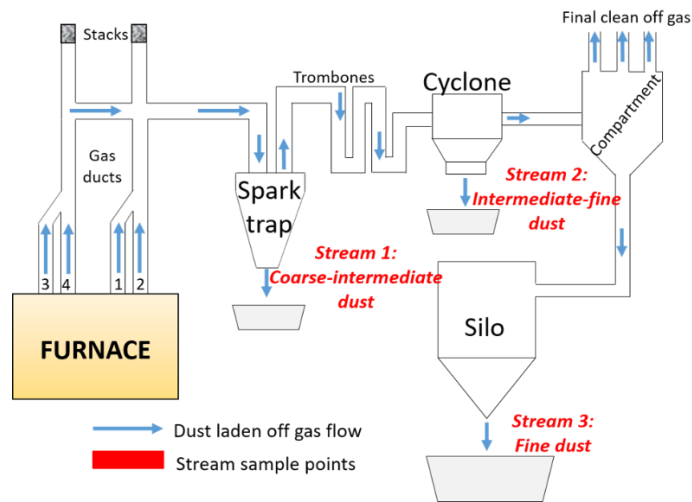
Figure 2: Schematic representation of smelter-dust treatment after smelting
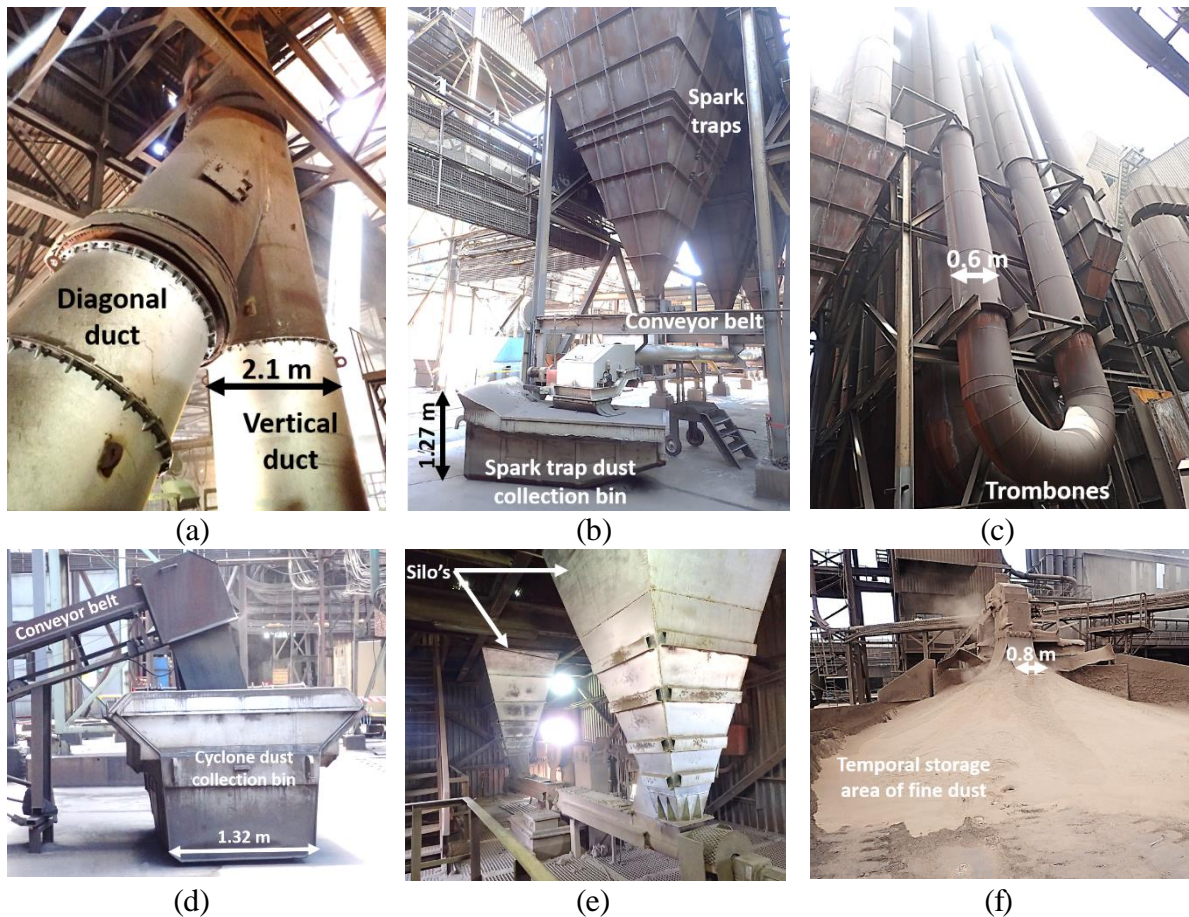
Figure 3: A collage of photographic images taken at the smelter showing some of the units in figure 2: (a) ducts showing diagonal and vertical connections, (b) the spark trap with collection bin for collecting dust from stream 1, (c) trombones for cooling dust laden off-gas, (d) cyclone for collecting dust from stream 2, (e) the silos where fine dust collects from stream 3, and (f) the temporary storage of stream 3 dust. All dimensions expressed in metres.

2.1.2 Duct blockage

According to engineering personnel, during furnace operation the vertical and diagonal sections of the off-gas ducts tend gradually to be blocked by dust in the off-gas. If left unchecked, the accumulation results in complete blockage of the ducts. Besides the sintering of dust as a possible mechanism, foaming could be another possible cause of duct blockages. This mechanism is encountered in ilmenite smelters. There, typically, the slag may foam so severely that molten material is pushed into the ducts where it solidifies, thereby blocking the duct (Jordan, 2011). This occurs in open-bath, closed-roof furnaces where the foamed material channels directly into the ducts. With the smelter in question, though, blockages from foaming are unlikely as the roof is semi-open—i.e., it does not seal to the sidewalls, and thus foam cannot channel directly into the ducts—and any tendency to foaming is dampened by a solid burden of 1–2 m sitting on top of the slag (Steenkamp et al., 2018). Thus, we can rule out the possibility of foaming as a possible mechanism of duct blockages.

Table 2 and Table 3 summarizes several adverse consequences of duct blockages, consequences highlighted by smelter engineering personnel and the production manager. These consequences manifest during normal smelting operation and during maintenance and furnace shutdowns.

As for clearing a blockage, during either short or long shutdowns, the smelter employs external contractors to do the work. They typically use a combination of pressurised water and jackhammers to remove mechanically the build-ups (Engineering Superintendent, pers. comm.).

Table 2: Adverse consequences of duct blockages (according to smelter engineering personnel and the production manager)

Consequences of blockages during normal smelting operations	
Factor affected	**Comments**
Operations	➢ It reduces the effectiveness of the baghouse. A secondary effect of this is that the entire furnace building is covered in dust, which requires sweeping.
Health	➢ Increases workers' exposure to dust, especially those working near the furnace bed. This may lead to an ailment known as manganism. ➢ During periods of high wind the airborne dust can be blown to nearby communities. Dust poses a health risk when inhaled.
Safety	➢ Dust can obscure the vision of personnel working near the furnace bed (e.g., during rabbling).
Environment	➢ Dust is a pollutant when borne by air or water. This pollution can be marked in the vicinity of the smelter.
Finance	➢ These restrictions on and consequences of operation will affect production, and thus revenue, adversely. ➢ The impact affects both variable and fixed costs.

Table 3: Adverse consequences of duct blockages—continued

Consequences during blockage clearance on shutdowns	
Factors affected	**Comments**
Finance	➢ Maintenance costs rise as external contractors are hired to clear the blockage.
Time	➢ Blockages harden in some areas, which then become difficult and time consuming to remove. This translates into losses in production.
Wear and tear	➢ The processes of putting scaffolding in place and clearing the blockage tend to damage the refractory in the off-gas duct.
Safety	➢ The process of removing a blockage places a contractor's safety at risk, as often a blockage is unstable, and shovelling and jackhammering is often required. ➢ The water used may trickle into the furnace and cause an eruption, which can cause an electrode to break or damage to the refractory.

2.2 Sintering overview

This overview describes the basic concepts in sintering, as well as some of the nature of sintering and related phenomena.

2.2.1 Sintering basics

Sintering is a phenomenon encountered in many instances where materials are heated to high temperatures. In simple terms it can be defined as a process whereby materials, usually in contact with each other, agglomerate when heated to an appropriate temperature (Kuczynski et al., 1967). According to Kuczynski et al. (1967) agglomeration is usually accompanied by a decrease in material porosity, an increase in the bulk density of the material, a rounding of sharp edges, and a decrease in particle surface area as particles aggregate. As expected, the more sintered the material, the more apparent these observations will be. In the current study, physical properties such as the particle porosity, bulk density, particle shape, and surface area will not be used to describe the degree of sintering. However, general comments on the degree of friability of agglomerated material – will be made, as well as measurements of the shrinkage/expansion of material—will be conducted. These, along with other physical features of the samples as observed under SEM, will provide useful insights into the degree of sintering in those instances where it is observed.

2.2.2 Mechanisms of sintering

In broad terms, mechanisms of sintering fall into two categories, namely, solid state and liquid state (German, 1996). This classification excludes other complex and rare variations of sintering, such as vapour and vitrification sintering (German, 1996). In solid-state sintering, heat is applied below the melting temperature of all the solids involved, and thus no liquid is formed that induces agglomeration (Leriche et al., 2017). In this case bonds between particles form due to solid-solid interactions. On the other hand, liquid-state sintering occurs through the formation of a liquid phase that acts as a binder between solid particles. In both mechanisms increased sintering progressively leads to an increase in particle size, and can usually be seen under SEM. The growth in particle size is concomitant with agglomeration. Particle boundaries distort over time (Leriche et al., 2017). Figure 4 illustrates this point schematically. Figure 5 illustrates the difference in mechanism between solid-state and liquid-state sintering. Figure 6

shows the external physical appearances of manganese dust, first as an unsintered, pressed pellet, then after sintering for 15 minutes at 1200°C; the third image shows a fragment of the sintered pellet. It is clear, and reported by numerous sources, that sintering can cause changes that are visible to the naked eye (Shen, 2009). Among these are changes in the dimensions of a sample, e.g., volume, height, and diameter. The shrinkage or expansion of a sample at a specific firing temperature can be determined from these changes (Bendaoudi et al., 2018; Quijorna et al., 2014; Romero et al., 2008) These three sources also report that expansion is usually the result of either phase transformations on sintering or bubble formations caused by gases (i.e., a bloating effect), whereas shrinkage results from liquid formation and/or densification of the material. Figure 7 shows a SEM micrograph depicting the microstructural appearance of a well sintered sewage sludge sample. One can see that the structure of the sample after sintering was both well-bonded i.e. good particle to particle attachment and porous.
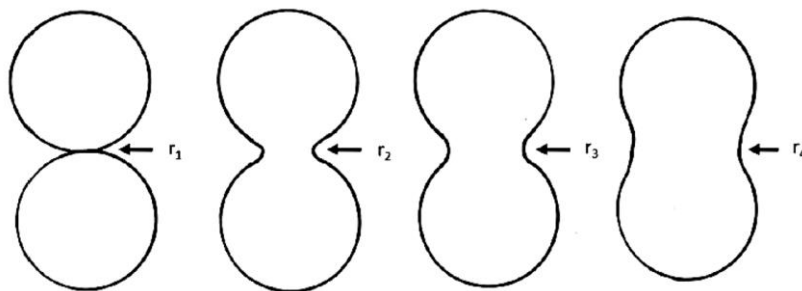
Figure 4: Sintering producing changes that result in grain size growth (Leriche et al., 2017)
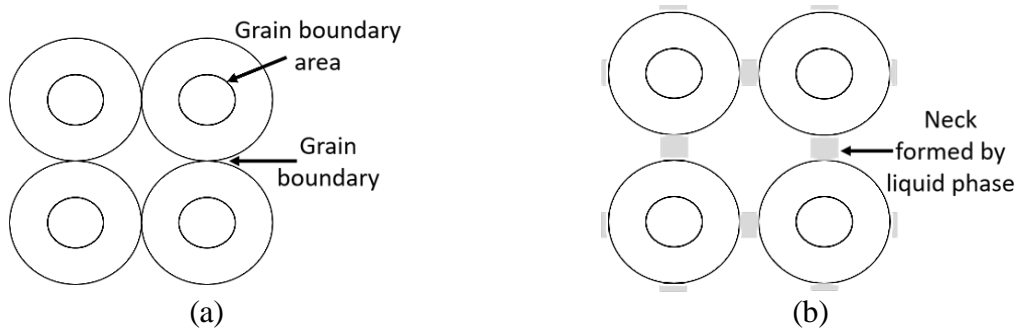
Figure 5: Schematic representation of (a) solid-state sintering, and (b) liquid-state sintering (Shimonosono et al., 2014)
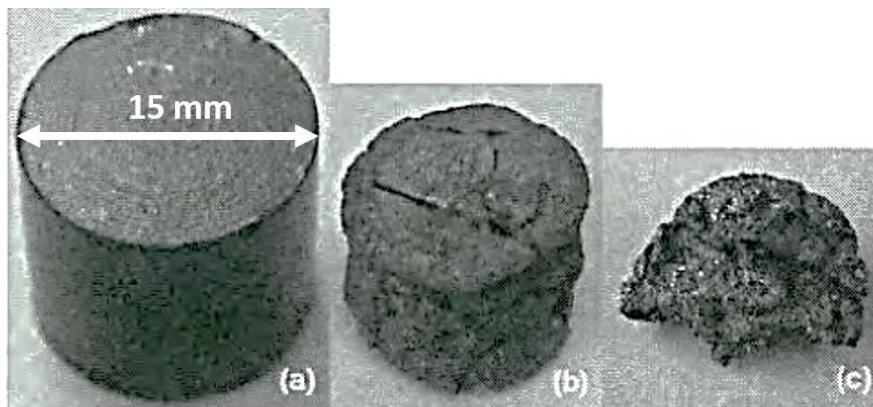
Figure 6: Photographs showing (a) an unsintered pellet, (b) a sintered pellet after 15 min at 1200°C, and (c) a fragment of sample b (after Shen, 2009)

For both solid- and liquid-state sintering, a number of parameters have a bearing on sintering, its mechanism and progression. These parameters include particle size, PSD, temperature, material composition, gas composition, applied pressure, and residence time (Kingery, W.D. et al., 1960; Rahaman, 2003). As a rule, in order to evaluate accurately the effect of any one parameter on sintering all other parameters must be kept constant. For that reason, in this study parameters such as gas composition, residence time, and applied hydraulic-press pressure are kept constant so that the effect of temperature and PSD on sintering can be determined. The following section describes how these parameters affect sintering.
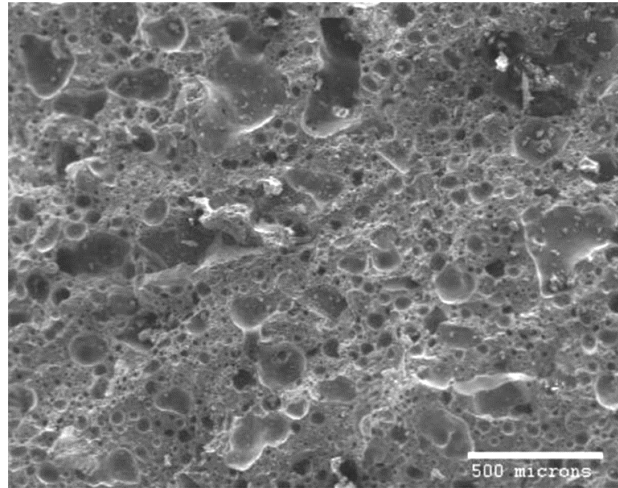
Figure 7: SEM micrograph showing the typical appearance of well sintered ash from sewage sludge (Cheeseman et al., 2003)

2.2.3 Sintering of manganese ores

Manganese ore fines along with coke/coal, dust/sludge, and in some cases fluxes and/or other additives are generally mixed together and then agglomerated by sintering to produce a lumpy and porous product. The sintering temperature varies with the type of manganese ore being processed. For example, Malan et al. (2004), who sought to optimise manganese sinter plants process parameters and design, quoted a sintering temperature of 950°C and higher. Riku (2001) in demonstration of the operation of the then new Outokumpu steel-belt pelletising-sintering process, stipulated a sintering temperature of at least 900°C depending on the type of ore. In a review of the sintering process as applied to manganese ores, Gordon et al. (2018) gives a temperature of between 800 and 900°C.

Given that manganese ores are sintered at these temperatures, sintering is a possibility in cases where the duct temperature is in this range.

2.2.4 Relationship between sintering and compressive strength

The compressive strength of a material is defined as the measure of the material's resistance to disintegration under a crushing load (Hsiao et al., 1995). To measure the compressive strength a standard compression test is used. ISO 4700 was developed for iron ores, but has been applied to other materials. In this work, the ISO 4700 method can be applied to measure – quantitatively, the strength of the manganese dust after high temperature firing.

A less conventional measurement of the sinter strength, which was developed by Kobayashi et al. (2014), may be used to provide qualitative indications of the strength of the fired manganese dust; it uses a sintering index scale based on the response of a sintered sample to a blow by a hammer. The degree of sintering is reported on a scale of 1 to 5, with 5 indicating a very well-sintered sample – very resistant to disintegration.

A relationship exists between the sintering progression of a sample, and its compressive strength (Bendaoudi et al., 2018; German, 1996). In general, as sintering is accompanied by a decrease in material porosity and an increase in particle size—i.e., an increase in material densification—the more sintered a material, the higher its compressive strength will be (German, 1996; Kingery, W.D. et al., 1960; Leriche et al., 2017; Rahaman, 2003). This is so because densification stops crack propagation by filling the air gaps with material of higher compressive strength (Bendaoudi et al., 2018; German, 1996; Leriche et al., 2017; Quijorna et al., 2014). Figure 8 illustrates how sintering generally decreases the volume of pores whilst increasing the size of the particles in a sample.

The relationship between sinter formation and compressive strength is useful in the current research in that it gives an indication of the degree of sintering with change in temperature and PSD. This serves as a valuable complement to the microstructural analysis conducted by SEM-EDS. It should be noted that despite the usefulness of compressive strength as a measure of sintering, the technique must be used in conjunction with a microstructural analysis technique – in this instance SEM-EDS, in order to confirm the presence of sintering. This is because factors not considered might affect the compressive strength or in rare instances a sample might show a decrease in compressive strength with an increase in sintering.
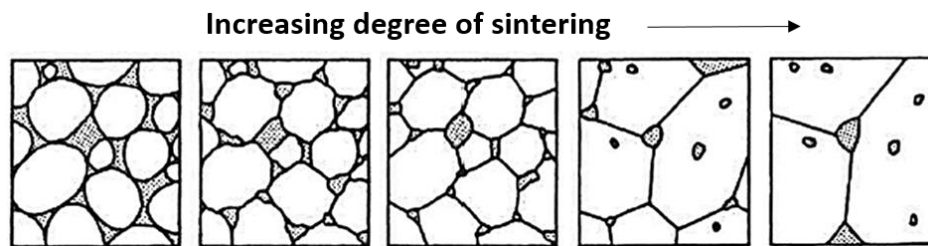
Figure 8: Conceptual sketches showing the general pore structure and particle size a sintering increases sintering. There is a decrease in porosity and an increase in particle size with sintering (German, 1996)

2.2.5   Relationship between firing temperature and compressive strength

Another relationship of interest is that between the firing temperature (otherwise known as the baking or sintering temperature) and compressive strength of sinters. As heating affects the particle arrangement, the firing temperature is expected to have a direct effect on the compressive strength. Several authors have reported on this relationship. (Shimonosono et al., 2014) for example, noted an almost linear increase in the compression strength with increase temperature for silicon carbide ceramics. (Hu and Wang, 2010) studied the same phenomena for yttria-stabilised zirconia ceramics; they, too, noticed the same relationship, but in their study the compression strength increased significantly with increasing temperature. The same observations were made in the sintering of Co-Cr-Mo/58S bioglass porous nano-composite, sewage sludge ash, and ceramic bodies from contaminated marine sediments (Dehaghani and Ahmadian, 2015)(Lin et al., 2006) (Romero et al., 2008). Several examples depicting the

proportionality between sintering temperature and compressive strength are shown graphically in Figure 9. Where sintering is being evaluated, it is typical for firing tests to be conducted in a muffle furnace (Quijorna et al., 2014; Shen et al., 2007; Wang et al., 2013).

(a)

(b)
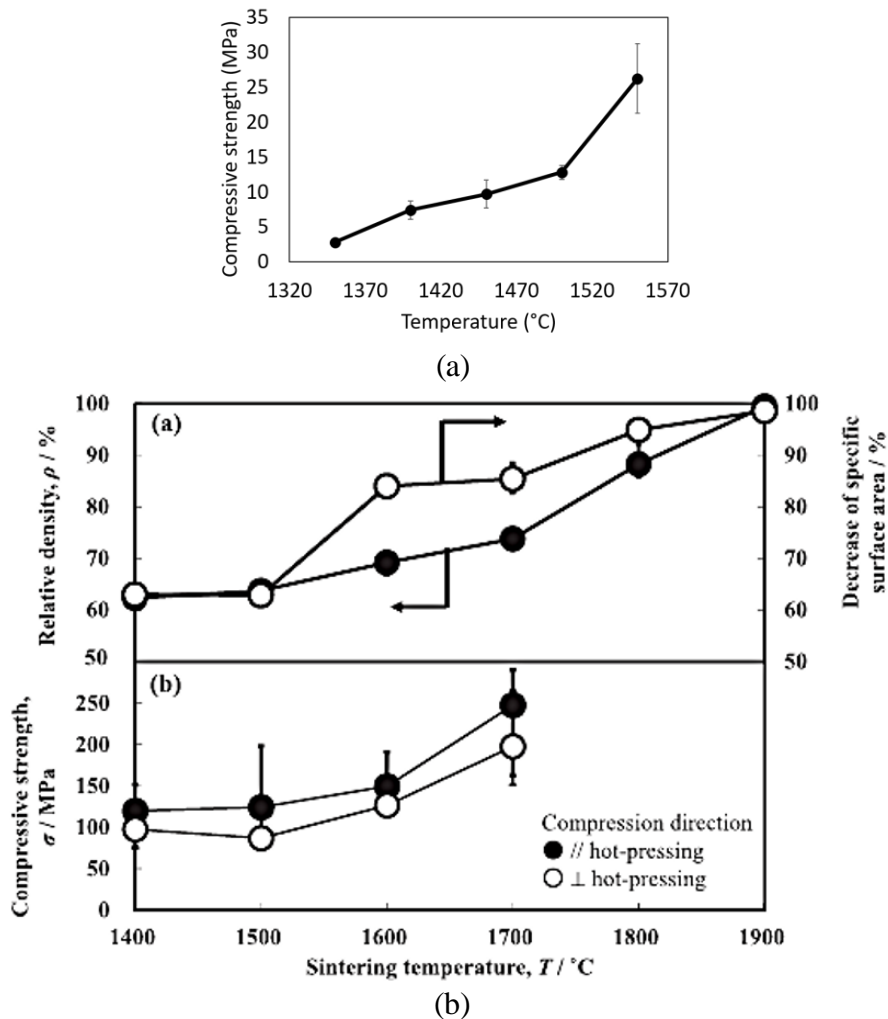
Figure 9: Compressive strength as a function of firing temperature: (a) for yttria-stabilised zirconia ceramics at 1350–1550°C (Hu and Wang, 2010); (b) for silicon carbide ceramics hot-pressed at 1400–1900°C; in addition the increases in relative density and decrease in specific surface area are also shown (Shimonosono et al., 2014)

2.2.6 Relationship between the particle size, PSD and compressive strength

As far as the relationship between PSD and compressive strength goes, it is known that the presence of coarse particles in a sample, assuming that they are present as the overwhelming dominant particle size in a sample with a very narrow PSD, increase the void fraction of that sample, i.e., increases the porosity of the sample. This is assuming that there's little to no fines to fill the interparticular voids between the coarse particles. The increase in the porosity of any material, decreases its compressive strength. Overall though, the largest bearing factor in terms of the compressive strength of a material in relation to the particular size, is the width of the distribution.

As for the relationship between absolute particle size and compressive strength, smaller particles generally have a higher compressive strength when compacted for sintering. This is

13

the case when compared to the same material compositionally and otherwise, but with larger particles. This was for example observed in the sintering behaviour of several materials e.g. refractory aggregates, 316 stainless steel, and metal powders (Park et al., 2013; Robertson and Schaffer, 2009; Varela et al., 1990). Figure 10 (a) depicts graphically one of those examples where the compression strength of titanium powder (represented here by the sintering density), increased with decreasing particle size (Robertson and Schaffer, 2009). The reason for the higher strength in cases of small particle sizes is that they pack much more densely than larger particles and will thus have a lower fraction of pores and increased particle to particle contact area (thus lower activation energy), compared to coarser particles compressed at the same pressure (Park et al., 2013). To summarise this a commonly accepted relationship is that that the higher the porosity of a material, or the larger the pore sizes; the lower will be the corresponding compressive strength (Dehaghani and Ahmadian, 2015; German, 1996; Hu and Wang, 2010; Rahaman, 2003; Romero et al., 2008). The rest of Figure 10, that is, (b-d), depicts graphically, several relationships between porosity, pore and particle size, temperature and compressive strength.

The implication of these observations is that, under similar firing conditions, the finest-sized material (stream 3), will have a higher compressive strength than the coarser dust (stream 1). This assumes that stream 1 is predominantly composed of coarse particles – with very few fine particles; and stream 3 is made of predominantly fine particles – with very few coarse particles. Furthermore, the compressive strength is expected to increase with an increase in firing temperature.

(a)   (b)

(c)

(d)
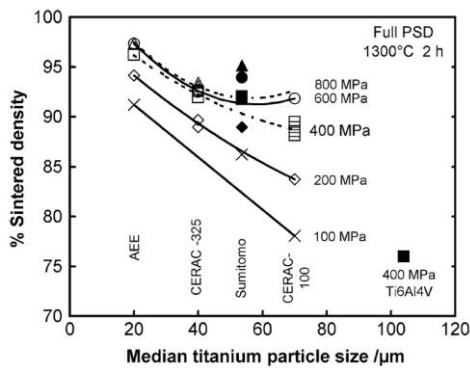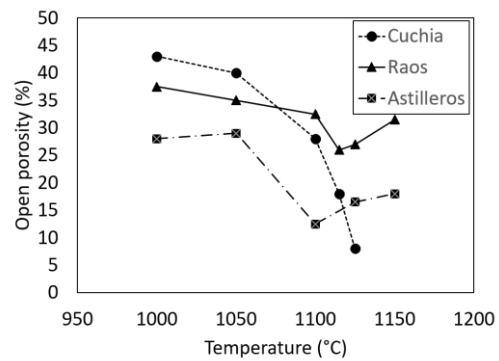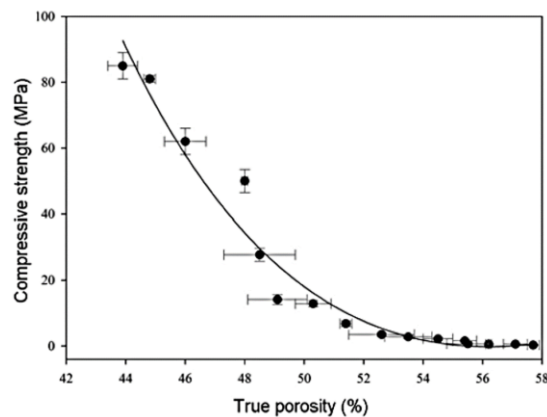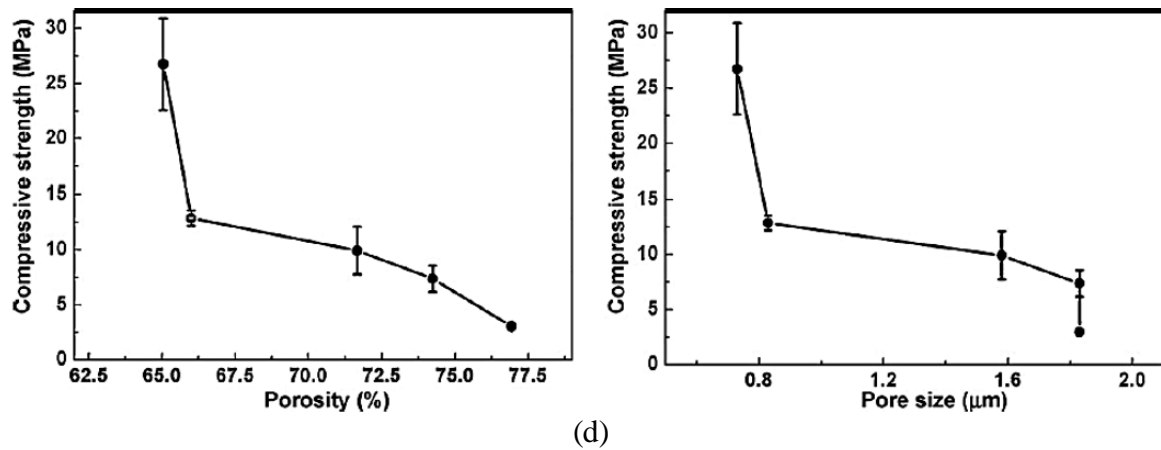
Figure 10: The effects of: (a) fired titanium powder particle size on the sintered density of titanium powder (Robertson and Schaffer, 2009); (b) temperature on the open porosity of ceramic bodies from contaminated marine sediments(Romero et al., 2008); (c) true porosity of the compressive strength of Co-Cr-Mo/58S bioglass porous nano-composites (Dehaghani and Ahmadian, 2015); (d) porosity and pore size on the compressive strength of yttria-stabilised zirconia ceramics(Hu and Wang, 2010)

2.2.7 Other parameters affecting sintering

Three other parameters—sintering time, sintering atmosphere, and heating rate—also have an effect on sintering. The following comments concerning them were drawn from literature:

- *Sintering time.* An increase in sintering time usually results in an increase in the extent of sintering in a material, as well as an increase in the compressive strength of that material. This increase however is not indefinite and reaches a peak at some point depending on the material being processed (Dehaghani and Ahmadian, 2015; Lin et al., 2006). Most sintering tests ran for 0 to 4 hours (Hu and Wang, 2010; Liu, 2017; Shimonosono et al., 2014)
- *Sintering atmosphere.* There is no standard effect of the composition of the atmosphere on sintering, although the gas atmosphere does play a role in sintering. Some of the factors that determine the relationship are the: composition of the gas, the inherent formation of gases (such as CO_2 when $CaCO_3$ dissociates in carbonate-rich ores), gas flow rate, solid material type, and the permeability of the solid to gas (Budin et al., 2017; German, 1996; Wang et al., 2001). Composition includes no gas at all—a vacuum, in other words (German, 1996). Since a natural air atmosphere would be used in this project (as is the case in the open/semi-open SAF where air ingress is a reality), it is expected that any carbon contained in the dust would be combusted, whilst the oxidation state of MnO_x and FeO_x species would also be impacted (Makino et al., 2013; Suarez et al., 2008; Zaki et al., 1997). The specific impact of carbon combustion and MnO_x-FeO_x oxidation, on sintering, will not be examined as it is beyond the scope of this dissertation.
- *Sintering heating rate.* As shown by (Chu et al., 1991; Stanciu et al., 2001), the heating rate has an effect on the sintering progression as well. Generally a decrease in heating rate results in increased sintering.

For the purposes of this study, these parameters are kept constant—or near enough for those that cannot be tightly controlled—in order to isolate the parameters that are in focus in the study, viz., temperature and PSD. Figure 11 demonstrates the effects of sintering time, atmosphere, and heating rate on a material.
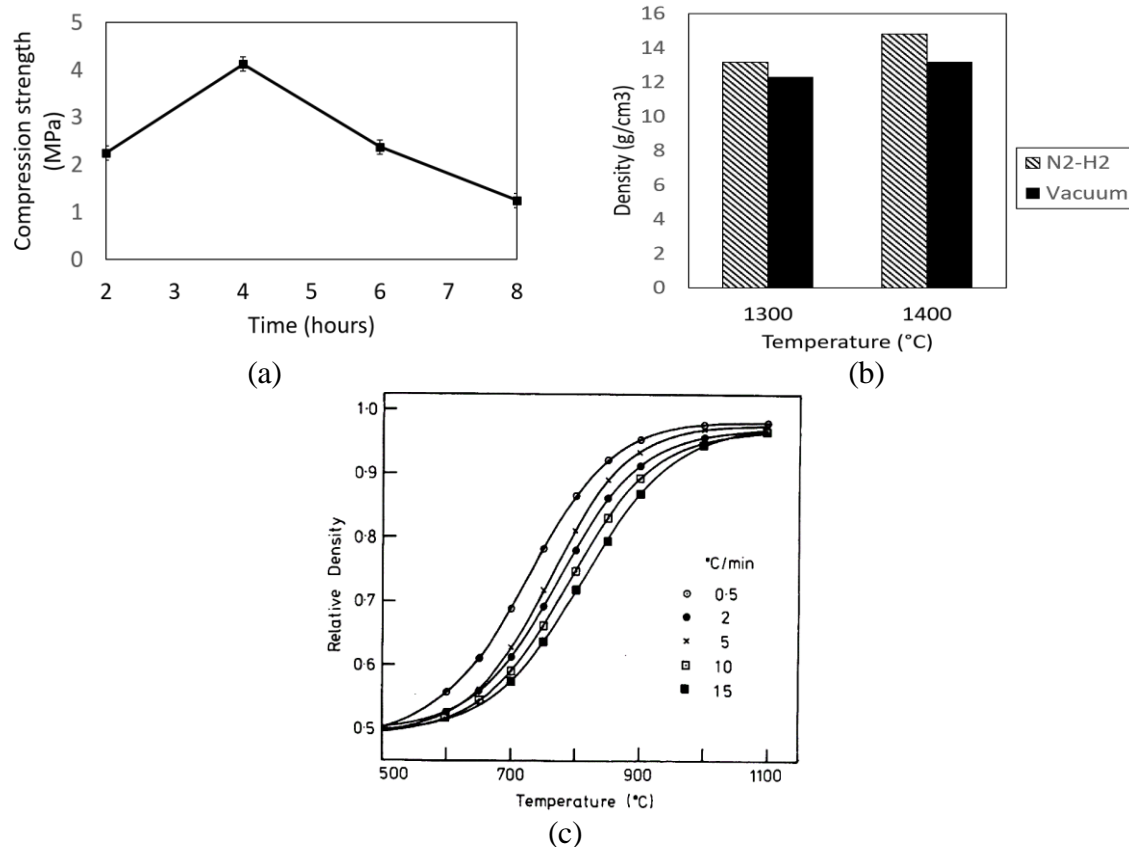
Figure 11: The effects of: (a) sintering time on the compressive strength of alumina foam ceramics (Liu et al., 2017); (b) atmosphere on the densification (measured using bulk density) of sintered tungsten carbide (Budin et al., 2017); and (c) heating rate on the densification (measured by density) of zinc-oxide powder (Chu et al., 1991)

2.3 Manganese furnace-dust characterisation

This section looks at what has been published on typical characterisation methods, and at the results of previous exercises in characterisation, especially at different manganese operations.

2.3.1 Background of manganese furnace dust

In the industry manganese dust refers to dust emanating from the off-gas of a high-carbon ferromanganese (HCFeMn), a SiMn, or a ferromanganese (FeMn) furnace. The dust is channelled either to the baghouse through ducts and stacks (for a dry off-gas treatment process) (Steenkamp et al., 2018), or to wet scrubbers to produce a sludge (for wet processes) (Gaal et al., 2010). Depending on the individual preference of each smelter, along with the environmental laws under that jurisdiction, the dust produced may be re-treated either for the recovery of valuables contained in the dust (Martins et al., 2008), or for the removal of impurities in the dust, prior to discarding it according to appropriate environmental waste regulations. Owing to the growing worldwide interest in waste valorisation, partly due to the depletion of natural resources and partly due to increasingly stringent environmental legislation, most smelters have characterised their off-gas dust with a view to possibly implementing a treatment process. The typical methods of characterisation and the findings for off-gas dust from SiMn, HCFeMn, and FeMn production are described in the following sections.

2.3.2 Particle size distribution

PSD describes the fractions of particles—foremost by volume, and if density is uniform, by mass—residing in intervals of size (Ujam and Enebe., 2013). There are different techniques for determining PSD, for example, screening using sieves (dry screening up to 38 μm particles, and wet screening below this size), Malvern Mastersize analyser (particles up to 0.02 μm) (Rawle., 2015). Of these techniques, the screening by sieves, which collects material, dry or wet, on a series of sieves of progressively finer aperture, is commonly employed for analysing furnace dust. This is especially so for electric arc furnace (EAF) dust (Xia., 1997). Typical measurements of the PSD of dust from silicomanganese, ferrosilicon, and ferromanganese operations are summarised in Table 4. In addition to the PSDs of dust from these operations, the PSD of dust from other non-manganese operations is included in the same table for comparison. From the table it can be seen that the majority of furnace dust, regardless of the operations from which it stems from, was fine-sized. It would be interesting to compare the PSD of the dust gathered from the smelter in question with those of other silicomanganese operations in Table 4; this would give further insights into the reasons behind the fineness of the dust particles-whether it's a result of the silicomanganese smelting process itself, or practises within each smelter.

Although a Malvern Mastersize analyser may be best for analysing very fine material e.g. those with d_{50} less than 10 μm, for the purpose of this study, screening using sieves technique is adequate, since only a general characterisation of the dust streams to coarse, intermediate, and fine PSD was sought.

Table 4: PSDs of EAF dust from several operations

Source of dust	Size fraction (μm)	Reference
FeMn, SiMn, and FeSi		
SAF sludge (FeMn and SiMn)	d_{50} = 1–4	(Gaal et al., 2010a)
SAF (FeMn and FeSi)	0.1–10 (20–30%); 10–40 (25-35%); 40–80 (10--40%); above 80 (20–40%)	(Vaish, 1994)
EAF (SiMn and FeMn)	90% < 2.83	(Kadkhodabeigi et al., 2015)
FeMn	80% < 45	(Kadkhodabeigi et al., 2015)
Different steels and ferrochrome (FeCr)		
EAF steelmaking	5% > 19	(Machado et al., 2006)
FeCr converter	10% > 9.94	(Omran and Fabritius, 2017)
EAF stainless steel	10% > 9.83	(Omran and Fabritius, 2017)
EAF carbon steel	10% > 9.2	(Omran and Fabritius, 2017)

2.3.3 Chemical composition

In various manganese and silicomanganese dust investigations observed in literature, the analysis of the chemical composition has always been one of the standard characterisation methods (Gaal et al., 2010a; Rama Murthy et al., 2018; Shen et al., 2007; Zhong et al., 2018) The chemical species typically analysed are Mn, Fe, Si, Al, Mg, Ca, Na, Zn, K, and P (Gaal et al., 2010a; Rama Murthy et al., 2018; Shen et al., 2007; Zhong et al., 2018). The non-metallic elements typically analysed are C, B, and S (Gaal et al., 2010a; Rama Murthy et al., 2018; Shen

et al., 2007). At times, especially when evaluating the environmental impact of waste, the oxides of or elements As, Cd, and Hg are also analysed (Gaal et al., 2010a). The techniques commonly used are X-ray florescence spectrometry (XRF), carrier gas hot extraction (LECO), and the two analyses associated with inductively coupled plasma (ICP-OES and ICP-MS) (Peng et al., 2008; Shen et al., 2007; Zhong et al., 2018). Of the techniques, XRF is favoured least because it is a semi-quantitative analysis and may not give exact accurate compositions. The elements listed in this section, except those analysed for environmental impact studies, are analysed in this study in order to evaluate the phase chemistry of the dust. This is especially important as the composition of dust plays a central role in sintering (Rahaman, 2003). Table 5 summarises chemical compositions of dust obtained from manganese and silicomanganese operations. Chemical compositions labelled "A" and "B" are reported in the literature and relate to the smelter that is the subject of this dissertation. It was unclear however which dust stream and which furnace were sampled.

Table 5: Chemical compositions of dust from several manganese operations:
A→ SiMn operation, B→ SiMn operation, C→ FeMn operation,
D→ SiMn/FeMn operation, E→ SiMn/FeMn operation, F→ SiMn/FeMn operation,
G→ FeMn operation, and H & I→ SiMn/FeMn operation (in mass %)

Species	Operation								
	A[†]	B[†]	C	D	E	F	G	H	I
MnO	35.1	31.6	61.1	26.6	21–45	34.8	42–46	—	—
$MnCO_3$	—	—	—	—	—	—	—	40.0	75
SiO_2	36.3	38.8	7.4	22.4	—	9.6	4–8	25.0	5
Fe_2O_3	1.4	1.2	6.7	1.2	—	2.1	10–12	1.0	2
CaO	7.4	8.0	2.6	4.6	—	—	8–10	6.0	4
MgO	6.8	7.3	3.8	3.1	—	—	—	—	—
Al_2O_3	4.0	3.6	4.1	3.9	—	—	8–12	3.0	2
K_2O	3.3	—	3.6	22.0	—	3.9	—	6.0	4
Na_2O	1.6	—	0.3	2.6	—	0.9	—	—	—
ZnO	0.3	0.4	—	2.1	0.1–2	2.7	—	—	—
Cl	2.0	—	—	1.7	—	—	—	—	—
SO_3	1.8	—	—	8.6	—	—	—	—	—
C	—	—	1.4	—	9–22	—	—	—	—
S	—	—	0.2	—	—	—	—	—	—
P	—	—	0.3	—	—	0.04	—	—	—
Pb	—	—	—	—	—	0.35	—	—	—
LOI	—	—	6.9	—	—	—	—	—	—
Total	100.0	90.9	98.4	98.8	30–69	54.4	72–88	81.0	92.0
Source	(1)	(2)	(3)	(4)	(5)	(6)	(7)	(8)	(8)

[†] Dust from the smelter that is the object of this study; — not reported;

Source (1) (Nkosi et al., 2011)(2) (Steenkamp et al., 2018); (3) (Rama Murthy et al., 2018); (4) Zhong et al., 2018; (5) Shen et al., 2007; (6) (Gaal et al., 2010a); (7) Vaish, 1994; (8) Riku, 2001

2.3.4 Phase-chemical composition

A full characterization of any dust sample must include details of phase-chemical compositions (by XRD and SEM-EDS) and the microstructural features, such as particle size, particle shape—angular particles typically indicate directly entrained raw dust; spherical particles are an indication of phases formed from liquid or condensed vapour (Guézennec et al., 2005)—and the associations of phases (by SEM-EDS). Literature reviewed for FeMn and SiMn dust showed that the techniques commonly employed for determining phase-chemical composition are XRD and SEM-EDS. Table 6 presents a summary of the typical phases encountered in SiMn and FeMn dust from different operations, phases identified by XRD. In addition to crystalline phases, (Ravary and Hunsbedt, 2013) also reported the presence of amorphous material in SiMn dust. One of those amorphous/semi-amorphous phases, as determined by a combination of XRD and SEM-RDS, is silica (Groot et al., 2013; Ravary and Hunsbedt, 2013). It would be useful to confirm the presence and amount of silica. Another noteworthy study would be to investigate its effect on sintering. Table 7 summarises the phase-chemical compositions of dust gathered from a previous study of the smelter in question. For reasons similar to those given for the bulk chemical composition, the phase-chemical compositions of dust examined in this study may differ from those examined in other studies.

In the current research, XRD and SEM-EDS are crucial not only for the initial phase-chemical characterisation of the sampled dust from the baghouse, but also for the evaluation of sintering in the fired sample products. In the case of the latter, these techniques provide a qualitative assessment of sintering. Figure 12 to Figure 16 and Table 8 show examples of qualitative changes recorded by SEM and XRD as a result of sintering. Each figure and table is explained briefly:

- The dust from a silicomanganese smelter (smelters A and B in Table 5) – from the image the following is seen: angular and spherical phases, a variety of phases including alloy (white) and slag (dark amorphous phase); the PSD is broad (see backscattered-electron [BSE] micrograph Figure 12).
- Sintering observed in Waelz slag from EAF dust – there is a clear progression of sintering with increasing temperature. This is especially clear in the test conducted at 1000°C and above (see Figure 13).
- Sintering observed in ceramic bodies from marine ceramics – sintering is seen to increase with increasing temperature. This is striking in the glass-like structure (with strong bonds) of the sample treated at 1150°C (see Figure 14).
- Sintering observed for a Co-Cr-Mo/58S bioglass porous nano-composite – there is a clear progression of sintering with temperature. This can be seen in the increased neck formation, which causes agglomeration as temperature increases (see Figure 15).
- A change in the particle size of manganese samples due to differences in sintering temperature (see Figure 16).
- Phase changes in manganese oxides as a result of sintering at 600–1000°C. These ores are from West Sumatra (Table 8).

19

Table 6: Summary of the typical minerals and phases found in FeMn and SiMn furnace dust from several operations (Shen et al., 2007; Zhong et al., 2018)

Main components	Chemical formula	Mineral name
Mn-O	Mn_3O_4	Hausmannite
	MnO_2	Pyrolusite
	MnO	Manganosite
Mn-Si-O	$MnSiO_3$	Pyroxmangite
Mn-CO_2	$MnCO_3$	Rhodochrosite
Mn-Ca-CO_2	$(Ca,Mn)CO_3$	Manganoan calcite
Si-O	SiO_2	Quartz
K-Mn-O	$K_2Mn_4O_8$	Potassium permanganate
K-S-O	K_2SO_4	Arcanite
	K_2S	Potassium sulphite
	K_2SO_3	Dipotassium sulphite
K-Cl	KCl	Sylvite

Table 7: Phase-chemical compositions of silicomanganese dust gathered from the smelter in this study. Phases identified by XRD (Nkosi et al., 2011)

Chemical formula	Mineral name (phase type)	Phase dominance
$CaMgSi_2O_6$	Diopside (slag phase)	Major
$Mn_7O_8(SiO_4)$	Braunite (ore mineral)	Major
$MnFe_2O_4$	Jacobsite (ore mineral)	Major
SiO_2	Quartz (ore mineral)	Major
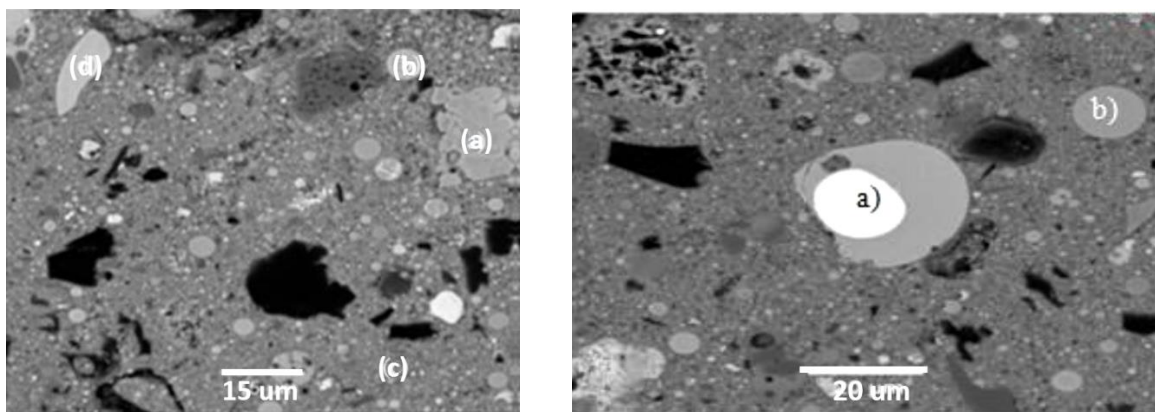
Figure 12: SEM BSE micrograph showing, left - micro-texture of EAF dust with (a) agglomerated phase, (b) spherical phase, (c) ultra-fine phases, and (d) irregularly shaped phase; and right - another section of the same dust sample with (a) homogenous alloy sphere corresponding to EAF dust, (b) homogeneous sphere of slag (silicate) composition (Nkosi et al., 2011)
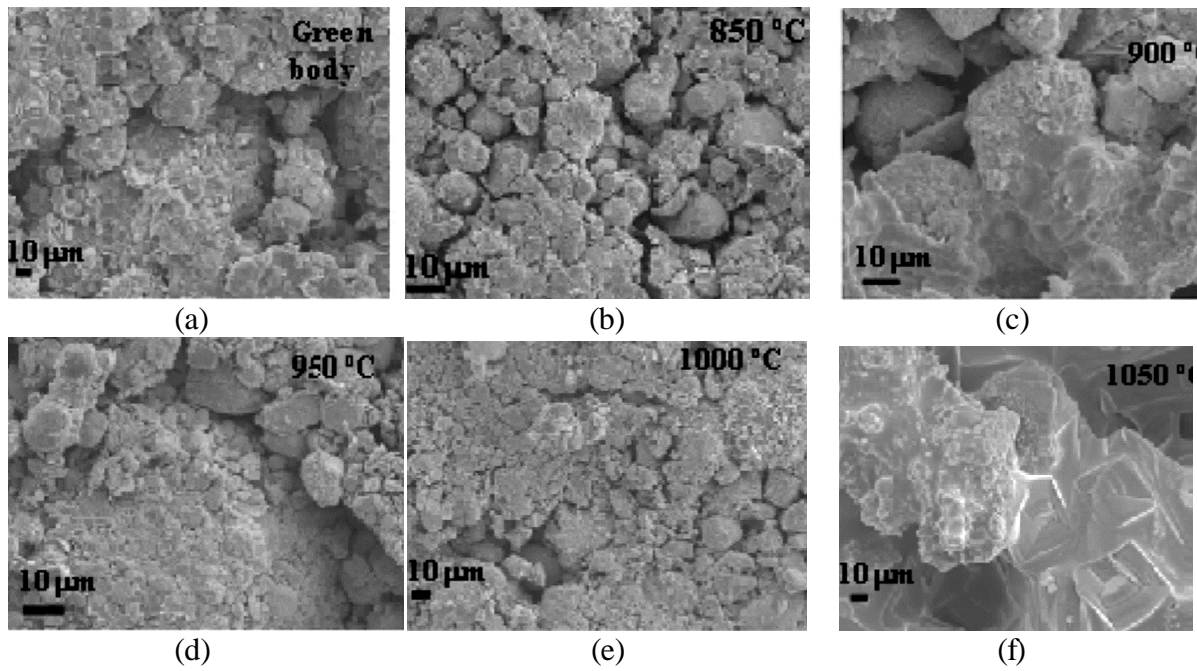
Figure 13: SEM secondary micrographs of Waelz slag fired at different temperatures (a) green body (unfired), (b) 850°C (incomplete sintering), (c) 900°C (incomplete sintering), (d) 950°C (incomplete sintering), (e) 1000°C (complete sintering), and (f) 1050°C (complete sintering) (Quijorna et al., 2014)
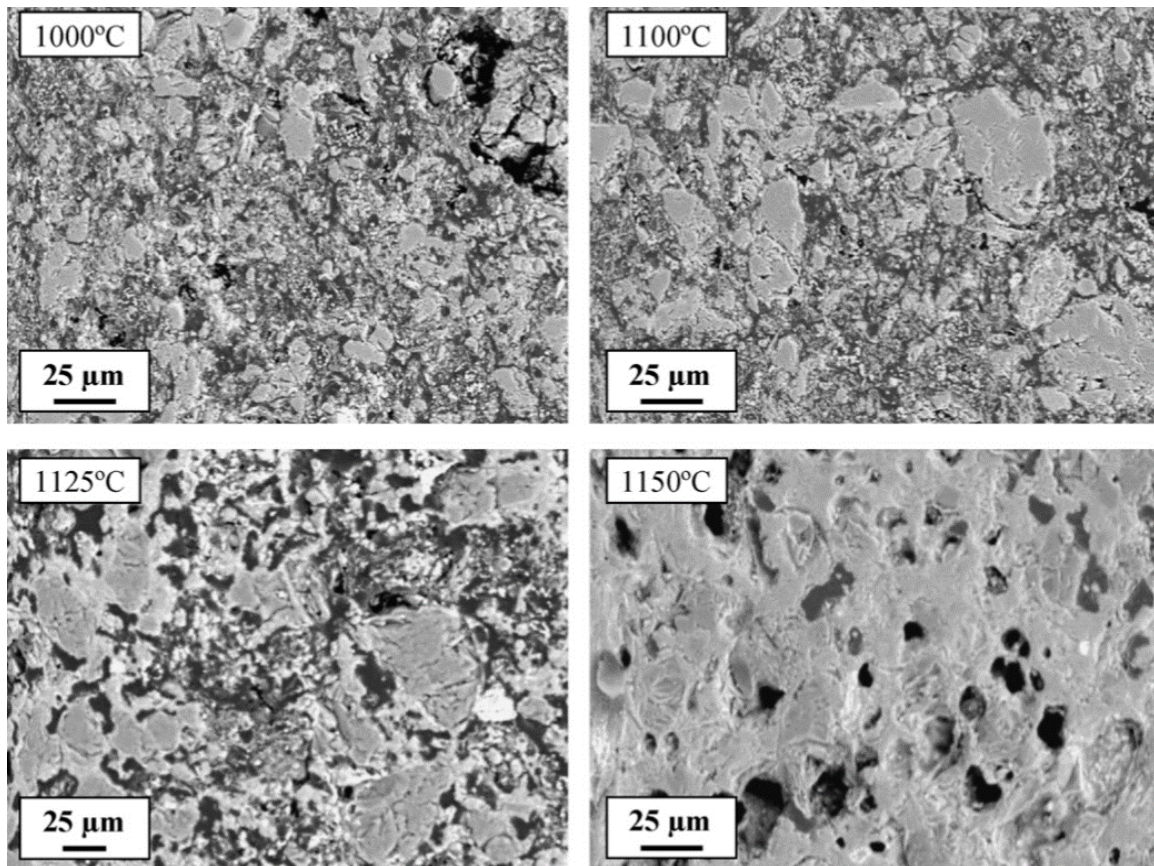
Figure 14: SEM BSE micrographs of compacts of Cuchia sediment fired at 1000–1125°C (Romero et al., 2008)

21
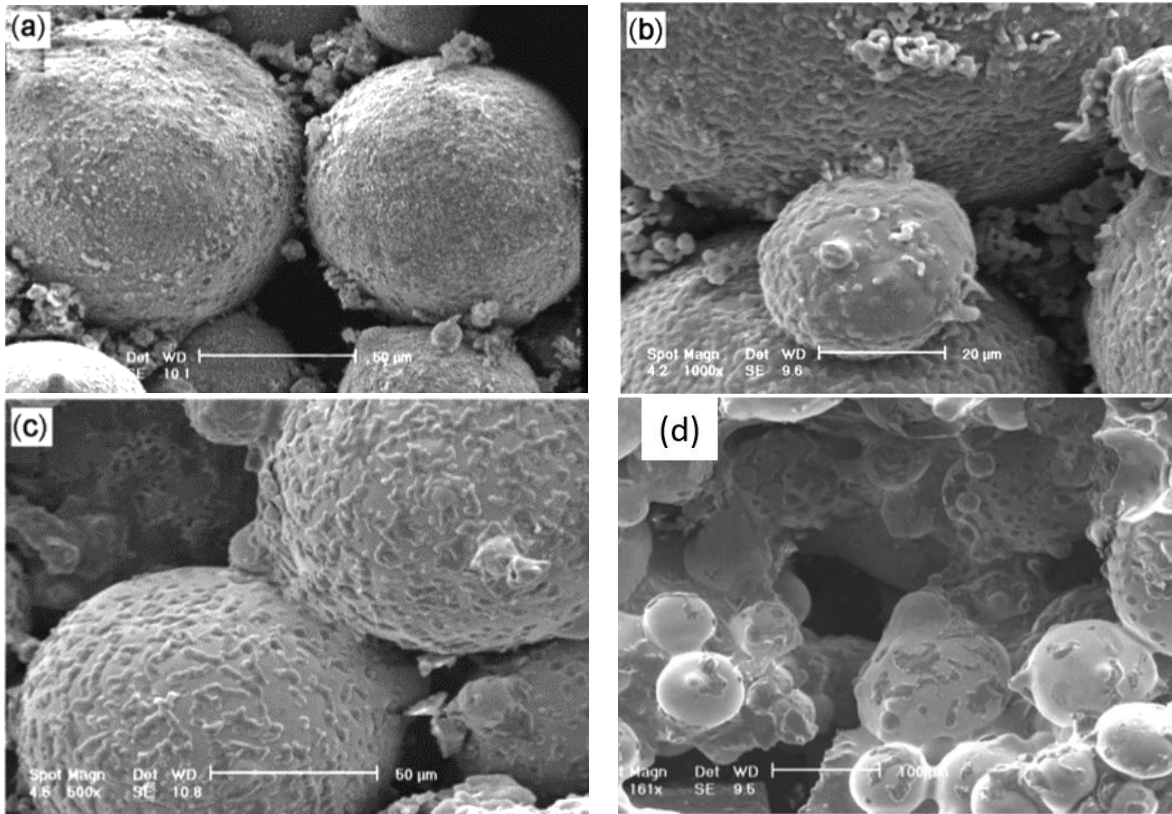
Figure 15: Example of sintering in a Co-Cr-Mo/58S bioglass porous nano-composite observed in SEM (secondary-electron images) for temperatures (a) 1100°C, (b) 1150°C, (c) 1200°C, and (d) 1250°C, all held at temperature for 3 hours (Dehaghani and Ahmadian, 2015)
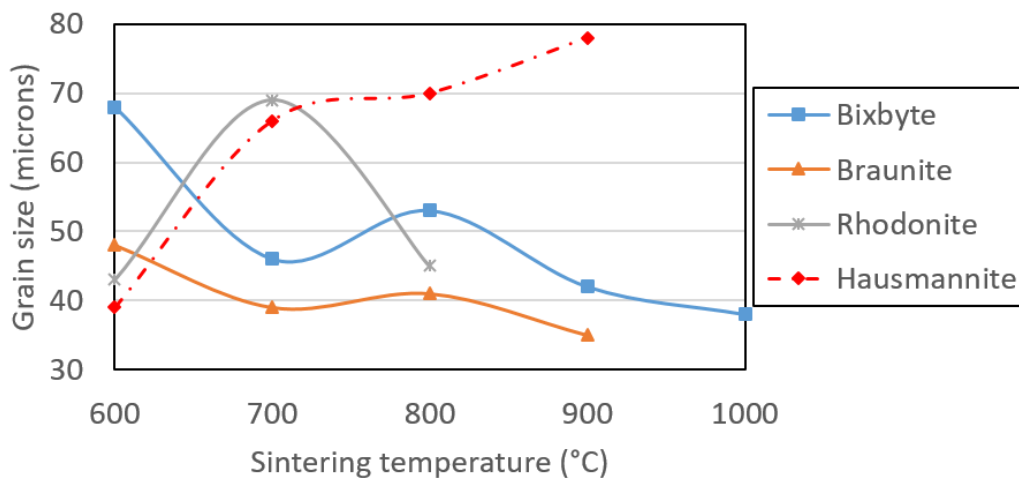
Figure 16: Changes in particle size of Mn-bearing phases with variation in temperature from 600 to 1000°C (Fauzi et al., 2018)

Table 8: Manganese oxide phases formed at different sintering temperatures.
Non-Mn-bearing phases are excluded (Fauzi et al., 2018)

Temperature (°C)	Phases					
	Pyrolusite	Hausmannite	Rhodonite	Bixbyite	Braunite	Coesite
26	✓	—	—	—	—	✓
600	—	—	✓	✓	✓	—
700	—	✓	✓	✓	✓	—
800	—	✓	✓	✓	✓	—
900	—	✓	—	—	✓	—
1000	—	✓	—	—	✓	—

2.4 Chemical thermodynamic evaluation

FactSage is a thermochemical software and database package that can run a range of desktop-based thermodynamic calculations, primarily those in pyrometallurgy (FactSage, 2007). It comprises several modules (these are the built-in channels where specific evaluations may be done), each with a unique feature that permits a specific evaluation. For example, the reaction module is used for evaluating single reactions; the predominance diagram module depicts the thermodynamically stable phases as a function of gas partial pressure; the phase diagram module for plots phase diagrams of interest. Of interest in this study is the equilibrium module, abbreviated to *Equilib*. The minimization of Gibbs free energy (coincident with equilibrium) drives it. The programme gives details of the phases (both compounds and solutions) thermodynamically stable under the specified conditions (FactSage, 2007).

For this study the equilibrium module is useful in that it sets out the effects of temperature on the formation of liquid and solid phases at equilibrium, phases induced by sintering. In addition to this, evaluations can be run to determine if the observed sintering of particles occurred through a solid or liquid mechanism. It does so by determining if the particles observed in the laboratory are solid or liquid at the firing temperature. This would otherwise be difficult and time-consuming; the theory gives a ready, good approximation.

It should be noted that since the thermodynamic evaluation does not account for reaction kinetics, FactSage does not evaluate the influence of PSD on sintering. Also, the programme assumes equilibrium, which is not always the case in reality, and thus discrepancies can exist between the practical observations and FactSage calculations (FactSage, 2007). The simple question that FactSage answers is whether the reaction is thermodynamically feasible or not (FactSage, 2007).

2.5 Optical pyrometry

An optical pyrometer measures the temperatures of surfaces. It does so by measuring the amount of thermal radiation released by incandescent bodies (Waidner and Burgess, 1905). One of the advantages a pyrometer has over thermocouples or resistance temperature detectors is that it can measure temperatures of objects from a distance without any physical contact between the object and the instrument or probe. Of importance in pyrometric measurements, however, is the calibration of the instrument, the setting of the specific emissivity of the object, and the setting of the correct distance relative to the measured object (Waidner and Burgess,

1905). One drawback of optical pyrometry is that dust can adversely affect the accuracy of measurements (Waidner and Burgess, 1905).

2.6 Sampling and statistics

Sampling is critical to accurate measurements. This section reviews general principles of sampling and the statistical treatment of measurements.

2.6.1 General principles of sampling

Sampling in metallurgical processes is a process whereby a portion of material is extracted from its whole—i.e., lot (Gy, 1979). The portion of material that is obtained from the lot is called a sample. A good or true sample in the technical sense is one that is collected in such a way that it represents (within acceptable levels of bias and precision) the lot in its physical and chemical characteristics (Dominy et al., 2018; Institution of Mining and Metallurgy (Great Britain) and The Institution Of Mining And Metallurgy, 1973; Keith, 1996; Smith and James, 1981). Samples that do not conform to the criterion give misleading, potentially damaging information about a population (Williams, 1978). According to Institution of Mining and Metallurgy (1973) and (Smith and James, 1981) no sample ever fully represents the lot in all respects. However, a number of sampling quality assurance tools can be applied to ensure that the sample characteristics are as representative of the lot characteristics as possible (Keith, 1996). Nine sample quality assurance procedures are listed below.

1. Adhere to sample protocol without fail (Keith, 1996)
2. Ensure that the sampler is suitably trained (Keith, 1996)
3. Protect collected samples from contamination (Institution of Mining and Metallurgy (Great Britain) and The Institution Of Mining And Metallurgy, 1973; Keith, 1996)
4. Set in place a good system for identifying samples (Keith, 1996)
5. Pre-plan your sampling procedure; ensure that it does not change (Keith, 1996)
6. Apply calibrations, especially for automated samplers (Keith, 1996)
7. Consider the size of a sample in light of the application (Smith and James, 1981; Williams, 1978). Williams (1978) reported that samples are typically <1% of a lot, and almost always <5% of a lot.
8. Collect many samples in instances where operations fluctuate significantly (Institution of Mining and Metallurgy, 1973)
9. Sample lots as randomly as possible (Williams, 1978)

In addition to these quality assurance procedures, (Gy, 1979) recommended that samples be selected systematically and randomly; it is by far the most common of selection schemes as it is nearly always reproducible. The recommendation was followed in this study. Sampling formed a key part in the project; it was used at several stages—in the collecting of off-gas dust from the smelter, in sub-sampling of the dust in the laboratory for subsequent analysis and test work, and in collecting the products of firing.

The collecting of samples by manual shovelling as well as homogenising the samples by sheet mixing are acceptable practices especially when gathering samples from large industrial processes (Institution of Mining and Metallurgy, 1973).

2.6.2 Statistical calculations

According to (Miller and Freund, 1976), statistical calculations can be run on any set of gathered numerical data, including those in the field of engineering (into which metallurgical

smelters fall), in order to analyse, interpret, and draw valid conclusions from the data. In the context of smelters, the data sets convey different information, e.g., chemical composition, mass, or power input. In this work two statistical tools were applied-the mean and the standard deviation. These properties are important in that they reduce a property to a number and what the variation is about that number. They were used to compare results throughout the investigation.

The definitions of the mean and standard deviation along with an explanations of where the formula was used, is shown in Table 9. The formulae that apply to both the mean and standard deviation are shown in Table 10. For ease in performing the calculations the functions provided by the Microsoft Excel 2013 package were used.

Table 9: Summary of statistical tools used in the current study and where they were used (Sykes et al., 2016)

Statistical tool	Definition	Where?
Mean	A measure of central tendency; refers to the average value out of a group of numbers	Dust composition and compressive-strength test results
Standard deviation	A measure of data spread, specifically how much variation there is within a group of values, i.e., variation from mean	Dust composition and compressive-strength test results

Table 10: Formulae used for statistical tools in this investigation (Sykes et al., 2016)

Statistical tool	Formula
Mean	$\dot{x} = \Sigma X/N$ where $\dot{x}$ = mean, ΣX = sum of all scores, and N = total number of scores
Standard deviation	$s = \sqrt{\Sigma(x - \dot{x})^2/(n-1)}$ where s = standard deviation, x = single score, $\dot{x}$ = mean, n = population

3 EXPERIMENTAL PROCEDURE

As the project scope falls into segments—work undertaken at the smelter, test work in the laboratory, and desktop studies—this section is conveniently divided into five stages as set out in "flowsheet" form (Figure 17). Except for stage 5, which was conducted concurrently with stage 3, the stages follow each other in chronological order. The steps detailing each task, the apparatus and instruments employed, and other relevant details pertaining that stage are now discussed.

Stage 1
- *Smelter-based work*
- Collection of dust samples
- Temperature measurements and data gathering

Stage 2
- *Laboratory dust-sample preparations*
- Preparation of the samples collected at the smelter (blending, splitting, characterisation)

Stage 3
- *Laboratory pellet-pressing and firing tests*
- Method development
- Pellet pressing, firing tests, and product handling

Stage 4
- *Fired-product examination (for sintering)*
- Physical strength measurements
- Phase-chemical composition measurements

Stage 5
- *Desktop thermodynamic evaluation*
- FactSage thermodynamic calculations to evaluate sintering

Figure 17: Flowsheet showing the five stages of the investigation

3.1 Stage 1: Smelter-based work

Stage 1 presents both the experimental procedures and some preliminary results obtained during the smelter-based work. This work was essentially divided into two parts. Part 1 entailed the collection of dust samples at the bag-house of the smelter. Part 2 entailed the development and subsequent measurement of the furnace duct temperatures.

3.1.1 Collection of dust samples

Dust samples from the smelter furnace bag-house were collected during normal furnace operation. They were collected from the three dust streams shown in Figure 18. (A more

detailed diagrammatic image of Figure 18 appears in Figure 2.) Care was taken in collecting the samples to ensure that they would be representative of the entire stream, especially as the subsequent laboratory sintering tests would use these samples. Care was also taken by for example wearing the dust mask – at all times during sampling - to minimise inhaling the hazardous dust. Other precautions taken were wearing flame retardant overalls, hard-hat, ear plugs, gloves, washing hands before eating, and showering immediately after plant visits. Also, on a yearly basis, Mintek also monitors the metallic-levels (including Mn) content of our blood stream.

To promote sample representability, a systematic approach to sampling was undertaken. This entailed, first, collecting the samples over a three-month period (from November 2018 to January 2019). In these three months, a total of five visits were made to the smelter; each visit lasting two days. This totalled ten days spent at the smelter collecting samples. Secondly, on each visit, samples were collected between 8 am and 4 pm at two-hourly intervals. Table 11 summarises the details of the daily sample collection schedule followed in each visit. A closed scoop was used to draw at random multiple-grab samples around the stream—between 0.8 kg and 5 kg of sample per interval. This sample, which was still hot as it emanated from the furnace, was temporarily stored in a metal drum, and then later transferred to a sealed and labelled plastic bag. Figure 19 shows photographs taken during sampling. At the end of three months, a total of 136 kg, 299 kg, and 70 kg of dust samples from streams 1, 2, and 3, respectively, were collected—that is, about 505 kg of dust over the three streams.

Details of the exact sample sizes collected from each stream, and the total sample size collected over the three months are reported in Appendix A (Table 29).
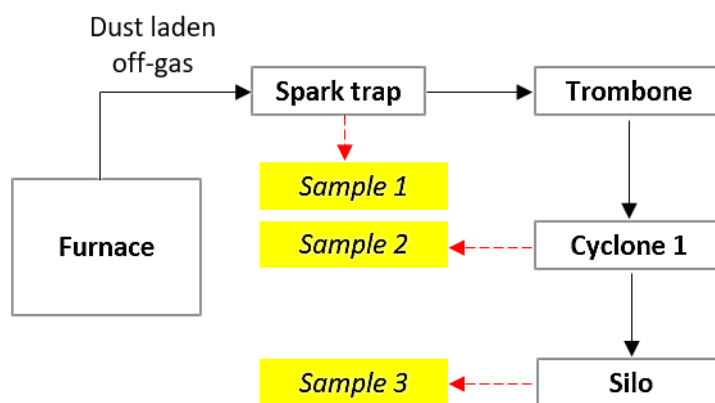
Figure 18: Schematic diagram of sampling points at the smelter
(Sample = stream)

Table 11: Details of the daily sample collection schedule for a single visit

Time	8 am[†]	10 am	12 pm	2 pm	4 pm
Day 1	S1, S2, S3	S1, S2, S3	S1, S2, S3	S1, S2, S3	S1, S2, S3
Day 2	S1, S2, S3	S1, S2, S3	S1, S2, S3	S1, S2, S3	S1, S2, S3

S stands for stream sample
[†] effectively covered the sample between 5 pm and 7 am

(a) Step 1 to step 3

(b)

(c)
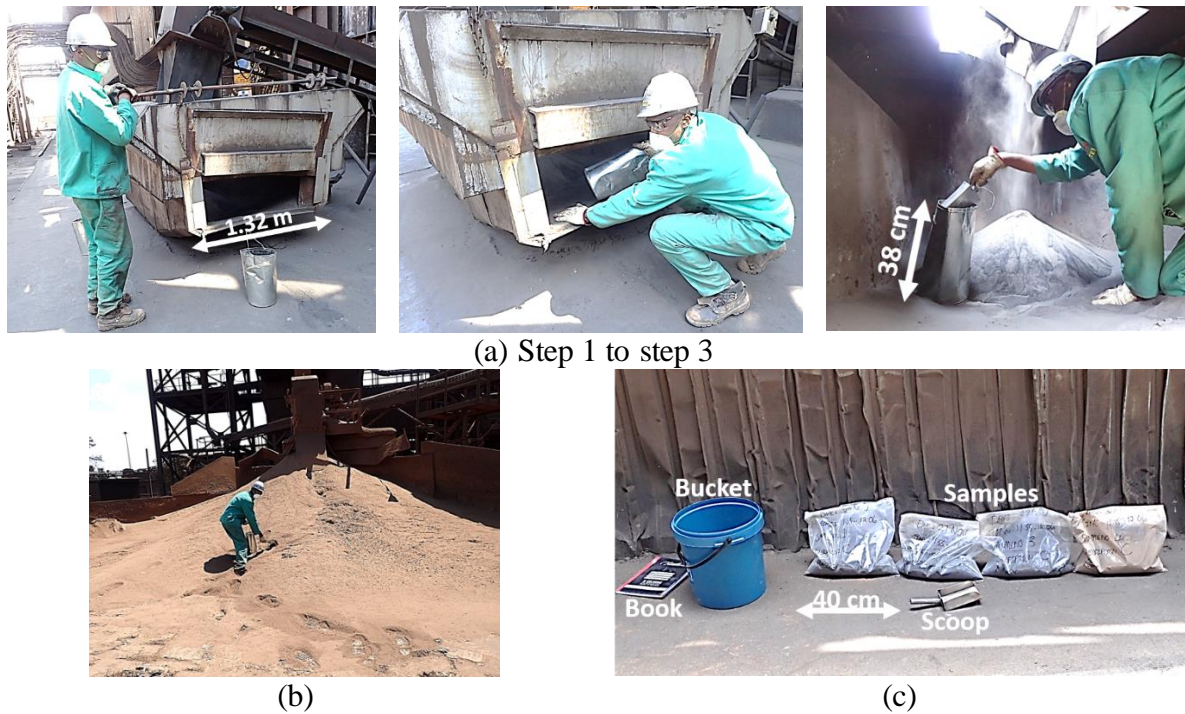
Figure 19: Photographs taken during sampling: (a) steps 1–3 of sampling in the cyclone bin, step 1 – opening of bin, step 2 – entrance into bin, and step 3 – sampling inside the bin; (b) sampling of stream 3 from silo discharge; and (c) bagged samples after sampling with bucket where samples are stored, book for records, and the scoop used for sampling

3.1.2 Temperature measurements and data gathering

The values of temperatures typically encountered in the vertical ducts where blockages commonly occur were required in order to select the temperatures that would be used in the laboratory tests for evaluating the potential of dust sintering. Unfortunately, these ducts did not have any thermocouples placed on their inner surfaces where blockages typically occur. The dust-laden off-gas temperature was not measured directly. Instead, the only installed thermocouple in these zones was one used to measure the water-cooled shell temperature. An alternative strategy had to be devised to get an estimate of typical duct temperatures during operations.

The first option explored was having multiple thermocouples across the duct cross-section. However, after consultation with the smelter manager and production superintendent, the cost of such an exercise (included in the costs would be repairs to a damaged steel structure caused by drilling into shell to insert thermocouples), along with fears that the inserted thermocouples could be damaged by dust-laden off-gas and so not work. Thus the option was discarded. A more feasible option, and the one pursued, was to estimate likely temperatures in the duct from, measurements of what would be maximum and minimum temperatures at extremities - in the duct. The closest measured point to the hottest zone of the duct, was the 'furnace bed'. At the other end, the coldest part of the duct was the cap i.e., at the top of the duct. Fortunately, the smelter had an existing thermocouple that measured continuously the dust-laden off-gas temperature in that section. To illustrate the approach, Figure 20-c shows the positions of the thermocouples (i.e., the shell and duct-cap thermocouple), and the position of the furnace bed relative to the duct where the maximum duct temperature was measured. It is fair to assume that the dust leaving the furnace bed would be at the highest temperature; its temperature would

steadily decrease up the length of the duct, reaching a minimum where the duct cap thermocouple is positioned.

(a)   (b)

(c)
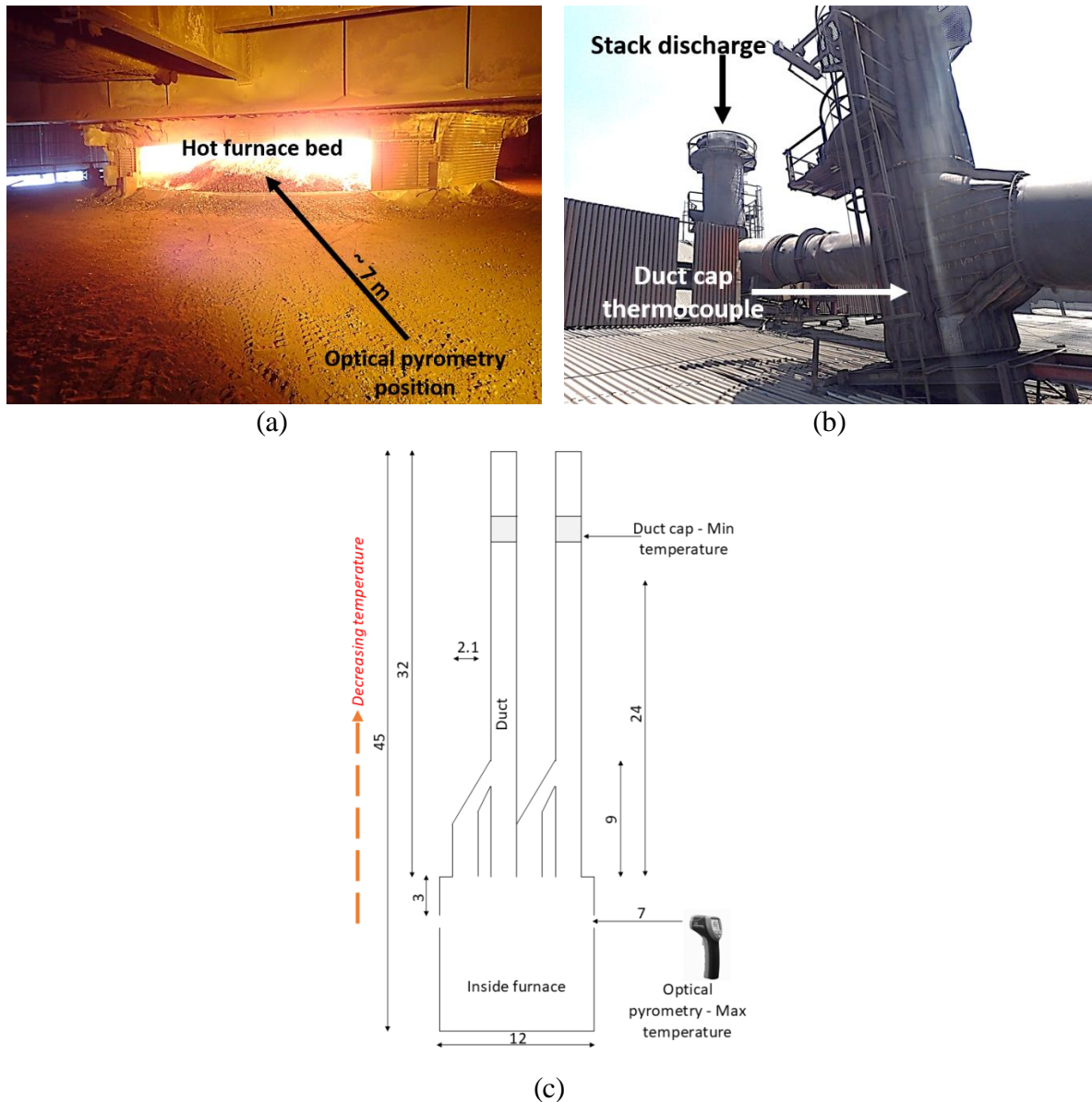
Figure 20: Photographs of (a) the hot furnace bed during operations (max temperature), and (b) the position of the duct cap thermocouple (min temperature). Schematic diagram showing (c) the positions of maximum and minimum temperature measurements (values, expressed in metres, denote close approximates based on engineering drawings)

The procedure used for collecting typical temperature data on the furnace bed and cap-end of the duct was as follows:

- *For the furnace bed (maximum temperature)*: A calibrated optical pyrometry (a Minolta/Land Cyclops 52 Infrared Thermometer) set at an emissivity of 0.7 φ (as there was generally no visible dust in the furnace bed the value was an appropriate setting) and a distance of infinity (to cover for the distance of 7 meters to the furnace bed). As with the physical samples, measurements were taken from 8 am to 4 pm over four days in January 2019 (This period covered every variation experienced in operation from furnace feeding rate changes to tapping.) Each time, four readings were captured from the same position,

but at different areas on the furnace bed. The record of the temperature readings over the four days is summarised in Table 12. The readings vary generally between 1000 and 1300°C. On a few occasions temperatures dropped below or above this range. The, highest temperature was 1375°C.

- *For the duct cap (minimum temperature)*: The production superintendent at the smelter provided a graph of temperatures in the duct cap (where a K-type thermocouple is installed) over a period of five days. The data covered both the temperatures observed during normal furnace operations and the temperatures observed after a shutdown. The graph is shown in Figure 21. The temperature was typically above 500°C and below 750°C.

Based on observation of the duct cap and furnace bed temperatures, the minimum and maximum temperatures selected for the laboratory sintering tests were 600 and 1300°C. Temperatures below 600°C are expected not to promote sintering i.e., an effect at lower temperatures should not differ significantly from an effect at 600°C. The maximum of 1300°C is lower than the peak of 1375°C. As the furnace bed is about 3 m away from the duct lower end, it is unlikely that actual temperatures in the duct will ever exceed this value.

Table 12: Temperature measurements of the furnace bed by pyrometry over four days (hottest zone)

08 January 2019				
	Reading (°C)			
Time	1	2	3	4
8 am	-	-	-	-
10 am	996	1136	1236	1177
12 pm	1221	1045	1290	1287
2 pm	1375	1263	1154	1281
4 pm	1115	1217	1089	1257
09 January 2019				
	Reading (°C)			
Time	1	2	3	4
8 am	1288	1142	1296	1277
10 am	1167	1058	1260	1214
12 pm	1120	1125	1100	1118
2 pm	1205	1141	1183	1068
4 pm	1226	1175	1255	1300
21 January 2019				
	Reading (°C)			
Time	1	2	3	4
8 am	1061	1240	1154	1134
10 am	936	933	1236	1272
12 pm	1249	1283	1367	1230
2 pm	1173	1271	1212	1167
4 pm	1112	861	1153	1162
22 January 2019				

Time	Reading (°C)			
	1	2	3	4
8 am	1118	1130	1135	1114
10 am	1218	1243	1201	1266
12 pm	1235	1243	1328	1225
2 pm	1115	1253	1270	1099
4 pm	-	-	-	-

- No measurement taken
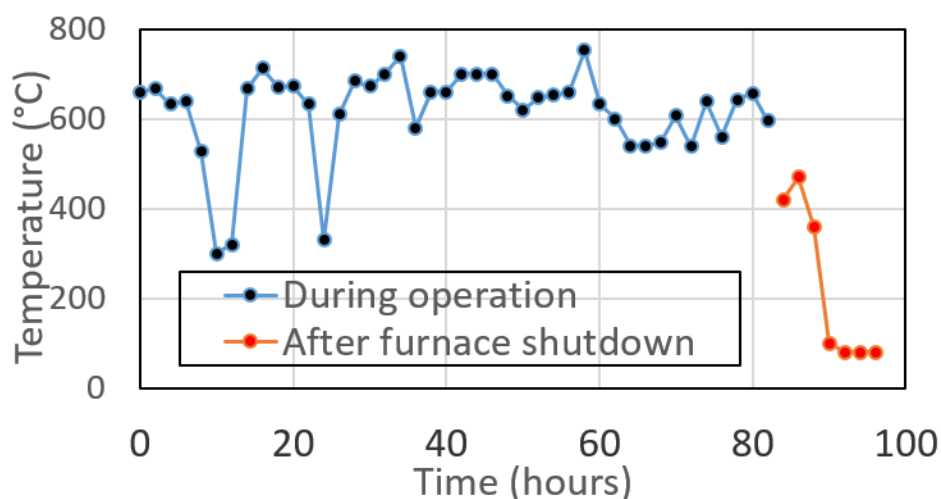
Figure 21: Duct cap temperatures during operation and after furnace shutdown (12 July to 16 July 2018)

3.2   Stage 2: Laboratory dust-sample preparation

The aim of this stage of the procedure, was to prepare the samples of smelter dust physically through drying, blending, and splitting for characterisation and sintering. Blending and splitting were particularly important for ensuring that a sample is homogenous from the onset. The entire flowsheet adopted in stage 2, including the sub-samples obtained throughout the process, is shown in Figure 22. Each stream was treated separately to avoid cross-contamination between streams.

The nature of the work undertaken at each stage is explained in this section.
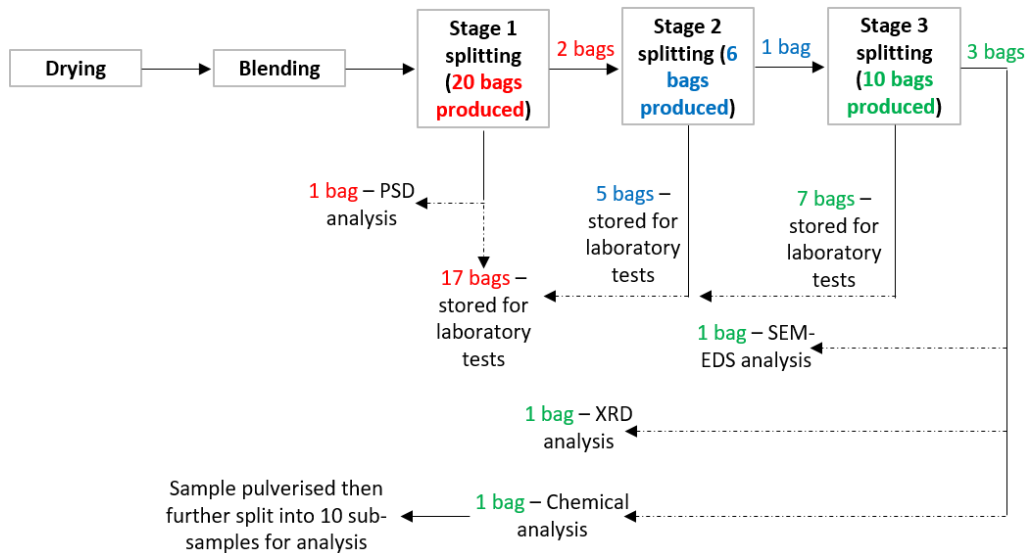
Figure 22: Complete flowsheet of stage 2 (bags represent the bags shown in Figure 19 filled will sample)

3.2.1 Drying

The dust samples (from streams 1-3) were first dried in an oven (Wirsam Scientific, model 220, one used for all oven drying in the project) in batches of 1-10 kg at 110°C for 24 hours. The drying condition were based on the American Society for Testing and Materials (ASTM C136). The mass loss due to the removal of non-crystalline moisture fell below 0.5% for all streams. Appendix B (Table 30) gives the exact mass losses recorded for each batch dried.

Each stream of dried material was then blended by laying it on a clean floor, then mixing it with a shovel i.e., the application of sheet mixing (Institution of Mining and Metallurgy , 1973). Blending was considered complete once the sample appeared homogenous to the naked eye. The photographs in Figure 23 show the blending process.

Figure 23: Photographs taken during manual blending of stream 1 dust: left –sample poured across the floor and right – shovel blending

3.2.2 Splitting

In order to promote further homogeneity within each dust stream, the bulk samples were taken through a rigorous sample splitting procedure. The steps are outlined in bullet points below.

- Step 1: Automated splitting of sample using a '*large*' rotating sample splitter (manufactured in-house at Mintek) – The splitter divided the sample into 20 sub-samples. Seventeen of the sub-samples were bagged and then stored for future use. One of the three remaining samples was taken for the PSD analysis. Whilst the other 2 sub-samples were taken for additional splitting. It was observed during the splitting of stream 3 that the sample tended to agglomerate into spherically shaped balls.
- Step 2: Automated splitting of sample using a '*medium*' 2407002 Kendrion rotating sample splitter – The 2 sub-samples obtained from large splitting, were then further split into 6 sub-samples. 5 of those 6 sub-samples were also bagged and stored along with the initial 17 samples, whilst the 1 sample was taken for further splitting using the small rotating sample splitter.
- Step 3: Automated splitting of sample using a '*small*' Fritsch Laborette 24 rotating sample splitter– The 1 sample was then further split into a further 10 sub-samples, each weighing around 200 g for sample 1 and 3, and around 420 g for sample 2. Of those 10 sub-samples, 7 were bagged and stored along with others, while the remaining 3 were taken separately for bulk chemical analysis, bulk phase chemical composition, and specific phase chemical composition. These methods are described in detail in section 3.2.4 to 3.2.6.

3.2.3 Particle size distribution

Screening was done so that the observed differences in streams PSD could be quantified. The PSD was determined using a MD-440 Pascall Engineering Ltd. vibrating screen. For stream 1 and 2, dry screening was undertaken. This entailed the usage of eleven screens (chosen based on preliminary screen test results), with screen mesh sizes ranging from 38 to 1000 microns (see Table 13 for exact sizes). Each screening run was conducting using 500 g of sample, for a total duration of 15 minutes. The same procedure was applied for stream stream 3, however, after the observation of continues balling of the sample during dry screening, wet vibrating screening was undertaken instead. Since preliminary results showed that stream 3 was extremely fine in comparison to stream 1 and 2, only a 38 micron screen was used to conduct the screening analysis. The results of the analysis was recorded as mass fractions (%) gathered from each screen size. Figure 24 shows a photograph image taken for stream 1 after screening. From this figure, the size distribution of the sample can be seen.

Table 13: Selected screen sizes used to screen dust samples (sizes in microns)

Stream	1	2	3
Mesh size	1000	1000	
	850	850	
	600	600	
	425	425	
	300	300	
	212	212	38
	150	150	
	106	106	
	75	75	
	53	53	
	38	38	
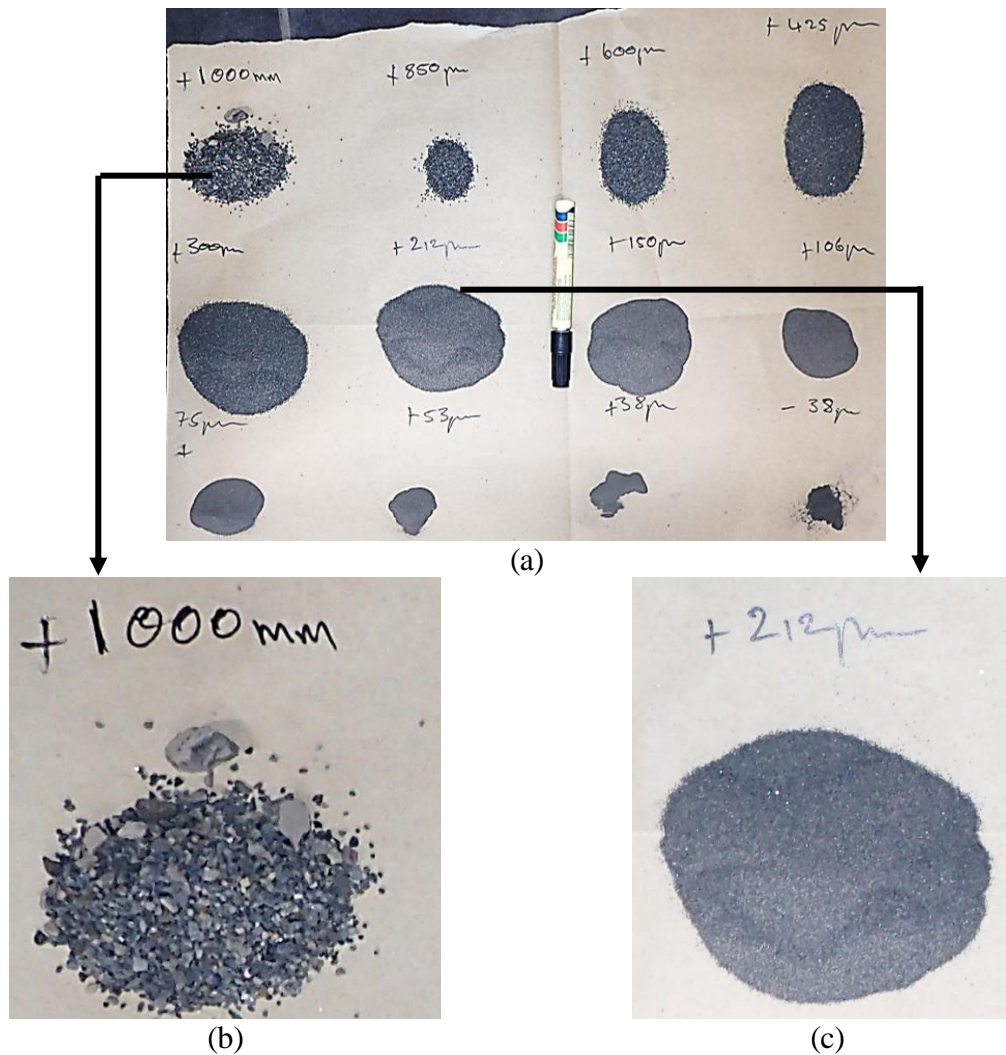
Figure 24: Photographs showing (a) PSD for stream 1, (b) +1000 um fraction, and (c) + 212 um fraction

3.2.4 Bulk chemical composition

The bulk chemical composition of each stream was determined using a Thermo Fisher Scientific iCAP 7600 ICP-OES Analyser (for analysis of typical ferromanganese base metal), a CS 744 LECO and CS 230 LECO instrument (for carbon and sulphur), a Spectrophotometer (for phosphorus), an Atomic Absorption Spectroscopy (for oxides of potassium and sodium), and ICP-MS (for boron).

ICP-OES analysis was conducted by fusing a known mass of the sample using a strong oxidizing agent, that is, sodium peroxide. The now fused material was then digested in HCl/HNO$_3$ acid, before assaying using the instrument. Carbon and Sulphur were analysed by oxidising both species in a combustion furnace, their reaction products, that is, CO_2 and SO_2, were then detected by an infrared detector. Phosphorus analysis was conducted by fusing the sample with a combination of sodium peroxide and sodium carbonate. The product of fusion was then leached in water. Ferrous iron was then added to precipitate P. The precipitate was then dissolved and complexed with an ammonium molybdate/vanadate reagent, forming a yellow complex. The complex was then extracted into a methyl iso-butyl ketone, and the P in the extract analysed spectrophotometrically.

With the Atomic Absorption Spectroscopy method, the sample was aspirated into a flame using a nebuliser. The emitted beam was received by the monochromator, which accepted and transmitted radiation at the specified wavelength and travelled into the detector. The detector then measured the intensity of the beam, producing a corresponding reading matching the intensity. With the ICP-MS technique, the sample was initially digested in a strong acid. The now liquid sample was then turned into fine mist by the nebuliser. The mist was then transported by inert argon gas into the plasma, where, it was ionised and then measurements of boron determined.

3.2.5 Bulk phase chemical composition

The bulk phase chemical composition of each stream was carried out on a finely pulverised sample by semi-quantitative XRD analysis, using a Bruker D8 advance Diffractometer (pulverisation was conducted using a TS250 vibratory disc mill in all instances). The instrument was run from 0 to 80° 2Θ, at a wavelength of Co K-alpha 1.7902 Å. The fluorescence was avoided by using filters. This method made use of the net intensity of the main peaks of the phases, with identification of the phases based on the crystal structure of crystalline phases which occurred in amounts of >3 mass%. Since a semi-quantitative methodology was adopted, the percentage of species reported was only relative, as it did not factor in the fraction of amorphous phases.

3.2.6 Specific phase chemical composition

Specific phase chemical composition of each stream was determined by SEM-EDS, using a Zeiss Evo MA15 SEM equipped with Bruker X-Flash detector, and an Energy Dispersive X-Ray Spectrometer. Prior to analysis, the as-sampled dust was first resin impregnated, then grounded and polished, and finally carbon coated before being analysed on SEM. The exact details of the preparation steps, excluding the pre-treatment i.e. step 1, as it was not applied in this case, are described in detail later in section 3.4.5.

SEM measurements were done at 20 kV, with backscattered electron micrographs generated to illustrate the microscopic appearance of each as-sampled dust stream. Elemental maps were also generated by measuring the characteristic X-Ray intensity of chemical elements relative to their lateral position. Variations in X-ray intensity indicated the relative concentration of the specific element across the recorded field of view. One or more maps were recorded simultaneously using image brightness intensity as a function of the local relative concentration of the elements present. These images guided the selection of points for EDS microanalysis.

The chemical composition of selected points in each of the streams were determined by EDS microanalysis. Oxygen, in phases where it was present, was calculated by stoichiometry. Since EDS did not measure carbon, the results were normalised. It should be noted though that carbon was mainly present as distinct black grains, and thus, apart from it being in solution in the alloy phase, it was unlikely to have been present in other phases.

3.3   Stage 3: Laboratory pellet-pressing and firing tests

Stage 3 covers firstly, the development of the pellet press and firing method. After that, the exact methods and steps undertaken to make pressed pellets as well fire the pellets for sintering evaluation are discussed in details.

3.3.1 Method development

Prior to the actual laboratory pellet formation by pellet-pressing and the subsequent firing tests, the methodologies for these activities had to be developed and fine-tuned, such that standard and non-biased procedures could be developed and then used for the actual testwork. In this section, the pellet-pressing and firing procedure are discussed under three main headings:

- Reason why the method had to be developed.
- The procedure undertaken in developing the method.
- The outcome of the method development.

Pellet-pressing method development

Reasons why method had to be developed – Several reasons necessitated the development of this method. The reasons are as follows:

1. Pellets are an effective way of analysing sintering behaviour, this has been demonstrated by several authors (Quijorna et al., 2014), (Adell et al., 2007), (Romero et al., 2008), and (Wang et al., 2001).
2. Since formation of pressed pellets relies on the application of a force on the material to compact it into shape (in this case a cylindrical shape), the force applied should be sufficient to promote the formation of pellets without compromising the PSD of the material. This is vital especially since PSD is one of the investigated parameters in this study.
3. To ensure that the formed pellets don't self-disintegrate before firing such that any disintegration observed would be as a result of the firing.
4. To determine the compressive strength sensitivity to the pellet height. Previous work done on pellets has shown that it is extremely difficult to ensure the same pellet height even within the same stream of sample. Hence, initial palletisation followed by compressive tests would give an indication of the pellets compressive strength sensitivity to height changes.
5. To obtain the best preparation method, taking into account the % water added to pellets, hydraulic press pellet applied pressure, and drying period (number of days).

The procedure undertaken in developing the method – The steps undertaken for the formation of pellets were as follows. Samples of between 200 g and 400 g, for each stream, were weighed using a Mettler Toledo MS3002S weighing balance, and then placed in containers. Water of various amounts i.e. 0%, 2%, 5%, and 10% (calculated as a percentage of the sample mass), were added into the sample and the two manually mixed using a spatula, until a consistent appearance was achieved. Pellets were then made using an OTC-P58 hydraulic press (discussed in detail in section 3.3.2) by inserting a sub-sample into a cylindrical mould, and then pressing the sub-samples into cylindrically shaped pellets at different pressures i.e. 3.5 MPa, 5 MPa, 7.5 MPa, and 10 MPa. The formed pellets were then oven dried at a temperature of 105°C for different time spans i.e. 1 day, 2 days, and 4 days. After drying, some pellets were selected for compressive strength tests. Table 14 shows a summary of the parameters applied to each stream during pellet formation.

Table 14: Summary of the parameters used during pellet formation as part of the method development (all pellets had a diameter of 30.9 mm)

Stream	Mass of pellet[#]	Water[*]	Pressure [@]	Drying (No of days)
1	37-40	0, 2, 5, 10	3.5, 5, 7.5, 10	1, 2, 4
2	30-38	0, 2, 5, 10	3.5, 5, 7.5, 10	1, 2, 4
3	24-28	0, 2, 5, 10	3.5, 5, 7.5, 10	1, 2, 4

[#] in gram (g); [*] in percentage (%); [@] in mega pascal (MPa)

Outcome of the pellet formation method development – Table 15 summarises the results obtained of the examined parameters for the pellet method development. From Table 15, it can be seen that the best combination of water, pressure, and oven drying time was 5%, 5 MPa, and 1 day respectively. Reasons for this was because water additions below 5% and below 5 MPa pellet pressure yielded weak pellets. The drying time on the other hand was found to have no effect on pellet formation.

To examine if the selected 5 MPa pressure did not compromise on the PSD of the pellets, pellets were prepared at different pressing pressures and then studied microscopically, from prepared polished sections (methodology for preparing all polished sections prior to SEM-EDS analysis discussed later). The PSD of these pellets under the SEM microscope was compared to the PSD of the original as-sampled dust. Results showing comparison between the as-sampled dust PSD and dust pressed at 5 MPa are shown in Figure 25. From the image, it is clear that a pressure of 5 MPa did not compromise on the PSD of any of the dust streams. Although some of the images appear to be different, this is a visual illusion and is only as a result of the compacted nature of the pressed pellets. Further evidence of this is shown in SEM images of pellets pressed at other pressures in Figure 61 of Appendix C. It was thus concluded that 5 MPa was the best pressure as it ensured both the formation of stable pellets, and as well as maintained the original PSD of the pellets.

Also evaluated in the pellet formation method development, was the effect of pellet height (whilst keeping the pellet diameter the same throughout, as standardised by the mould) on the compressive strength of the material. Figure 26 shows the results of that study. From the results it was clear that there was no correlation i.e. within a dust stream, between the pellet height and its corresponding compressive strength. In fact, the results obtained where within the same range regardless of the changes in height. Thus, pellets of the same stream with different heights (within the specified range in this study), can be used with full confidence in that the compressive strength will be similar (i.e. an insignificant effect within an acceptable standard deviation).

Table 15: Summary of the best outcomes for the pellet formation method development

Water			Pressure			Drying time		
%	Formed	Comment	MPa	Formed	Comment	Days	Formed	Comment
0	S1, S2 (No)		3.5	S1 (No)		1[@]	Yes	
2	S1 (No)		5[#]	Yes	5 MPa	2	Yes	1 day
5[*]	Yes	5% best	7.5	Yes	best	4	Yes	drying
10	Yes		10	Yes				

[*] 5% water was the lowest amount of water that promoted pellet formation (without pellet disintegration); [#] 5 MPa was the lowest pressure that promoted pellet formation (without

changing PSD of streams as shown in Figure 25); @ 1 day drying was the most optimal drying time as it yielded the same mass loss as 2 and 4 days drying.

(a) Stream 1 (As-sampled)

(b) Stream 1 (5 MPa pellet)

(c) Stream 2 (As-sampled)

(d) Stream 2 (5 MPa pellet)

(e) Stream 3 (As-sampled)

(f) Stream 3 (5 MPa pellet)
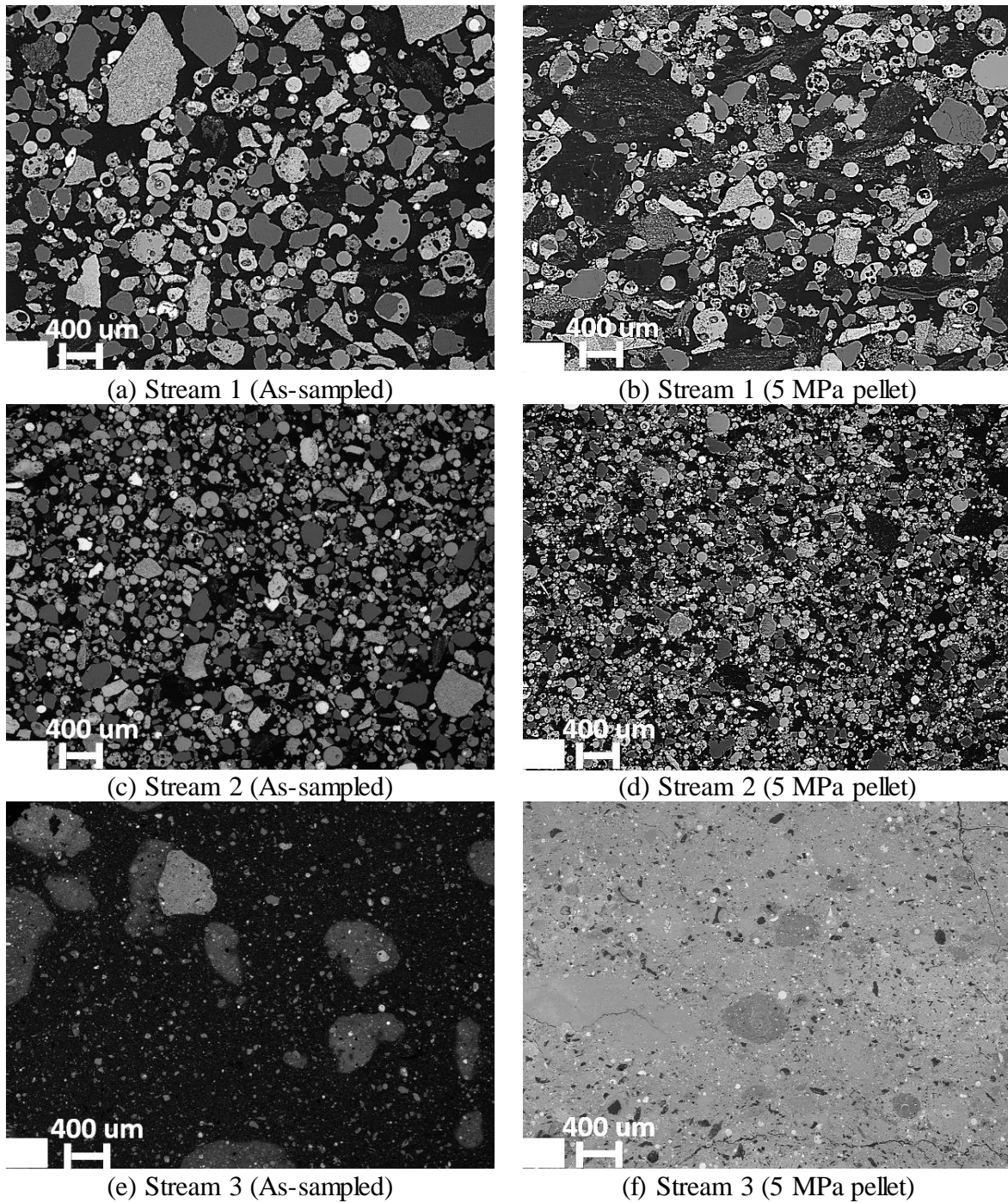
Figure 25: SEM BSE micrographs comparing the PSD of as-sampled dust with the dust compressed at 5 MPa
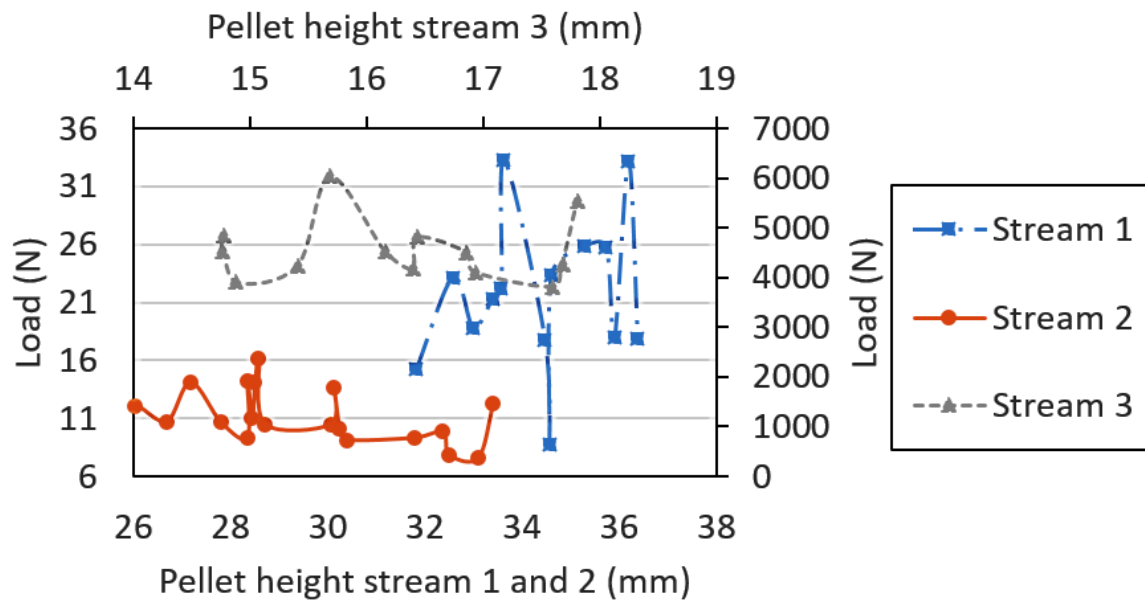
Figure 26: Graph showing benign effect of changing pellet height (for the same pellet diameters) on the compressive strength for all the dust streams (Average: stream 1 = 21.7, stream 2 = 11.2, and stream 3 = 4560.7; standard deviation: stream 1 = 6.6, stream 2 = 2.3, and stream 3 = 631.4; all in newton's (N))

Firing tests method development

Reasons why method had to be developed – Several reasons necessitated the development of this method. The reasons are as follows:

1. It was important that the pellets were subjected to a similar temperature. Muffle furnaces are notorious for having a steep temperature gradient across the muffle furnace. Thus to avoid this, a temperature profile across the muffle furnace had to be performed.
2. To determine the length of the muffle furnace hot zone such that the correct number of pellets could be treated on every run bearing this limitation.
3. To determine the length of hot zone such that the positioning of the tray carrying the pellets could be known.
4. To establish the heating profile of the furnace i.e. if the set heating rate conformed to the actual heating rate.
5. To examine whether the program temperature, the furnace temperature (measured by the furnace thermocouple), and data logger (connected to an external thermocouple with the tip placed to touch the back end of the muffle furnace), were in agreement.

The procedure undertaken in developing the method – A muffle furnace (discussed in detail in section 3.3.3) was used for all the firing tests. Since the main considerations were heating rate validation and the temperature gradient across the length of the furnace, two procedures are described.

Procedure 1: Heating rate – A K-type thermocouple was placed through a thermocouple port on the door of the closed muffle furnace (purchased from AE furnaces, see photographic image labelled Figure 27 for visual appearance of set-up). The tip of the thermocouple was made to touch the back end of the furnace. The furnace heat-up was commenced at room temperature, at a heating rate of 10°C/minute using a CAHO P961 controller (i.e. the typical heating rate used for muffle furnace operations). Using this heating rate, three sets of tests were performed to a final temperature of 600°C, 700°C, and 800°C. The aim of these tests was to determine the

consistency of the heating rate over a number of different final temperatures. In order to evaluate the heating rate, temperature readings of the program temperature, furnace temperature, and data logger (the latter using an Agilent 34970A data acquisition unit), readings were recorded in 5 minute intervals. The data logger readings were from the K-type thermocouple installed through the port of the muffle furnace door. From the recordings, graphs depicting the profile were drawn.

Procedure 2: Temperature gradient across the length of the furnace – A temperature gradient measurement, conducted at each of the final temperatures above, commenced once the data logger temperature stabilised (i.e. about 10-15 minutes after reaching temperature). In this, the same K-type thermocouple connected to the data logger was used. Since the muffle furnace was 45 cm in length, it was decided that temperature recordings be taken every 5 minutes in 4 cm interval. As such the temperature recordings were taken at 45 cm (i.e. back of muffle furnace), 41 cm, 37 cm, 33 cm, 29 cm, 25 cm, 21 cm, 17 cm, 13 cm, and 9 cm (close to the furnace door). Based on physical observations of the interior of the muffle furnace, recordings at 5cm and 1 cm were considered too cold to be taken. From the results, a graph was then constructed to depict the temperature gradient across the length of the furnace.
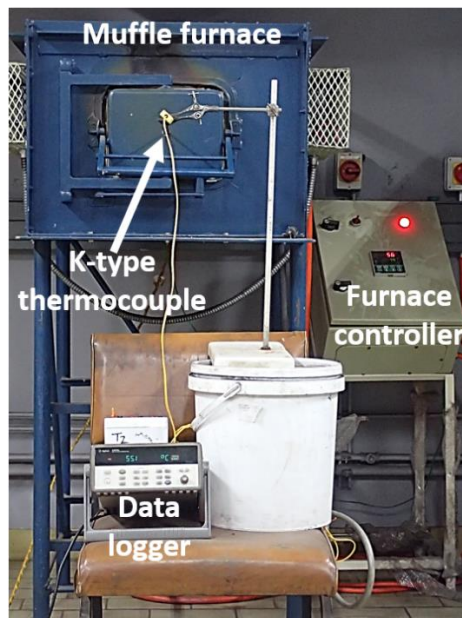
Figure 27: Photograph showing muffle furnace set-up during the method development

Outcome of the firing method development – The heating rate profiles for a targeted temperature of 600°C, 700°C, and 800°C are shown in Figure 28. From the graphs, it is clear that the set rate was achieved in all instance. One consistent discrepancy observed in all the graphs was that beginning at around 250°C, the data logger temperature was observed to be higher than both the program and furnace temperature. This necessitated an adjustment in the program temperature (by different margins for each targeted temperature as highlighted in section 3.3.3) such that the targeted temperature could be obtained.

Figure 29 shows a graphical representation of the temperatures recorded across the length of the muffle furnace. From the graph, a consistent hot zone spanning 20 cm within a +5°C deviation, can be observed for all the temperatures. The result meant that the tray used to carry the pellets should be limited to a maximum of 20 cm from the back of the furnace to ensure that the pellets are subjected to the same temperature range.
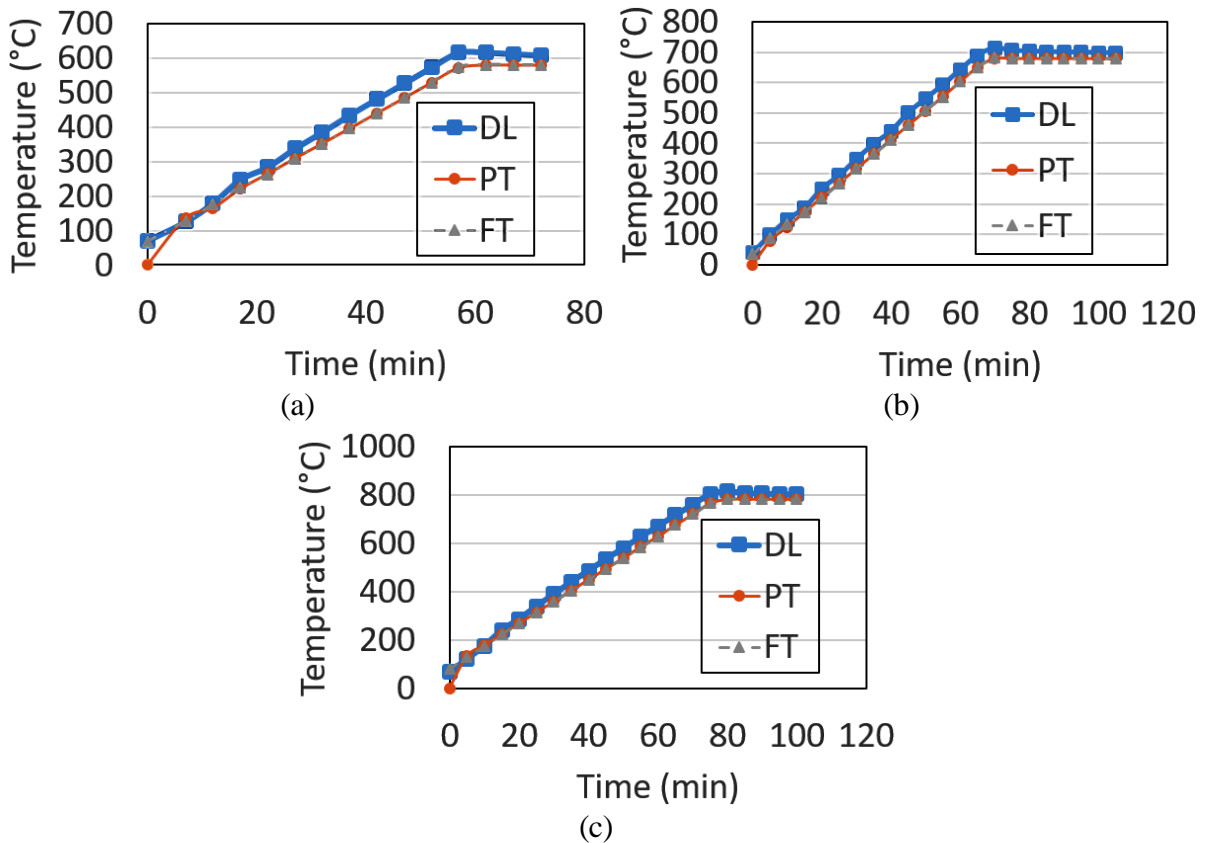
Figure 28: Graphs depicting the heating profiles for a targeted temperature of: (a) 600°C, (b) 700°C, and (c) 800°C. Heating rate of 10°C/min; DL = data logger thermocouple, PT = program temperature, and FT = furnace temperature.
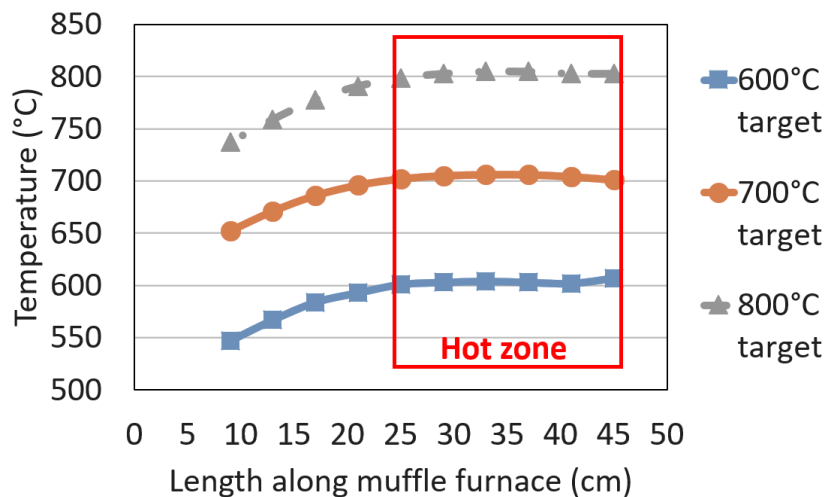
Figure 29: Temperature gradient across the length of the muffle furnace for a targeted temperature of 600, 700, and 800°C (The front of the muffle furnace was at 0 cm and the back was at 45 cm; the hot zone was between 25-45 cm for all temperatures)

3.3.2 Pellet pressing

After the method development stage, the actual test work commenced with the formation of pellets (i.e. pellet pressing). The step-by-step procedure followed for pressing the pellets, and the corresponding photographic images taken of the main utensils and equipment used during

41

this process, are described below. Since the same procedure was used, regardless of the type of stream treated, the procedure described applies in the same fashion for all streams. It should be noted that the pellets were formed using the bagged and stored sub-samples generated during large rotary splitting as discussed in section 3.3.2. The below steps are arranged chronologically.

Step 1: Weighing and mixing

Firstly, a sample was weighed using a Mettler PJ300 weighing balance. The weighed sample, typically between 200-800 g each, was then transferred to a 5 L bucket. Water amounting to 5% by mass relative to the sample was also then weighed, and subsequently mixed with the sample. The actual amount of sample and water used for each mixture throughout the project is shown in the Appendix B section as Table 31. To promote consistent mixing of the sample and water, a spatula was used to stir the mixture together.

Step 2: Pellet pressing

Once the sample and water were well mixed (as indicated by a consistent appearance), a sub-sample of mass indicated in Table 14, was withdrawn and transferred into a cylindrically shaped steel mould. The same mould was used throughout the project and consisted of the following three main components namely, a bottom stopper (which ensured that the sample did not escape from the bottom of the mould during compaction), the main cylindrical section (had an internal diameter of 30.9 mm and gave the cylindrical shape of the pellets whilst ensuring that the starting pellet diameter was the same throughout), and a top stopper (ensured that sample did not escape from the top of the mould and allowed for hydraulic pressing of the pellet). Once the mould was packed with sample, it was placed on an OTC P58 hydraulic power unit (i.e. hydraulic press). Through the application of a downward force on the mould using the hydraulic press lever, wet pellets were formed at a pressure of 5 MPa. Photographic images of the hydraulic press along with other utensils used (e.g. the mould) are shown in Figure 30.
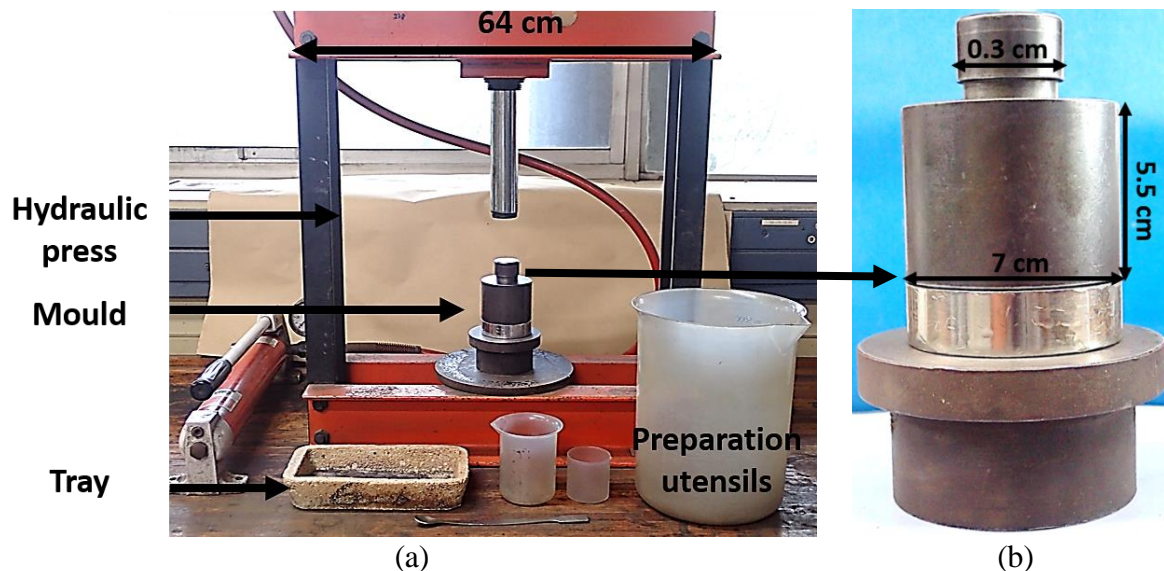
Figure 30: Photographs depicting (a) the hydraulic press with various other components, and (b) close-up image of the mould)

Step 3: Drying of the pellets

The formed pellets were then placed in already weighed fireclay trays (supplied by Engchem, with ID = 19.5 cm and breath of 10 cm). Fireclay trays were selected based on their capability to withstand, without degradation, temperatures greater than 1300°C. In each tray, ten wet pellets from stream 1, stream 2, and stream 3 sample, were placed. The tray, now carrying wet pellets subsequent to weighing, were placed in a laboratory drying oven, which was set at 105°C, for 24 hours at this temperature. A photographic image depicting the wet pellets inside the fireclay trays prior to drying is shown in Figure 31.
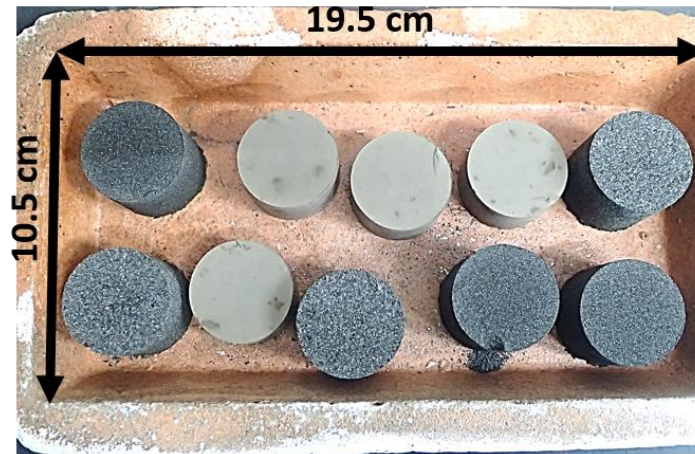
Figure 31: Fireclay tray carrying ten pellets prior to oven drying

Step 4: Pellet storage in desiccator

At the end of the 24 hour drying period, the tray was removed hot from the oven and then immediately stored in a desiccator. Throughout the project, the desiccator acted as an intermediate storage between drying and firing, as well as between firing and fired pellet product examination. The reasons for the usage of the desiccator was firstly to protect the pellets from rehydrating by placing them in an environment devoid of moisture, as well as keeping the pellets integrity prior to their examination. This is a common practise during sintering testwork (Lin et al., 2006).

On average, the mass loss due to pellets drying was 4%. Actual batch by batch recordings of the mass loss due to drying of pellets is shown in the Appendix C as Table 32.

3.3.3 Firing tests (Sintering)

Firing tests entailed the treatment of pellets at high temperature. At this point, the fireclay tray carrying the dried pellets was taken out of the desiccator and loaded into a cold muffle furnace (same muffle furnace previously mentioned). Since the muffle furnace hot zone was already determined during the method development, careful attention was placed in all instances to align the tray in the hot zone (i.e. 25-45 cm zone from the front of the muffle furnace). The muffle furnace set-up, as pictured in photographic image labelled Figure 27, and schematic diagram labelled as Figure 32 consisted mainly of an outer steel shell (i.e. structure of the furnace), an inner lining of alumina refractory board (i.e. provides insulation), Kanthal silicon carbide elements (i.e. resistance elements for generating heat), a furnace control unit (i.e. where schedule is set-up), and an alumina refractory lined furnace door (i.e. provide door insulation). The furnace door had a small opening in the centre where an external K-type thermocouple was inserted and externally connected to a data-logger (as seen in Figure 27). A 3-D and cross-

sectional representation of the muffle furnace, showing the positioning of the aforementioned components inside the muffle furnace, is shown in Figure 32.

(a)

(b)
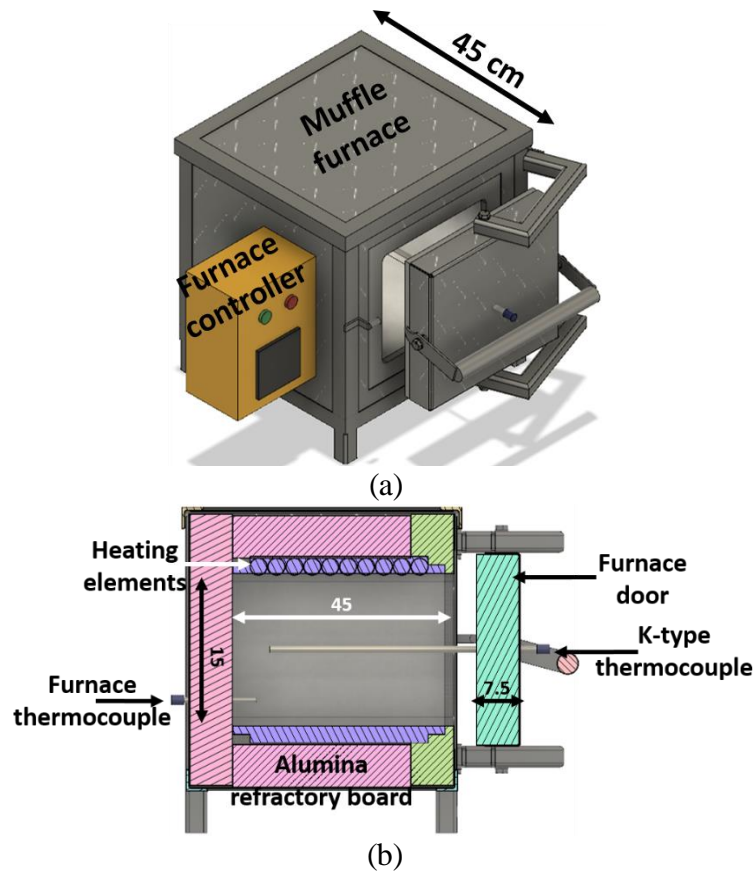
Figure 32: Various depiction of the muffle furnace used for firing components: (a) 3-D view of slightly open furnace, and (b) Cross-sectional view showing the interior of the furnace (all dimensions in cm, with diameter of heating elements 1.4 cm)

Once the muffle furnace set-up was complete, the furnace heating and cooling cycle was set on the furnace control unit. A standard heating and cooling rate of 10°C/min, as well as a residence time of 4 hours at temperature, was applied for all the tests. Tests were conducted in the prevailing air atmospheres (i.e. no gas was purged into the furnace but surrounding air induced an oxidising conditions as confirmed later in the bulk chemical composition of the fired sample), from 600 to 1300°C, in 100°C steps. For each stream at a certain temperature e.g. stream 1 at 600°C, a total of 41 pellets were fired. This amounted to 328 fired pellets for each stream across all the temperatures, and a total of 984 fired pellets over the entire project. Considering that a batch consisting of 10 pellets was treated on each muffle furnace run, a sum total of 99 runs (excluding failed runs due to load shedding etc.) were conducted over the entire project. Table 16 gives a summary of the firing tests matrix over the entire project.

It should be noted that the mass of the tray loaded with pellets before and after firing was recorded in all instances, so that the average mass loss could be determined for every temperature. The mass loss observed were believed to be as a result of several contributions i.e. loss of mass of tray, loss of mass by additional drying, and loss of mass by possible sample vaporisation (of volatile species e.g. C). The latter would be analysed by comparing the chemical analysis before and after sintering. Also, excavating samples from the off-gas and analysing them for C-content (amongst others) will confirm the absence of C in sintered material, thus, ensuring the validity of the method. A summary of the average mass loss for

44

each temperature is shown in Table 17. The complete table summarising the test by test mass loss as a result of firing throughout the project is shown in the Appendix section C as Table 33. Furthermore, graphical images showing the actual heating profile for each temperature are shown in the same appendix as Figure 60. The heating profiles exclude the 4 hours residence time at temperature, as well as the cooling cycle.

Table 16: Summary of firing test matrix for the whole project

Temperature (°C)	Stream	No of pellets fired	Pellet distribution for analysis	
			Compression test	SEM-EDS
600	1	41	40	1
	2	41	40	1
	3	41	40	1
700	1	41	40	1
	2	41	40	1
	3	41	40	1
800	1	41	40	1
	2	41	40	1
	3	41	40	1
900	1	41	40	1
	2	41	40	1
	3	41	40	1
1000	1	41	40	1
	2	41	40	1
	3	41	40	1
1100	1	41	40	1
	2	41	40	1
	3	41	40	1
1200	1	41	40	1
	2	41	40	1
	3	41	40	1
1300	1	41	40	1
	2	41	40	1
	3	41	40	1

Table 17: Mass loss at each firing temperature as a percentage of the original mass

Temperature (°C)	Average mass loss (%)
600	8
700	8
800	9
900	9

1000	8
1100	11
1200	10
1300	-

- Could not determine due to pellet melting and subsequent leakage

3.4 Stage 4: Fired dust product examination

Stage 4 of the project was aimed at evaluating sintering of the fired pellets. This was principally done through several approaches, firstly by examining the physical observation of the pellet after firing. Secondly by examining the compressive strength of the pellets as a direct function of temperature. Thirdly, by analysing the pellets phase chemically through a combination of SEM-EDS and XRD. The adopted approach to analysing the pellets for sintering behaviour is typical of sintering investigations (Dehaghani and Ahmadian, 2015). The SEM-EDS analysis is particularly useful as an examination of sintering, since the microstructural features of the pellets can reveal distinct characteristics that point to sintering. XRD assists in the identification of phases that can also point to sintering (especially solid-state sintering). The procedures undertaken at this stage are discussed below.

3.4.1 Physical appearance

Physical appearance was analysed by describing the observed exterior of the pellets upon firing, as well as the measurement of the diameter of the pellet upon firing. For the latter, a digital Vernier caliper was used with diameter of the pellet determined by placing the pellet in the middle of the two caliper jaws i.e. the fixed and adjustable jaws. The adjustable jaw was then adjusted until both jaws touched the pellet. At this point the diameter of the pellet was presented in millimetres (mm) on the screen of the caliper.

3.4.2 Compression tests

For the evaluation of the compressive strength of the pellets, a calibrated 3366 Instron compressive strength instrument was used. The procedure applied to perform the compression strength test entailed, placing a single pellet in the middle of the bottom fixed steel plate. After this, an increasing compressive axial load was applied to the pellet by the top flexible steel plate which pressed against the pellet (pellet was literally sandwiched between the two plates), until a point where the pellet failed completely (i.e. pellet cracked from top to bottom). The maximum load achieved at the point of pellet failure (i.e. peak load in newton's (N)) was automatically logged onto the computer as the maximum compressive force of the pellet. Figure 33 shows a photographic image of the Instron instrument, as well other photographic image depicting the sequential steps taken to determine the compressive strength of the pellets. Generally the compressive strength is reported in MPa (calculated as force over area), however, since all the pellets had the same cross-sectional (749.9 mm^2) area it was considered satisfactory to report the results in terms of force, in newton.

Experience from previous compressive strength measurements (of different materials) has shown the tendency for fluctuations in the compressive strength results. As such, it was considered wise to perform a number of repeats on the pellets fired under the same conditions, to increase the statistical degree of confidence of the results. To this end then, a total of 40 repeat tests (chosen to improve accuracy of results) for each temperature and stream number e.g. stream 1 at 600°C, were conducted. From the 40 results, both the mean compressive load as well as the standard deviation were determined.
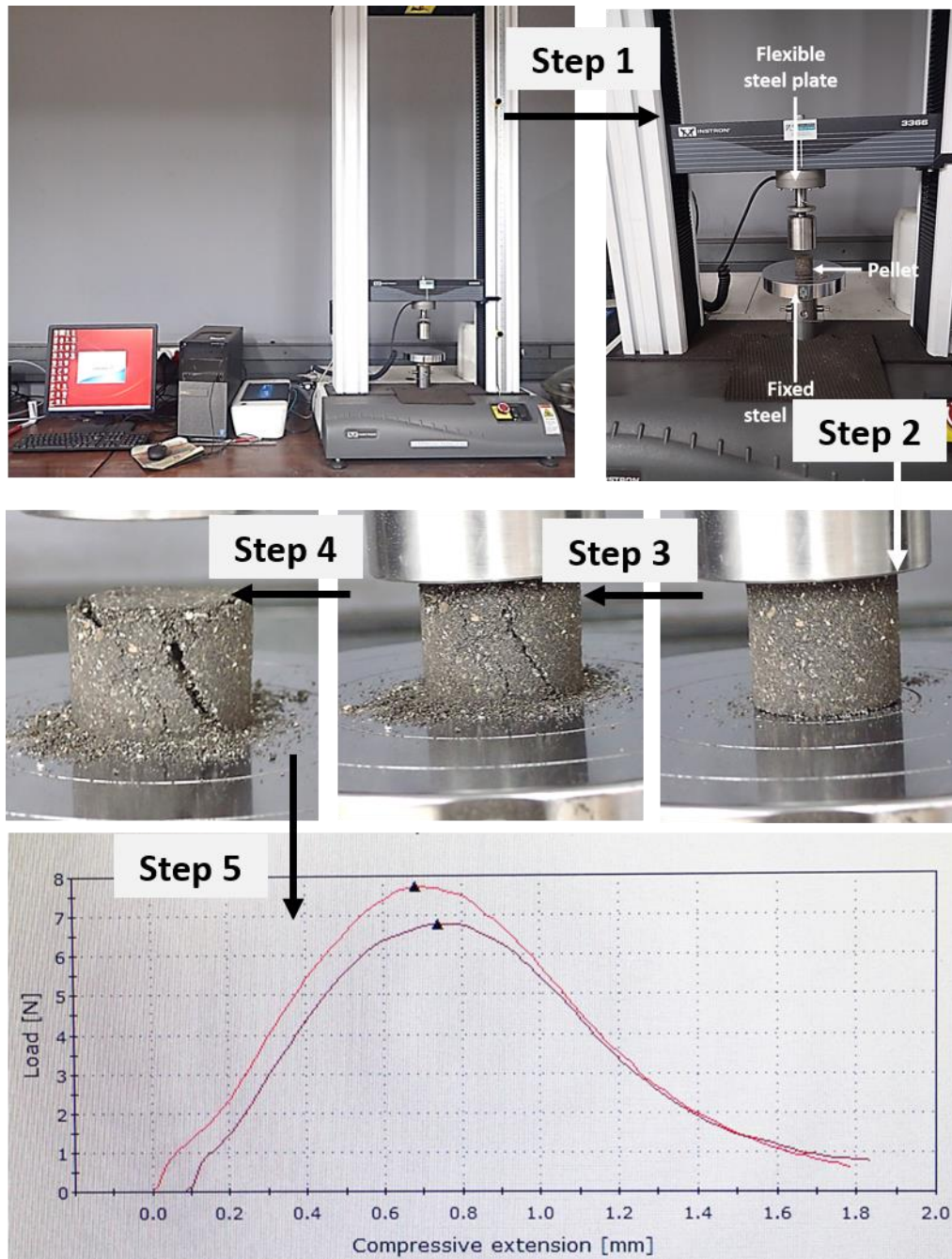
Figure 33: Step by step compression strength test procedure showing, Instron instrument components, step 1 - shows fixed and flexible steel plate along with pellet placed in position 1, step 2 - shows initial load applied on pellet, step 3 - peak load applied on pellet before complete cracking, step 4 – cracked load with removed load, and step 5 – graphical presentation of load with triangle shape indicating peak load

3.4.3 Bulk chemical composition

The 40 pellets that had undergone compressive strength testing, for each firing temperature, were mixed and then finely pulverised. From the mix a sub-sample was collected and then submitted for bulk chemical composition analysis. The same analytical techniques and steps described in section 3.2.4, were used for the analysis.

3.4.4 Bulk phase chemical composition

From the same pulverised sample lot reported in section 3.4.4, another sample was collected and taken for bulk phase chemical composition analysis using the XRD-semi quantitative analysis technique. The same procedure as described in section 3.2.5, was used for this analyses.

3.4.5 Specific phase chemical composition

The remaining fired pellet from the 41 fired pellet was analysed for the specific phase chemical composition using the SEM-EDS technique in the exact fashion as described previously. Analysis by SEM-EDS centred on generating micrographs to observe the presence of sintering, elemental maps to determine the distribution of elements and identify any sintering patterns within the sample (e.g. particle to particle joints, neck formations etc.), and EDS point analysis to determine the composition of particles as part of the process to identify the sintering mechanism.

Prior to analysis, each pellet for each firing temperature was taken through a five step preparation process as highlighted below.

- Step 1 - Pre-treatment: The pellet was initially placed inside a 50 mm plastic vial. A mixture of Akasel Aka-resin liquid epoxy and Akasel Aka-cure slow hardener, at a mixing ratio of 25:3 respectively, was then poured onto the pellet. To promote impregnation of the pellet by resin, the vial was taken to an N86KN.18 KF LAB Laboport vacuum degassing unit for about 10 minutes. To promote rapid hardening of the resin, the vial was subsequently heated in a Labcon 3138M pressure vessel set at 60°C, for about 1 hour. The overall aim of the pre-treatment step was to secure the pellet prior to subsequent steps. This was considered crucial to ensure that any neck formation and telling material arrangement would not be distorted prior to the SEM-EDS analysis.
- Step 2 - Cutting and resin treatment: The resin impregnated pellet was then strategically cut into a thin slice (smaller section of the pellet representing a sub-unit), in such that it could be fitted into a round shaped mould. After placing it in the mould, a mixture of the resin and hardener, as described above, was added. After this, the same impregnation and hardening process was followed. The aim of this step was twofold: a) to obtain a smaller section of the pellet for analysis, and b) to further impregnate the pellet in resin such that the next step of preparation could be easily undertaken.
- Step 3 – Grinding and polishing: The surface of the resin impregnated pellet was then taken through multiple grinding and polishing phases. Grinding entailed firstly pre-grinding the impregnated pellet on a 220 grit resin-bonded diamond grinding disk. This was followed by further grinding now using a 600 grit resin-bonded diamond grinding disk. The overall intention of grinding was expose the surface of the pellet by grinding off the top layer of the resin. Polishing was undertaken using a Struers PAN-W cloth 6 µm diamond polishing suspension, followed by a Struers MOL cloth 3 µm diamond polishing suspension, and then a Struers FLOC cloth 1 µm diamond polishing suspension. Polishing was aimed at improving the visibility of the samples under SEM.
- Step 4 - Carbon coating: The polished sections were taken to a Polaron E6300 vacuum evaporator for carbon coating of its surface. This was so that the sample surface would be conductive for subsequent SEM analysis.
- Step 5 – SEM-EDS analysis: The final step was analysis of the prepared section under the SEM-EDS. The same procedure as described in section 3.2.6, was used for this analyses

3.5 Stage 5: Desktop equilibrium thermodynamic evaluation

Desktop equilibrium thermodynamic calculations were conducted using FactSage™ 7.3 software. All calculations were conducted in the Equilib module. Three databases were selected in all cases, namely, FT-oxide database (for oxides solutions, including slag), FactPS (which covered all pure substances including gases, pure oxides, and pure elements), and the FSstel database (a steel database that looks at all the species encountered in steelmaking, these are similar for the silicomanganese process). The units °C (degrees Celsius), atm (atmosphere), J (joules), g (grams, with a starting mass of 100 g of the inputs), and L (litres) were also used in all cases. Two main equilibrium calculations were performed throughout this investigation, these are described in bullet form below:

- Equilib calculation 1: This entailed determining the amount of liquid (in mass %) formed on firing each dust stream, to a final temperature of 600 to 1300°C (in 100°C steps). In performing this calculation, the as-sampled dust bulk chemical analysis was used as the input to FactSage. To simplify the calculations, all species analysed were assumed to be present in their most common form with K as K_2O, Na as Na_2O, Al as Al_2O_3, Ca as CaO, Fe as FeO, Mg as MgO, Mn as MnO, Si as SiO_2, and C as C. To evaluate whether such an assumption was reasonable, Mn was varied to Mn^{2+}, Mn^{3+} and Mn^{4+}, whilst Fe was varied to Fe^{2+} and Fe^{3+} (at PO_2 of 0.17 atm and total pressure of 1 atm). The variation in oxidation states of Fe- and Mn-oxides, showed no significant change in amount of liquid formed (for the most part <2% change as demonstrated in the example in Figure 34 and Table 18). From these calculations, a graph depicting the predicted equilibrium change in liquid formation, with change in firing temperature was constructed.
- Equilibrium calculations 2: This entailed determining whether some of the particles observed to have sintered together, where solid or liquid (% liquid calculated and shown as '%L'), at the firing temperature where the pellet was fired at. These calculations assisted in classifying and then explaining whether the observed sintering of particles was by solid or liquid state mechanism. Unlike, Equilib calculation 1, where particle was observed to be of a crystalline phase identified by XRD and present in the database, the input chemical formula was inserted as such in FactSage.
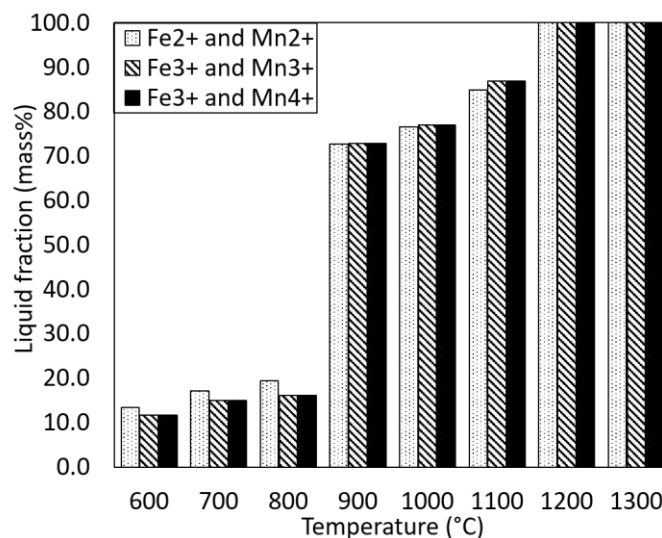
Figure 34: The effect of varying Fe and Mn oxidation on liquid formation (The example was for a composition of: MnO/Mn₂O₃/MnO₂ (12.64/14.06/15.49%), FeO/Fe₂O₃ (2.32/3.32%), Al₂O₃ (2.65%), CaO (3.50%), MgO (1.83%), SiO₂ (66.55%), Na₂O (4.04%), and C and S (both 0%)) (Calculations performed using FactSage 7.3 software, at PO₂ of 0.17 atm)

Table 18: Corresponding table showing the liquid formed (in mass %) as a function of change in temperature and the Fe/Mn oxidation states

Temperature (°C)	600	700	800	900	1000	1100	1200	1300
Fe/Mn oxidation state	Liquid fraction (mass %)							
Fe^{2+}/Mn^{2+}	13.4	17.1	19.4	72.8	76.6	84.9	100.0	100.0
Fe^{3+}/Mn^{3+}	11.7	14.9	16.1	72.8	77.0	86.9	100.0	100.0
Fe^{2+}/Mn^{4+}	11.7	14.9	16.1	72.8	77.0	86.9	100.0	100.0

3.6 Assumptions

For this project several assumptions were made especially in the design of the test matrix. The assumptions as well as their respective justifications, are discussed in Table 19.

Table 19: Assumptions and the justifications thereof made for this study

Assumption	Justification
Sub-samples collected from the whole are representative	Careful attention was placed when sampling material from whole.
Applied firing temperatures are in agreement with duct temperatures	Careful measures applied to decide on the min and max temperatures.
A prevailing air atmosphere is encountered in the ducts of the furnace. Thus, the laboratory tests are conducted in an air atmosphere.	Since the roof of the furnace is largely open, air ingress is expected. This is further justified by the observed combustion of CO gas on the surface of the furnace bed. Also in SAF ferrochrome producing processes, the off-gas was reported to have about 90% air (European Commission, 2010)
Although according to literature the sintering time has a bearing on the degree of sintering observed. Four hours across the board is sufficient for sintering to be observed in this case.	Most literature cited sintering times lower than four hours with success. A number of articles stipulated four hours where discernible sintering was observed.
Points chosen for assessment of localised sintering are reasonable representative of the whole sample.	Based on the premise of good sampling techniques prior to firing test and selection of variations of particle joints at each firing temperature.
Composition input to FactSage is within reasonable accuracy.	Careful was attention was placed when analysing the as-sampled dust streams.

4 RESULTS

The results are presented in a sequence that follows closely the experimental procedure followed: first the results relating to sintering in the smelter-based work are presented (section 4.1), then the rests conducted in the laboratory (sections 4.2 to 4.5).

4.1 Smelter duct observations

Some of the images taken during a duct inspection, for a short shutdowns period, are shown in Figure 35. Figure 35 (a) shows one of the ports, along the diagonal section, after being opened. As seen in the image, the duct contained dust material that had formed a hard crust, blocking the port. Figure 35 (b), shows an image taken during the removal of the dust in the vertical section (the dust was not removed from the diagonally section as this activity was considered unsafe). Observations made during the dust removal was that in some areas, the dust was hard and crusty, and thus couldn't be dislodged by hand. An axe was used instead. Figure 35 (c), was taken after the removal of the dust from the port. Figure 35 (d), shows a portion of the interior of the duct with some hanging dust along the duct, which may have resulted by sintering. Figure 35 (e) shows the completely blocked duct during the long shutdown.

Since the actual analysis of the dust observed along the duct was not conducted (due to mainly sampling and time constraints), whether the observed hanging dust was as a result of sintering of material could not be confirmed. Indications, however, based on the hardness of the dust as well as the crustiness in some places seemed to at least point to the possibility of sintering as a contributing mechanism to this.
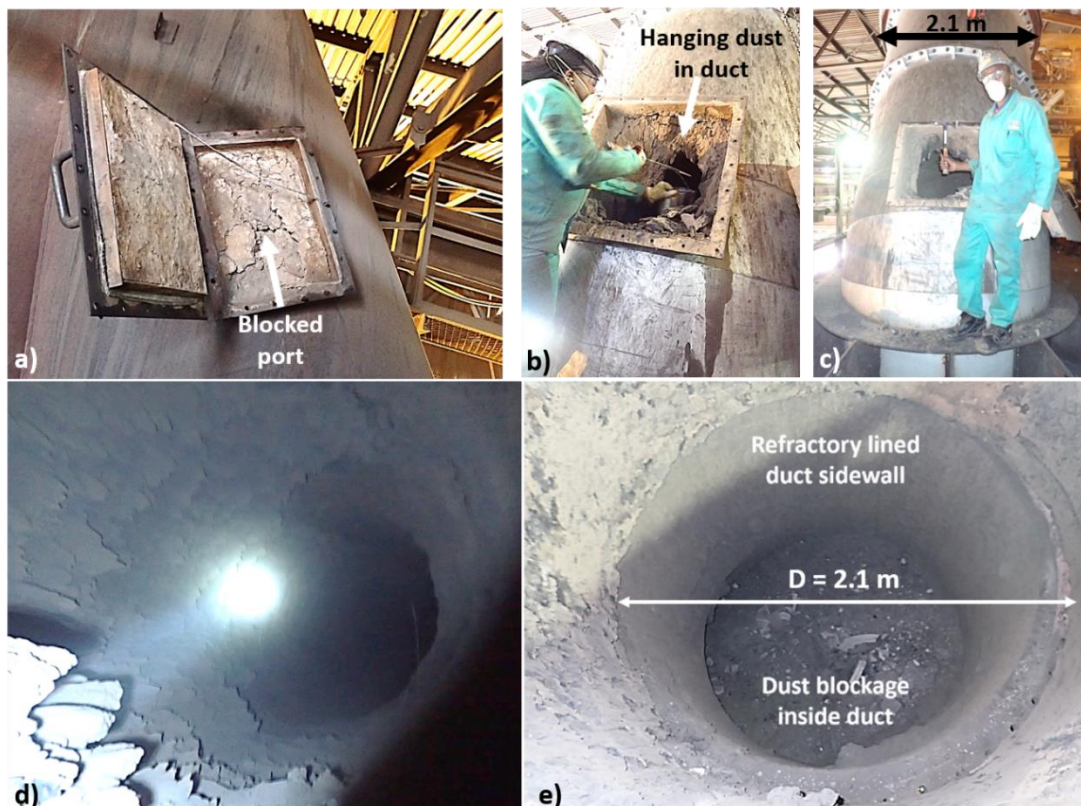
Figure 35: Photographs taken during the duct inspection, (a) blocked port in diagonal section, (b) clearing of blocked port, (c) appearance of port after clearance of dust material, (d) appearance of duct interior through shining torch light, and (e) completely blocked duct during long shutdown.

51

4.2 As-sampled dust characterisation

Section 4.2 presents the results of the characterisation of the as-sampled dust prior to firing. Presented in this section is the physical appearance, PSD analysis, bulk chemical composition, bulk phase chemical composition, as well as the specific phase chemical composition, for stream 1, 2, and 3.

4.2.1 Physical appearance

A photographic image showing the as-sampled dust appearance for stream 1, 2, and 3, is shown in Figure 36. Along with the image are pictures of the pressed pellets with its corresponding as pressed diameter for each stream. From the figure, a visible difference was observed in the colour (i.e. stream 1: grey with touches of black and white, stream 2: grey, and stream 3: brown), as well as the particle size of the dust. The difference in PSD is quantified in section 4.2.2.

Figure 36: Photograph showing physical appearance of stream 1-3 (stream 1: far left, stream 2: middle, and stream 3: far right; d= diameter of pressed pellet)

4.2.2 Particle size distribution

The particle size distributions per stream, are presented in Figure 37. From the figure, it was observed that stream 1 had the highest fraction of coarse particles (i.e. 70% of particles were above 212 microns), followed by stream 2 with 13% of its particles above 212 microns. Stream 3 on the other hand had the highest proportions of fines, with 89% of particles below 38 microns.

Comparing these results with literature, stream 3, which had the finest particle size with 89% of its particles passing 38 microns, closely resembled the PSD of SiMn dust reported by (Gaal et al., 2010) for a sludge producing SAF operation i.e. a wet dust treatment process. Furthermore, even though the work done by (Nkosi et al., 2011) did not report on the PSD of the dust for the exact same smelter in question here, judging from the SEM micrographs reported earlier in Figure 12, the relative fineness of the particles suggests that these are representative of stream 3 dust. One would expect that under the same firing temperature and pressed pellet strength, sintering if present, would be most pronounced in stream 3 compared to stream 1 and 2, due to a lower degree of inter-particular pores (Romero et al., 2008), (Hu and Wang, 2010), (Dehaghani and Ahmadian, 2015), and (German, 1996).

52
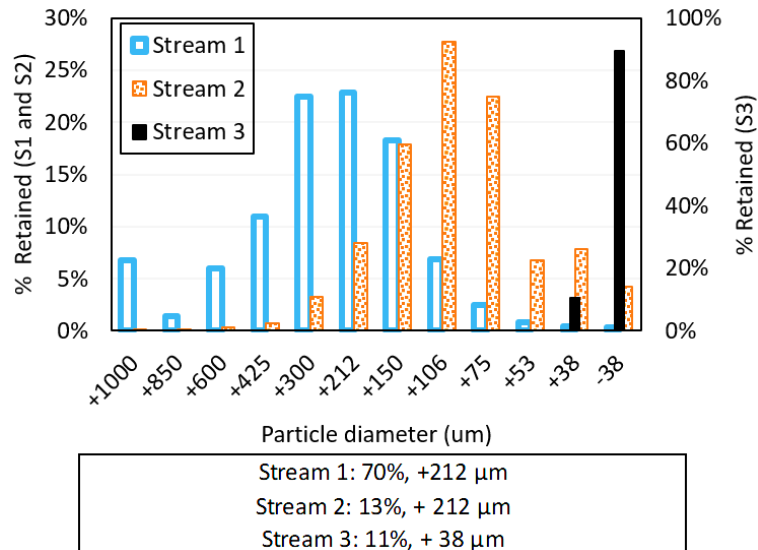
Figure 37: Bar graph showing screen analysis results for stream 1-3 (S = stream)

4.2.3 Bulk chemical composition

Table 20 gives a summary of the chemical analyses of stream 1, 2, and 3. The results are presented in terms of the mean composition for each specie calculated over ten measurements. A standard deviation value is also included in the table. The complete set of analyses are available in Table 35 in Appendix D.

It was acknowledged from the onset that the chemical compositions presented here were not reflective of the actual phase chemistry of the dust, and that the chemical formula assigned herein were only included for the simplification in the presentation of the results, as well as for ease in comparison with literature data.

The following observations were made from chemical analyses:

- The major species were MnO and SiO_2, at 25-32% and 34-43% respectively.
- Condensed volatile species such as potassium, sodium, and zinc were also detected. The average composition for these three species ranged between 1% and 4% K_2O, 0% and 2% Na_2O, and <0.05% and 0.26% ZnO. For all three species, the highest amounts were observed in stream 3. Since these species are well-known for encouraging the formation of low melting glass phases (Baxter and DeSollar, 1996), (Lin et al., 2006), and (Hasanuzzaman et al., 2015), the potential for liquid-state sintering of the dust during firing was deemed feasible. The potential for such was even more likely for stream 3 where the highest levels of these species was seen.
- Stream 1 and 2 had similar chemical compositions, whilst the chemical composition of stream 3 was significantly different. Thus, similar sintering behaviours were expected for stream 1 and 2. However, since there was a difference in the particle size, which has a direct effect on the kinetics of the interactions, a difference in the extent of interactions and strength of resulting sinter was expected.
- Stream 3 contained about 5% more MnO, 3% less FeO, 3-4 % more MgO, 8-10% less SiO_2, and 4-6% less C than stream 1 and stream 2.
- The carbon content was highest in stream 1 (i.e. coarsest fraction), and lowest in stream 3 (i.e. finest fraction).
- Comparing the as-sampled dust chemical compositions to that reported in literature for the same smelter by (Steenkamp et al., 2018) and (Nkosi et al., 2011), also indicated in Table

53

20 as 'L1' and 'L2' respectively, it once again seemed, as was the case with the PSD, that the chemical composition presented in literature, resembled more closely that of stream 3. It would seem then that the previous investigation conducted on the dust from this SiMn producing smelter were from stream 3. This is somewhat not unsurprising, as although the smelter does not keep a daily record of the amount of dust produced in each stream, visual observations whilst at the smelter seemed to indicate that by far stream 3 represented the bulk of the dust. This in significant in light of the current sintering evaluation study as it would mean that of the three streams, stream 3 would be the most contributing stream to any observed sintering.

Table 20: Summary of chemical analysis results for streams 1-3 presented as the mean and standard deviation as well as literature composition from the same smelter (mass % as received from the analysis division)

Str.	MnO	FeO	Al_2O_3	CaO	MgO	SiO_2	Na_2O	K_2O	C	S	ZnO	Total
1[#]	25.2	4.3	2.7	9.7	3.9	41.9	0.5	1.2	10.1	0.5	<0.05	100.0
Std.	0.7	0.1	0.1	0.3	0.1	0.5	0.0	0.1	0.2	0.0		0.9
2[#]	25.7	4.0	3.3	8.9	4.4	43.1	0.4	1.5	8.8	0.3	0.06	100.5
Std.	0.7	0.1	0.1	0.3	0.1	1.0	0.1	0.6	0.1	0.0	0.01	2.6
3[#]	31.8	1.0	2.9	8.3	7.7	34.0	1.7	4.1	4.0	0.9	0.26	96.8
Std.	0.9	0.0	0.1	0.4	0.2	0.6	0.1	0.6	0.1	0.0	0.01	1.9
L1	31.6	1.1	-	8.0	7.3	38.8	-	-	-	-	0.4	-
L2	35.1	1.3	4.0	7.4	6.8	36.3	1.6	3.3	-	-	0.3	-

Str. = stream; Std. = standard deviation; L1 = literature 1; L2 = Literature 2; - means not reported; P_2O_5 = 0.05% for all streams; B = <0.1% for all streams;

4.2.4 Bulk phase chemical composition

In terms of the bulk phase chemical composition determined by XRD, all streams contained a significant amount of amorphous (non-crystalline) material. This was shown by the humps without defined peaks along the XRD diffractograms (see graphs in Figure 38). The presence of amorphous material was not surprising, as the same was reported for a SiMn sludge by (Ravary and Hunsbedt, 2013). The same graphs also shows peaks that are representative of crystalline phases. Those crystalline phases identified, along with their relative abundance, excluding the amorphous material, are shown in Figure 38. The following was observed from the table.

- For stream 1 and 2, the same predominant phase was identified as quartz. Other minor and trace phases identified were diopside, braunite, and hausmannite (in both streams); tephroite and Jacobsite (in stream 1 only); leucite and bustamite (in stream 2 only).
- For stream 3, among the crystalline phases quartz was present in intermediate quantities. Unlike stream 1 and 2, diopside, braunite, hausmannite were also present in intermediate quantities. Leucite and bustamite were present in trace amounts similar to stream 2.
- The comparison of the streams showed that most phases were present in some amounts either in all streams, or in two streams. The only exception was tephroite and Jacobsite which was present in trace amounts in stream 1. It is likely that these two phases might have also been present in the other streams in extremely quantities below the 3% detection limit.

- The XRD results also showed that there was a mixture of ore minerals e.g. braunite, quartz, hausmannite, Jacobsite, and slag phase e.g. diopside. This observation was also noted by (Nkosi et al., 2011).
- Comparing these phases observed here with what has been seen in literature (as presented in Table 6 and Table 7), all the phases identified were typical of FeMn and SiMn producing processes with the exception of bustamite, tephroite, and leucite.

Colour	Red	Magenta	Lime
Phase	Quartz	Diopside	Braunite
Colour	DarkRed	DarkOrange	
Phase	Hausmannite	Bustamite	
Colour	Olive	Gold	
Phase	CaMn silicate	Tephroite	
Colour	LightSteelBlue	Blue	
Phase	Leucite, syn	Jacobsite	
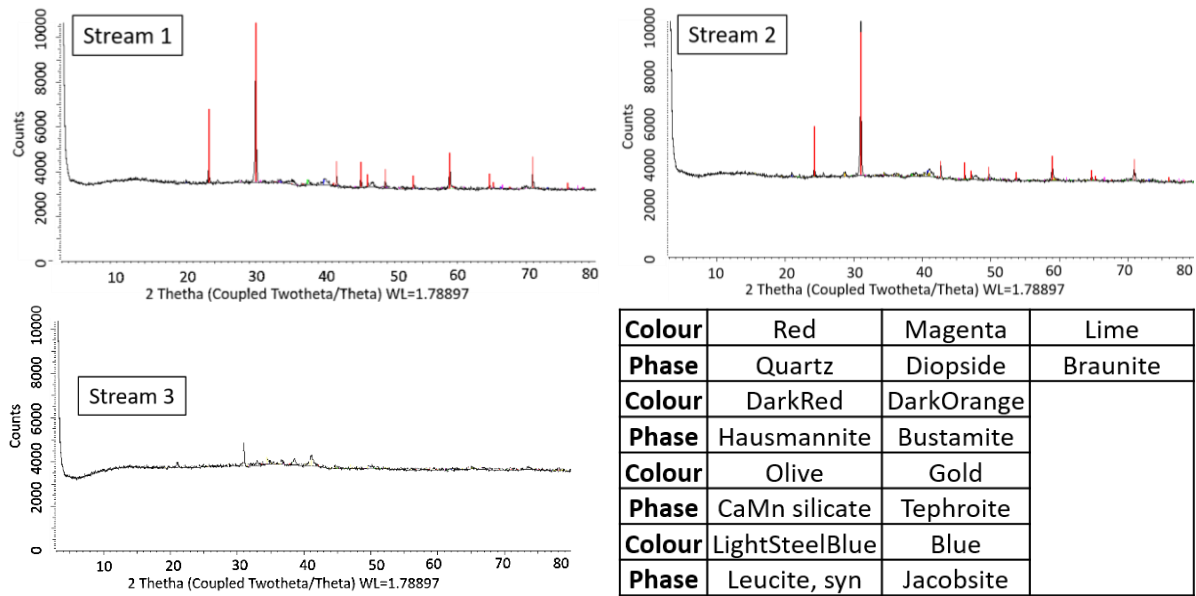
Figure 38: XRD diffractograms showing phase counts for as-sampled dust for stream 1, 2, and 3. The colour coding is shown in the table on the bottom right

Table 21: Summary of the identified phases, and their relative abundance in the as-sampled dust (calculation excluded amorphous material), for as-sampled dust stream 1-3 (with predominant >50%; major = 30-50%; intermediate = 15-30%; minor 5-15%; trace <5%)

Phase	Chemical Formula	Relative abundance		
		Stream 1	Stream 2	Stream 3
Quartz	SiO_2	Predominant	Predominant	Intermediate
Diopside	$CaMg(SiO_3)_2$	Minor	Trace	Intermediate
Braunite	Mn_7SiO_{12}	Trace	Minor	Intermediate
Leucite, syn	$KAl(Si_2O_6)$		Trace	Trace
Tephroite	Mn_2SiO_4	Trace		
Hausmannite	Mn_3O_4	Trace	Minor	Intermediate
Bustamite	$(Mn,Ca)SiO_3$		Trace	Trace
Jacobsite	$MnFe_2O_4$	Trace		
CaMn silicate			Trace	Minor

4.2.5 Specific phase chemical composition

The specific phase chemical composition section, presents the results, for each stream, of the SEM-EDS analysis undertake for the as-sampled dust. The results were presented separately for each stream. At the end of the section i.e. section 4.2.5.1, each streams results is compared against another, as well as against literature.

4.2.5.1 Stream 1

Figure 39 (i.e. the entire 'A'-section), shows a SEM BSE micrograph of the general overview of stream 1 dust sample. In order to zoom in more closely to the details of the sample, a portion of the 'A'-section was captured and examined, as shown in the rectangular marked 'B'-section in Figure 39. The following observations were made from section 'B':

- Firstly, the sample was composed of a mixture of angular particles (angular shape indicates). According to ((Guézennec et al., 2005), the former shapes were formed by directly entrained raw material dust in solid state, whilst according to (Martins et al., 2008) and (Guézennec et al., 2005), the latter shapes are formed from liquid or condensed vapour. The distribution of particle shapes, estimated by observation of the microstructure in Figure 39b, was 75% and 25% respectively.
- Secondly, the sample had a mixture of both coarse (largest particle had a measured diameter of above 1500 µm. Measurement conducted using the scale-bar on the bottom left of the image,) and fine particles (smallest particle with measured diameter below 50 µm).
- Thirdly, there was a noticeable difference in the particles colour scheme, even with the black and white images. For example, dark grey particles were observed that resembled quartz. Also, distinctively white particles were also observed that resembled alloy. Other particles such as angular particles that appeared to be manganese ore as well as black particles that resembled carbon were also observed.
- Lastly, in terms of the particles packing arrangement, most particles were in close proximity to one another. A closer look through a zoom in function in word revealed that most particles where not in contact with each other i.e. closely packed but not sintered.
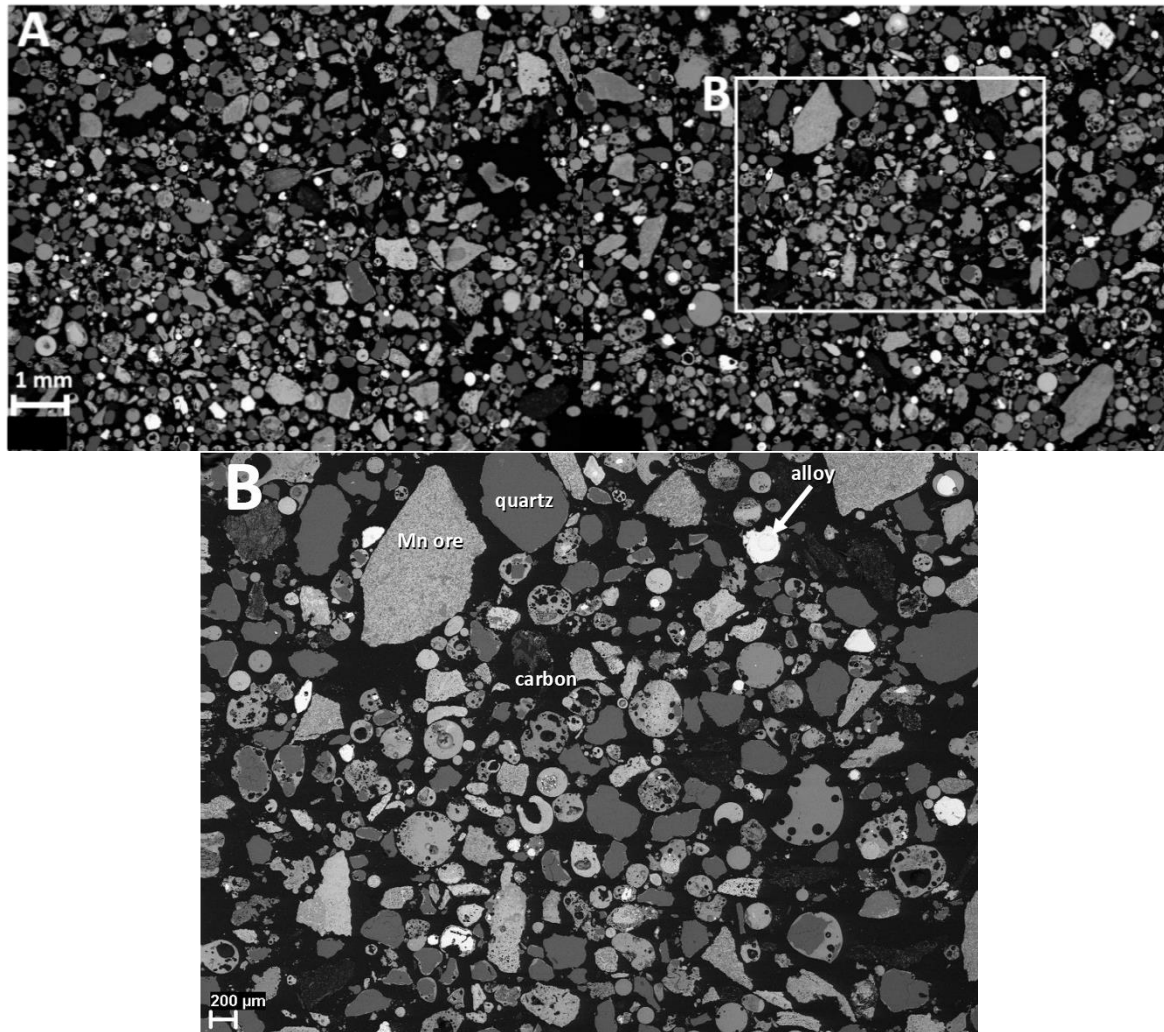
Figure 39: SEM BSE micrographs showing microscopic appearance of stream 1 (A: overview), B: subsection of A with various grains labelled based on grey scale micrograph)

To obtain a general idea of the elemental distribution within the 'B'-section, SEM BSE elemental maps were constructed, as shown in Figure 40. The maps mainly revealed a dominance of Fe and Mn in the white alloy particles, a definite presence of Na and K species at various concentrations all-over the sample (in certain instances associated together), and a high proportion of quartz grains, which supports the observation that quartz is the predominant phase in stream 1 observed from the XRD results.

For further analysis of the details of the micrographs, two areas within section 'B' were explored. These are marked as 'C' and 'D' in section 'B'. SEM BSE micrographs were generated, as shown in Figure 41, together with EDS point analyses of specific phases. Generic names of the type of composition were also assigned. It should be noted that to maintain consistency throughout the discussion of the results, the same generic names, as well as the colour scheme for the BSE maps were used as presented in Figure 40.

It was observed in Figure 41 that the main particles found were glass slag (indicated by points 2-5, 11, 14, 17 and 18), manganese ore (points 9 and 12), a manganese iron calcium oxide phase (points 6-8), a carbonate (points 10 and 13, identified by carbon), and an alloy phase corresponding to silicomanganese (points 15 and 16) (Steenkamp et al., 2018). The glass phase observed, especially in point 2, 11, and 14, surrounded the quartz grain.
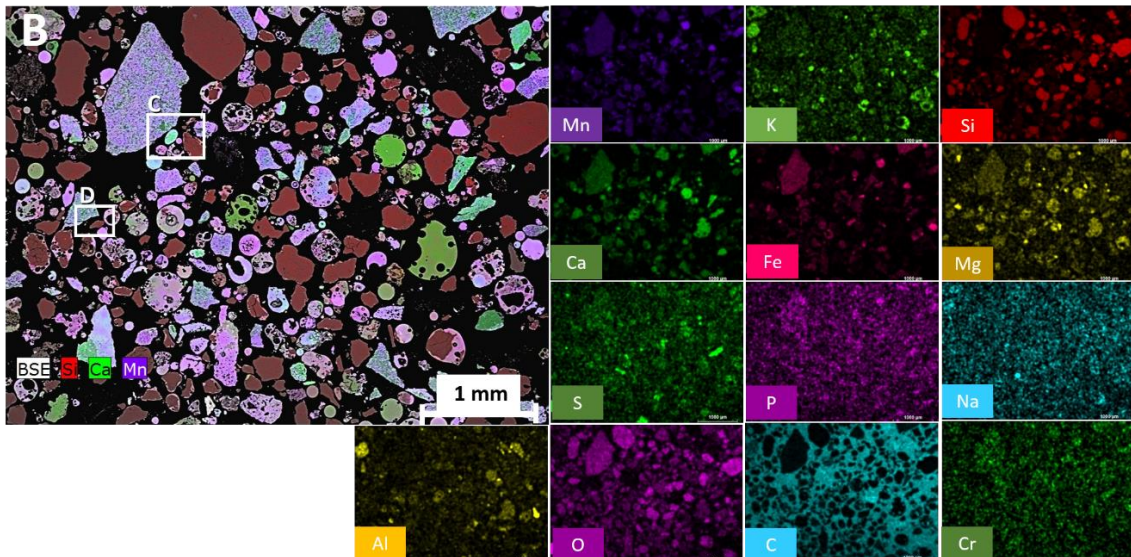
Figure 40: Elemental mappings for 'B'-section showing elemental distribution
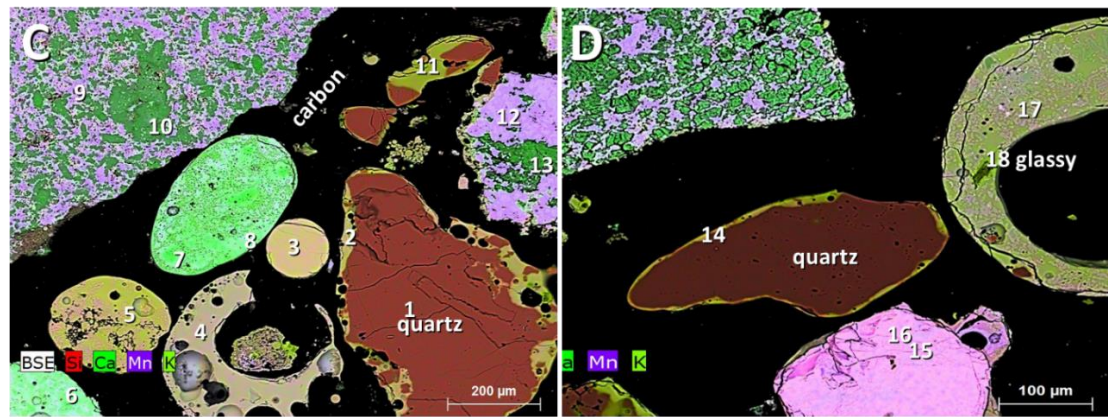
Point	O	Na	Mg	Al	Si	S	K	Ca	Mn	Fe	Type
1	53.3				46.7						Quartz
2	37.2	0.7	2.1	2.5	18.8		2.1	7.9	24.3	4.4	Glass slag
3	34.0	1.2	1.2	1.3	16.0		3.2	2.3	39.3	1.6	Glass slag
4	37.2	0.5	3.5	1.7	16.2	1.4	0.8	10.8	27.7	0.2	Glass slag
5	36.5	2.1	3.3	0.8	18.6	0.5	4.9	2.0	31.1	0.2	Glass slag
6	26.5		1.3	0.3	1.7			28.0	32.1	10.0	MnFeCa oxide
7	28.0		1.8	0.0	0.7	0.7		44.8	22.0	1.9	MnFeCa oxide
8	26.9		2.0	0.1	2.1			28.7	34.7	5.4	MnFeCa oxide
9	24.6				3.2			0.8	46.1	25.3	Mn-ore
10	27.5		5.6	0.0	0.2			39.0	26.7	1.0	Carbonate
11	40.5	1.2	4.6	2.7	22.6		3.9	8.5	16.0		Glass slag
12	23.6				1.7				66.0	8.8	Mn-ore
13	31.0		1.1		1.4	2.8		55.7	8.0		Carbonate
14	40.2	1.5	1.6	1.0	25.5		5.0	2.9	22.3		Glass slag
15					10.8				68.8	20.4	Alloy
16					19.8				65.1	15.1	Alloy
17	33.6		3.9	1.1	13.6		0.5	6.8	40.4		Glass slag
18	35.6	0.8	1.9	4.6	14.7		2.7	9.9	29.9		Glass slag

Figure 41: EDS analysis results for section 'C' and 'D' (With Mn: manganese, Fe: Iron, and Ca: calcium; results in mass %. "O" was calculated using stoichiometry in all instances)

58

4.2.5.2 Stream 2

Figure 42 shows a number of SEM BSE micrographs depicting the microstructural features of stream 2. Section 'A' in the first micrograph shows the overview of the sample. From section 'A', a sub-section i.e. section 'B' maps, were taken, in order to examine the element distribution of the sample. Similar to stream 1, a large proportion of quartz grains were observed, K and Na were also present with their concentrations high in certain places, and alloy was also observed. The only major difference compared to stream 1 was the overall finer particle size in stream 2 when compared to stream 1 (e.g. the largest particle was only about 750 μm in diameter, with smallest particle still <50 μm in diameter). Nonetheless, both angular and spherical particles were still observed, at the same distribution as stream 1.

In order to examine more closely the chemical composition of some of the particles in stream 2, section 'C' which represents a sub-section of section 'B', was captured, and EDS point analysis were done on some of its particles, as shown in the labelled coloured micrograph Figure 42-section 'C'. The EDS analyses are shown in the ensuing table in Figure 42.

From the EDS analysis some of the same phases such as glassy slag (indicated by points 2, 3, 7, 9 and 23), quartz (indicated by points 1, with a glassy slag rim feature as observed for stream 1), Mn-ore (points 8, 10, 16, and 17), carbonate (points 22), an alloy of the same composition as stream 1 (points 18 and 19), and a manganese iron calcium oxide phase (points 6 and 11) were identified. In addition to these, a manganese calcium silicate crystalline phase, as well as a high manganese iron oxide and three other types of glassy slags of differing compositions, conveniently named as, glass slag a, glass slag 1, and glass slag 2, were identified.
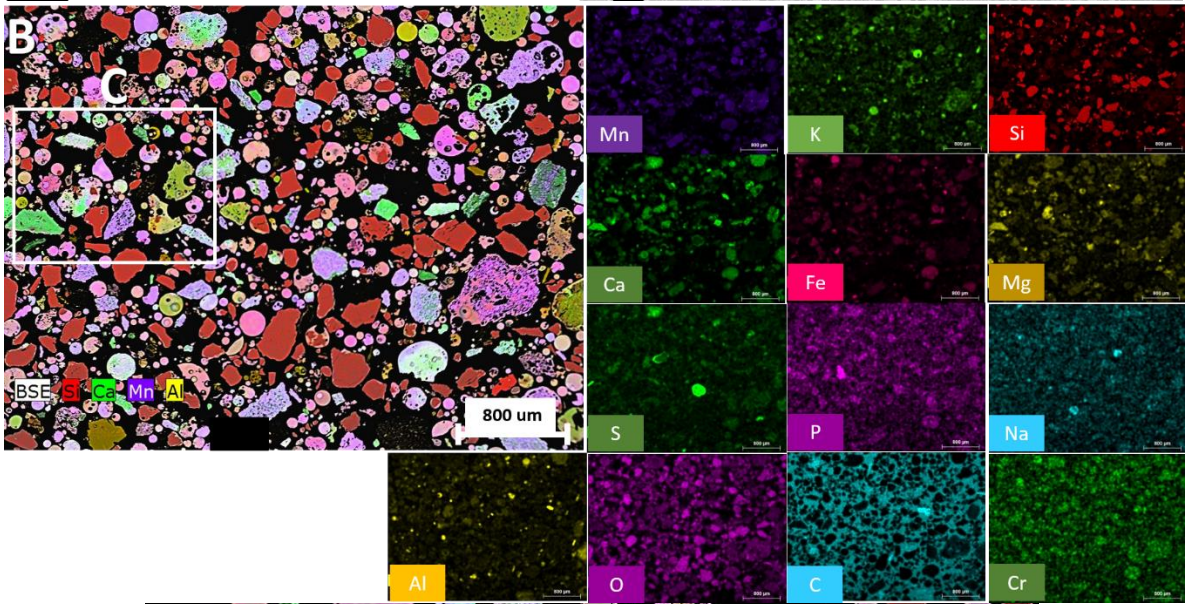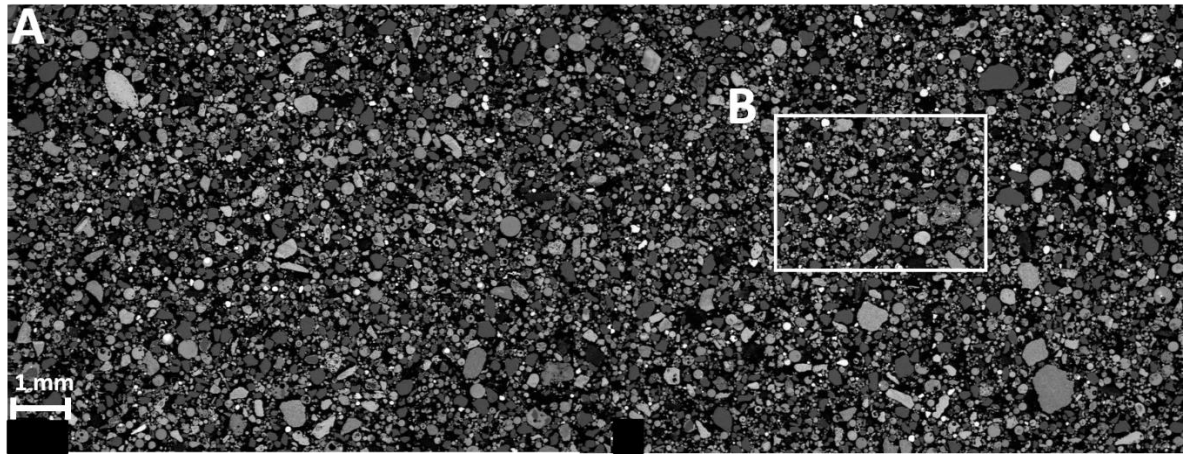
Point	O	Na	Mg	Al	Si	S	K	Ca	Mn	Fe	Name
1	53.3				46.7						Quartz
2	36.0	1.3	4.1	1.9	16.8		2.4	6.2	31.3		Glass slag
3	39.9	0.7	8.7	0.9	20.5	0.8	1.0	3.0	24.6		Glass slag

#											
4	27.6				7.7				64.7		Mn ore
5	37.0	0.9	5.3	2.8	16.0		1.7	14.4	21.8		Glass slag 1
6	27.4		0.3	0.3	1.8			41.4	26.1	2.7	MnFeCa ox
7	33.6	0.6	2.4	2.8	12.8		0.8	8.6	33.1	5.2	Glass slag
8	25.4				4.2			1.0	64.1	5.4	Mn ore
9	37.1	2.0	3.6	1.9	18.5		4.0	8.1	24.9		Glass slag
10	27.1	0.3	4.5	0.6	3.2		0.2	10.0	54.1		Mn-ore
11	28.0		0.5	0.3	0.5	0.5		51.6	18.7		MnFeCa oxide
12	24.4		1.0		1.5	0.3		3.7	61.6	7.6	High Mn, Fe-ox
13	24.3		2.1	0.2	1.3			3.4	51.4	17.2	High Mn, Fe-ox
14	33.1		1.4	0.5	13.4			13.6	38.0	0.0	MnCaSi ox
15	28.4		1.3	0.5	7.0			6.9	55.8	0.0	MnCaSi ox
16	23.4		0.4		1.0			1.3	70.1	3.8	Mn ore
17	22.9		0.3		0.4			0.4	71.0	5.0	Mn ore
18					10.3				71.6	18.1	Alloy
19					20.2				64.4	15.4	Alloy
20	43.1	1.3	1.0	2.1	29.5		6.1	4.1	13.0		Glass slag a
21	40.1		9.8	2.9	15.8	1.3	0.3	21.9	7.8		Glass slag 2
22	28.4		9.0					39.6	23.0		Carbonate
23	38.1	1.5	7.2	1.2	19.1		3.4	7.2	22.4		Glass slag

Figure 42: SEM BSE micrographs showing overview of stream 2 dust under the microscope i.e. 'A'-section, elemental distribution in 'B'-section, and EDS point analysis in 'C'-section (ox: oxide, red circle: showing glass slag rim feature as observed in stream 1)

4.2.5.3 Stream 3

Figure 43 shows two SEM BSE micrographs of stream 3 as-sampled dust. Section 'A' is an overview image at the same scale as section 'A' for stream 1 and 2. Section 'B', which is a sub-section taken from section 'A', shows various maps highlighting the elemental distribution of the sample. From the micrographs, both angular and spherical particles were observed (with distribution unclear due to fineness of samples). It was evident that the particles of stream 3 were much finer than those of stream 1 and stream 2 e.g. the coarsest particle was only 183 um with most particles being extremely fine. Due to this extreme fineness in particles, some of the particles tended to lump together forming larger agglomerates. This phenomena is commonly encountered in fine dust particles as highlighted by (Rughubir and Bessinger, 2007) and (Guézennec et al., 2005).

The colour scheme in the mappings presented in section 'B' of Figure 43, had a general purple overtone. This indicated that a large proportion of the particles were in oxide form, since purple was used as an indicator of oxygen. Potassium and sodium were present as in stream 1 and 2, they were particularly concentrated in the agglomerated particle on the top left of section-'B', in association with calcium, magnesium, manganese, iron, and sulphur to some extent. A detailed study of the maps revealed that apart from the distinct red coloured quartz grain, most of the particles could not be easily identified as their extreme fineness prevented the ability to isolate the particles from one another. This difficulty is illustrated by the SEM BSE micrograph along with EDS point analysis Figure 44. From the image, it was seen that despite the significant magnification of the image, particles could not be isolated from one another, and thus the EDS point analysis represented by point 1-5 had quite similar compositions since they were more representative of a group of particles than a single particle.
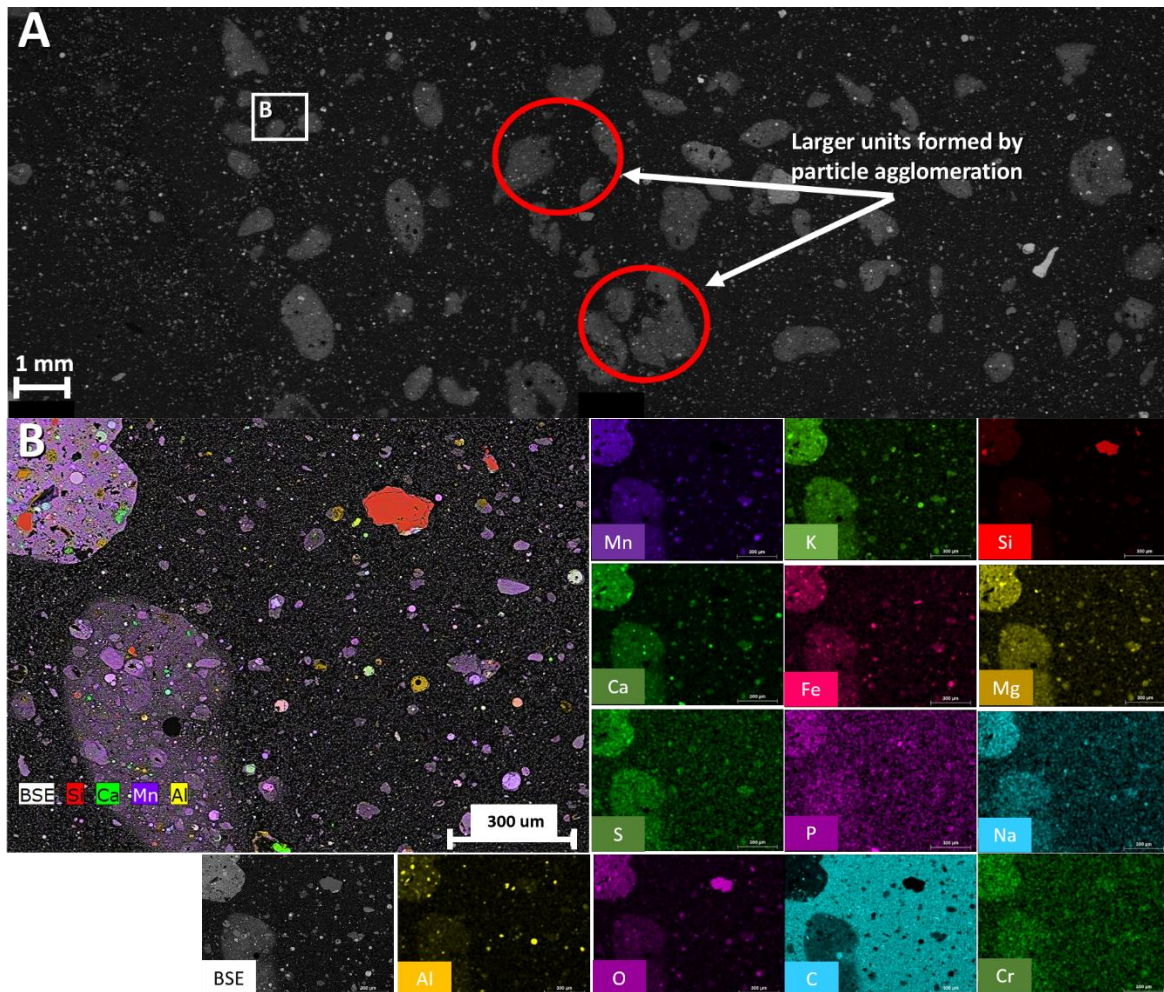
Figure 43: SEM BSE micrograph showing overview of as-sampled stream 3 dust i.e. section-'A' and elemental maps section-'B'
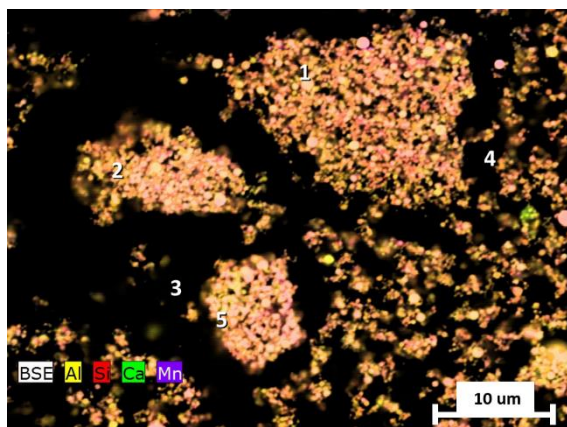
Point	O	Na	Mg	Al	Si	S	K	Ca	Mn	Fe
1	36	2	6	1	15	1	3	5	30	
2	36	1	5	1	15	1	4	6	31	
3	36	1	5	1	15	1	4	6	30	
4	36	2	5	1	15	1	4	5	30	
5	33	1	4	1	13	0	4	4	29	11

Figure 44: SEM BSE micrograph (left figure) with accompanying EDS point analysis (right table)

4.2.5.4 Comparison between the three streams together and against literature

As shown in the PSD analysis of the three streams, under the SEM microscope, it was evident that stream 3 had the finest particle size, followed by stream 2. The dust in all streams was made up of angular entrained raw materials dust, as well as spherical dust formed from liquid

or condensed vapour. Although the specific phase chemistry of stream 3 could not be determined with precision due to the extremely fine nature of the particles that made it difficult to isolate grains during EDS point analysis, it was clear that stream 3 contained some phases that were similar to stream 1 and 2 e.g. the brown-reddish quartz grains, and the pink spherical alloy phase (no alloy peak was observed in XRD probable due to low amounts of alloy or an poorly defined alloy crystal structure). Stream 1 and 2 had similar phases such as: MnFeCa-oxide, Mn-ore, alloy, and carbonate. Also, in both streams, glassy slag phases with significant amounts of low melting K and Na phase were identified, these were part of the amorphous materials seen in the XRD patterns. In some parts the glassy slag surrounded the quartz grains. Based on this observation, and depending on the melting temperature of these glassy slag, there lies a definite potential for liquid-state sintering if these phases are liquid (or partially liquid) at the firing temperature, and thus act as an intermediate neck between solid particles. Since K and Na species were also present in stream 3, the same phenomena is possible here.

Furthermore, a comparison of the SEM BSE micrograph for stream 3 especially as shown in Figure 26f and Figure 57 unfired pellet (i.e. the compressed unfired pellet), with SEM BSE micrographs shown in Figure 12 (as shown in literature), showed again that stream 3, based on the particle characteristics, was the dust stream in view in the previous studies.

4.3 Fired pellets characterisation

Section 4.3 presents the results of the characterisation of the fired pellets. Presented in this section is the physical appearance (highlighting each stream separately), compressive strength (each stream separately), bulk chemical composition, bulk phase chemical composition, and specific phase chemical composition, for stream 1, 2, and 3.

4.3.1 Physical appearance

The physical appearance highlights some of the external changes that occurred to the pellets (e.g. bonding of particles as a result of sintering), during firing to different temperature.

4.3.1.1 Stream 1

Selected photographic images showing the physical appearance of fired stream 1 pellets, along with its diameter after firing at 600°C to 1300°C, are shown in Figure 45. A detailed description of the temperature specific observations for each pellet, is shown in the accompanying Table 22.

The following main points were extracted from the images:

- Generally there was no marked difference in the pellets physical appearance for the pellets that were fired at 600°C to 1000°C. A major change was observed particularly at 1100°C, where some parts of the pellets had a slightly wetted external appearance. The wetly appearance may have been as a result of liquid formation as predicted by FactSage which predicted a formation of 33% liquid at this temperature (see Figure 46). Also, a higher proportion of pores surfaced at 1100°C, as more particles appeared to be bonded together (this was also observed at 1200°C). From 1200°C, total melting of the pellet was now fully observed, resulting in the total deformation of the original pellet shape. Again, this observation was in-line with thermodynamic predictions which estimated a formation of 90% liquid, with the remaining 10% representing gas formation (see Figure 46). The melting experienced at these high temperatures resulted in the formation of a compact unit upon solidification. The black and green phase observed at 1300°C was an immiscible slag

phase containing mainly manganese and iron, as well as significant levels of calcium and potassium.

- In terms of pellet friability, the pellets became markedly less friable with increasing firing temperature i.e. increasing firing temperature increased pellet stability.
- Interestingly, the pellet diameter remained the same from 600°C to 900°C. Thereafter, a gradual expansion in diameter was encountered until 1100°C.

(a) 600°C

(b) 700°C

(c) 800°C

(d) 900°C

(e) 1000°C   (f) 1100°C

(g) 1200°C
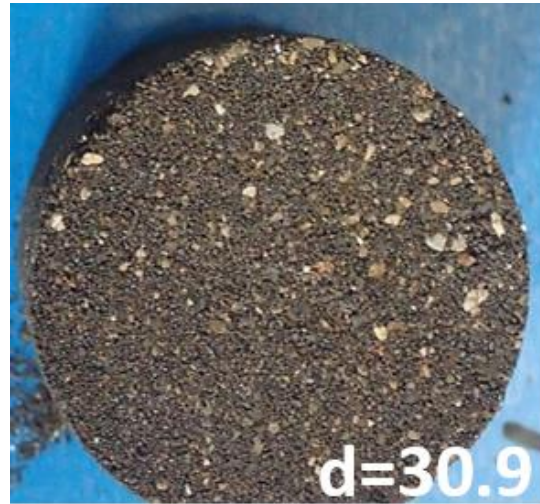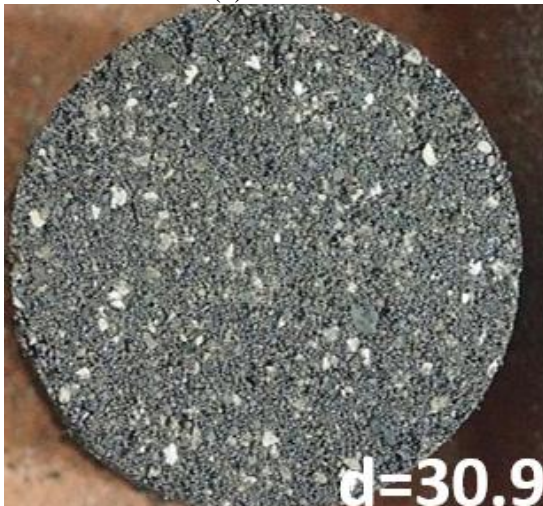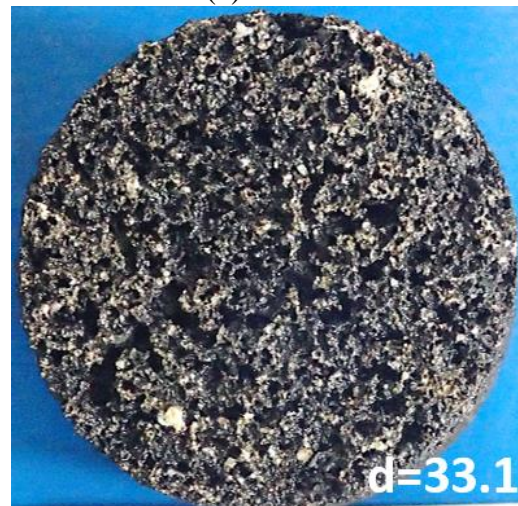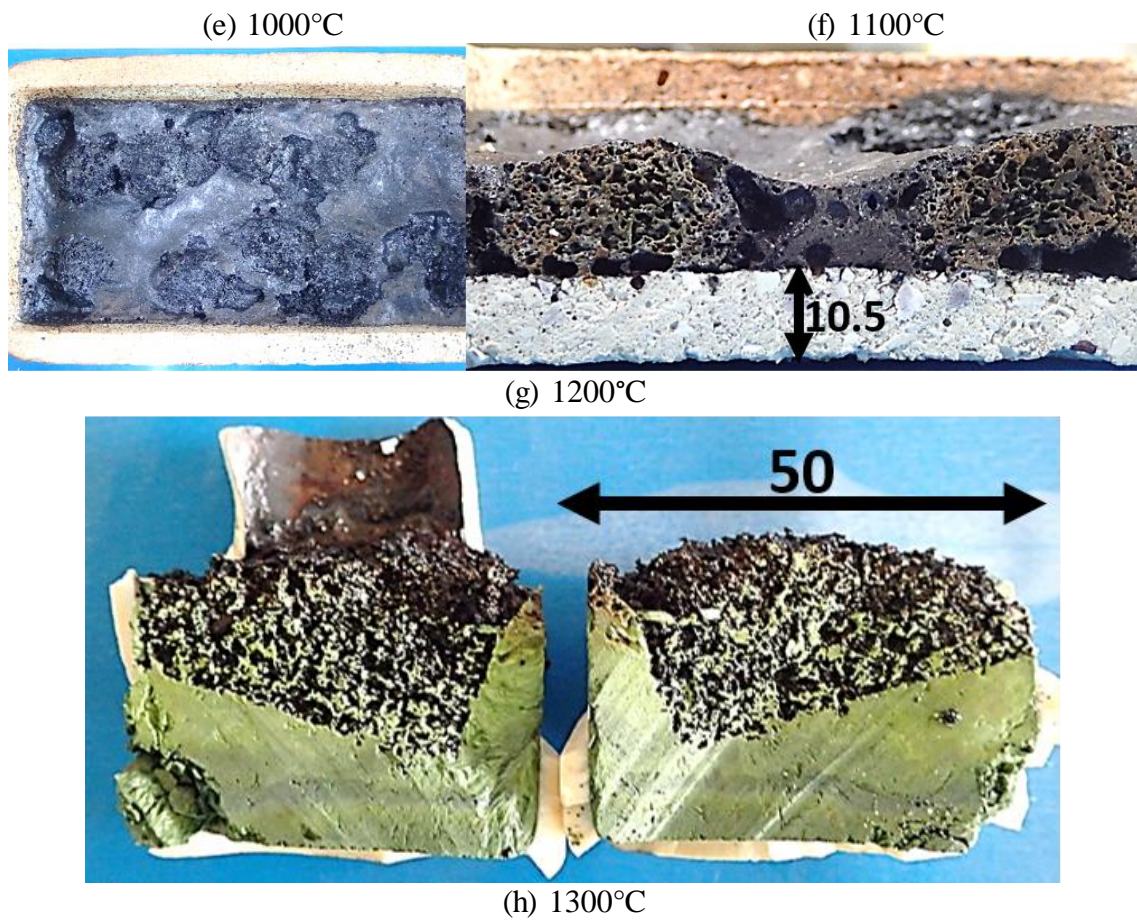
(h) 1300°C

Figure 45: Stream 1 pellets appearance after firing from 600°C to 1300°C (d = diameter of pellet; all values in the images are in millimetres)

Table 22: Stream 1 summary of physical observations of photographic images

Temperature (°C)	Observations
600	➢ No change in original pellet diameter and appearance. ➢ Original mixture of coarse and fine particles still visible.
700	➢ Similar observation to 600°C.
800	➢ Similar observation to 600 and 700°C pellets.
900	➢ Minor expansion in pellet diameter (less than 0.5% change). ➢ Original grains still visible.
1000	➢ Significant expansion of pellet diameter (~ 3% increase). ➢ Grains still visible in pellet.
1100	➢ Pellet appeared wet in some places. Large number of pores now appeared in pellet especially from the bottom of pellet where image was taken from. Pellet surface had a slight concave bend that was not visible in the image. ➢ Pellet slightly stuck on the tray in some instances. ➢ A large overall diameter expansion of 7%.
1200	➢ Left figure (top view) showing pellets of stream 1 that melted significantly in the tray. Only traces of the original pellet shape remained. ➢ Right figure (cross-section view) of cut tray. Definite melting observed (massive appearance) with a high degree of porosity in some areas. Tinges of green observed in some of the surfaces.
1300	➢ Bottom green portion melted completely and formed a massive unit that resembled the typical manganese slag. ➢ Top black portion formed an immiscible second slag phase.
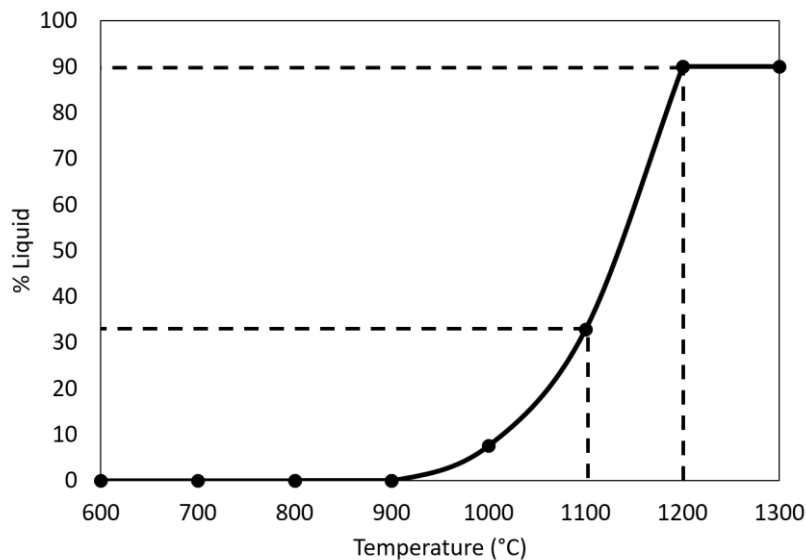
Figure 46: FactSage thermodynamic equilibrium calculation for stream 1 predicting % liquid formation with change in firing temperature (Used FactSage^{TM} 7.3, PO$_2$ of 0.17 atm)

4.3.1.2 Stream 2

Selected photographic images showing the physical appearance of stream 2 pellets, along with its diameter after firing from 600°C to 1300°C, are shown in Figure 47. Table 23 also summarises some of the observation made of the physical appearance of each pellet after firing.

The following overall observations were made from the images.

- There was no marked difference in the physical appearance of pellets fired at 600°C to 1000°C. A major change was observed in the pellets fired from 1100°C and forward. At 1100°C, the pellets had a dark and wetted appearance similar to what was observed for stream 1. Again, as shown in the graph in Figure 48, FactSage thermodynamic equilibrium calculations predicted a significant rise in liquid formation from about 3% at 1000°C, to 38% at this temperature. This may have been the reason for the observed wetted appearance. At 1200°C, the pellets melted substantially, in a manner similar to stream 1. At 1300°C, the sample melted completely forming two immiscible slag phases i.e., a green compact slag and a black porous slag. Again, similar to stream 1, by 1200°C, the prediction were for very high liquid formation i.e. in excess of 90%.
- Similar observations were made as was the case in stream 1 regarding the pellet friability i.e. that the pellet friability decreased with increasing firing temperature.
- The pellet diameter decreased with increasing temperature.

(a) 600°C   (b) 700°C

(c) 800°C   (d) 900°C

(e) 1000°C   (f) 1100°C

(g) 1200°C
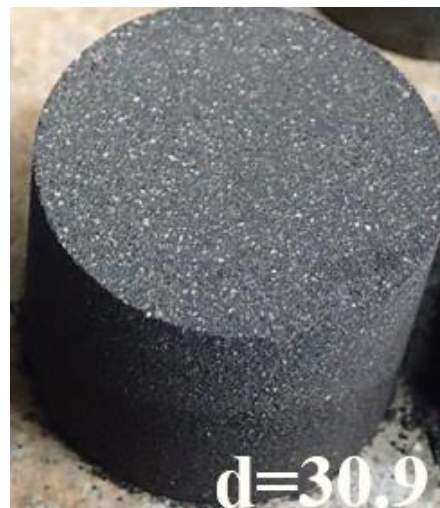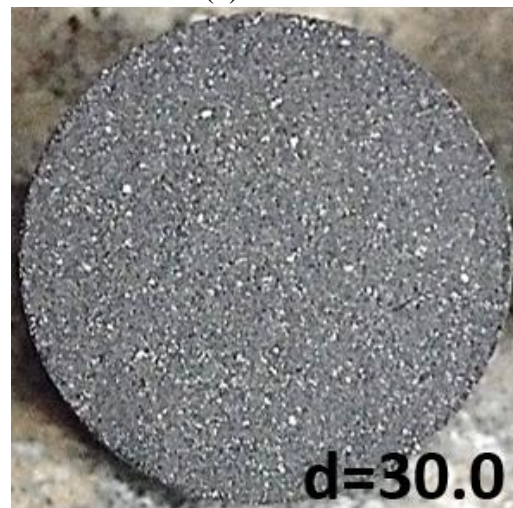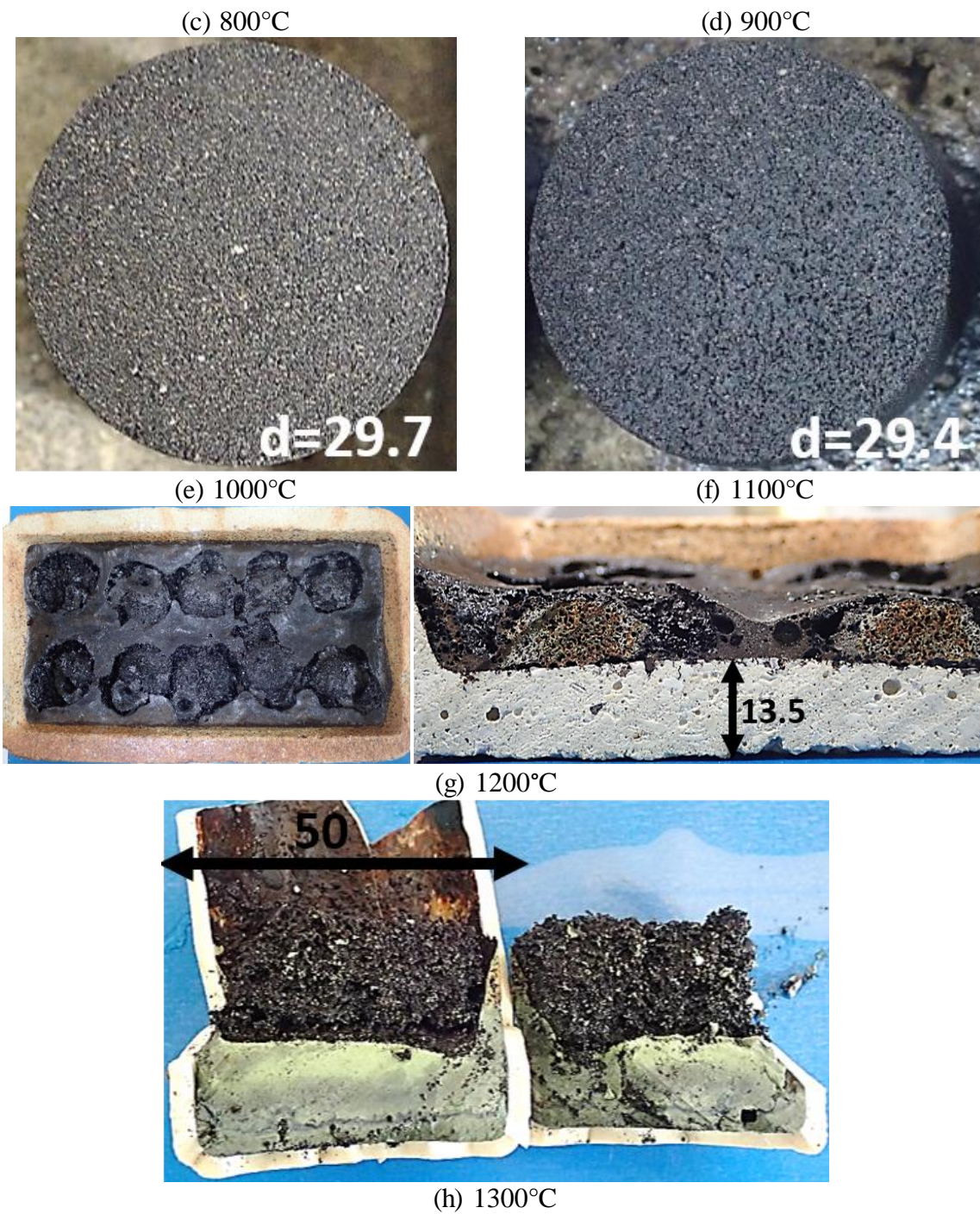
(h) 1300°C

Figure 47: Stream 2 pellets appearance after firing from 600°C to 1300°C (d = diameter of pellet; all values in the images are in millimetres i.e. mm)

Table 23: Stream 2 summary of photographic image observations

Temperature (°C)	Observation
600	➢ No change in original pellet diameter. ➢ Original appearance of pellet prior to firing maintained.
700	➢ Similar observations to 600°C.
800	➢ Similar textural appearance to 600 and 700°C pellets. ➢ Shrinkage in pellet diameter by ~ 3%.
900	➢ No significant difference in textural appearance. ➢ No change in pellet diameter from 800°C. ➢ Original grains still visible.
1000	➢ Diameter further decreased to an accumulated shrinkage of ~ 4%. ➢ Grains still visible in pellet.
1100	➢ Pellet appeared wet (large areas with a black texture). Pellet surface had a slight concave bend (not visible in the image shown above). ➢ Diameter further decreased to an accumulated shrinkage of ~5%. ➢ Pellet was observed in certain instances to slightly stick to the tray.
1200	➢ Left figure (top view), showing pellets of stream 2 that melted significantly in the tray. Only traces of the original pellet shape remained. ➢ Right figure (cross-sectional view), of cut tray. Definite melting observed (massive appearance) with a high degree of porosity in some areas. Tinges of green observed in some of the surfaces.
1300	➢ Bottom green portion melted completely and formed a massive unit resembling the typical manganese slag. ➢ Top black portion also melted but was highly porous. The pores could have been formed by escaping gases.
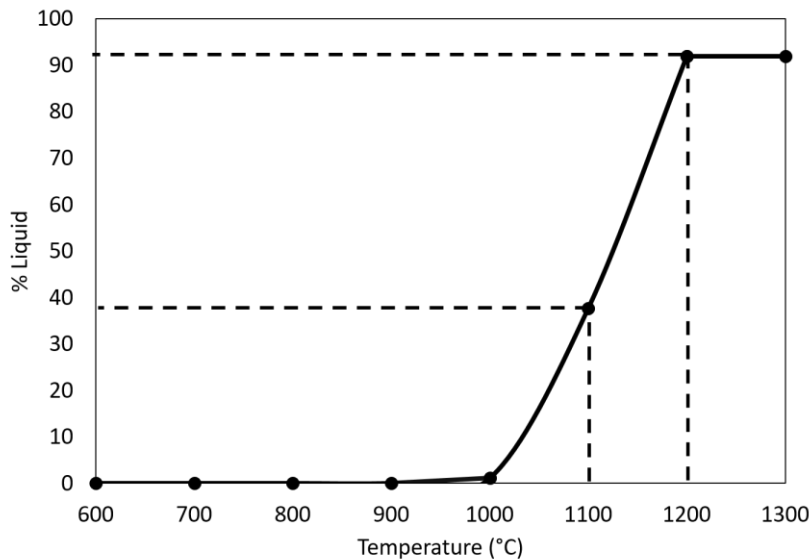
Figure 48: FactSage thermodynamic calculation for stream 2 predicting % liquid formation with change in firing temperature (Used FactSage^{TM} 7.3, PO_2 of 0.17 atm)

4.3.1.3 Stream 3

Selected photographic images showing the physical appearance of stream 3 pellets, along with the pellet diameters after firing at 600°C to 1300°C, are shown in Figure 49. A detailed description of the observations made of the pellets appearance after firing, is shown in Table 24.

The summary of the main observations are as follows:

- The pellets fired at 600 and 700°C were similar in physical appearance despite the difference in their diameters. From 800°C, the pellets appearance changed with every change in firing temperature. One noticeable change was the increasingly grey appearance adopted by the pellets with increasing temperature. By 1000°C the grey appearance was even more pronounced.
- At 1100°C, the pellets appeared to have melted (FactSage predicted 40% liquid formation at this stage, see Figure 50), and caused a distortion in the shape of the pellets. It appeared as though bubbling had taken place in the pellets resulting in the expansion of its volume. From 1200°C, the pellets completely melted as shown in Figure 49. This was in-line with FactSage predictions, which again predicted a high liquid formation at this temperature.
- No significant difference in pellet friability was observed due to the inherent high strength of these pellets from compaction.
- Compared to stream 1 and 2, the pellet diameter decreased significantly with increasing firing temperature i.e. a total of 18% compared to 5% shrinkage for stream 2, and 5% expansion for stream 1. This is further demonstrated by the graph in Figure 51.

(a) 600°C

(b) 700°C

(c) 800°C

(d) 900°C

(e) 1000°C

(f) 1100°C
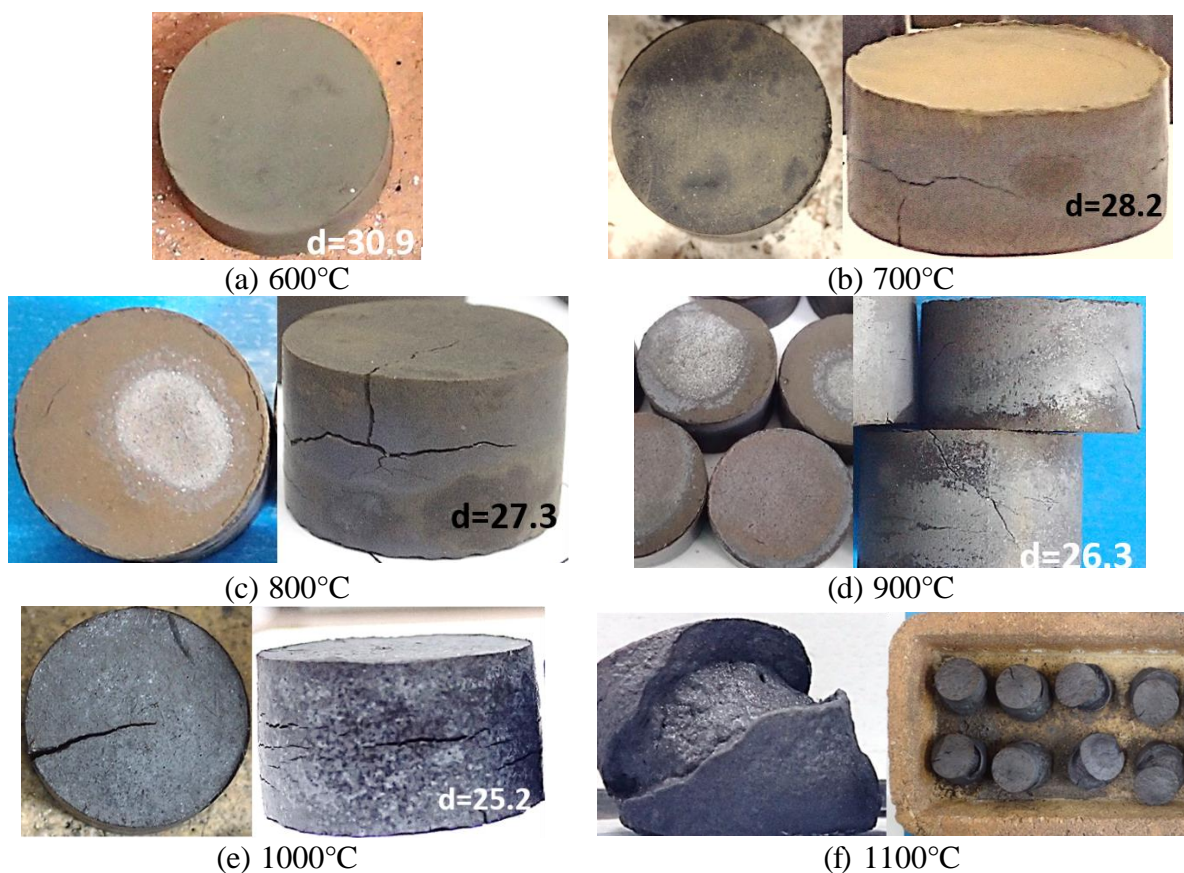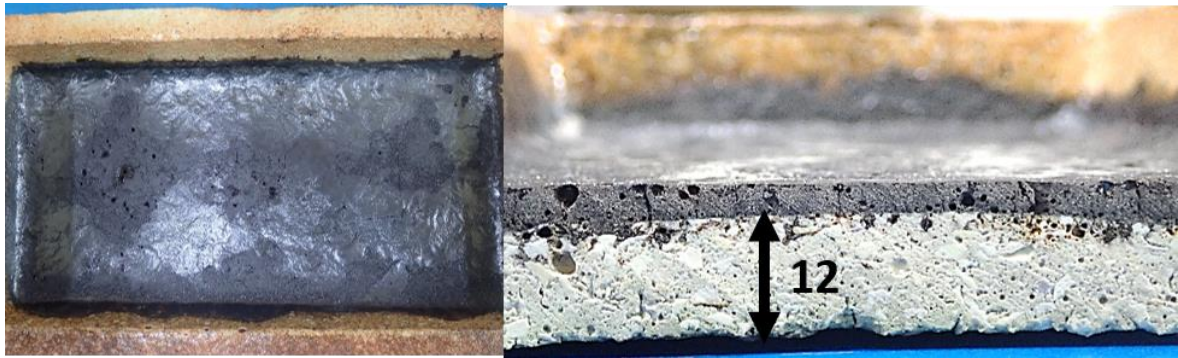
(g) 1200°C
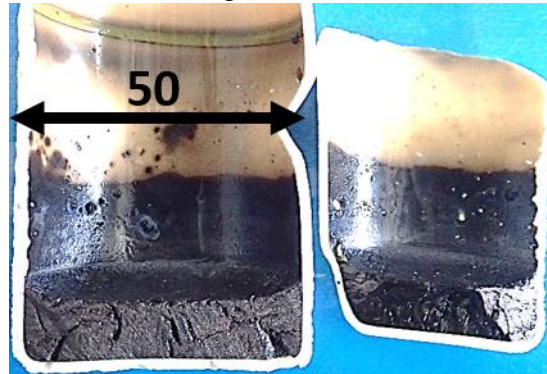
(h) 1300°C

Figure 49: Stream 3 pellets appearance after firing at 600°C to 1300°C (d = diameter of pellet; all values in the images are in millimetres i.e. mm)

Table 24: Stream 3 summary of photographic image observations

Temperature(°C)	Observation
600	➢ No change in original pellet diameter. ➢ Original appearance of pellet prior to firing maintained.
700	➢ Similar textural appearance to the pellet fired at 600°C. Small cracks observed in some instances on the side of the pellet. ➢ Significant shrinkage of ~ 9% in pellet diameter compared to 600°C.
800	➢ A distinct white (with tinges of red) patch appeared in most of the pellets. The patch covered anything between 15-30% of the pellet. ➢ Cracks were in most instances more pronounced. ➢ Shrinkage in the pellet diameter up to ~ 12%.
900	➢ Patch was larger than at 800 °C in certain instances. It covered almost the entire top section of the pellet. Some patches where dimly white with a red background. Sides of the pellets appeared wet and had a dark shiny tinge on the surface. ➢ Cracks mostly disappeared. ➢ Shrinkage increased to 15% compared to original diameter.
1000	➢ Patch disappeared completely. Pellets were now completely grey with wetly appearance now more pronounced. Cracks were observed in some pellets. ➢ Diameter was reduced by ~ 18% compared to original diameter.
1100	➢ Pellets completely lost shape and had a bloated appearance (completely grey in colour). ➢ Pellets often stuck to tray.
1200	➢ Left figure (top view), shows pellets of stream 3 that completely melted in tray. ➢ Right figure (cross-section), of cut tray. Sample formed one thin uniform layer of molten material that was grey to black in colour.
1300	➢ Sample melted completely forming one layer of uniform molten material that had a black shiny appearance.
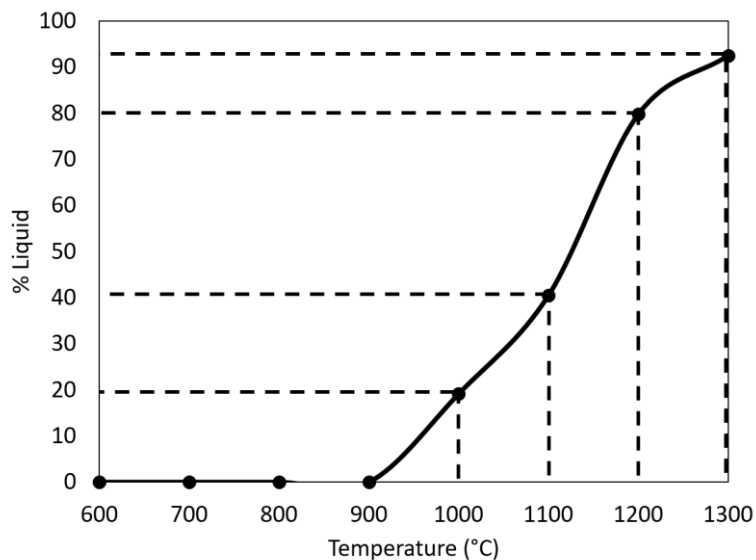
Figure 50: FactSage thermodynamic calculation for stream 3 predicting % liquid formation with change in firing temperature (Used FactSage^{TM} 7.3, PO$_2$ of 0.17 atm)

4.3.1.4 Comparisons between the three streams

A graph depicting the change in pellet diameter with change in firing temperature, for the three streams, is shown in Figure 51. From the graph, the fired stream 1 dust was observed to have experienced a gradual expansion in its diameter, especially from 1000°C to 1100°C. On the contrary, stream 2 (from 800°C) in its diameter with increasing firing temperature. This commenced as early as 800°C, and picked up at 1000 and 1100°C. Similarly, stream 3 experienced a shrinkage in its diameter, commencing at an even lower temperature of 700°C, all the way to 1000°C. By 1100°C, the sample showed melting and a phenomena called bloating (Quijorna et al., 2014), leading to a distortion in its pellet shape. It should be noted though when making a comparison between stream 2 and 3, that the latter experienced the most severe shrinkage as shown by the steep downward curvature of the graph in Figure 51. This phenomena of material expansion and shrinkage upon firing has been reported as a common sintering effect (Shen, 2009), (Romero et al., 2008), and (Adell et al., 2007). Expansion is associated with either phase transformation (or new phase formations) (Łada et al., 2018), and/or body bloating caused by the escape of volatile material (Quijorna et al., 2014), whilst shrinkage is usually associated with liquid formation or densification of pellet as a result of decreased surface energy (Romero et al., 2008).
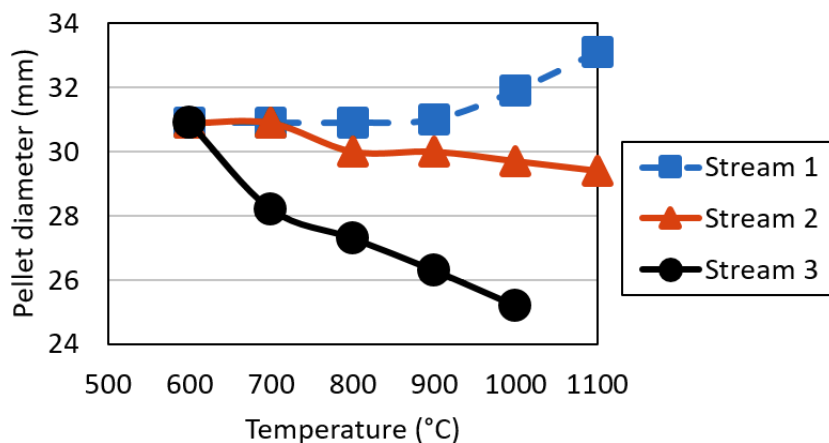
*Figure 51: Graphical representation of change in pellet diameter with change in temperature (% change = ((original diameter – final diameter)/original diameter)*100)*

Another comparison between the streams was the temperature at which a distinctly wet appearance was observed in the fired pellets. For all the streams 1 and 2, this observation was distinctly made at 1100°C, interestingly this coincided with FactSage calculations, which estimated a steep increase in liquid formation from 0 to 8% between 600 to 1000°C across the streams, to between 33 to 40 % at 1100°C. Complete melting was experienced in all streams by 1200°C.

Another feature that has been reported elsewhere as a function of sintering is the formation of a concave (or convex) shape on the surface of the pellet. This phenomenon was slightly observed in the higher temperature ranges i.e. at 1000 and 1100°C, for all the streams.

4.3.2 Compression strength

This section summarises the results of the compression strength tests performed on stream 1, stream 2, and stream 3 fired pellets. The results are presented graphically, based on the mean compressive strength from measurements of 40 pellets. Also included next to each graph, is a table showing the standard deviation at each temperature, as well as the % change in the compressive strength i.e. difference between the compressive strength at the present temperature, compared to that of the preceding temperature. The actual numerical values of the compressive strength for each pellet, are shown in Table 36 of Appendix D. The results in the section are presented separately for each stream.

4.3.2.1 Stream 1

Figure 52 shows a graphical representation of the change in compressive strength (on y-axis as 'load'), as a function of temperature (on x-axis), for stream 1. The graph showed an overall increase in the compressive strength of the pellets, with increasing temperature. The increase was particularly steep at 1100°C. This was captured by the % change results in the accompanying table in Figure 52, which showed a 1021% change, compared to a 188% change at 1000°C. The compressive strength of pellets fired at 1200 and 1300°C could not be reported due to melting that took place at these temperatures.

Temperature (°C)	Std.	% change
600	1.2	-
700	1.1	112
800	2.0	66
900	7.7	231
1000	27.6	188
1100	400.4	1021
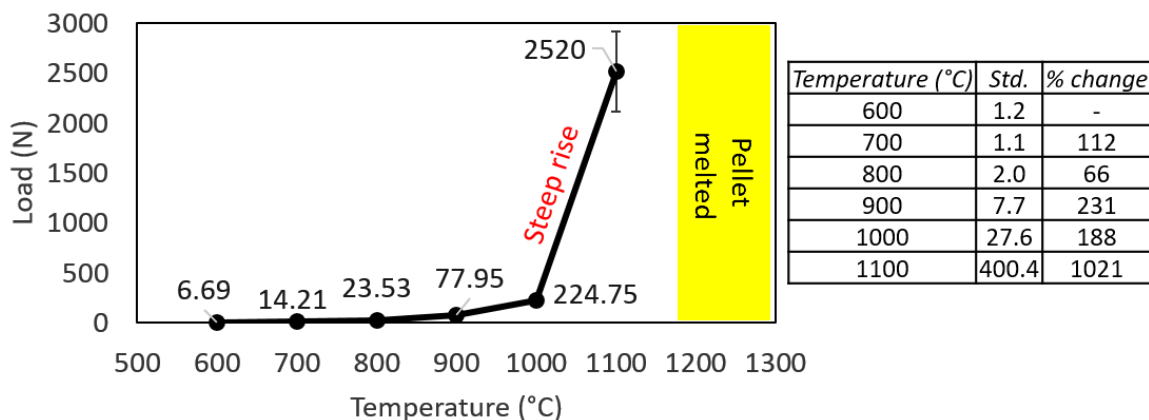
Figure 52: Graphical representation of compressive strength of stream 1 pellets as a function of temperature. The table on the right shows standard deviation values at each temperature, as well as the % change in pellet strength. (Std. = stdev = standard deviation)

4.3.2.2 Stream 2

Figure 53 shows a graphical representation of the compressive strength of the pellets, as a function of temperature, for stream 2. From the figure and accompanying table on the right, an increase in the compressive strength of the pellets, with increasing firing temperature, was observed. A steep rise in the compressive strength at 1100°C (a rise of 1597% compared to 304% for 1000°C), was also seen. Lastly, the compressive strength of the pellets fired at 1200 and 1300°C could not be reported due to the melting of its pellets.

All three aforementioned observations were very similar to those witnessed for stream 1.
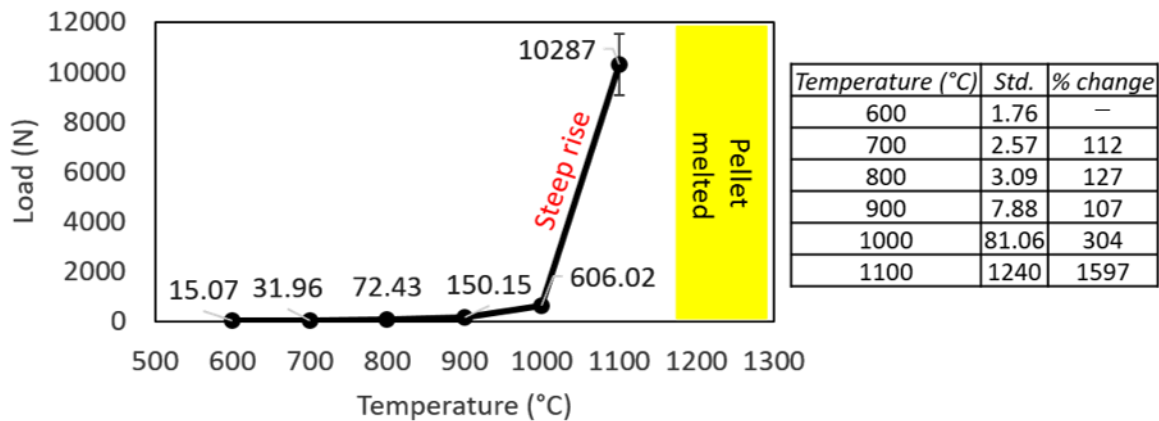
Figure 53: Graphical representation of compressive strength of stream 2 pellets as a function of firing temperature. Right table shows standard deviation and % change values at each temperature

4.3.2.3 Stream 3

Figure 54 shows a graphical representation of the compressive strength (in Newton) of the fired pellets for stream 3 dust, as a function of firing temperature. Similar to stream 1 and stream 2, a general increase in the compressive strength of pellets with increasing firing temperature was observed (with the exception at 800°C). Compared to stream 1 and stream 2, the % increase encountered for stream 3 temperature by temperature, were not as steep. In fact, there were overlaps in the compressive strength values between 700°C to 900°C, as shown by the error bars depicting the standard deviation. This suggested that the compressive strength of the pellets in this temperature range was not that dissimilar. The major increases in the compressive strength was encountered at 700°C and 1000°C, a change of 46 and 39% respectively. The compressive strength of the pellets fired at 1100 to 1300°C could not be determined, due to major deformation of the pellet at 1100°C, and complete melting of the pellets at 1200 and 1300°C.
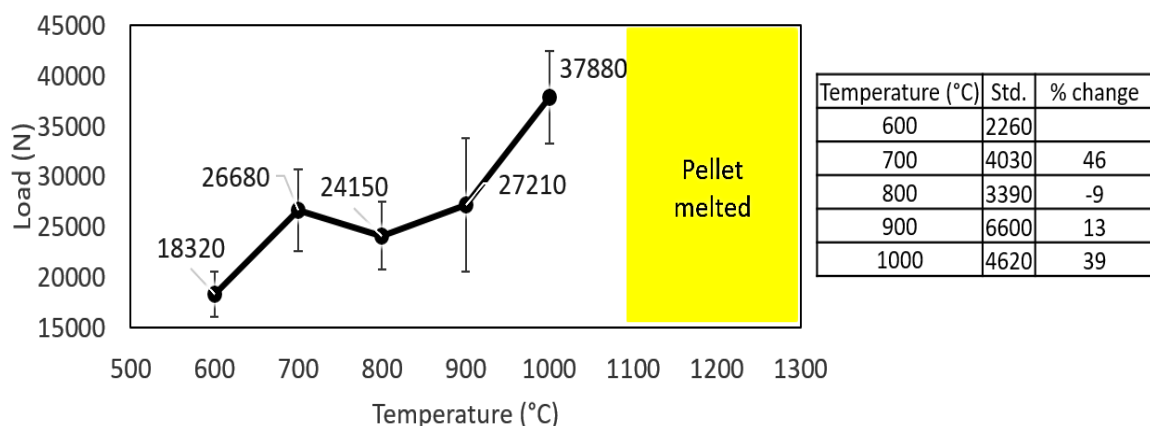
Figure 54: Graphical representation of compressive strength of stream 3 pellets as a function of firing temperature. The right table shows standard deviation values as well as the % change values at each temperature (N = newton; Std. = standard deviation)

4.3.2.4 Comparison between the three streams

A comparison of the compressive strength values for stream 1, 2, and 3 showed that at all firing temperatures, stream 3, followed by stream 2, had the highest compressive strength. The

difference in the compressive strength between stream 1 and 2 were minor, especially at low temperature, but gradually became higher, with the highest difference observed at 1100°C where the compressive strength of stream 2 was about 5X greater than that of stream 1 i.e. 2520 N for stream 1, and 10287 N for stream 2. Comparing stream 3 with stream 1 and 2, an even higher difference in the compressive strength values was observed. For example, at 600°C, the compressive strength of stream 3 was higher by an order of magnitude of 4 and 3 compared to stream 1 and 2 respectively. This difference reduces to an order of magnitude of 1 (compared to stream 1), and only about 3X higher compared to stream 2 at 1000°C.

It is evident from these observations that the finer the particle size, the higher the compressive strength of the pellet, fired at the same temperature. The difference in the compressive strength values between two different particle sizes seemed to increase with decrease in particle size, the difference became progressively less pronounced with increasing firing temperature.

4.3.3 Bulk chemical composition

The bulk chemical composition of the fired pellets for stream 1, 2, and 3, is shown in Table 25. From the table, the main change to in the chemistry of the fired sample compared to the as-sampled dust, was the reduction in the carbon content. In almost all the cases, the carbon was reduced from 10.1% for stream 1, 8.8% for stream 2, and 4.0% for stream 3, to below 1% after firing. This reduction was probable due to oxidation of carbon since an air atmosphere was employed for the work. Most of the other species remained the same or slightly increased (including Na_2O and K_2O), whilst species such as MnO and SiO_2 showed a more significant increase owing to their high initial value in the as-sampled dust. The increase in the concentration of some of the species was only arbitrary and may be traced to the reduction in carbon.

Table 25: Bulk chemical composition of fired samples for stream 1, 2, and 3 (in mass %)

Temp (°C)	Stream	MnO %	FeO %	Al₂O₃ %	CaO %	MgO %	SiO₂ %	Na₂O %	K₂O %	C %	P₂O₅ %	S %
600	1	29.35	4.87	2.49	9.10	3.96	46.76	0.50	1.66	0.58	0.53	0.50
	2	28.60	4.27	2.90	8.21	4.46	45.80	0.66	1.73	0.42	0.46	0.32
	3	33.70	1.04	2.61	6.67	7.19	36.38	1.75	3.37	0.07	0.36	0.96
700	1	30.10	5.03	2.43	9.13	3.95	46.87	0.46	1.36	0.28	0.44	0.52
	2	29.70	4.40	3.06	8.62	4.61	46.01	0.61	1.78	0.19	0.46	0.32
	3	33.45	0.95	2.55	6.65	7.13	36.38	1.73	1.98	0.11	0.32	0.97
800	1	29.20	4.90	2.63	9.26	3.96	45.80	0.49	1.41	0.21	0.48	0.55
	2	29.30	4.47	3.11	8.63	4.56	46.22	0.58	1.63	0.14	0.18	0.32
	3	33.90	0.98	2.64	6.94	7.26	36.17	1.79	3.11	0.02	0.34	0.95
900	1	29.50	4.85	2.73	9.54	3.98	45.37	0.50	1.48	0.17	0.37	0.55
	2	29.75	4.50	3.04	8.56	4.52	46.44	0.62	1.13	0.12	0.30	0.31
	3	34.10	0.97	2.59	6.84	7.31	36.59	1.97	3.20	0.01	0.34	0.96
1000	1	30.30	4.97	2.48	9.05	4.01	37.24	0.49	1.37	0.12	0.44	0.45
	2	29.40	4.44	3.01	8.36	4.42	46.87	0.58	1.75	0.01	0.47	0.24
	3	34.30	0.99	2.64	6.90	7.37	36.59	1.71	3.07	0.01	0.41	0.94
1100	1	29.60	4.79	2.67	8.88	3.94	47.40	0.49	0.96	0.06	0.36	0.11
	2	30.10	4.39	3.09	7.94	4.43	47.29	0.55	1.63	0.04	0.33	0.03
	3	35.80	0.98	2.75	6.80	7.44	38.09	1.74	4.10	0.07	0.38	0.82
1200	1	28.90	4.58	4.52	8.38	3.71	46.87	0.66	1.72	0.22	0.52	0.05
	2	28.70	4.66	4.41	7.56	4.22	47.51	0.66	1.58	1.07	0.42	0.10
	3	35.20	1.17	2.75	7.08	7.69	38.95	1.84	2.81	0.07	0.46	0.01
1300	1	30.10	1.92	2.27	9.48	5.30	47.29	0.49	1.33	1.71	0.33	0.57
	2	27.60	2.02	3.12	8.01	5.60	47.08	0.54	1.52	2.89	0.44	0.30
	3	33.30	1.08	3.80	6.83	7.22	39.16	1.95	3.16	0.05	0.13	0.11

- ZnO (<0.05 for stream one and 2 in all cases, and between 0.23 for stream 3 in all cases)

4.3.4 Bulk phase chemical composition

4.3.4.1 Stream 1

Table 26 shows the crystalline mineral phases identified, at each firing temperature, for stream 1 dust. The overlaid diffractograms showing the specific peaks are included in Appendix D, as Figure 64. A Comparison of the phases observed for the sample fired at 600°C and beyond with the as-sampled dust results presented in Table 21, showed that the same crystalline phases were present at 600°C, as were in the as-sampled dust, with the exception of Jacobsite. Unlike, the as-sampled dust, the slag phase diopside was now present in intermediate instead of minor amount. With increasing firing temperature i.e. from 700 to 800°C, the same phase that were present at 600°C remained. From 900°C, four main changes were observed. Firstly, the quartz content started gradually decreasing, from predominance (at 800°C), to major (at 1000°C), to intermediate (at 1000°C), to minor (at 1100°C), to complete disappearance at by 1200°C. This

observation showed that increasing the firing temperature resulted in a gradual depletion of quartz. Secondly, the phases that were present in trace amounts such as braunite, tephroite, and hausmannite disappeared by 1100°C. Thirdly, two new phases were formed from 900°C, namely, bustamite and ramsdellite (MnO_2). These two phases co-existed even at 1100°C. Fourthly, the slag phase diopside remained fairly constant throughout, but then disappeared by 1200°C.

Table 26: Identified crystalline mineral phases of stream 1 dust fired at 600-1300°C (all numerical values in °C) (calculation excluded amorphous material and range is exactly the same as that presented in Table 21)

Phase	Relative abundance							
	600	700	800	900	1000	1100	1200	1300
Quartz	Pred	Pred	Pred	Major	Inter	Minor		
Diopside	Inter	Inter	Inter	Major	Major	Inter		
Braunite	Trace	Trace	Minor	Trace	Trace			
Tephroite	Minor	Trace	Trace	Trace	Trace			
Hausmannite	Trace	Trace	Trace	Trace	Trace			
Bustamite				Inter	Major	Pred	Pred	Pred
Ramsdellite				Trace	Trace	Trace	Trace	Trace
Jacobsite					Trace	Trace		

- Pred = Predominant; Inter = Intermediate; Ramsdellite formula = MnO_2.
- Predominant >50%; major = 30-50%; minor 5-15%; trace <5%, of the crystalline phases.

4.3.4.2 Stream 2

Table 27 shows the crystalline mineral phases identified, at each firing temperature, for stream 2 dust. The overlaid diffractograms showing the specific peaks are included in Appendix D, as Figure 64. A Comparison of the phases observed for the sample fired at 600°C and beyond with the as-sampled dust results presented in Table 21, showed the following observation. Firstly, the same crystalline phases were present at 600°C, as were in the as-sampled dust, with the exception of bustamite and CaMn-silicate. Secondly, a new phase, Jacobsite, was seen at 600°C; it remained constant and then disappeared completely at 1200°C. Thirdly, quartz, remained the same at 600°C to 900°C, and then decreased from 1000°C, by 1200°C, only trace amounts of quartz were observed. Fourthly, the diopside content was higher at 600°C compared to the as-sampled material. It also disappeared by 1200°C. Fourthly, braunite, tephroite, and hausmannite remained fairly constant and then disappeared by 1200°C (this was the same observation for stream 1). Lastly, bustamite and ramsdellite, which had started being detected at 1000°C and 800°C respectively, remained in the sample even after 1100°C.

Table 27: Identified crystalline mineral phases of stream 2 dust fired at 600-1300°C (all numerical values in °C) (calculation excluded amorphous material)

Phase	Relative abundance							
	600	700	800	900	1000	1100	1200	1300
Quartz	Pred	Pred	Pred	Pred	Inter	Inter	Trace	Trace
Diopside	Inter	Inter	Inter	Inter	Inter	Trace		
Braunite	Trace	Trace	Minor	Minor	Trace	Trace		
Tephroite	Minor	Minor	Minor	Trace	Trace	Trace		
Hausmannite	Trace	Trace	Trace	Minor	Trace	Trace		
Bustamite					Major	Pred	Pred	Pred
Ramsdellite			Trace	Trace	Trace	Trace	Trace	Trace
Jacobsite	Trace	Trace	Trace		Trace	Trace		

- Pred = Predominant; Inter = Intermediate; Ramsdellite formula = MnO_2.

- Predominant >50%; major = 30-50%; minor 5-15%; trace <5%, of the crystalline phases.

4.3.4.3 Stream 3

Table 28 shows the crystalline mineral phases identified, at each firing temperature, for stream 3 dust. The overlaid diffractograms showing the specific peaks are also included in Appendix D, as Figure 64. A Comparison of the phases observed for the sample fired at 600°C and beyond with the as-sampled dust results presented in Table 21, showed the following observations. Firstly, the same crystalline phases were present at 600°C, as were in the as-sampled dust, with the exception of leucite, bustamite and CaMn-silicate. Secondly, two new phases, namely, Jacobsite and tephroite, were formed at 600°C; tephroite remained almost throughout the firing process, while Jacobsite disappeared after 1100°C. Thirdly, quartz, was present as a trace specie and then disappeared by 1100°C. Fourthly, the diopside content was higher at 600°C compared to the as-sampled material i.e. present as a predominant specie instead of the intermediate amounts in the as-sampled dust. It remained as a minor species at 1300°C. Fourthly, three new phases were formed at higher temperatures, namely, spinel, hematite, and bustamite. Lastly, a number of phases, namely, diopside, leucite, tephroite, bustamite, spinel, and hematite remained as crystalline phases even after 1000°C. These crystalline phases were present in various amounts even at 1300°C.

Table 28: Identified crystalline mineral phases of stream 3 dust fired at 600-1300°C (all numerical values in °C) (calculation excluded amorphous material)

Phase	Relative abundance							
	600	700	800	900	1000	1100	1200	1300
Quartz, low	Trace	Trace	Trace	Trace	Trace			
Diopside	Pred	Pred	Pred	Pred	Major	Minor	Trace	Minor
Braunite	Minor	Minor	Minor	Minor	Pred			
Leucite, syn			Trace	Trace	Trace	Minor	Trace	Minor
Maghemite					Trace			
Tephroite	Trace	Trace		Trace		Major	Pred	Major
Hausmannite	Trace	Trace	Trace	Trace	Trace		Trace	Trace
Bustamite, syn					trace	Inter	Minor	Inter
Jacobsite, syn	Trace	Trace	Trace	Trace	Trace			
Spinel						Minor	Minor	Minor
hematite							Trace	Trace

- Pred = Predominant; Inter = Intermediate; Ramsdellite formula = MnO_2.
- Predominant >50%; major = 30-50%; minor 5-15%; trace <5%, of the crystalline phases.

4.3.4.4 Comparison between the three streams

A comparison of the XRD results for the three streams revealed the following:

- For all three streams, as a result of firing, the concentration of quartz was observed to decrease. This reduction in the quartz concentration was gradual. In the case of stream 1 and stream 3, quartz was below the 3% detection limit at 1200°C and 1100°C respectively. In the case of stream 2, quartz remained as a trace element by 1200°C.
- For all three streams the slag phase diopside was higher in the samples fired at 600°C, than the original as-sampled dust. It seemed as though firing even at low temperature caused an increase in either the crystallinity or number of diopside crystalline phases.
- For stream 1 and stream 2, after 1100°C, the main crystalline phases observed were ramsdellite and bustamite, all other phases, except trace amounts of quartz, had disappeared after this temperature. On the contrary, stream 3 contained a number of phases, namely, diopside, leucite, tephroite, hausmannite, bustamite, spinel, and hematite, even after 1100°C.
- Jacobsite was observed as a new phase that had formed in trace amounts for stream 2 and 3 at 600°C. The opposite effect was noted for stream 1.
- In contrast to Jacobsite, bustamite and CaMn-silicate, was not found detected at 600°C, for stream 2 and 3.

4.3.5 Specific phase chemical composition

This section presents the results obtained of the SEM-EDS analyses of the fired pellets. Of particular interest were the changes in the particle shape with changing temperature, the particle to particle interactions, the type of joints between particles, and the chemical composition of some of the particles that were observed to be in contact at each firing temperature. The term 'joint' or 'contact' in this section, was used to refer to, either direct particle-to-particle

connection between two or more particles, or the connection of two or more particles through an intermediate rim i.e. neck formation. For ease of flow of this section, the results of each stream were presented separately.

4.3.5.1 Stream 1

SEM BSE micrographs showing an overview of the fired pellets for stream 1, are shown in Figure 62 of Appendix D. From the overviews, subsections were taken for analysis, at each of the firing temperatures. The sub-section images presented in the form of SEM BSE micrographs, are shown in Figure 55. From Figure 55, the following observations were made.

- *Pressed pellet (no firing)* – Particles maintained their original shape prior to compression i.e. both angular and spherical particles were still observed. Most particles were not joined together as may be seen in image no 1 and 2.
- *At 600°C* – Particles maintained their original shapes. A few particles were observed to be in contact with one another e.g. particle A and B (micrograph 4), also C and D through an intermediate rim i.e. D (micrograph 5). The particle contact in both cases seemed minor, and overall more localised i.e. observed in very few instances around the sample. The results of the EDS point analysis performed on point A-E in the coloured micrograph 4 and 5, are shown in the accompanying table. The analysis revealed that two glassy slags with different compositions (labelled conveniently as glass slag and glass slag a) were in direct contact as per micrograph 4. A green, calcium rich phase was also directly joined to glass slag a. An intermediate rim that seemed to join glass slag 2 and the CaMgMnFe-oxide was also observed in micrograph 5. An analysis of this rim revealed that it was a pure manganese oxide that had possible formed by oxidation of the silicomanganese alloy, labelled point C. FactSage calculations of the percent liquid of particle A to E showed that particle A, C, D-rim, and E, were completely solid at the firing temperature of 600°C. Glass slag a labelled as particle 'B', which was in direct contact with particle 'A', was composed of 47% liquid. This meant that in all probability the liquid form of the particle may have encouraged sintering with solid particle A. Thus, both solid-state sintering between particles 'C' and 'E' through an intermediate solid 'D-rim', as well as liquid-state sintering of a different kind than that reported by literature was observed.
- *At 700°C* – There was no change in original particle shape. However, a few more particles, compared to 600°C, were observed to exhibit localised joining. Nonetheless, an evaluation of the entire field, showed that the majority of particles remained unattached. To the naked eye some of these joints e.g. L, seemed to be as a result of an intermediate liquid rim. In the case of particle 'I' and 'J', the grain boundaries were completely distorted. EDS point analyses of F to M are shown in the accompanying table. From the table, it was seen that the intermediate layer between particle K and M was a glassy slag (labelled as glass slag 1). The Mn-oxide rim was again found to be an intermediate rim between an alloy and a quartz grain having a surrounding coating of glass slag. Point I and J with a distorted grain boundary were quite similar in composition barring a few species. FactSage calculations of the percent liquid of particle F to M showed that all the particles were completely solid at the firing temperature of 700°C i.e. % liquid was zero for all particle. Thus, the observed sintering, even between particles 'K' and 'M' through an intermediate L-rim, were as a result of solid-state sintering.
- *At 800°C* – There was no change in the original shapes of particles. The particle arrangement seemed to be slightly more compact (i.e. more particles closer to surrounding particles, with more localised joints), than for lower firing temperatures. Some of the intermediate rims between particles, which were also observed in some cases in the lower

temperature, appeared to be larger (see micrograph 10 and 12). A complex joint, made out of multiple species, was observed in micrograph 11. EDS point analysis of the intermediate rim i.e. no 'O', between glass slag 1 and glass slag 2, showed that it was a high iron ferromanganese oxide (high Fe, FeMn oxide). FactSage calculations of the percent liquid of particles N to V showed that all the particles, except for particles S and U, were completely solid at 800°C. As for particle 'U', it contained very minor liquid < 1% and thus in practical could be considered a solid. Particle 'U' on the other side was made out of 50% liquid at this temperature. With all this in mind, it seemed then that the particle labelled 'P' and 'N' with the 'O' rim exemplified solid-state sintering of a number of phases. The same was true for the complex mix of Q, R, S and T. On the other hand, liquid-state sintering through rim-'U' was seen between two solid particles, namely, glass slag 1 (V) and quartz.

- *At 900°C* – The overall particle shape was maintained as before. Instead of the localised joints only, as with previous temperatures, a few networks i.e. groups of joint particles, as seen in micrograph 13 and 14 were observed (shown by red lines in micrograph 13). The contact area among some of the particles was now even bigger than before. The rim around quartz grains (e.g. at F1, G1, I1, K1, and L1), which typically acted as an intermediate joint between particles, seemed to be bigger. EDS point analysis of this rim showed that its composition was similar to 'glass slag a' as identified previously in some instances. As with the lower temperatures an alloy with a Mn-oxide rim, which acted as an intermediate joint between particles, was identified. One type of joint encountered which was not glass slag or Mn-oxide rim based was a high MnFe-oxide, which had layers of MnCaSi-oxide that were directly joint to glassy slag 2. Despite the observations of a few network of particles joined together, much of the sample did not exhibit this and thus remained unattached (see Figure 62 in Appendix D). FactSage calculations of the percent liquid of particles X to N1 showed that all the particles, except for the particles labelled as C1, D1, F1, G1, I1, and L1, were completely solid at 900°C. As for particle C1, it contained a very small fraction of liquid i.e. 3% and thus in practical it could be considered to be solid. All the other particles had a liquid fraction of above 20%. Thus, a classification of the observed sintering was as follows: X-Y (solid-state), X-A1B1 (solid-state), X-quartz (solid-state), X-alloy through Z-rim (solid-state), alloy-D1 through Z-rim (liquid-state), E1-quartz through F1-rim (liquid-state), M1-quartz through L1-rim (liquid-state), H1-alloy (solid-state), alloy-quartz through G1 rim (liquid-state), and J1K1-quartz through I1-rim (liquid-state sintering). The sintering observed at 900°C was both solid-state and liquid-state, networks (i.e. chains of sintered particles) were observed to have started forming.

- *At 1000°C* – The particle shape appeared slightly more distorted than at 900°C especially with the increase in what appeared to be liquid-like material around some of the particles (see micrograph 15 and 16). From the coloured micrograph 16-19, the liquid-like material all around the sample appeared to have three distinct composition as per the three dominant colours in the micrographs, namely, red, green, and yellow. EDS analysis, as presented in image 16-19, showed that the red (dominant) material indicated by point Q1, T1, and W1 was glass slag 'a', containing high concentrations of low melting oxides of K and Na, the green material as indicated by U1, was a high sulphur calcium silicate, and the yellow material had a composition similar to glass slag 2 as encountered in the previous temperatures. Interestingly, no direct particle-to-particle bonds were observed, instead in all instances, these liquid-like materials seemed to act as intermediate joints between two or more particles. As in the case of the samples fired at lower temperatures, distinct particles of quartz and Mn ore were still observed. FactSage calculations of the percent liquid of particles O1 to A2 showed that all the particles, except for the particles labelled as P1, Q1, S1, T1, and W1, were completely solid at 1000°C. As for particle P1 and S1, the liquid fraction was only 6% and 16% respectively. The particle Q1, T1, and W1 had a high liquid

fraction of 72%, 77%, and 74% respectively. This high liquid containing phases were that belonging to glass slag 'a' and appeared to be the main liquid sintering the surrounding coarse particles such as quartz, glass slag 1, KAlSiNa-oxide, glass slag, and glass slag together. In other cases such as the particles around Z1 and A2, although glass slag 'a' was also seen surrounding the quartz grains and may have contributed to the observed sintering, there also appeared to be some evidence of solid-state sintering between Z1 and A2.

- *At 1100°C* – The particle shapes were severely distorted. The previously encountered spherical shapes, as well as the angular shapes seemed to have largely disappeared, with the minor exception of quartz, alloy, and a very irregular Mn-ore grain (see labelled micrograph 21). There was a complete formation of network joints of material throughout the sample (i.e. universal networks were formed, see micrograph 20 and 21). This is especially clear in the overview image in Appendix D labelled as Figure 62-1100°C. The formation of complete networks made it difficult to isolate certain phases since all the particles were mixed. Thus, apart from the aforementioned particles, as well as the clearly discernible K and Na rich glassy slag 'a' (in micrograph 22), most EDS point analysis results showed a chemistry resembling a complete mixture of phases. As a result it wasn't possible to evaluate particle to particle interactions to examine whether solid state or liquid-state sintering was at play. Nevertheless, the presence of the glass slag 'a' phase throughout the sample, especially surrounding the quartz grains, as well as the complete distortion of particle shapes that resulted in a uniform sintered structure, pointed to a liquid-state sintering mechanism.

- *At 1200*°C – Most particles were no longer observed with the exception of quartz grains, alloy prills (strong pink colour), a CaMgMnSi-oxide (light pink colour), and a mixture 2 consisting of Mn ore and other components (see micrograph 24 and accompanying table). The particle network, as highlighted at 1100°C, was still observed over the entire sample (see image 23). The unison green colour, with flashes of pink, was mostly observed throughout the sample again highlighting the extensive melting and subsequent mixing that took place. FactSage calculations of the percent liquid of mix 1, mix 2, and the CaMgMnSi-ox showed a high liquid fraction at the firing temperature of 1200°C. This was especially true for mix 1 which had an 80% liquid fraction. Since mix 1, formed the bulk of the sample observed, it would seem that a liquid-state sintering mechanism governed the observed sintering of particles.

- *At 1300°C* – There was complete melting and subsequent solidification that resulted in the formation of a compact structure. No distinct particles were observed (not even the quartz grains). The SEM BSE micrograph labelled as 25 and 26 depicts this.

Pressed pellet (no firing): 1) Overview image, and 2) Close up image

Pt	O	Na	Mg	Al	Si	S	K	Ca	Mn	Fe	Type	% L
A	35	0.9	4.6	0.6	16.4			1.8	1.8	38.9	glassy slag	0
B	40	4.2	0.6	0.8	25.7	0.4	7.9	2.9	17.3		glassy slag a	47
C					19.2				52.0	28.9	alloy	0
D	23				0.4	0.3	0.2	0.3	75.6		glassy slag 2	0
E	33		23.9	0.3	3.2			17.4	16.4	5.9	CaMgMnFe-oxide	0
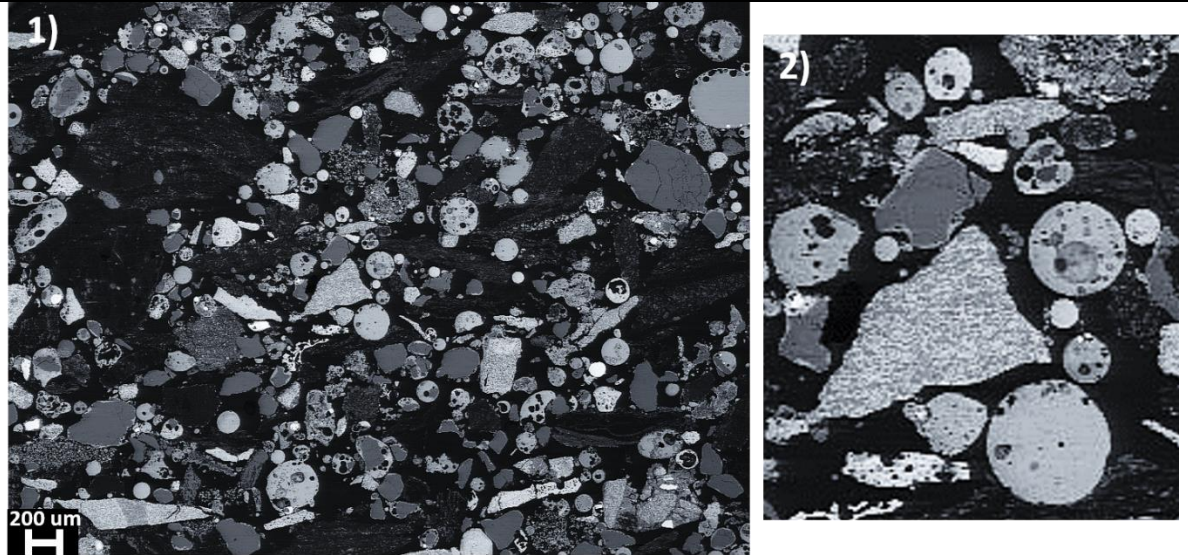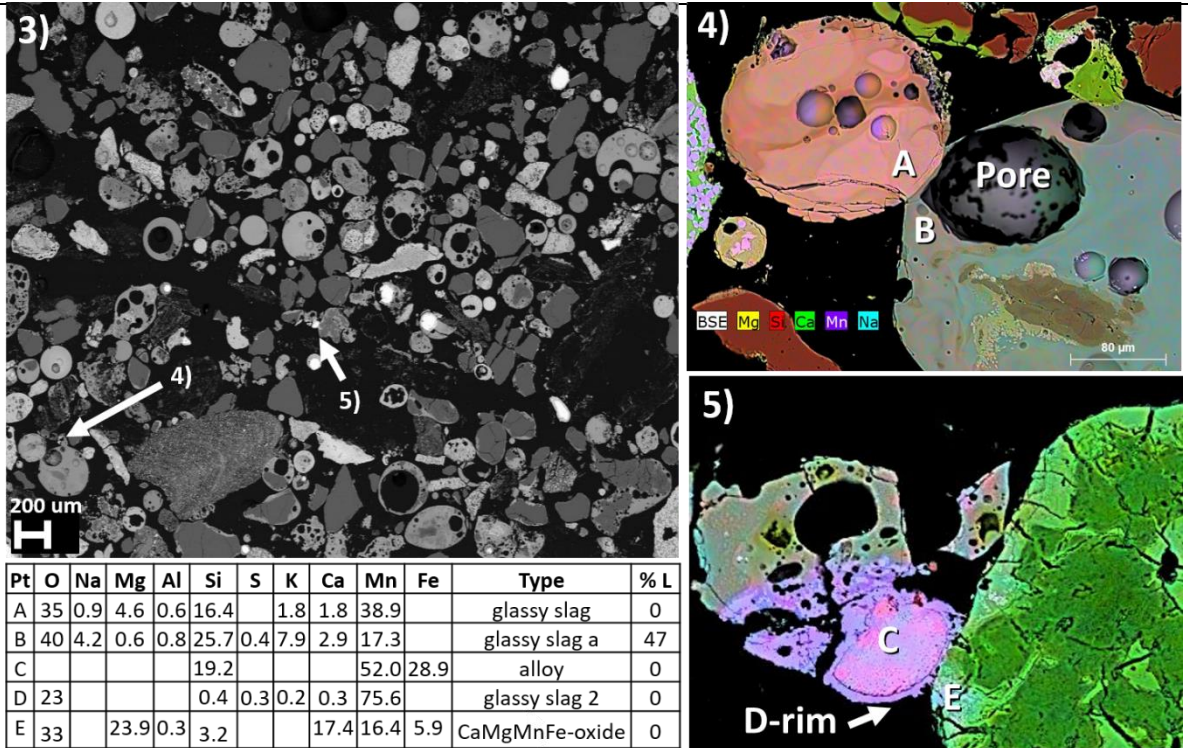
Fired at 600°C with: 4) particle 'a' joint directly with particle 'b', and 5) particle 'c' joint to particle 'e' through a manganese oxide rim i.e. 'd-rim' (with O = oxygen, Na = sodium, Mg = magnesium, Al = aluminium, Si = silicon, S = sulphur, K = potassium, Ca = calcium, Mn = manganese, Fe = iron, Pt = point, and % L = percent liquid).

Pt	O	Na	Mg	Al	Si	S	K	Ca	Mn	Fe	Type	% L
F	37	0.5	2.5	0.6	19.8		1.2	1.1	37.6		Glassy slag	0
G	23	0.2	0.0	0.0	0.2		0.0	0.1	76.8		Mn-oxide	0
H	36		11.4	0.4	14.9		0.2	4.6	32.4		Glass slag 1	0
I	37		3.7	1.9	16.6	0.2	1.8	17.3	21.6		Glass slag 1	0
J	35		5.1	1.8	15.2		3.3	8.0	28.5	2.7	Glass slag 1	0
K	35		2.4	1.8	12.5	1.0	0.5	18.0	28.9		Glass slag 1	0
L	32		1.2	1.4	11.1	1.0	0.3	6.6	46.1		Glass slag 1	0
M	38		2.2	1.8	20.2	0.3	1.2	9.6	26.3		Glass slag 1	0
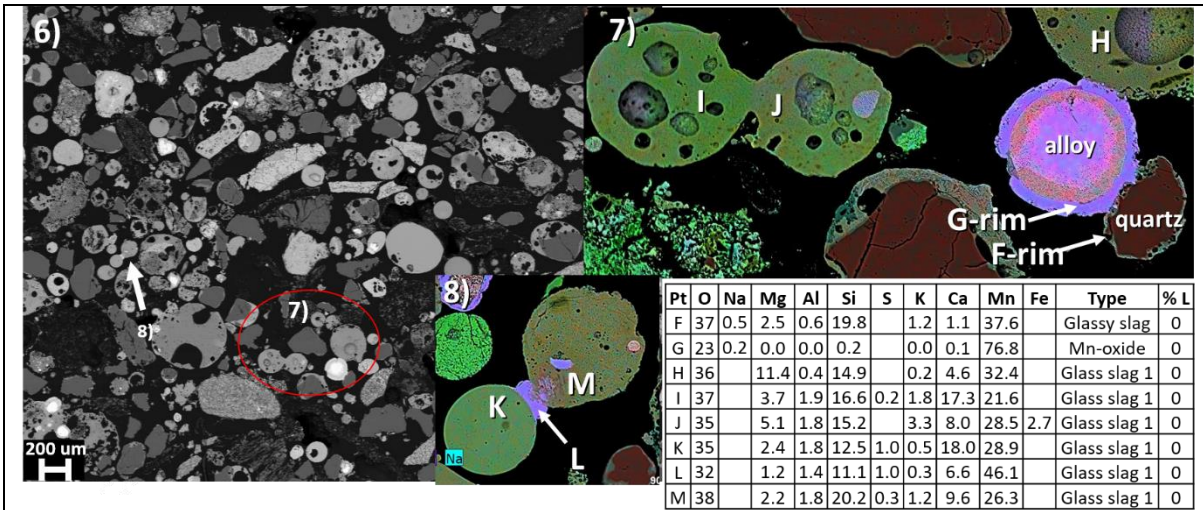
Fired at 700°C with: 7) different particle joints i.e. direct and through an intermediate layer, and 8) particle 'k' joint to 'l' through a glass slag 1 rim i.e. L.

Pt	O	Na	Mg	Al	Si	K	Ca	Mn	Fe	Type	% L
N	33		2.9	0.6	13.6	0.4	4.3	45.3		Glass slag 1	0
O	22							31.5	46.1	High Fe,Mn-oxide	0
P	40	0.9	5.1	2.2	18.8		27.0	6.0		Glassy slag 2	0
Q	27		3.2		4.4		2.0	63.9		Mn-ore	0
R	34	0.7	6.0	1.1	12.3	0.4	9.2	33.5	3.0	Glassy slag	0
S	23	0.3	1.1	0.1	0.1	0.0	0.1	72.7	2.7	Mn-oxide	<1
T					20.2			57.3	22.4	Alloy	0
U	43	3.2	1.5	0.5	30.4	8.6	1.1	10.3	1.6	Glassy slag a	50
V	39	0.3	2.6	0.2	21.4	0.4	14.4	21.4	0.6	Glass slag 1	0

Fired at 800℃ with :10) FeMn-oxide intermediate rim joining particle 'n' and 'p', 11) complex joints between Mn-ore, glass slag, Mn-oxide, and SiMn alloy, 12) glass slag a rim between quartz and glass slag 1 (at N: phosphorus is 0.4%, sulphur is 0.2% at R)
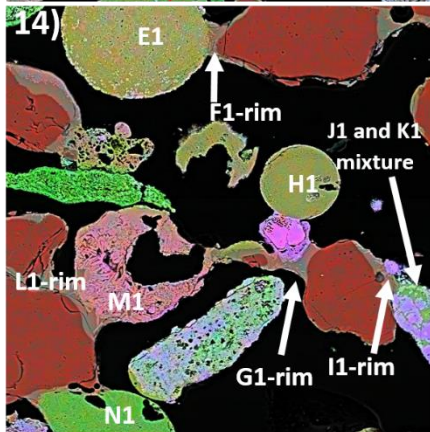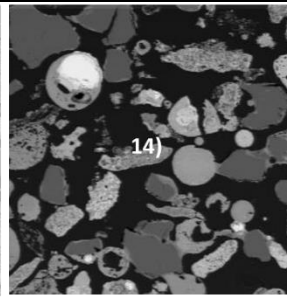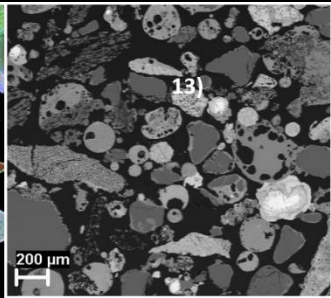
Pt	O	Na	Mg	Al	Si	S	K	Ca	Mn	Fe	Type	% L
X	40		3.5	1.9	19.1	0.5	0.2	26.9	8.3		Glassy slag 2	0
Y	36		0.6	1.6	17.5	0.1	1.8	8.9	33.3		Glassy slag 1	0
Z	23								77.4		Mn-oxide	0
A1	24		2.3	0.9	0.1			0.9	58.4	13.7	High Mn, Fe-oxide	0
B1	34		2.5	1.8	12.2			23.9	21.7	3.7	Glass slag 1	0
C1	30	0.6	2.2	0.9	9.2		0.7	5.6	38.2	12.5	Glassy slag	3
D1	41	1.9	1.7	0.6	27.2		4.7	3.4	17.0	2.3	Glassy slag	40
E1	34		4.5	0.6	13.3		0.3	10.5	30.9	6.1	Glass slag 1	0
F1	44		1.5	0.6	32.4		7.7	0.9	10.7	2.0	Glass slag a	23
G1	43	2.5	0.7	0.5	31.3		7.5	0.9	13.3		Glass slag a	66
H1	37		4.0	2.4	16.4		1.8	13.0	25.8		Glassy slag 1	0
I1	44		0.6	0.7	32.0		6.9	2.6	13.3		Glass slag a	39
J1	23		1.6	0.2	0.1		0.0	0.4	74.4		Mn-oxide	0
K1	34		1.8	1.2	12.8		1.0	25.9	23.3		Glass slag 1	0
L1	44		1.0	0.8	32.2		8.0	0.5	13.8		Glass slag a	38
M1	36		4.0	0.6	17.8	0.4	0.9	1.5	38.8		Glassy slag	0
N1	37		1.6	3.2	16.4	0.1	0.4	23.9	17.1		Glass slag 1	0

Fired at 900℃ with: 13) Multiple particles bonded most on Mn-oxide alloy rim, as well as direct particle to particle bonds between particle 'x' and 'y', as well as 'x' and 'A1&B1' composite, 14) Multiple particles joint mostly by intermediate glass slag 'a'.

Pt	O	Na	Mg	Al	Si	S	K	Ca	Mn	Fe	Type	% L
O1	37		2.6		18.9			18.8	20.1	2.4	Glassy slag 1	0
P1	38	0.5	3.0		20.9		0.2	6.0	30.4	1.5	Glassy slag	6
Q1	42	2.4	0.9	0.9	29.2		5.6	0.7	10.5	3.9	Glassy slag a	72
R1	46	3.1		21.8	21.4		7.4				KAlSiNa-oxide	0
S1	39	0.7	3.1	0.6	23.0		1.2	8.0	24.0		Glassy slag	16
T1	43	2.4	0.8	0.9	31.3		6.6	0.9	8.4	5.3	Glassy slag a	77
U1	40				7.2	9.4		43.7			High S CaSi	0
V1	39		0.5	1.2	20.7		0.1	28.2	10.1		Glassy slag 2	0
W1	44	2.2	0.5	1.1	32.1		5.7	0.9	8.6	4.7	Glassy slag a	74
X1	43				18.7			36.7	1.4		High S CaSi	0
Y1	36		0.4	0.2	8.8	4.2		43.7	4.3	2.3	Glassy slag 2	0
Z1	37		0.7	0.6	5.8	7.2		35.9	11.2	2.1	Glassy slag 2	0
A2	40	1.1	4.9	4.4	17.0			27.6	4.7	0.8	Glassy slag 2	0

Fired at 1000°C with: 15) and 16) Large scale image showing overview of sample appearance. Despite the amount of liquid-like material increasing and resulting in the joining together of networks of particles, most particles maintained their original shape. 17), 18), and 19) EDS point analysis of specific areas around the material. Networks between particles seemingly from the three liquid like rims of different compositions. Red phase containing significant amounts of oxides of K and Na was observed.
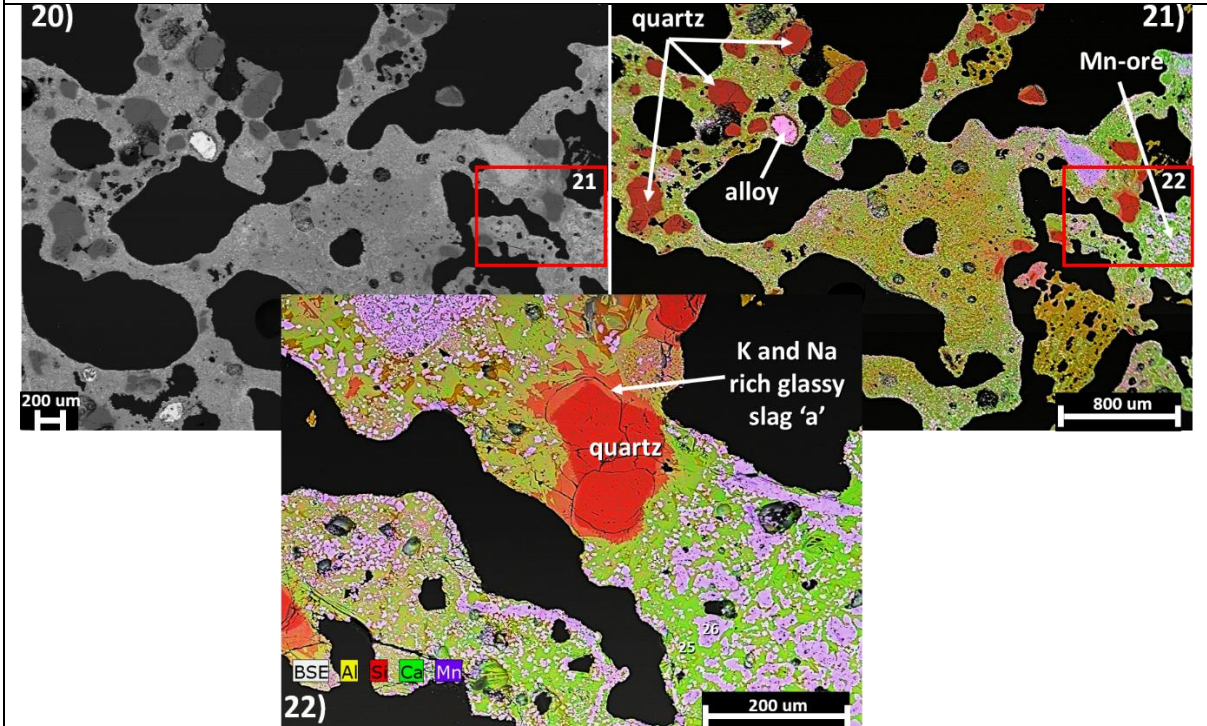
Fired at 1100°C with: 20) Overview image showing complete networks, 21) coloured version of image 20 showing only Mn-ore, quartz, and alloy that could be easily discernible, and 22) close-up image showing K-Na oxide rich rim around quartz.

87

Point	O	Mg	Al	Si	Ca	Mn	Fe
mix 1	38.6	2.7	0.9	20.7	13.1	22.9	0.6
CaMgMnSi-ox	33.3	6.2		13.1	4.0	43.0	0.6
mix 2	23.6	3.6			0.4	72.4	
	34.9	4.5	0.2	13.9	16.6	29.5	

Fired at 1200°C with: 23) Overview image showing complete networks that formed throughout the sample, and 24) Close-up image showing networks as well as some of the particles that were still observed e.g. quartz, alloy etc. Mixtures indicated a blend of material. (Mix 1: S = 0.2%, and K = 0.2%; mix 2: S =0.5%)

Fired at 1300°C with: 25) Overview image of completely melted compact sample, and 26) close-up image showing complete disappearance of all particles due to melting and recrystallization

Figure 55: SEM BSE images showing the microstructural features of stream 1 sample fired from 600 to 1300°C, also included in some cases is a table of the EDS point analyses around the map ('ox' refers to oxide; 'type' refers to generic names given to particles/species to differentiate the general chemistry from each other. Species with similar (but not exact) compositions were grouped together; Map elemental colour scheme similar to that which was used for the characterisation of the as-sampled dust)

4.3.5.2 Stream 2

SEM BSE micrographs showing an overview of the fired pellets for stream 2, are shown in Figure 63 of Appendix D. Similar to stream 1, sub-sections of the overview images were taken at each firing temperature, in order to perform the same analysis. The sub-section images are shown in Figure 56. The following summarised observations were made at each firing temperature.

- *Pressed pellet (no firing)* – Similar to stream 1, the unfired pressed pellets maintained a mixture of both angular and rounded particles. Most particles were in close proximity but were not directly in contact, as shown in micrograph I and II.
- *At 600°C* – The particles maintained their original shapes with both angular and spherical particles observed. It appeared as though some particles were slightly in direct contact to one another as shown especially in micrograph 2 and 3. From micrograph 2 and 3, three direct particle to particle joints were observed between, i) a particle made out of a mixture of high Mn Fe-oxide and High Fe Mn-oxide joint to another high Fe Mn-oxide particle, ii) a mixture of high Mn Fe-oxide and glassy slag 1 joint directly to another glass slag particle, iii) a high Mn Fe-oxide particle joint to a glass slag 1 particle. Overall the contact between particles was not only localised but seemed minor in most instances. FactSage calculations of the percent liquid for particle A to H showed that all the particles were completely solid at the firing temperature of 600°C i.e. 0% liquid at the firing temperature. Thus, solid-state sintering was observed between throughout the sintered particles analysed.
- *At 700°C* – There was no noticeable change in the original shape of particles. However, as was the case for stream 1, a few more particles, compared to 600°C, were observed to be joint locally together. Nonetheless, most particles as observed in micrograph 4 seemed to have remained unattached. Micrograph 5 and 6 show a number of these joints that were observed to be as a result of an intermediate purple rim between particles. EDS point analysis of this purple rim revealed that it was manganese oxide for all the cases. The green rim between particle N and L (see micrograph 5), had a composition that resembled glass slag 1. FactSage calculations of the percent liquid for particle I to R showed that all the particles were completely solid at the firing temperature of 700°C. Thus, solid-state sintering was observed throughout the particles even with the rims between the particles.
- *At 800°C* – Both angular as well as rounded particles were still observed. From the overview micrograph no 7, it appeared as though slightly more particles than for 600 and 700°C were joint together. Visible small networks of particles joint together were also observed to have started forming in some areas (examples of these are seen in micrograph labelled 8 and 9). There were a variety of rims observed to be joining the particle networks together e.g. glass slag rim 'a' at point Y (also seen before for stream 1), a Mn-oxide rim at point T (seen before in stream 1 as well as at 700°C for stream 2), and a high K MnFeAlSi-oxide in D1 (not encountered anywhere previously). Direct particle to particle bonds were also observed between particle A1 and B1, as well as between E1 and F1. The compositions of each point are provided in the accompanying table. FactSage calculations of the percent liquid of particles S to F1 showed that all the particles, except for the particles labelled Y, Z, and C1, were completely solid at 800°C. The fraction of liquid was low at 12% for particle Z and C1, whilst a higher fraction of liquid at 49% was seen for glass slag 'a' i.e. particle Y. Considering these observation, both solid-state and liquid-state sintering was observed at 800°C. Solid-state sintering was observed between S-U-V through a solid intermediate rim of Mn-oxide i.e. T-rim, between A1-B1, between E1 and F1, and between E1 and C1 through an intermediate solid D1-rim. Liquid-state sintering on the other hand was promoted largely by the Y-rim surrounding quartz which acted as a rim (neck) between

89

quartz and two glass slag 1 particles on opposite sides of the quartz grain. It is unclear whether particle 'Z' and 'C1' would have yielded liquid-state sintering with the low 12% liquid fraction observed.

- *At 900°C* - The overall particle shape was maintained. One significant feature that was not observed in the previous temperatures for stream 2, was the large liquid-like joining rim that was observed in H1 and K1. This rim, identified as glass slag 'a' through EDS analysis, acted as a binder between a number of particles, thus causing the formation of the observed networks in micrographs 11 and 12. In micrograph 11, the network is between a number of quartz particles, a glass slag, and glass slag 2. In micrograph 12, the networks were between quartz, a high Fe CaMnSi-oxide, and MgMn-oxide particle. Direct particle to particle joints were also observed as in the case of M1 and N1 i.e. two glass slags with slight variations in compositions. FactSage calculations of the percent liquid of particles G1 to N1 showed that all the particles were completely solid at 900°C, except for the glass slag 'a' particles labelled as H1 and K1. These two particles had a liquid fraction of 66% and 33% respectively. Considering this, as was the case with the observed sintering at 800°C, both solid-state sintering as well as liquid-state sintering was observed between the particles. Solid-state sintering was observed between the following particles: M1-N1 i.e. two particles corresponding to a glass slag composition. Liquid-state sintering with glass slag 'a' acting as the rim between a number of particles was observed between a number of quartz grains, glass slag, and glass slag 2 i.e. quartz-I1-G1 bonded by H1, as well as between quartz, MgMn-oxide, and a high Fe, CaMnSilicate bonded by K1. At this temperature larger networks of sintered particles were starting to form.

- *At 1000°C* – Some angular as well as rounded particles were still observed, although at this temperature, most of these particles appeared to be significantly distorted with no clearly defined grain boundaries between particles. There were also signs of liquid formation in various parts of the sample. This was especially seen around the edges of most particles as well as in the rim between networks of particles (see micrograph 15). This liquid-like red material indicated by letter Q1, W1, and T2 was analysed by EDS, the results showed that it was glass slag 'a' (encountered in stream 1). The green material indicated by point V1 and X1 was also analysed and found to be a calcium rich glass slag 2. Similar to stream, no direct particle to particle joints were observed. FactSage calculations of the percent liquid for particles O1 to A2 showed most of the particles had a significant proportion of liquid at the firing temperature of 1000°C. This was so with the exception of quartz, O1, V1, X1, P1, and T1. None of these solid particles seemed to be in-direct contact to one another, instead, the largely liquid phase glass slag 'a' showed by Q1, W1, and A2 for the glass slag 'a', as well as R1, S1, Y1, and Z1 seemed to have bonded these various particles together into a network of sintered particles. Thus, liquid-state sintering was observed in this instance with a number of particles sintered together by various liquid intermediate phases. At this firing temperature the networks of sintered particles where even larger than the previous temperatures.

- *At 1100°C* – Particle shapes were severely distorted. With the previously encountered spherical shapes having disappeared almost entirely, and only few angular shapes observed (see micrograph 16-18). Long networks of joints were also formed more universally around the sample. As can be observed in the coloured micrograph no 17 and 18, these chains of material joint together had different compositions as can be seen by the difference in colours. The EDS analysis of some of these phases are shown in the accompanying table. From the results, several compositions were identified that conformed to glass slag 'a' (in red), glass slag 1 (green), a KAlSi-oxide phase (brown), a MnMgFe-oxide, as well as a high Mn Fe-oxide. It was difficult to define the interaction boundaries as almost all the particles were intermixed together. FactSage calculations of the percent liquid for particles B2 to F2

showed that the dominant green glass slag 1 particles labelled as C2 contained 59% liquid at 1100°C. Also, the glass slag 'a' phase which had also been noted in the lower temperatures contained 58% liquid. Particles D2, E2, and F2 were all completely solid at temperature. Bearing in mind these observations it seemed as though the particles were sintered together by liquid-state sintering with glass slag 1 and glass slag acting as the binding phases.

- *At 1200°C* – Most particles were no longer observed with the exception of quartz grains (see micrograph 20). The structure and networks were even more pronounced than at 1100°C. Complete bonding of structure can be attributed to widespread melting followed by re-solidification.

- *At 1300°C* – Complete melting and recrystallization resulted in the formation of a compact structure upon solidification. No distinct particles were observed (not even quartz). SEM BSE micrograph labelled no 21 and 22 showed this.
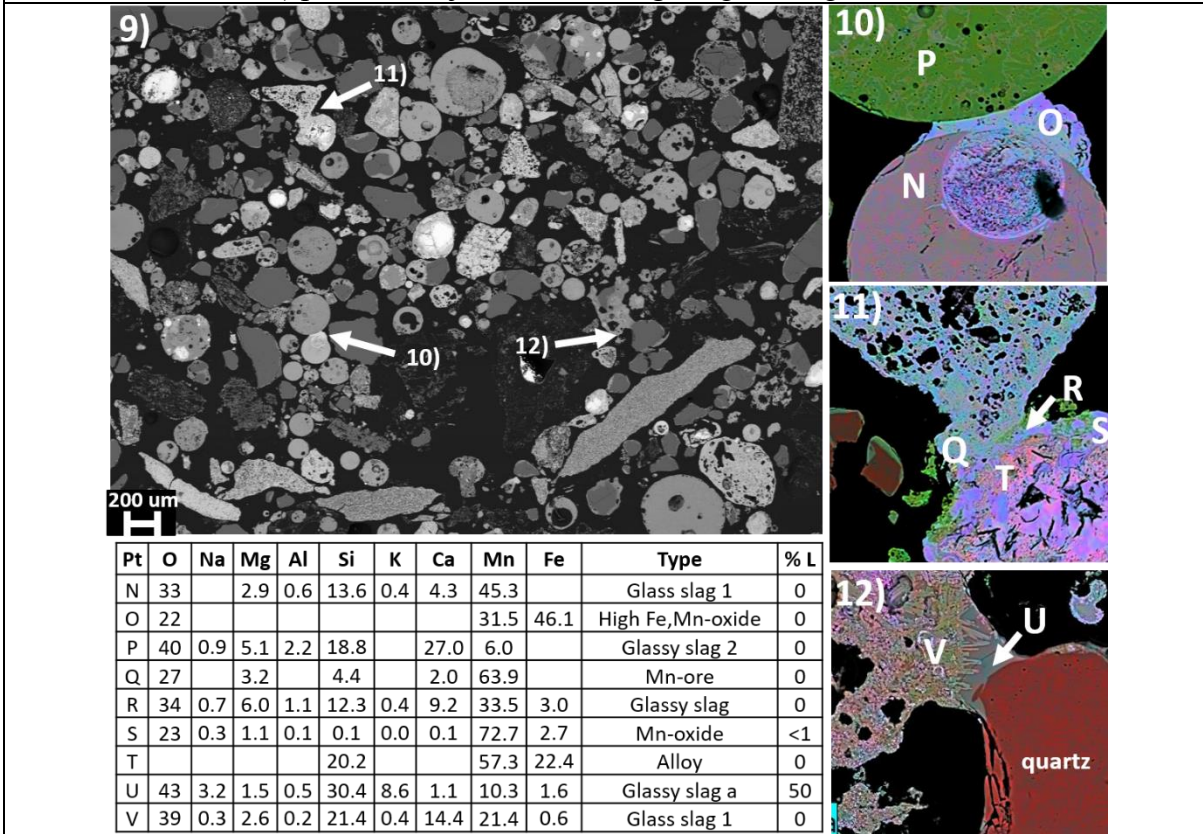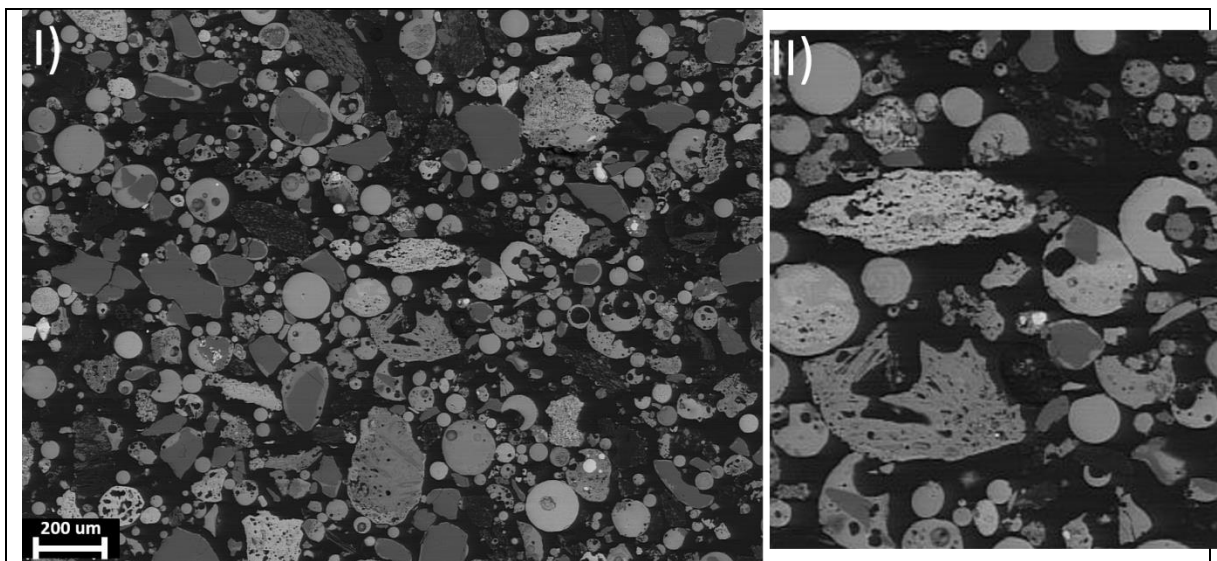

Pressed pellet (no firing): 1) Overview image, and 2) Close up image
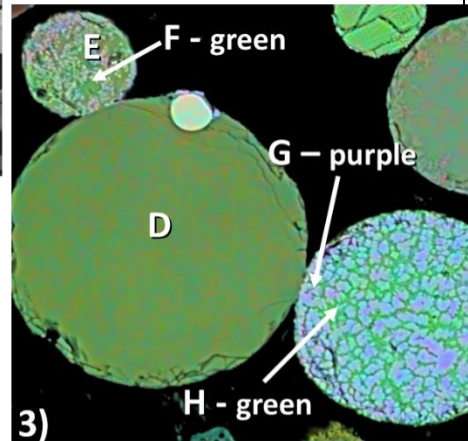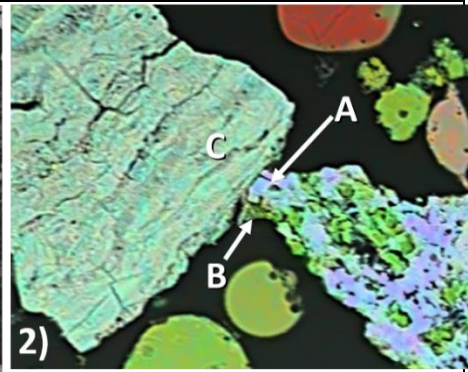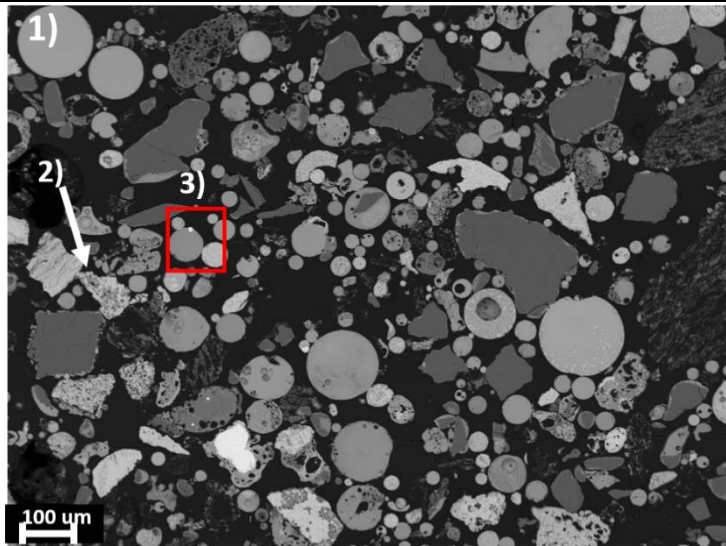
Pt	O	Na	Mg	Al	Si	S	K	Ca	Mn	Fe	Type	% L
A	24	1.2	1.4	0.3	1.6			3.0	57.7	10.4	High Mn, Fe-oxide	0
B	28	1.1	3.3	0.6	4.9	0.3	0.8	8.5	13.1	39.4	High Fe, MnCaSi	0
C	22							0.5	1.9	75.3	High Fe,Mn-oxide	0
D	39	0.5	2.2	1.7	21.0		1.6	13.3	20.8		Glass slag 1	0
E	27	0.5	5.1	0.6	3.3		0.1	3.7	53.5	6.6	High Mn, Fe-oxide	0
F	34	0.6	4.3	1.6	12.7	0.4	0.4	14.6	27.2	3.8	Glass slag 1	0
G	24		1.5		0.8			6.3	58.9	8.6	High Mn, Fe-oxide	0
H	28		0.9	0.4	5.4			21.5	35.7	7.8	Glass slag 1	0

Fired at 600°C with: 2) a particle consisting of a mixture of 'a' and 'b' composition joint directly with particle 'c', and 5) particle 'd' joint to a mixture of particle 'e' and 'f' on one side, and a mixture of 'g' and 'h' on the other side.
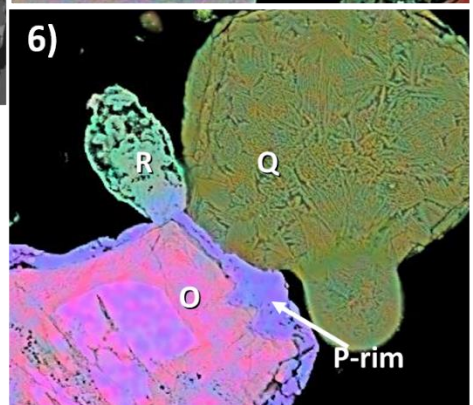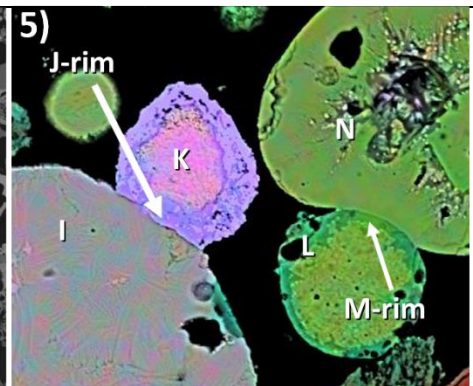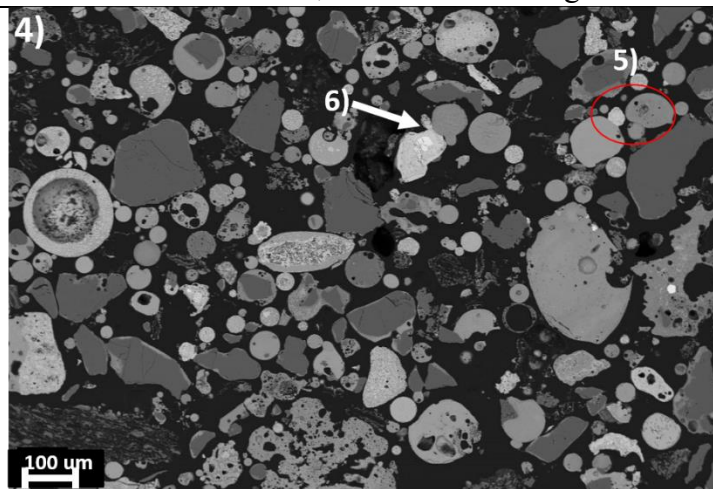
Pt	O	Na	Mg	Al	Si	K	Ca	Ti	Mn	Fe	Type	% L
I	35	0.5	1.5	0.7	17.4	2.0	3.5		39.4		Glassy slag	0
J	22								77.4		Mn-oxide	0
K					21.7				37.8	40.5	Alloy	0
L	37	0.5	11.7	2.4	14.8	0.8	6.1		23.5	2.9	MnMgCaSi	0
M	39	0.4	4.2	1.6	20.6	1.1	9.9		23.2	0.3	Glassy slag 1	0
N	41	3.4	2.3	14.2	14.4	1.3	12.5	1.1	10.3		MnAlCaSi-ox	0
O					28.3				50.6	21.1	Alloy	0
P	23								77.4		Mn oxide	0
Q	38	1.0	8.5	0.8	18.6	2.8	2.9		27.7		Glassy slag	0
R	33	1.0	2.5	10.4	7.1	8.6	2.7		33.3		High K, MnAlSi-ox	0

Fired at 700°C with: three joints formulated by an intermediate rim, namely, Mn-oxide between I and K (image 5) and OQR (image 6), as well as a glassy slag 1 rim between L and N in image 6.

Pt	O	Na	Mg	Al	Si	K	Ca	Mn	Fe	Type	% L
S	38		3.0	1.7	18.8	1.9	8.6	27.9		Glass slag 1	0
T	23							77.4		Mn-oxide	0
U					20.9			62.9	16.2	Alloy	0
V	23		1.3	0.1	0.5		0.9	66.3	7.5	High Mn, Fe-oxide	0
W	37		6.7	2.2	16.7	1.6	6.9	28.4		Glass slag 1	0
X	35		4.1	0.6	14.6	0.4	15.3	30.1		Glass slag 1	0
Y	43	1.9	0.6	0.6	31.3	7.5	1.0	13.9		Glass slag a	49
Z	26	0.6			5.6	1.8		37.4	28.5	MnFeSi-glass	12
A1	35		4.3	0.8	16.2	0.8	3.0	39.3		Glassy slag	0
B1	34		1.6	0.7	14.7	0.7	8.4	37.1	3.2	Glass slag 1	0
C1	45	0.9			9.9	28.6	15.7			KAlSiNa-oxide	12
D1	38	1.3	2.8	8.0	16.9	6.5	2.2	17.8	6.2	High K, MnFeAlSi	0
E1	40	3.7	1.4	18.0	11.1	2.1	11.5	10.0	1.1	MnAlCaSi-ox	0
F1	38	1.5	2.2	9.7	14.8	0.4	10.6	19.2	3.0	MnAlCaSi-ox	0

Fired at 800°C with: 8) networks of particles varying in particle size beginning to form mostly through an intermediate rim, and '9) other networks by direct particle to particle.' EDS point analysis results are given in the accompanying table.

Pt	O	Na	Mg	Al	Si	S	K	Ca	Mn	Fe	Type	% L
G1	35		4.6	1.1	16.4		1.9	4.9	35.7		Glass slag	0
H1	44	2.1	1.1	0.7	31.8		6.9	0.6	10.3	2.9	Glass slag a	66
I1	38		5.1	1.3	16.1		0.3	30.3	8.3	1.0	Glass slag 2	0
J1	37		2.8	1.7	18.3		0.3	14.0	16.9	8.7	High Fe, CaMnSi	0
K1	42		1.0	1.6	28.8		7.0	2.2	7.5	9.3	Glass slag a	33
L1	38		54.1						7.6		MgMn-oxide	0
M1	35		1.1	3.3	16.6		5.1	5.9	29.3	3.4	Glass slag	0
N1	33		3.3	0.5	13.1	0.2	0.7	1.4	47.7	0.4	Glass slag	0
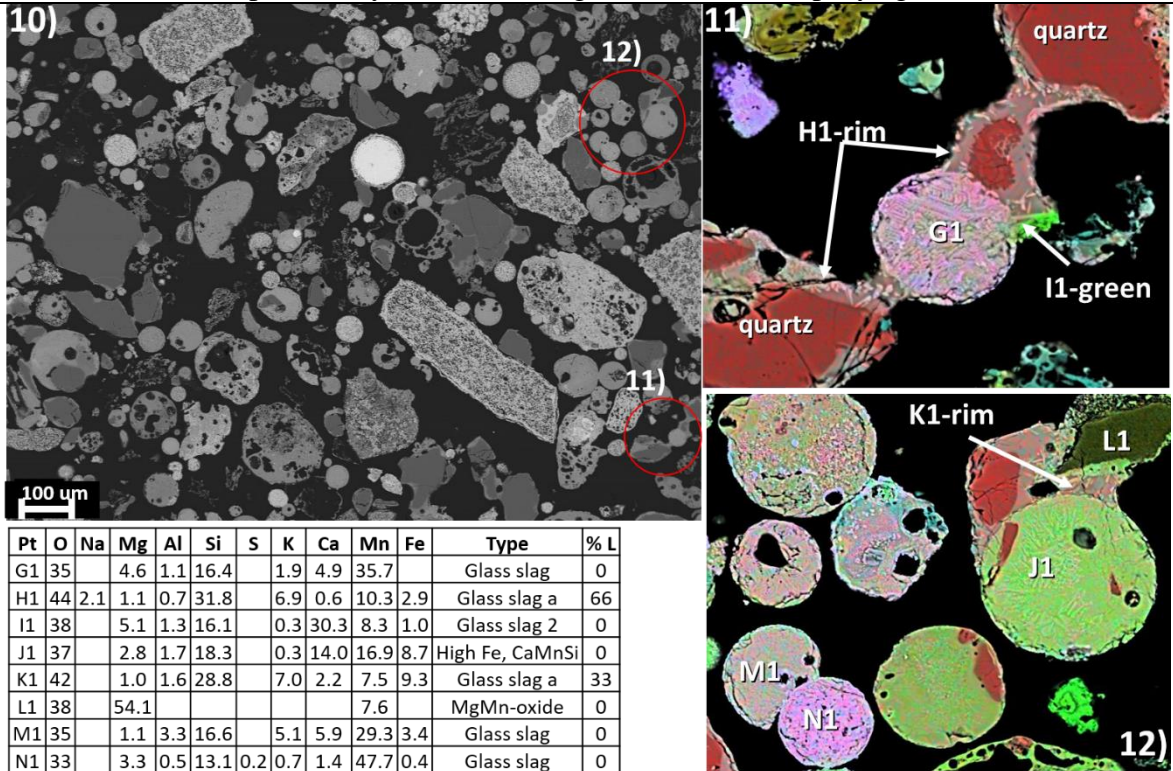
Fired at 900°C with: 10) Overview of particle interactions, 11) network formed between five different particles held together by a liquid-like (to be confirmed) glass slag 'a', and 12) other network of particle (i.e. between L1. J1, and quartz), as well as direct particle to particle bond between M1 and N1.

94
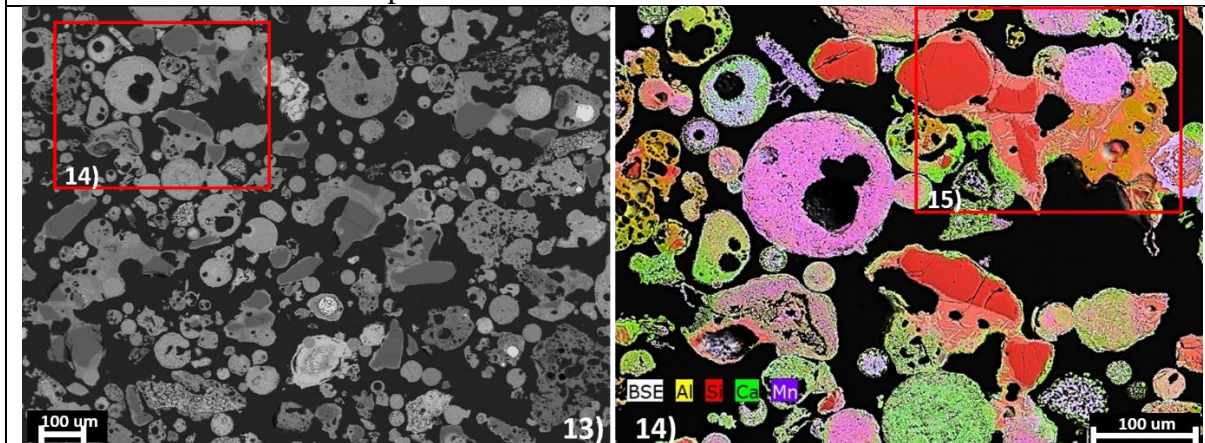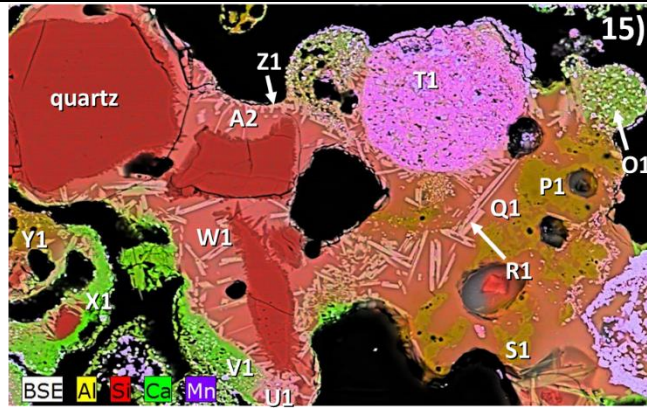
Pt	O	Na	Mg	Al	Si	K	Ca	Mn	Fe	Type	%L
O1	36		0.7	1.0	17.4	1.6	14.6	24.4	4.4	Glass slag 1	0
P1	45	0.6		21.1	20.1	13.1		0.4		KAlSiNa-oxide	4
Q1	46	1.3	0.6	3.7	32.5	6.4	1.0	8.9		Glass slag a	79
R1	39	0.6	2.2	0.8	22.3	1.2	6.0	28.2		Glass slag	17
S1	45	2.3	0.4	9.2	28.5	9.8	0.5	4.2		KAlSiNa-oxide	25
T1	33	0.2	3.9	0.4	13.3	0.4	0.9	48.2		MnMgSi-oxide	4
U1	39	0.4	2.9	0.5	21.9	0.7	6.1	28.9		Glass slag	10
V1	40		4.5	6.7	16.7		19.7	10.7	2.0	Glass slag 2	0
W1	44	2.2	0.6	1.1	31.6	6.7	1.4	9.0	3.6	Glass slag a	75
X1	39		1.3	0.3	20.6		27.7	11.2		Glass slag 2	0
Y1	45	2.6		10.3	26.7	10.6	1.5	2.2	1.3	KAlSiNa-oxide	30
Z1	39	0.7	1.7	0.5	22.6	1.3	6.7	27.9		Glass slag	17
A2	44	2.1	0.7	1.4	32.4	7.0	1.1	10.8		Glass slag a	74

Fired at 1000°C with: 13) overview of showing sample appearance after firing at 1000°C, 14) section of (13) showing all-round appearance of liquid-like material in red and green, and 15) zoomed in section of (14) with analysis of composition of different phases that formed a strong network together.
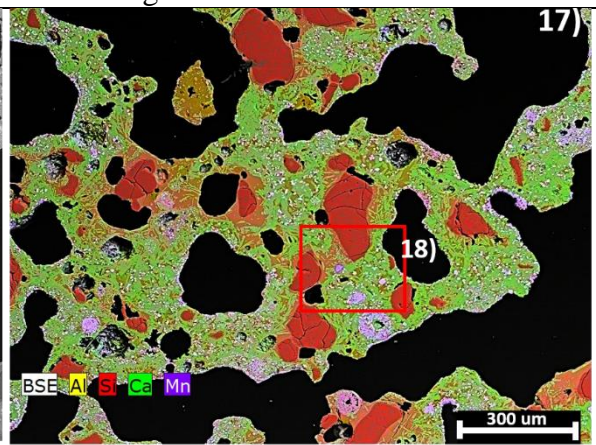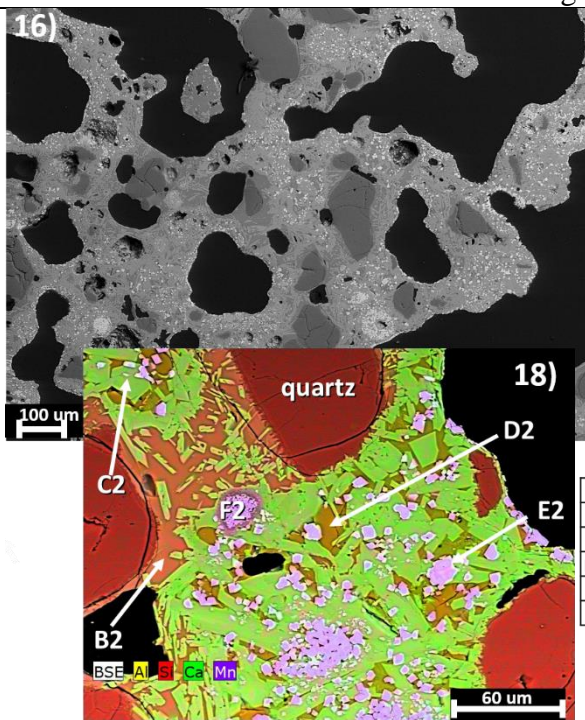
Pt	O	Na	Mg	Al	Si	K	Ca	Ti	Mn	Fe	Type	%L
B2	45	2.2	0.8	2.7	32.4	5.0	1.5	0.3	5.9	3.8	Glass slag a	58
C2	37		3.6		18.8		13.9		26.7		Glass slag 1	59
D2	43			11.8	25.1	18.8			0.5	0.7	KAlSi-oxide	0
E2	28		10.3	0.7	3.3		0.2		41.5	16.0	MnMgFe-oxide	0
F2	25		2.4	2.4	0.4		0.6	0.4	49.6	19.5	High Mn, Fe-oxide	0

Fired at 1100°C with: 16) and 17) Overview image showing the formation of large networks throughout the sample, 18) section of image (17) showing an intermixture of phases as illustrated by the accompanying compositional analysis in B2-F2.
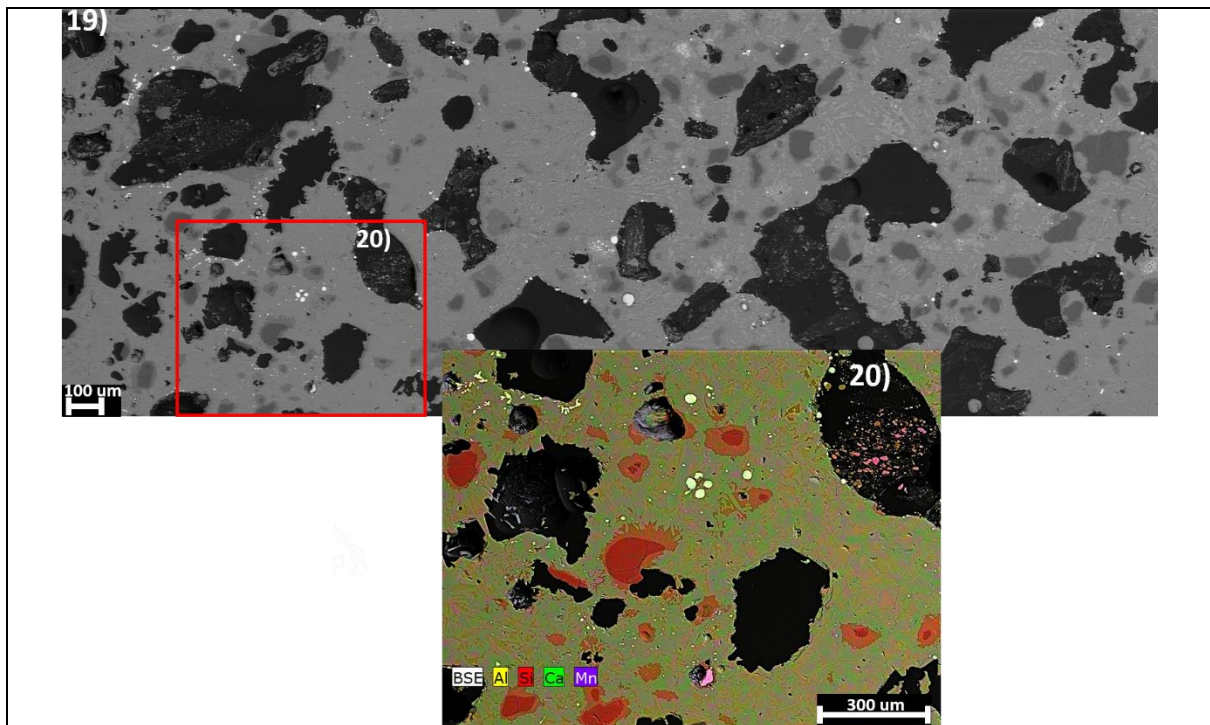
Fired at 1200°C Fired with: 19) Overview image showing complete large networks that formed possible during solidification of the material following melting, 20) close-up BSE image showing networks as well as some of the quartz particles that were still observed.
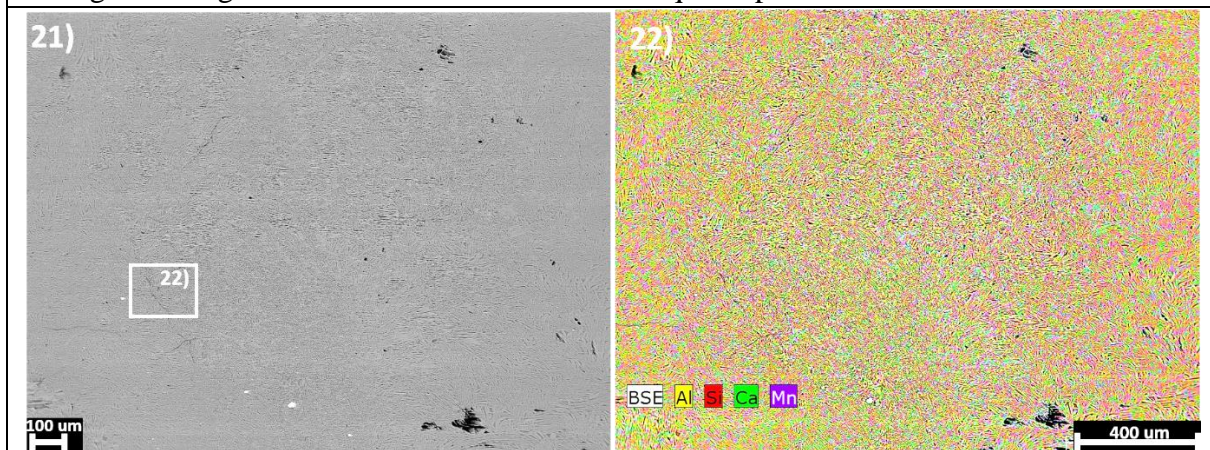
Fired at 1300°C with: 21) Overview image of completely melted compact sample, and 22) close-up BSE image showing complete disappearance of all particles due to melting and solidification.

Figure 56: SEM mappings as well as BSE images showing the microstructural features of stream 2 sample fired from 600 to 1300°C ('ox' refers to oxide; 'type' refers to generic names given to particles/species to differentiate the general chemistry from each other. Species with similar (but not exact) compositions were grouped together; Map elemental colour scheme similar to that which was used for the characterisation of the as-sampled dust)

4.3.5.3 Stream 3

SEM BSE images showing an overview of the appearance after firing for stream 3, are shown in Figure 57. Unlike for the previous streams, particle to particle interactions could not be examined for stream 3, as the extreme fineness of particles coupled with an overall mixing of phases made such an analysis extremely difficult (same with EDS point analysis). Thus, the

results are discussed only in terms of the general observations made over the entire sample. EDS point analysis were performed in a few instances as in most occasions particles could not be distinguished from one another especially at the lower temperatures. The following summarised observations were made at each firing temperature.

- *Pressed pellet (no firing)* – Sample contained coarse and fine particle, as well as angular and rounded particles (see micrograph no 1). Due to the inherent fineness of the material, particles were in direct contact from the compression stage.
- *At 600°C* – Coarse and fine particles, as well as angular and rounded particles, were still observed. There was no noticeable difference in the microstructural appearance of the sample fired at 600°C when compared to the original pressed pellet.
- *At 700°C* – A few of the coarse as well as fine the particles were still observed. However, some coarse particle grain boundaries were not as defined as before i.e. it appeared as though the particles were beginning to fade away. As highlighted by the red border, some parts of the sample now appeared to have a distorted appearance.
- *At 800°C* – A few spherical particles were still observed, although most of them now were intermediate in size and were even more faded. The texture of the overall sample appeared to be compact compared to the previous temperatures.
- *At 900°C* – The overall microstructural appearance was similar to that of the sample fired at 800°C. One noticeable difference was an area on the top right (highlighted by the red border), that seemed to point to show indications of melting.
- *At 1000°C* – The microstructural appearance was completely different when compared to all the lower temperature microstructures. The sample appeared to be more uniform as well as more inter-joint. More pores surfaced (which usually indicates melting and gas formations). Fine particles were not as noticeable. Alloy particles, carbon particles, as well as a few fading rounded particles were also observed. To zoom into some of the details of the microstructure, a coloured BSE micrograph and a few EDS point analyses were performed to determine the composition at different points (see image and accompanying table). From the image, it was observed, as previously stated, that even at high magnification complete isolation of the various phases and analysis of the interaction thereof was nearly impossible. Thus, a thorough analysis of the types of joints formed was not possible. Notwithstanding this, EDS analysis performed revealed that stream 3 contained some phases that were similar in composition to stream 1 and stream 2, those were, a glassy slag, glass slag 1, MnMgSi-oxide and a KAlSiNa-oxide (shown in point 'B-E'). One new phase composition that was not detected previously even in stream 1 and 2 was a MnKNaSiCl-oxide, as indicated by point 'A'. FactSage calculations of the percent liquid for particles A to E showed that all of the particles analysed were completely solid at 1000°C. Although, the fineness of the particles prevented a thorough analysis of the kind of sintering encountered for this stream, it would seem that both solid-state and liquid-state sintering where present at this temperature. The former was supported by the solid particles A to E, the latter was supported by the development of large gassy type pores.
- *At 1100°C* – The sample appeared to be even more compact. In this case the original fines as well as the coarse particles had disappeared completely since the sample had melted quite considerably, and then solidified to form a compact unit. Most parts of the sample were dense. Pores were also observed although this seemed smaller and less abundant compared to 1100°C. From the overview micrograph no 7, a sub-section was taken as indicated by the red rectangular border. EDS point analysis of the various distinct phases were performed, and the identified phases were labelled accordingly as shown in the coloured SEM BSE micrograph. A large number of phases identified were similar to those at 1000 °C. One noticeable difference from the coloured BSE image was that for 1100°C,

the crystals appeared to be much larger. This observation indicates that already at 1000°C, liquid formation had already started occurring and may have been partly the reason for the observed compact structure. Some of the phases identified as seen in the coloured micrograph were Mn-ore, glass slag 'a', glass slag. Glass slag 1, and KAlSiNa-oxide, from previous analysis done with stream 1 and 2, glass slag 'a', glass slag, and KAlSiNa-oxide always contained a significant level of liquid at temperatures below this. It would appear than that at 1100°C, these would be liquid. Thus, liquid-state sintering was a possibility in this instance.

- *At 1200°C* – The pores had now virtually disappeared due to the complete melting and re-solidification of the sample. Several different crystals were observed i.e. from angular well-defined crystals, to lamellar type. These were believed to have formed during the solidification of the liquid melt.
- *At 1300°C* – Similar observations to 1200°C, with dominant lamellar crystals.

Pressed pellet

Fired at 600°C
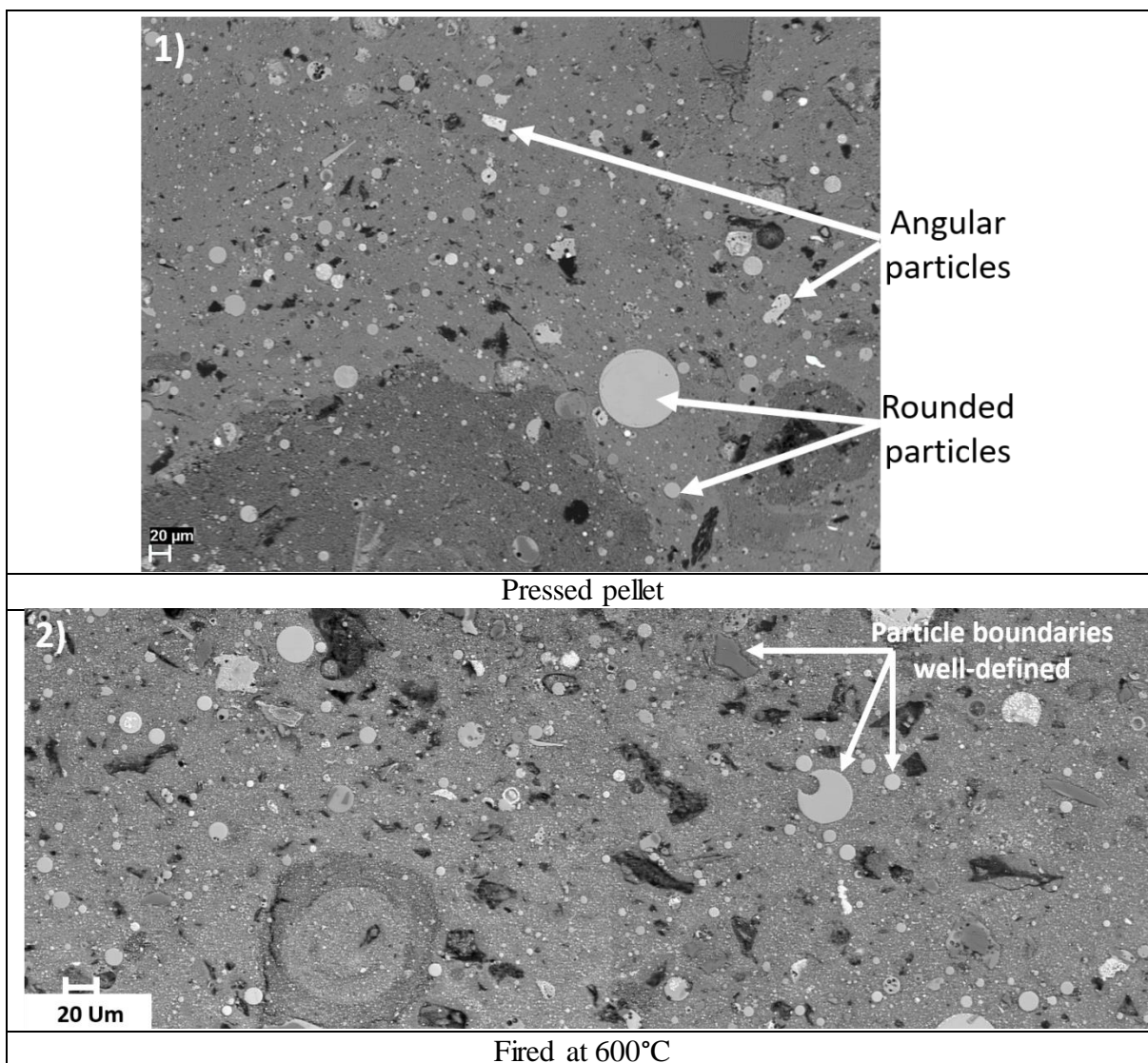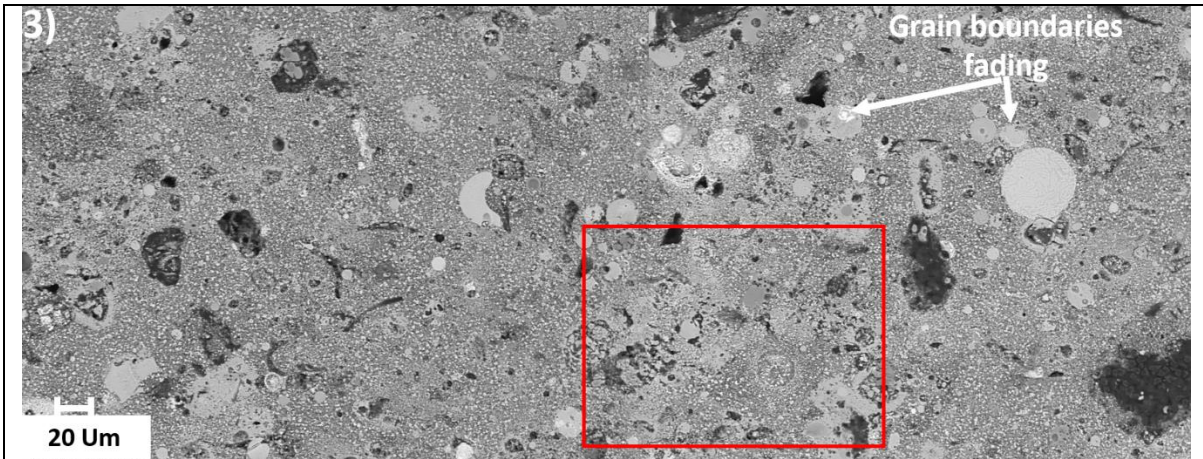
Fired at 700°C
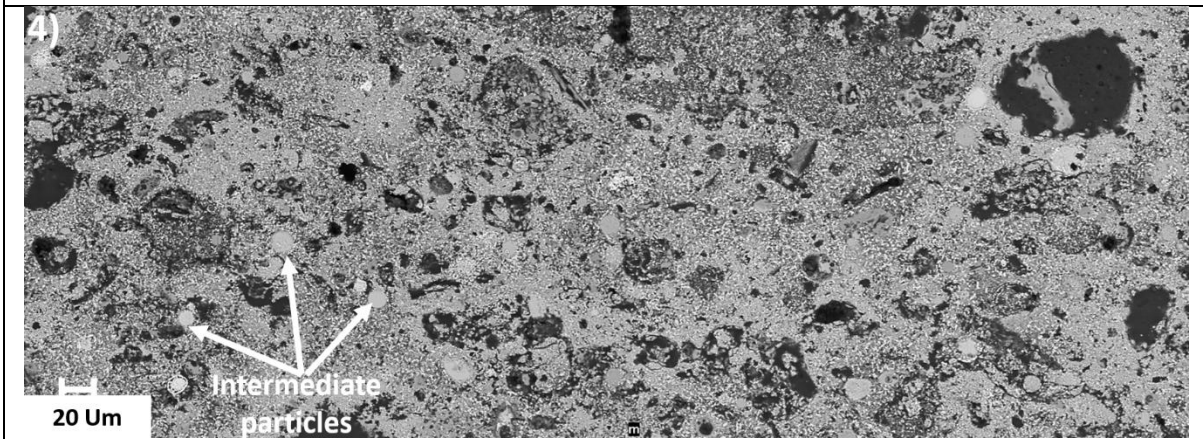
Fired at 800°C
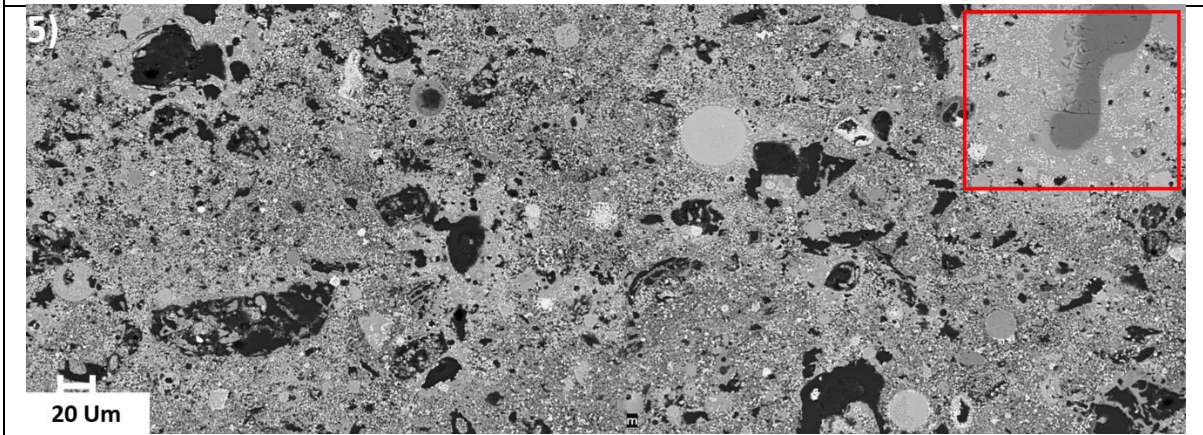
Fired at 900°C
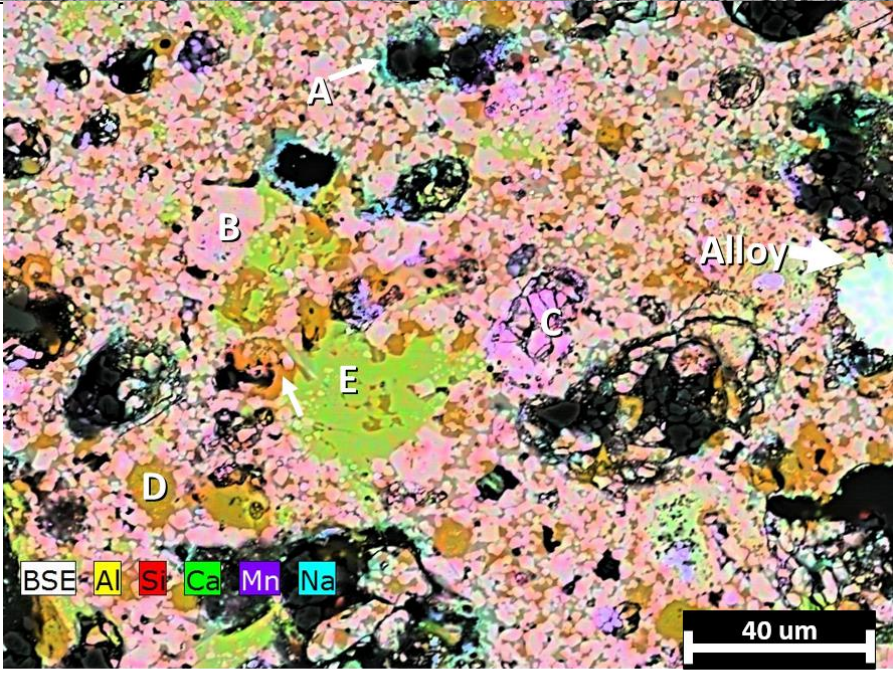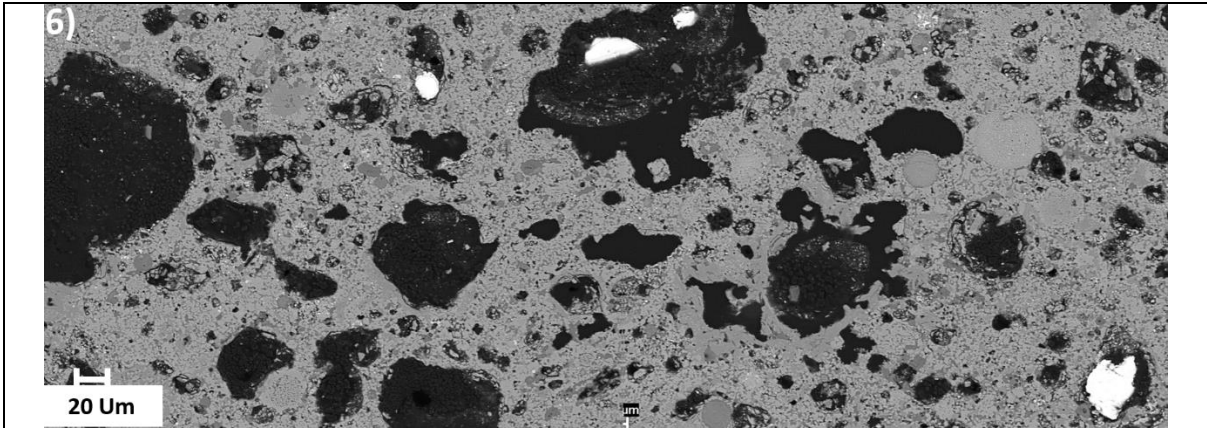
Pt	O	Na	Mg	Al	Si	Cl	K	Ca	Mn	Type	% L
A	32	8.9	1.0	4.8	16.4	15.2	6.9	1.7	12.7	MnKNaSiCl-ox	0
B	34		6.5		13.1			9.0	37.7	Glass slag	0
C	31		1.8	0.2	11.2			2.0	54.2	MnMgSi-oxide	0
D	40	1.1		17.6	16.9		23.2		0.9	KAlSiNa-ox	0
E	38		2.6		19.4			19.9	20.4	Glass slag 1	0

Fired at 1000°C with: 6) Overview image, and BSE image as well as table highlighting phase compositions.
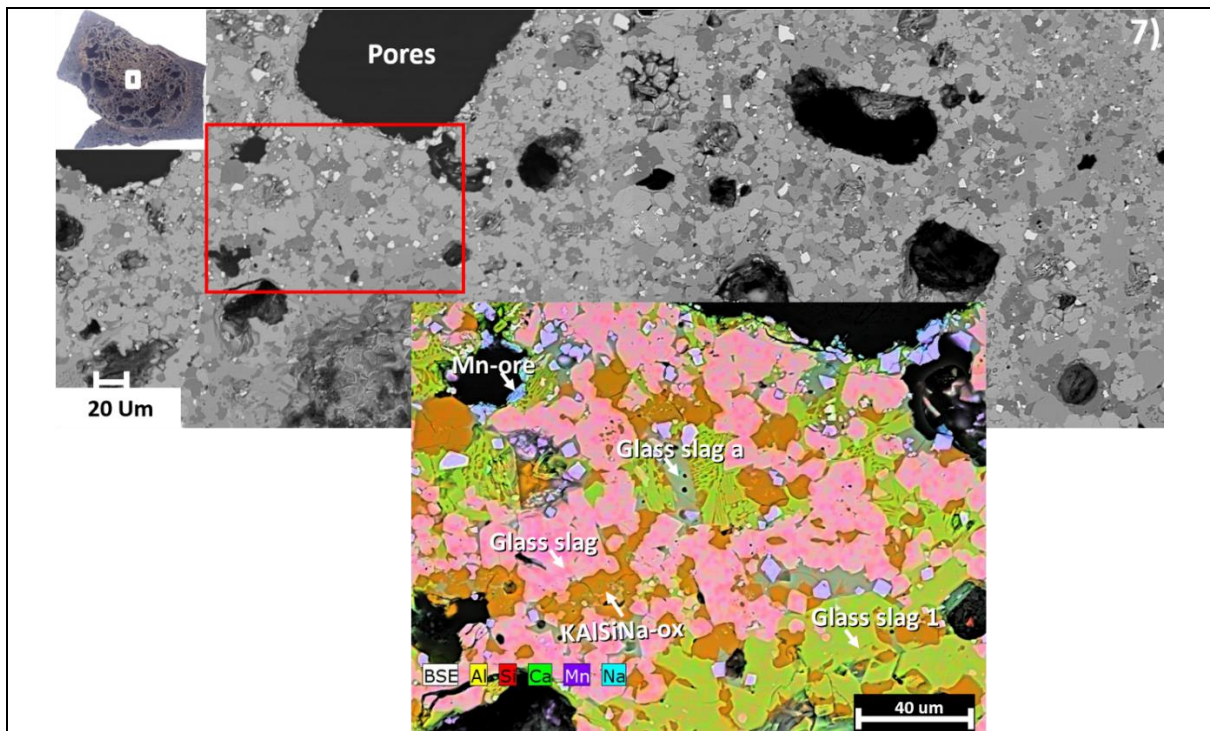
Fired at 1100°C: with 7) Overview image, and BSE image highlighting the different phases
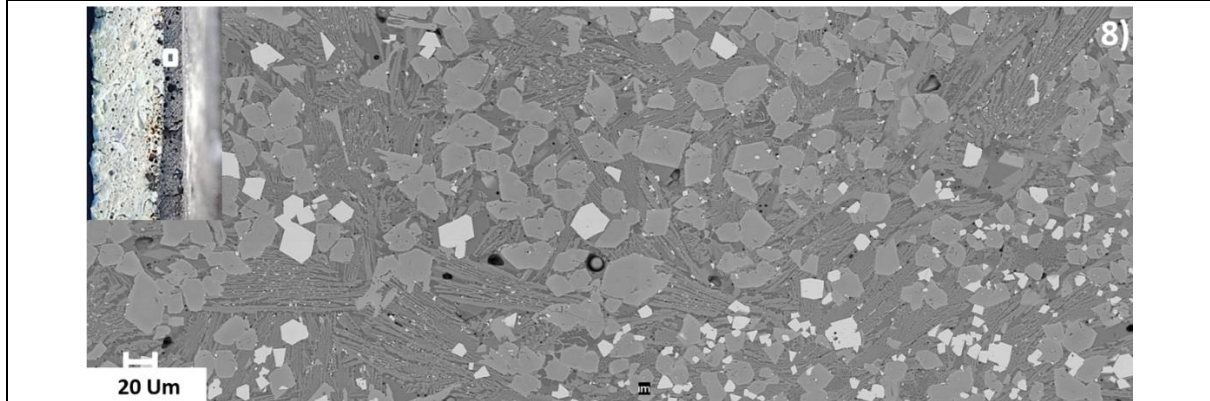
Fired at 1200°C
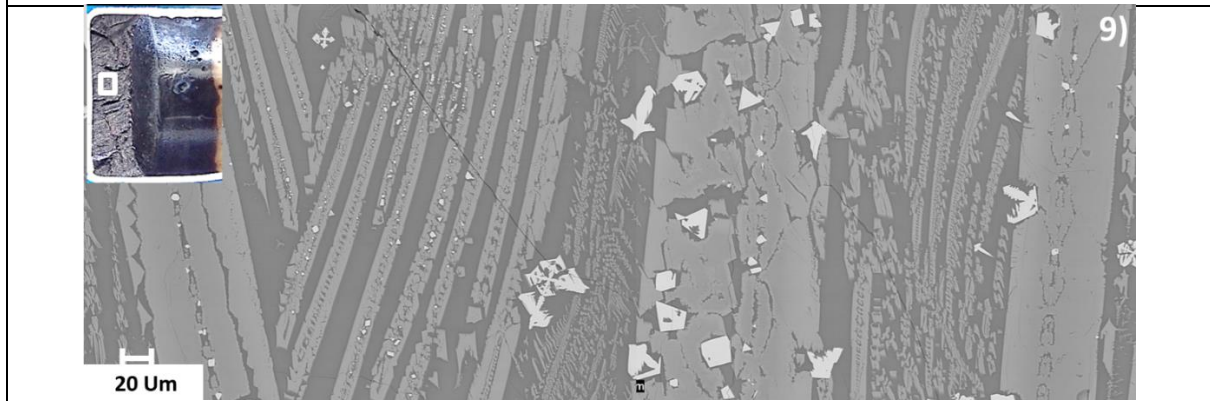
Fired at 1300°C

Figure 57: SEM mappings as well as BSE images showing the microstructural features of stream 2 sample fired from 600 to 1300°C ('ox' refers to oxide; 'type' refers to generic names given to particles/species to differentiate the general chemistry from each other. Species with similar (but not exact) compositions were grouped together; Map elemental colour scheme similar to that which was used for the characterisation of the as-sampled dust)

4.3.5.4 Comparison between the three streams

A comparison of the specific phase chemistry combined with FactSage equilibrium calculations showed a number of observations. The results of the comparison are presented for each temperature below. The bulk of the comparison focussed on stream 1 and 2 since the extreme fineness of stream 3 limited the ability of conducting a thorough particle to particle analysis of sintering.

- At 600°C: For both stream 1 and 2, solid-state sintering was observed whereby three solids where observed to have sintered together. In addition to the solid-state sintering, for stream 1, unusual sintering between a single solid particle and a partially liquid particle was observed. The liquid particle corresponded to 'glass slag a'. Despite this observation for both streams, the large proportion of the sample remained unsintered. This was the same for stream 3.
- At 700°C: For both stream 1 and 2, solid-state sintering combinations of various kinds were observed. In the one instance, neck formation between two particles were observed (for stream 1 only). In another instance, two solids were bonded together by an intermediate solid rim (for stream 1 and 2). The rim was determined to be pure Mn-oxide. In the case of stream 3, the textural appearance of the sample changed, seemingly pointing to increased sintering although the exact mechanism could not be discerned at this point. Despite these observations, similar to 600°C, for all three streams, the large proportion of the sample appeared to remain unsintered.
- At 800°C: Again for both stream 1 and 2, solid-state sintering was observed. In addition to solid-state sintering, for both streams, 'glass slag a' was observed to be an intermediate partially liquid rim joining solid particles together i.e. liquid-state sintering. Still yet, despite the increase in the number of sintered particles, a large proportion of the sample appeared to be still unsintered. Again for stream 3, a noticeable change in sample texture was observed pointing to increased sintering of sample.
- At 900°C: Similar to the observations made in the previous temperatures, solid-state sintering was observed for stream 1 and 2. In addition to solid-state sintering, there was an increase in prominence of liquid-state sintering for both streams, with 'glass slag a' acting as the partially liquid intermediate rim. One distinction at this temperature for both streams was that liquid-state sintering was often observed to be between more than two solid particles. For stream 3, the textural features were similar to that of 800°C.
- At 1000°C: For both stream 1 and 2, multiply solid particles that were now distorted in their particle shape were joined together by intermediate liquid particles (networks of joints observed). This indicated the definite presence and dominance of liquid-state sintering through partially liquid intermediate rims between solid particles. For stream 1, the partially liquid intermediate rims were identified as 'glass slag a' and 'glass slag', whilst for stream 2, in addition to those of stream 1, a KAlSiNa-oxide partially liquid phase was also observed. These partially liquid phases were also observed for stream 3. This observations pointed to a possibility in similarity in the sintering mechanism for all the streams.
- At 1100°C: For stream 1 and 2, the networks of joints indicating sintering that were observed at 1000°C, increased significantly. These were observed throughout the sample. Liquid-state sintering was observed with analysis of stream 2 revealing that 'glass slag a' and 'glass slag 1' seemed to act as the intermediate rim combining the rest of the solid particles together. 'Glass slag a' as well as 'glass slag 1' was also observed throughout the stream 3. This like in the case at 1000°C, may point to the same liquid-state sintering mechanism.

- At 1200-1300°C: For all the streams, the sintering maximum temperature seemed to have been exceeded at 1100°C. Thus, complete melting of the sample was observed at both temperatures.

5 DISCUSSION

In this section, some of the main results that relate to the research questions mentioned in section 1.3 are discussed.

5.1 Is there a potential for dust to sinter in the off-gas duct

Our observations of samples from the smelter (two of them; see sections section 3.1.2 and 4.1) and test work in the laboratory (four of them; see sections 4.2 and 4.3), point to there being sound evidence of sintering in the off-gas duct of the smelter in question, and therefore grounds for supporting the view that sintering is a contributing factor (at least) to the blockages in the ducts. The observations are discussed in detail in the following sections.

Duct temperature measurements

Measurements of the duct temperatures showed that the duct temperatures typically ranged between 600°C to 1300°C (see Table 12 and Figure 21), during normal furnace operation. Considering, as reported by (Jorma, D et al., 2001), (Gordon et al., 2018), and (Malan et al., 2004) that the measured duct temperature range fell within the typical range where manganese ores mixed with carbon reductant and other constituents are agglomerated by sintering, as well as the fact that the analysis of the as-sampled dust samples showed that all the dust samples contained manganese ore and carbon (see section 4.2.4 and 4.2.5), sintering was theoretical likely to take place.

Smelter duct observations

Another indication that pointed to the potential for dust to sinter in the off-gas duct where the physical observations made of the ducts during a long furnace shutdown. In particular, observations of the blocked port by agglomerated dust (see Figure 35 a-b), dust sample build-up along the interior sidewall of the ducts (see Figure 35 d), as well as a section of the duct that was completely blocked (see Figure 35 e). In all these examples, the dust had agglomerated to form a lump, and thus the agglomeration may have been as a result of continuous sintering.

Another possible indicator of sintering during the inspection, may have been the observed difference in the strength of the build-ups that formed along the duct. Some build-ups were crusty and not easy to dislodge using an axe (example is the dust in Figure 35 a), whilst other build-up were dusty and relatively easy to dislodge (example is the in Figure 35 b). The fact that there was a discrepancy in the relative ease in dislodging of the dust may have pointed to some of the dust being sintered, and/or a difference in the extent of sintering. This claim is further substantiated by the sintering index scale presented by (Kobayashi et al., 2014).

Macroscopic changes (Shrinkage and expansion behaviour)

In this investigation macroscopic changes in the dimensions of the samples i.e. shrinkage and expansion, where encountered as shown in the photographs presented in section 4.3.1. Both shrinkage as well as expansions were observed, depending on the sample in consideration. These changes, as highlighted by literature, are typically indicative of sintering (Quijorna et al., 2014), (Romero et al., 2008), and (Bendaoudi et al., 2018).

Compressive strength

Another compelling indication of the potential for the dust to sinter in the off-gas duct was the observed changes that occurred to the compressive strength of the fired dust samples, when

fired at the typical duct temperatures (changes are shown in section 4.3.2). This observation was in agreement with literature that points out that sintering results in the changes of the compressive strength of materials (German, 1996) and (Bendaoudi et al., 2018).

Bulk phase changes (XRD)

As reported by (Fauzi et al., 2018), sintering of manganese ore is usually accompanied by phase changes (see Table 8). These phase changes can be either the disappearance of previously existing phases, or the appearance of new phases as a result of sintering (Fauzi et al., 2018). Since phase changes were encountered in this investigation as was reported in Table 26, Table 27, and Table 28, these may be indicative of the sintering of the sample. It is acknowledge though that not all phase changes point to sintering.

Microstructural changes (SEM)

An even stronger pointer to the potential of sintering of the off-gas duct was the observation of the microstructural features of the fired dust samples. Two sintering related changes were observed under the microscope. Firstly, various dust particles were observed to attach together upon firing (see images in section 4.3.5 for instances of localised as well as universal sintering). This was significant as the examined as-sampled dust prior to firing did not show the same attachments. This attachment of particles as a pointer to sintering has been shown elsewhere in literature (Romero et al., 2008), (Shimonosono et al., 2014), and (Leriche et al., 2017). Secondly, sintering has been documented to result in changes in the grain sizes of the sintered particles (Fauzi et al., 2018) and (German, 1996). Again, observing the microstructure of the of the SEM micrograph images in section 4.3.5, changes in the grain sizes of the particles were observed with change in firing temperature; especially at the higher temperature end. This again, suggested the sintering of the particles.

All six reasons given and explained in this section pointed to the definite potential of the sintering of the dust. Under the microscope through SEM-EDS analysis, this sintering was confirmed as particles were observed to attach together depending on the firing temperature.

5.2   What is the mechanism of sintering?

Both solid-state and liquid-state sintering mechanisms were observed during the firing of the as-sampled dust (section 4.3.5 shows this especially when comparing the fired samples with the unfired samples as the latter showed no signs of solid or liquid state sintering). In the case of solid-state sintering, it was observed clearly between the temperature ranges of 600 to 900 °C. From 1000°C onwards, it appeared as though liquid-state sintering was the sole mechanism of sintering. In terms of the number of particles that were observed to have sintered together in solid-state sintering, for the aforementioned temperature at most three particles were observed to have sintered together. There were four types of solid-state sintering configurations observed, namely, i) two or more solid particles joint by an intermediate solid rim of MnO that formed by oxidation of one of the solid alloys (this kind of configuration was not seen in the literature evaluated), ii) two solid particles that formed a neck as grain boundaries disappeared and particle size increased (configuration reported in literature by (Leriche et al., 2017), iii) three solid particles combined together in series along the grain boundaries (configuration seen a few times and reported in literature by (Shimonosono et al., 2014)), iv) and two solid particles combined along the grain boundaries without any neck formation (configuration seen a number of times reported in literature by (Shimonosono et al., 2014)). Diagrammatic models depicting the aforementioned configuration of the observed solid-state sintering are presented in Figure 58 below. For ease of reference, spherical shapes of equal sizes (even though this was not the

case in reality) were used to simplify the models. The temperatures where the exact mechanism of sintering was observed was also shown for each configuration.

Of the four solid-state sintering presented in Figure 58, type i) was the most common as it was encountered in all four temperatures i.e. from 600- 900°C. As mentioned this type of configuration was unique in that an oxide rim made of pure Mn-oxide seemed to have formed, under the oxidising conditions, through the oxidation of the manganese component in the SiMn alloy. Considering that of all species manganese had the highest concentration in the alloy, as well as the observation from the equilibrium diagram that the lines for the formation of MnO and SiO_2 are relatively close to each other, it can be justified why the oxidation of manganese was favoured. It seemed then that this solid Mn-oxide layer encouraged the formation of these sinters.

Another observation of the solid-state sintering mechanism as observed in the results presented in section 4.3.5 and the model configuration in ii), iii), and iv), was that sintering was between different phases. These included different slag phases such as high MnSi-oxide bearing slag and high MnCaSi slag, as well as ore particles such as carbonates as well as conventional Mn-ore. The significance of these observation was that it revealed that the solid-state sintering mechanism was not dependent on a particular phase.
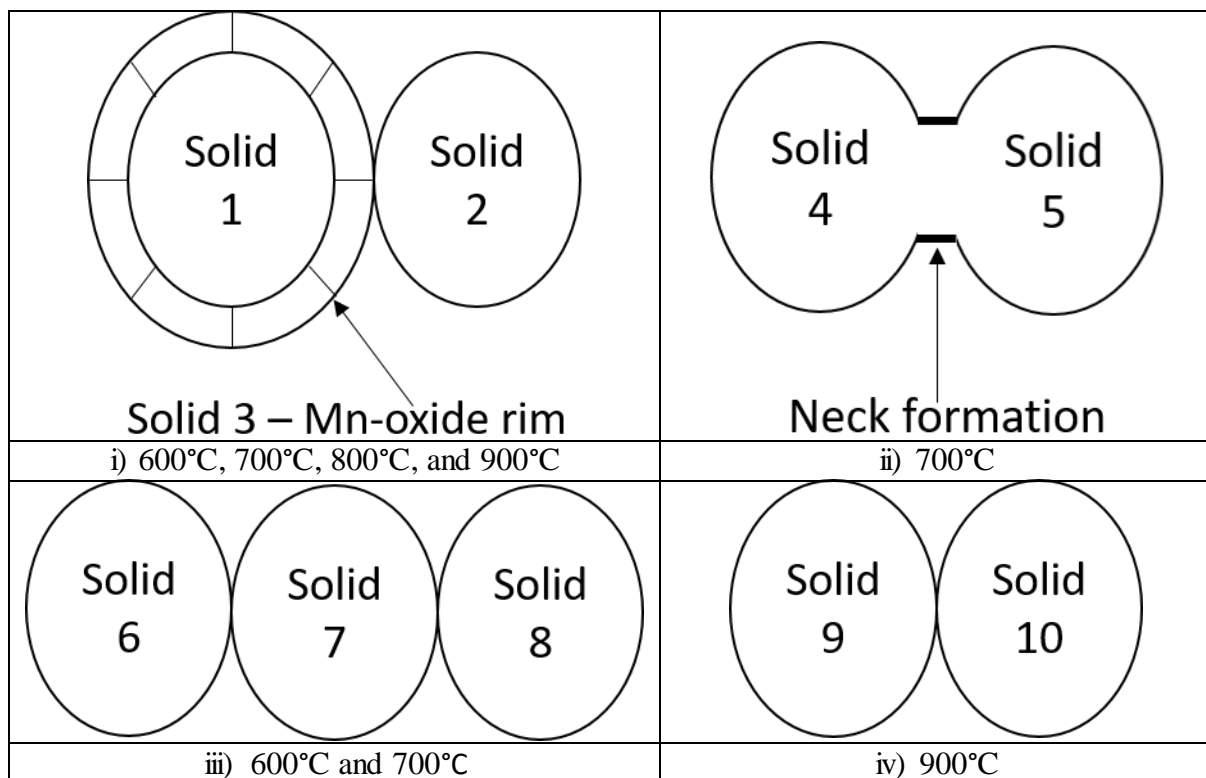
Figure 58: Models depicting the observed solid-state configurations during the firing of the dust (solid 1 – mostly SiMn alloy with one exception where a solid glass slag 1 was observed; solid 3 – mostly Mn-oxide with one exception where MnFe-oxide was observed)

In the case of liquid-state sintering, sintering was also observed as early as 600°C, and subsequently between 800 to 1100°C. The configurations models at each of these temperatures are shown in Figure 59. From these models a progression in the sintering extent with increasing temperature was gathered. This means that the amount of liquid formed increased with temperature, causing an increase in the extent of liquid-state sintering across the sample. This

was such that from 1000°C, the observed sintering seemed to be only by liquid-state sintering. Another observation of the liquid-state sintering observed was that from 600 to 900°C, Liquid 1 corresponding to 'glass slag a', with high potassium (6.9- 8%) and high sodium (0- 4%), was the only liquid intermediate rim acting as an intermediate neck between solid particles. The high potassium and sodium values significantly reduced the melting point of this phase making it partially molten (47% liquid content) even at temperatures as low as 600°C. From 1000°C, other phases with lower potassium and sodium values, which were previously solid at the lower temperatures such as 'glass slag', 'glass slag 1', KAlNaSi-oxide, formed liquid at this temperature and assisted in the promotion of liquid-state sintering.

When one compares the configuration of the observed liquid-state sintering with what was gathered from literature, the configurations observed at 800- 1100°C were similar to those reported by (Shimonosono et al., 2014), (Leriche et al., 2017), and (German, 1996). However, the configuration displayed at 600°C was not seen in the surveyed literature. It may be that this configuration represented the early stages of sintering (Leriche et al., 2017), (Rahaman, 2003), and (German, 1996).

i) 600°C (Liquid 1 – 'Glass slag a')

ii) 800°C
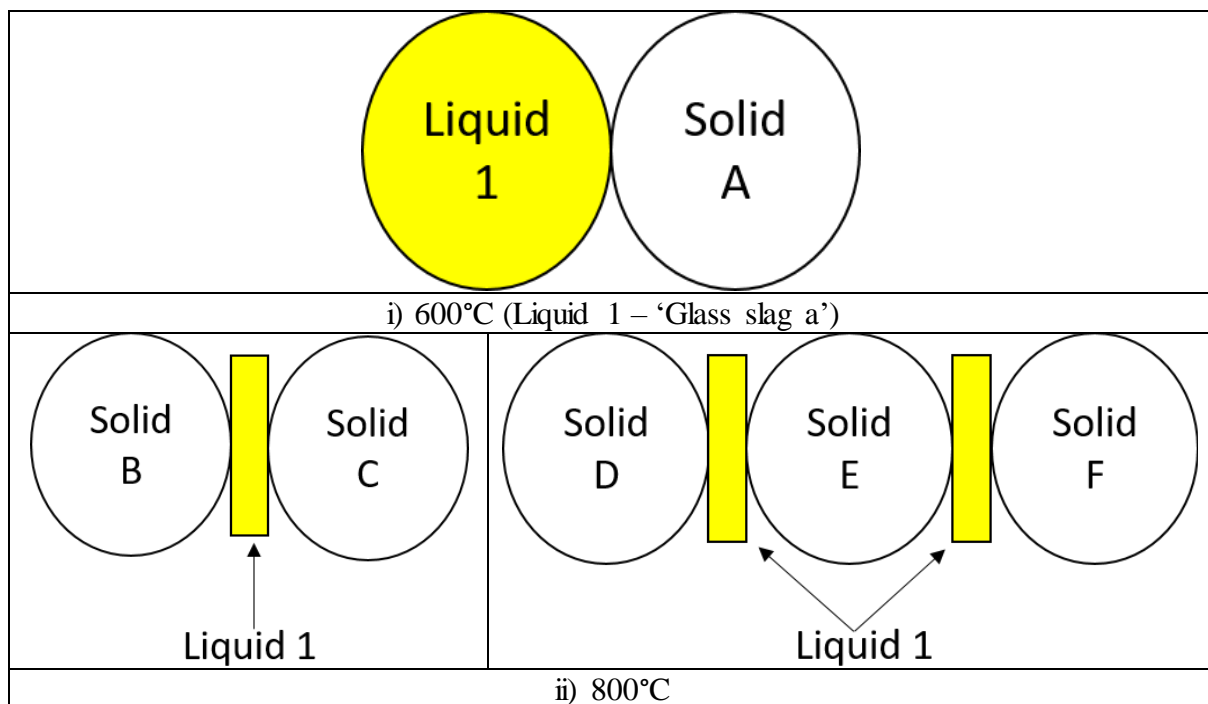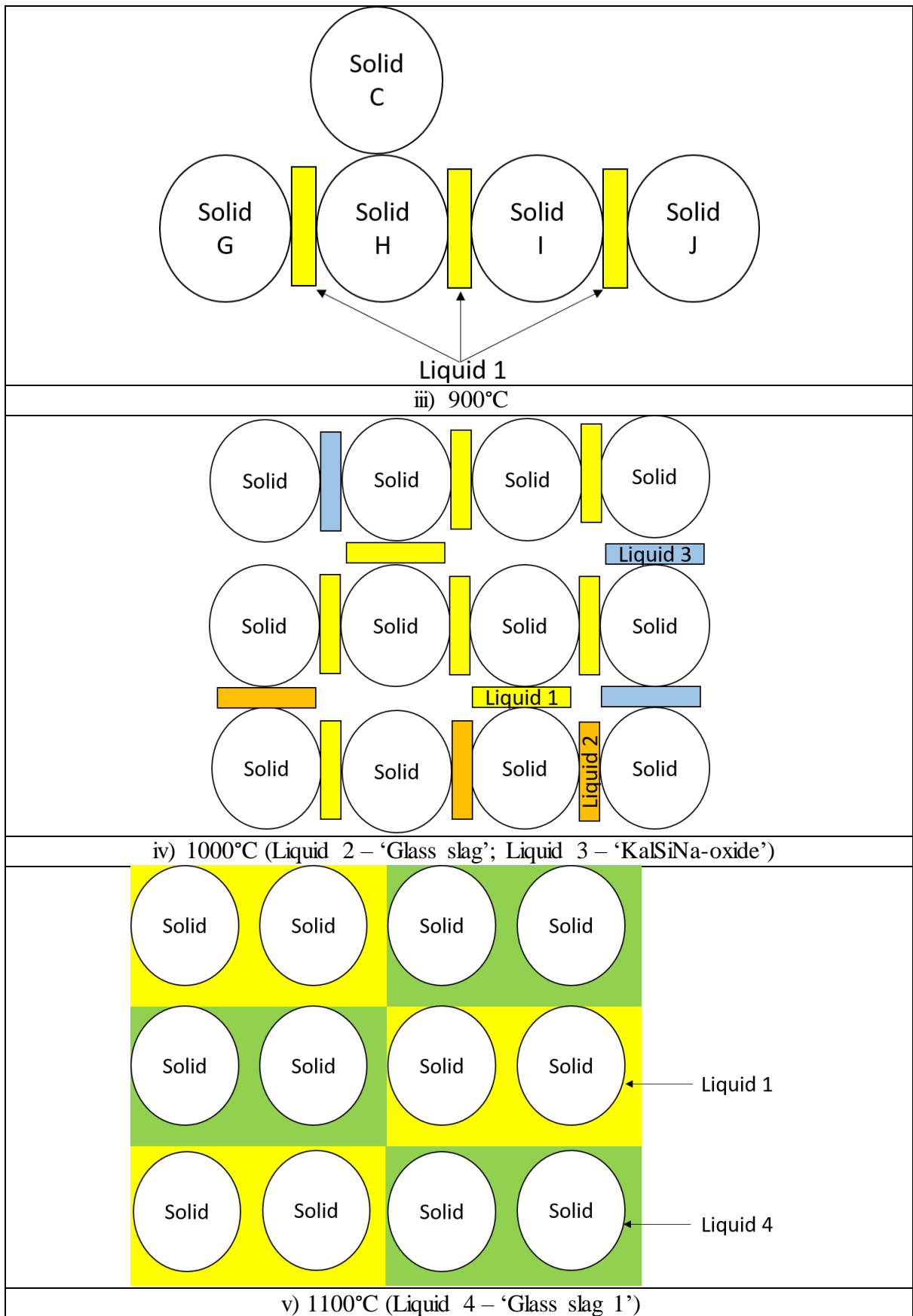
Figure 59: Configuration models of the observed liquid-state sintering at each firing temperature

108

5.3 Does the firing temperature have an effect?

The temperature was found to have an effect on both the sinter formation and the compressive strength of the dust. The observed effects are described in separate headings below.

Effect on sinter formation

The effect of temperature on sinter formation was seen both at a macroscopic (naked eye) as well as at a microscopic level. In terms of the macroscopic level (as presented in section 4.3.1), the changes in temperature i.e. the increase in the firing, for a fixed PSD e.g. for all coarse particles, resulted in an increasingly more stable and less friable sinter. The same observation was made with the analysis of the intermediate or fine size particles only. Another macroscopic observation was that at higher temperatures i.e. 1000°C and 1100°C, there was an increase visibility of liquid formation, this pointed to sinter formation being increasingly promoted by a liquid-state mechanisms. On a microscopic level (as presented in the SEM micrographs of section 4.3.5), a change in the degree of sintering was observed with changing temperature. This translated to the formation of long chains of network of bond indicating increased sinter formation, as the firing temperature was increased. For example, when evaluating the microstructures of the coarse PSD only as presented in Figure 55, the progress of sinter formation was seen as an increasing amount of particles began to attach together, with increasing firing temperature. This was so pronounced that by 1100°C, a complete network joining all the particles was observed. This arrangement was not seen in the lower temperatures, and showed that for the exact same PSD, changing the firing temperature results in changes in sinter formation. Beyond 1100°C, sinter formation was replaced by complete melting, since the firing temperature seem to go beyond the sintering threshold (Shen, 2009).

Effect on compressive strength

Similar to sinter formation, the change in firing temperature had a direct effect on the compressive strength of the dust sinters even when the PSD was fixed. For example, the compressive strengths of the coarse particles, fired at 600°C and 1000°C, was 7 N and 224 N respectively. This meant that the compressive strength of the dust was increased by two orders of magnitudes as a result of increasing the firing temperature. The same changes, albeit not at the same order of magnitude, were observed after evaluating the intermediate and fine samples only. That is, increasing the firing temperature resulted in an increase in the compressive strength. The increase was most pronounced at 1100°C for the coarse PSD only, 1100°C for the intermediate fraction only, and 1000°C for the finest fraction only.

In light of the above, changes in the firing temperature were observed to have a direct effect on both the sinter formation, as well as the compressive strength. The effect which is in agreement with literature was directly proportional, in that increasing the firing temperature promoted an increase in the sinter formation as well as the compressive strength of the dust (Shen, 2009), (Quijorna et al., 2014), (Adell et al., 2007), (Romero et al., 2008), (Dehaghani and Ahmadian, 2015), (Hu and Wang, 2010), (Ghasali et al., 2016), (Wang et al., 2013), (Shimonosono et al., 2014), (J. Liu, 2017), and (Bendaoudi et al., 2018). The idea is that increasing the firing temperature promotes sample densification which in turn increases the particle to particle contact, leading to increases in the compressive strength of the dust (Dehaghani and Ahmadian, 2015), (Hu and Wang, 2010), (German, 1996), and (Romero et al., 2008).

5.4   Does PSD have an effect?

The PSD was found to have an effect on both the sinter formation and the compressive strength of the dust. The observed effects are described in separate headings below.

Effect on sinter formation

The effect of temperature on sinter formation was seen both at a macroscopic as well as at a microscopic level. At a macroscopic level (as presented in section 4.3.1), the effect is most pronounced at higher temperatures. For example a comparison of the sinter formation at 1000°C, for the different dust size fractions presented in Figure 45 (coarse fraction), Figure 47 (intermediate fraction), and Figure 49 (fine fraction), it can be observed that the finest size fraction shows a more-wetted appearance and appears to be more sintered than the preceding coarser fractions. This was further substantiated by the steep shrinkage in its diameter i.e. 18% shrinkage, compared to 3% expansion and 4% shrinkage, for the coarser and intermediate fraction respectively. Furthermore, at 1100°C, sintering of the finest size fraction resulted in an expansion caused by body bloating (Quijorna et al., 2014), a phenomena that did not occur in the coarser size fractions. At a microscopic level, similar to the observations made at a macroscopic level, the effects of PSD on sinter formation were most pronounced in the fine particle size. This can be seen in the SEM micrographs presented in Figure 55 to Figure 57. From the micrographs, the microstructural appearance of the fine stream is markedly different from those of the coarser fractions. The fine fraction was more densified i.e. a lower voidage fraction, and more particles were in direct contact at all temperatures indicating more intense sinter formation especially at the higher temperatures.

Effect on compressive strength

Similar to sinter formation, the change in PSD had a direct effect on the compressive strength of the dust sinters for a fixed temperatures. For example, at 800°C, the compressive strengths for the coarse, intermediate, and fine dust fraction was 24 N, 72 N, and 24 150 N, respectively. Another example is at 1000°C, were the compressive strength was 2520 N, 10287 N, and 37880 N, respectively. These compressive strength values showed that decreasing the particle size resulted in an increase in the compressive strength of the dust. The extent of this increase in compressive strength seemed to increase with decrease in particle size i.e. the difference in the compressive strength values are more pronounced between the fine fraction and intermediate fraction, compared to the intermediate fraction and the coarse fraction.

In light of the above, both the sinter formation and compressive strength were observed to be affected by the PSD of the dust samples. The effect was inversely proportional in that the finer the particle size, the more pronounced the sinter formation as well as the compressive strength. This observation can be explained by the fact that finer particles have an inherently higher surface area compared to coarser particles of the same. This means that the finer particles will be more in contact and will also have a lower fraction of voids when compressed together under the same pressure as the coarse particles. The increased contact lowers the surface energy and thereby promotes increased sintering (German, 1996) and (Romero et al., 2008). Furthermore, the lower voidage fraction compared to the coarse particles increases the compressive strength of the sample (Dehaghani and Ahmadian, 2015) and (Hu and Wang, 2010). This effect of the PSD on sinter formation and compressive strength was in agreement with literature presented by (German, 1996), (Hu and Wang, 2010), (Dehaghani and Ahmadian, 2015), and (Romero et al., 2008).

6 CONCLUSIONS

Following an evaluation of sintering as a potential cause of blockages in a duct of a submerged arc furnace applied in silicomanganese production, I summarize my findings:

- There was sound evidence of sintering in the off-gas duct of the smelter in question, and therefore grounds for supporting the view that sintering is a contributing factor (at least) to the blockages in the ducts.
- Both solid- and liquid-state sintering were observed. The former was more localised– observed only in some areas in the sample–and most prominent at firing temperatures of 600–900°C. The latter was observed between 600–1100°C; it was prevalent at 1100°C, where long networks of sintered materials were observed.
- The firing temperature was found to have an effect on sinter formation and compressive strength. The relationship in conveniently summarised as, increases in the firing temperature promotes formation of strong and stable sinters – increases sinter formation and the compressive strength of the sinters formed.
- The PSD was also found to have an effect on sinter formation and the compressive strength of the formed sinters. In summary, it was found that finer particle promoted increased sinter formation which then resulted in stronger sinters.

7 RECOMMENDATIONS

In light of the assumptions made during this investigation, the observations during the study, and the outcomes of the study, the following recommendations are made. The recommendations focus on potential future studies that could be done to supplement and further solidify the work conducted in this dissertation. Each recommendation includes an explanation of the premise that sparked the thought.

- *Proposal 1:* Proposal of the same investigation as presented in this dissertation, with a change in the gaseous atmosphere in which dust is fired in; that is, from the air atmosphere applied in this research, to a CO_2 rich atmosphere.
  Reason for proposal 1: During normal operation of the furnace at the smelter in question, CO gas is commonly observed to combust in the freeboard area as it reacts with air that enters through the open roof (see Figure 20); CO is converted to CO_2. Although the air ingress dilutes this gas, it would be interesting to investigate–for occasions where dilution might be minor leaving a gas mixture that is rich in CO_2–whether or not the sintering behaviour would be the same as reported in this dissertation.
  How study 1 would be conducted: Such a study would be conducted using the same apparatus presented here with the only change being the purging in of CO_2 gases into the furnace.
- *Proposal 2:* To determine the minimum compressive strength required for the dust to form a stable blockage.
  Reason for proposal 2: The conditions in the off-gas ducts are extremely volatile with the dust laden off-gas typically travelling at an average speed of 15 m/s (Steenkamp et al., 2018). Whether or not the sinters formed in this investigation, especially at the lower temperatures i.e., 600-900°C, can withstand these conditions without breaking is uncertain. A study of this nature would provide insight into this question and even show the minimum duct temperature required to form a stable blockage by sintering. This information could potentially be used to design a cooling system that would ensure that ducts are sufficiently cooled to a temperature where a stable blockage would not be formed.
- *Proposal 3:* To study the typical mass distribution of stream 1, stream 2, and stream 3, as they are mechanically separated in the baghouse of the smelter. At present the smelter does not weigh the daily dust generation from each stream. The information gained from this exercise would be used to prepare various stream mixes in proportion to the typical %mass distribution of the three streams. This in turn would be used to determine the effect of mixing of streams on the sintering behaviour of the dust.
  How study 3 would be conducted: Gathering mass distribution data can be easily done by recording the daily masses weighed for each stream over a period of time. The same experimental procedure as stipulated above would be used for the testwork.
- *Proposal 4:* Investigate the effect of furnace atmosphere on the extent of sintering. This will also help in understanding the effect of varying oxidation state, especially Mn and Fe, on sintering.

8 REFERENCES

Adell, V., Cheeseman, C.R., Ferraris, M., Salvo, M., Smeacetto, F., Boccaccini, A.R. (2007). Characterising the Sintering Behaviour of Pulverised Fuel Ash using Heating Stage Microscopy. *Materials Characterization,* **58**(10), 980–988.

Baxter, L., DeSollar, R. (1996). *Applications of Advanced Technology to Ash-Related Problems in Boilers*. New York: Springer Science & Business Media.

Bendaoudi, S.-E., Bounazef, M., Djeffal, A. (2018). The Effect of Sintering Temperature on the Porosity and Compressive Strength of Corundum. *Journal of the Mechanical Behaviour of Materials*, **27**(3-4), 1-3.

Budin, S., Ria Jaafar, T., Asri Selamat, M. (2017). 'Effect of Sintering Atmosphere on the Mechanical Properties of Sintered Tungsten Carbide'. *The International Conference on Composite Material, Polymer Science and Engineering*. Toyama, 24-25 June. Japan: X-academy.

Cheeseman, C.R., Sollars, C.J., McEntee, S. (2003). Properties, Microstructure and Leaching of Sintered Sewage Sludge Ash. Resources, Conservation and Recycling, **40**(1): 13–25.

Chu, M.Y., Rahaman, M.N., Jonghe, L.C., Brook, R.J. (1991). Effect of Heating Rate on Sintering and Coarsening. Journal of the American Ceramic Society, **74**(6): 1217–1225.

Dehaghani, M.T., Ahmadian, M. (2015). Effect of Sintering Temperature and Time on the Mechanical Properties of Co–Cr–Mo/58S Bioglass Porous Nano-Composite. *Bulletin of Materials Science*, **38**(5): 1239–1246.

Dominy, S. and O'Connor, L. and Glass, H. and Purevgerel, S., Xie, Y. (2018). Towards Representative Metallurgical Sampling and Gold Recovery Testwork Programmes. *Minerals MDPI*, **193**(8): 1-34.

European Commission. (2010). *Best Available Techniques (BAT) Reference Document for the Non-Ferrous Metals Industries*: Industrial Emissions Directive. Available at: https://eippcb.jrc.ec.europa.eu/reference/bref/nfm/jrc107041_nfm_bref_2017.pdf (Accessed: 01 August 2019).

Fauzi, A., Ratnawulan, Putri, P.J. (2018). Effect of Sintering Temperature on Crystal Structure and Grain Size of Manganese Ores from West Sumatra. Journal of Physics, **1040**(1): 1-7.

Gaal, S., Tangstad, M., Ravary, B. (2010). 'Recycling of Waste Materials from the Production of FeMn and SiMn', *The Twelfth International Ferroalloys Congress: Sustainable Future*. Helsinki, 6-9 June. Finland: Outotec oyj.

German, R.M. (1996). *Sintering Theory and Practice*. New York: John Wiley & Sons, Inc.

Ghasali, E., Yazdani-rad, R., Rahbari, A., Ebadzadeh, T. (2016). Microwave sintering of aluminum-ZrB$_2$ Composite: Focusing on microstructure and mechanical properties. Materials Research, **19**(4): 765-769.

Gordon, Y., Nell, J., Yaroshenko, Y. (2018). 'Manganese Ore Thermal Treatment Prior to Smelting', *Russian Scientific and Practical Conference of Students, Graduate Students and Young Scientists*: *Heat Engineering and Computer Science in Education, Science and Production*. Yekaterinburg, 19-23 November. Russia: Knowledge E

Groot, D.R., Redtmann, T., Steenkamp, J. (2013). 'The Recovery of Manganese and Generation of Avaluable Residue from Ferromanganese Slags by a Hydrometallurgical Route', *The thirteenth International Ferroalloys Congress: Efficient Technologies in Ferroalloy Industry*. Almaty, 9-13 June. Kazakhstan: SMS Siemag.

Guézennec, A.-G., Huber, J.-C., Patisson, F., Sessiecq, P., Birat, J.-P., Ablitzer, D. (2005). Dust Formation in Electric Arc Furnace: Birth of the particles. *Powder Technology, 157*(1-3): 2–11.

Gy, P. (1979). *Sampling of Particulate Materials*: *Theory and Practice*. Amsterdam: Elsevier Scientific Pub. Co.

Hasanuzzaman, M., Rafferty, A., Sajjia, M., Olabi, A.G. (2015). *Production and Treatment of Porous Glass Materials for Advanced Usage, in: Reference Module in Materials Science and Materials Engineering*. Amsterdam: Elsevier Inc.

Hsiao, H.M., Daniel, I.M., Wooh, S.C. (1995). A New Compression Test Method for Thick Composites. *Journal of Composite Materials*, **29**(13): 1789–1806.

Hu, L., Wang, C.A. (2010). Effect of Sintering Temperature on Compressive Strength of Porous Yttria-Stabilized Zirconia Ceramics. *Ceramics International*, **36**(5): 1697–1701.

Institution of Mining and Metallurgy (Great Britain). (1973). '*Sampling in the Mineral and Metallurgical Processing Industries*: P*apers Presented at a Meeting Held in London, 1973'*. London, 2 July. The Institution of Mining and Metallurgy.

Liu, J., Chu, Z., Jia, C., Ding, R., Yuan, G. (2017). Effects of Sintering Time on Microstructure and Properties of Alumina Foam Ceramics. *Journal of Ceramic Science and Technology*, **8**(4): 499-504.

Jordan, P., (2011). Evaluation of Reductants used for Ilmenite Smelting Based on CO_2 Reactivity (Boudouard reaction) Measurement. *Journal of the Southern African Institute of Mining and Metallurgy,* **111**(1), 385–392.

Jorma, D, Helge, K, Paivi, O, Riku, S, (2001). 'Sintered Manganese Ore and Its Use in Ferromanganese Production', *The Ninth International Ferroalloys Congress*. Quebec, 3-6 June. Canada: Ferroalloys Association.

Kadkhodabeigi, M., Ravary, B., Hjertenes, D.O. (2015). 'Modelling of Off-gas and Particles Flow under Roof of a Closed Submerged Arc Furnace', *The fourteenth International Ferroalloys Congress*. Kiev, 31May-4 June. Ukraine: SMS Group.

Keith, L.H. (1996). *Principles of Environmental Sampling*. Washington, DC: American Chemical Society.

Kingery, W.D., Bowen, H.K., Uhlmann, D.R. (1960). *Introduction to Ceramics*. New York: Wiley.

Kobayashi, Y., Todoroki, H., Kirihara, F., Nishijima, W., Komatsubara, H. (2014). Sintering Behaviour of Silica Filler Sands for Sliding Nozzle in a Ladle. ISIJ International, **54**(6): 1823-1829.

Kuczynski, G.C., Hooton, N.A., Gibbon, C.F. (1967). *Sintering and Related Phenomena*. California: Gordon and Breach Science Publishers.

Łada, P., Miazga, A., Konopka, K., Szafran, M. (2018). Sintering Behavior and Thermal Expansion of Zirconia–Titanium Composites. *Journal of Thermal Analysis Calorimetry*, **133**: 55–61.

Leriche, A., Cambier, F., Hampshire, S. (2017). *Reference Module in Materials Science and Materials Engineering: Sintering of Ceramics*. Philadelphia: Elsevier Ltd.

Lin, K., Chiang, K., Lin, D. (2006). Effect of Heating Temperature on the Sintering Characteristics of Sewage Sludge Ash. *Journal of Hazardous Materials,* **128**(2-3): 175–181.

Liu, J. (2017). Effects of Sintering Time on Microstructure and Properties of Alumina Foam Ceramics. *Journal of Ceramic Science and Technology*, **8**(4): 499-544.

Machado, J., Brehm, F., Moraes, C., Santos, C., Vilela, A., Cunha, J. (2006). Chemical, Physical, Structural and Morphological Characterization of the Electric Arc Furnace Dust. *Journal of Hazardous Materials,* **136**(3): 953–960.

Makino, A., Hojo, M., Shintomi, M. (2013). Combustion Rate of Solid Carbon in the Axisymmetric Stagnation Flowfield Established over a Sphere and/or a Flat Plate. *Journal of Combustion*, **2013**: 1–22.

Malan, J., Barthel, W., Dippenaar, B.A. (2004). 'Optimising Manganese Sinter Plants Process Parameters and Design', *Tenth International Ferroalloys Congress: Transformation through Technology*. Cape Town, 1-4 February. South Africa: SAIMM.

Martins, F.M., Neto, J.M. dos R., Cunha, C.J. da. (2008). Mineral Phases of Weathered and Recent Electric arc Furnace Dust. *Journal of Hazardous Materials,* **154**(1-3), 417–425.

Miller, I., Freund, J.E. (1976). *Probability and Statistics for Engineers*. New Jersey: Prentice-Hall.

Nkosi, S., Steenkamp, J.D., Groot, D.R., Gous, J. (2011). 'Hydrometallurgical Process for the Recovery of Manganese from Pelletized Silicomanganese Submerged Arc Furnace Dust', Fray International Symposium. Cancun, 4-7 December. Mexico: Flogen Technologies Inc.

Omran, M., Fabritius, T. (2017). Effect of Steelmaking Dust Characteristics on Suitable Recycling Process Determining: Ferrochrome Converter (CRC) and Electric Arc Furnace (EAF) Dusts. *Powder Technology,* **308**, 47–60.

Park, D.Y., Lee, S.W., Park, S.J., Kwon, Y.-S., Otsuka, I. (2013). Effects of Particle Sizes on Sintering Behavior of 316L Stainless Steel Powder. *Metallurgical and Materials Transaction A*, **44**(A), 1508–1518.

Peng, C., Guo, Z., Zhang, F. (2008). Discovery of Potassium Chloride in the Sintering Dust by Chemical and Physical Characterization. *ISIJ International,* **48**(10): 1398–1403.

Quijorna, N., de Pedro, M., Romero, M., Andrés, A. (2014). Characterisation of the Sintering Behaviour of Waelz Slag from Electric Arc Furnace (EAF) Dust Recycling for Use in the Clay Ceramics Industry. *Journal of Environmental Management*, **132**: 278–286.

Rahaman, M.N. (2003). *Ceramic Processing and Sintering*. Boca Raton, Florida: CRC/Taylor & Francis.

Rama Murthy, Y., Kapure, G.U., Tripathy, S.K., Sahu, G.P. (2018). Recycling of Ferromanganese Gas Cleaning Plant (GCP) Sludge by Novel Agglomeration. *Waste Management*, **80**: 457–465.

Ravary, B., Hunsbedt, L. (2013). 'Progress in Recycling Sludge from Off-gas Cleaning of Manganese Alloy Furnaces', *The Thirteenth International Ferroalloys Congress*: Efficient Technologies in Ferroalloys Industry. Almaty, 9-13 June. Kazakhstan: SMS Siemag.

Rawle, A.F., (2015). Best Practice in Laser Diffraction – A Robustness Study of the Optical Properties of Silica. *Procedia Engineering*, **102**(2015): 182-189.

Riku, S. (2001). 'Sintered Manganese Ore and its Use in Ferromanganese Production', *The Ninth International Ferroalloys Congress*. Quebec, 3-6 June 2001. Canada: Ferroalloy association.

Robertson, I.M., Schaffer, G.B. (2009). Some Effects of Particle Size on the Sintering of Titanium and a Master Sintering Curve Model. *Metallurgical and Materials Transaction A*, **40**(A): 1968–1979.

Romero, M., Andrés, A., Alonso, R., Viguri, J., Rincón, J.Ma. (2008). Sintering Behaviour of Ceramic Bodies from Contaminated Marine Sediments. *Ceramics International*, **34**(8): 1917-1924.

Rughubir, N., Bessinger, D. (2007). 'Furnace Dust from Exxaro Sands KZN', *The 6th International Heavy Minerals Conference*. Hluhluwe, 9-14 September. South Africa: SAIMM.

Shen, R. (2009). 'Reduction of Zinc Oxide in Sintering of Manganese Furnace Dust'. PhD thesis, The University on New South Wales, Cardiff.

Shen, R., Zhang, G., Dell'Amico, M., Brown, P., Ostrovski, O. (2007). 'A Feasibility Study of Recycling of Manganese Furnace Dust', *Infacon XI*. New Delhi, 18-21 February. India: The Indian Ferro Alloy Producers Association.

Shimonosono, T., Ikeyama, S., Hirata, Y., Sameshima, S. (2014). Compressive Deformation of Liquid Phase-Sintered Porous Silicon Carbide Ceramics. *Journal of Asian Ceramic Societies,* **2**(4): 422–428.

Smith, R., James, G.V. (1981). *The Sampling of Bulk Materials, Analytical sciences monographs.* London: Royal Society of Chemistry.

Stanciu, L.A., Kodash, V.Y., Groza, J.R. (2001). Effects of Heating Rate on Densification and Grain Growth during Field-Assisted Sintering of Alpha Al_2O_3 and $MoSi_2$ Powders. *Metallurgical and Materials Transactions,* **32**(10*): 2633-2638.

Steenkamp, J.D., Maphutha, P., Makwarela, O., Banda, W.K., Thobadi, I., Sitefane, M., Gous, J., Sutherland, J.J. (2018). Silicomanganese Production at Transalloys in the Twenty-Tens. *Journal of the Southern African Institute of Mining and Metallurgy*, **118**(3): 309–320.

Suarez, L., Schneider, J., Houbaert, Y. (2008). High-Temperature Oxidation of Fe- Si Alloys in the Temperature Range 900-1250°C. *Defects and Diffusion Forum*, **273-276**: 661-666.

Sykes, L.M., Gani, F., Vally, Z. (2016). The Meaning of the MEAN, and other Statistical Terms Commonly used in Medical Research. *South African Dental Journal*, **71**(6): 274-278.

Ujam, A.J., Enebe, K.O. (2013). Experimental Analysis of Particle Size Distribution using Electromagnetic Sieve. *American Journal of Engineering Research*, **2**(10): 77-85.

Vaish, A.K. (1994). Pollution Control in Ferro-Alloys Production: 4th Refresher course on Ferro Alloys, 12-14 January.

Varela, J.A., Whittemore, O.J., Longo, E. (1990). Pore size evolution during sintering of ceramic oxides. *Ceramics International,* **16**(1990): 177-189.

Waidner, C.W., Burgess, G.K. (1905). Optical Pyrometry. *Bulletin of the Bureau of Standards*, 1(2): 188-254.

Wang, H., Wang, X., Lang, Y., Chu, S. (2013). 'New Process for Sintering Chromite Concentrate with Continuous-Strand Sinter Machine', *The Thirteenth International Ferroalloys Congress*. Almaty, 9-13 June. Kazakhstan: SMS Siemag.

Wang, K.S., Sun, C.-J., Liu, C.Y. (2001). Effects of the Type of Sintering Atmosphere on the Chromium Leachability of Thermal-Treated Municipal Solid Waste Incinerator Fly Ash. *Waste Management*, **21**(1): 85-91.

Williams, B. (1978). *A Sampler on Sampling. Wiley series in probability and mathematical statistics.* New York : Wiley.

Xia, K.D. (1997). 'Recovery of Zinc from Zinc Ferrite and Electric Arc Furnace Dust'. PhD thesis, Queen's University, Kingston.

Zaki, M.I., Hasan, M.A., Pasupulety, L. (1997). Thermochemistry of manganese oxides in reactive gas atmospheres: Probing redox compositions in the decomposition course MnO2 ~ MnO. *Thermochimica Acta,* **303**(1997): 171-181.

Zhong, Y., Qiu, X., Gao, J., Guo, Z. (2018). Recovery of Soluble Potassium from Electric Arc Furnace Dust of Manganese Alloy Production: Characterization and Water Leaching Kinetics. *ISIJ International,* **58**(1): 194–200.

APPENDICES

APPENDIX A.   SMELTER DATA

Table 29: Table summarising the mass of the collected samples over 3 months (mass presented in kg)

	Sample	Day 1: 27 November 2018					Day 2: 28 November 2018				
	Sample	1	2#	2#	3	Total	1	2#	2#	3	Total
Period A	Time	07:55-08:05					07:55-08:05				
Period A	Mass	3.804	4.724	4.564	2.411	15.502	3.389	3.468	3.173	1.859	11.889
Period B	Time	09:55-10:05					09:55-10:05				
Period B	Mass	4.024	4.327	4.253	1.980	14.584	2.852	3.337	2.513	1.364	10.066
Period C	Time	11:55-12:05					11:55-12:05				
Period C	Mass	2.799	3.524	3.632	1.789	11.744	1.263	2.752	2.994	1.665	8.675
Period D	Time	13:55-14:05					13:55-14:05				
Period D	Mass	2.765	3.215	3.792	0.938	10.709	2.507	2.271	2.802	1.736	9.315
Period E	Time	15:55-16:05					15:55-16:05				
Period E	Mass	2.641	3.213	3.764	1.067	10.684	2.160	3.085	2.664	1.660	9.569
	Total	16.031	19.002	20.004	8.185	**63.223**	12.170	14.913	14.146	8.284	**49.513**

	Sample	Day 3: 11 December 2018					Day 4: 12 December 2018				
	Sample	1	2#	2#	3	Total	1	2#	2#	3	Total
Period A	Time	07:55-08:05					07:55-08:05				
Period A	Mass	2.111	2.804	3.232	1.299	9.446	2.807	3.186	3.538	1.845	11.376
Period B	Time	09:55-10:05					09:55-10:05				
Period B	Mass	2.434	2.634	-	1.181	6.250	2.595	1.946	2.698	1.661	8.900
Period C	Time	11:55-12:05					11:55-12:05				
Period C	Mass	2.365	2.735	2.888	0.929	8.916	2.738	3.049	3.422	1.312	10.520
Period D	Time	13:55-14:05					13:55-14:05				
Period D	Mass	2.632	3.025	3.093	1.143	9.892	3.395	3.682	3.628	1.374	12.080

Period E	*Time*	15:55-16:05					15:55-16:05			
	Mass	2.807	3.195	4.182	1.336	11.520	3.476	3.084	3.564	1.549	11.672
	Total	12.350	14.393	13.394	5.887	**46.024**	15.010	14.947	16.850	7.741	**54.548**

		Day 5: 18 December 2018					**Day 6: 19 December 2018**			
	Sample	*1*	*2#*	*2#*	*3*	*Total*	*1*	*2#*	*2#*	*3*	*Total*
Period A	*Time*	07:55-08:05					07:55-08:05			
	Mass	2.941	3.776	3.379	2.024	12.121	2.831	2.751	3.549	1.719	10.850
Period B	*Time*	09:55-10:05					09:55-10:05			
	Mass	3.468	3.957	3.363	2.234	13.021	2.866	2.813	2.483	1.488	9.650
Period C	*Time*	11:55-12:05					11:55-12:05			
	Mass	2.812	3.166	3.368	1.156	10.502	2.776	2.460	3.489	1.427	10.153
Period D	*Time*	13:55-14:05					13:55-14:05			
	Mass	2.856	3.547	3.653	1.237	11.293	2.872	2.736	3.179	1.549	10.337
Period E	*Time*	15:55-16:05					15:55-16:05			
	Mass	2.908	3.311	3.621	1.402	11.241	2.778	3.267	3.254	1.473	10.772
	Total	14.986	17.756	17.384	8.053	**58.178**	14.123	14.027	15.955	7.656	**51.761**

		Day 7: 08 January 2019					**Day 8: 09 January 2019**			
	Sample	*1*	*2#*	*2#*	*3*	*Total*	*1*	*2#*	*2#*	*3*	*Total*
Period A	*Time*	07:55-08:05					07:55-08:05			
	Mass	2.727	2.641	2.499	0.966	8.834	2.8961	2.6687	2.9269	1.0624	9.554
Period B	*Time*	09:55-10:05					09:55-10:05			
	Mass	2.397	2.174	2.815	1.122	8.509	3.0162	2.5847	2.396	0.8595	8.856
Period C	*Time*	11:55-12:05					11:55-12:05			
	Mass	2.880	2.715	2.608	0.995	9.198	2.8477	2.7965	2.7699	0.8317	9.246
Period D	*Time*	13:55-14:05					13:55-14:05			
	Mass	2.3876	2.9494	3.1498	1.1191	9.6059	2.8295	2.7304	2.9611	0.9726	9.494
Period E	*Time*	15:55-16:05					15:55-16:05			

		1	2#	2#	3	Total	1	2#	2#	3	Total
	Mass	2.851	3.056	2.883	1.068	9.859	2.6975	2.6192	3.2127	1.1371	9.667
	Total	13.242	13.536	13.956	5.271	**46.004**	14.287	13.3995	14.2666	4.8633	**46.816**
				Day 9: 21 January 2019					**Day 10: 22 January 2019**		
	Sample	1	2#	2#	3	Total	1	2#	2#	3	Total
Period A	Time			07:55-08:05					07:55-08:05		
	Mass	2.575	2.848	3.787	1.766	10.975	2.061	2.810	2.463	1.538	8.871
Period B	Time			09:55-10:05					09:55-10:05		
	Mass	2.689	2.651	2.018	1.223	8.581	2.358	3.401	2.975	1.432	10.166
Period C	Time			11:55-12:05					11:55-12:05		
	Mass	2.213	2.462	2.269	1.261	8.206	2.270	2.001	2.121	1.159	7.552
Period D	Time			13:55-14:05					13:55-14:05		
	Mass	2.070	2.412	2.600	1.279	8.360	2.417	2.712	2.197	1.542	8.868
Period E	Time			15:55-16:05					15:55-16:05		
	Mass	2.326	2.653	2.790	1.381	9.150	2.443	2.64	1.743	1.192	8.018
	Total	11.873	13.025	13.464	6.910	**45.272**	11.549	13.564	11.499	6.864	**43.476**
				Grand total over the 3 months							
			Stream	1	2	3	Grand total				
			Total	135.621	299.480	69.715	504.815				

Sample collected from cyclone bin 1 and bin 2; - No sample available in bin; **Total sample collected on that day**

APPENDIX B. SAMPLE PREPARATION STAGE

Table 30: Record of all results for bulk sample drying

	Stream 1			Stream 2			Stream 3		
	Mass (kg)			Mass (kg)			Mass (kg)		
Test	Before	After	Loss	Before	After	Loss	Before	After	Loss
1	7.713	7.697	0.21%	8.357	8.363	-0.07%	4.873	4.773	2.06%
2	5.886	5.881	0.08%	6.322	6.316	0.10%	2.388	2.386	0.10%
3	6.876	6.832	0.64%	8.492	8.488	0.05%	2.745	2.743	0.06%
4	7.599	7.596	0.04%	8.905	8.898	0.08%	5.411	5.409	0.04%
5	6.693	6.687	0.08%	8.244	8.237	0.08%	4.450	4.446	0.09%
6	4.985	4.977	0.15%	5.599	5.593	0.12%	2.209	2.206	0.12%
7	5.517	5.508	0.16%	5.848	5.845	0.06%	4.346	4.345	0.04%
8	7.908	7.898	0.13%	9.826	9.819	0.07%	4.002	4.002	-0.01%
9	5.061	5.052	0.18%	9.304	9.301	0.03%	4.678	4.663	0.32%
10	7.530	7.523	0.09%	8.832	8.829	0.03%	4.383	4.376	0.16%
11	8.520	8.504	0.19%	5.678	5.677	0.01%	4.817	4.802	0.32%
12	7.951	7.941	0.13%	8.695	8.693	0.02%	5.074	5.046	0.56%
13	5.701	5.715	-0.24%	8.197	8.189	0.10%	2.958	2.953	0.19%
14	4.628	4.613	0.33%	8.455	8.452	0.04%	3.964	3.957	0.19%
15	8.181	8.172	0.11%	8.540	8.540	0.00%	2.859	2.856	0.10%
16	5.498	5.495	0.05%	7.782	7.776	0.08%	5.730	5.657	1.27%
17	8.544	8.533	0.13%	4.010	3.999	0.27%	5.511	5.506	0.10%
18	5.804	5.800	0.07%	6.579	6.549	0.46%	4.181	4.172	0.22%
19	7.159	7.154	0.07%	9.752	9.738	0.14%	3.875	3.869	0.17%
20	8.094	8.088	0.07%	8.690	8.688	0.02%	4.008	4.003	0.12%
21	1.679	1.678	0.05%	9.414	9.394	0.21%	2.486	2.482	0.18%
22	6.167	6.157	0.17%	8.796	8.781	0.17%	4.368	4.358	0.22%
23	7.310	7.305	0.07%	9.078	9.070	0.09%	2.461	2.457	0.15%
24	7.412	7.412	0.00%	5.818	5.810	0.13%			
25	4.447	4.446	0.04%	9.393	9.394	-0.01%			
26	9.174	9.171	0.03%	9.011	9.010	0.01%			
27	8.775	8.769	0.07%	8.307	8.304	0.04%			
28				5.455	5.454	0.02%			
29				5.846	5.844	0.04%			
30				9.608	9.606	0.02%			
31				8.574	8.570	0.05%			
32				8.982	8.967	0.17%			
33				6.483	6.483	0.01%			
34				9.635	9.632	0.03%			
35				9.441	9.396	0.48%			
36				8.579	8.571	0.09%			
37				8.830	8.821	0.10%			
38				7.471	7.459	0.16%			
		Average	0.11%			0.09%			0.29%

Table 31: Pellets mixture recipe preparations throughout the project (mass in gram)

	Stream 1		Stream 2		Stream 3	
Batch	Sample	Water	Sample	Water	Sample	Water
1	300.002	15.003	300.007	15.018	200.014	10.032
2	300.017	15.076	300.001	15.056	200.096	10.010
3	380.005	19.022	380.003	19.054	210.003	10.514
4	400.005	20.062	350.006	17.508	190.009	9.540
5	400.003	20.037	340.002	17.034	190.006	9.503
6	400.005	20.054	340.001	17.058	200.003	10.033
7	400.003	20.069	340.006	17.061	240.001	12.062

120

8	400.001	20.047	340.003	17.017	260.001	13.045
9	450.004	22.571	400.003	20.048	430.002	21.587
10	450.004	22.556	450.000	22.576	430.006	21.587
11	600.004	30.053	500.002	25.040	300.007	15.059
12	600.005	30.060	500.006	25.043	290.006	14.556
13	600.006	30.042	350.006	15.538	490.009	24.594
14	550.003	27.537	440.008	22.079	380.000	19.098
15	550.006	27.586	460.000	23.037	350.002	17.556
16	510.006	25.532	520.003	26.028	350.002	17.826
17	550.007	27.533	460.003	23.068	380.007	19.047
18	550.001	27.554	460.050	23.063	380.006	19.075
19	550.004	27.559	460.005	23.045	430.005	21.550
20	900.003	45.081	740.007	37.556	100.000	5.036
21	600.009	30.040	620.004	31.107	250.007	12.574
22	800.003	40.045	840.002	40.034		
23	400.007	20.069	700.000	35.064		
24	400.009	20.054	360.000	18.074		
25	400.006	20.073	360.002	20.088		

Table 32: Batch by batch mass loss of dried pellets throughout the project

Batch	Mass (Before drying)	Mass (After drying)	Loss
1	1257.35	1247.54	4%
2	1165.09	1155.51	4%
3	1219.82	1210.68	4%
4	1134.71	-	-
5	1174.46	1164.58	4%
6	1195.66	1185.31	4%
7	1210.34	1201.70	4%
8	1122.69	1114.73	4%
9	1212.23	1203.35	4%
10	1220.48	1210.74	4%
11	1110.07	1103.26	3%
12	1186.47	1178.05	4%
13	1182.45	1172.86	4%
14	1119.78	1110.20	4%
15	1162.42	1152.42	4%
16	1197.11	1187.15	4%
17	1115.02	1107.12	4%
18	1225.01	1217.20	3%
19	1193.4	1184.27	4%
20	1180.14	1170.45	4%
21	1106.38	1099.05	4%
22	1148.11	1136.90	4%
23	1139.63	1131.70	3%
24	1175.39	1165.51	4%
25	1227.10	1217.24	4%
26	1167.78	1161.81	3%
27	1282.85	1270.53	4%
28	1203.57	1192.70	4%
29	1113.54	1104.74	4%
30	1190.46	1182.36	4%
31	1146.76	-	-
32	1158.19	-	-
33	-	-	-
34	-	-	-
35	-	-	-

36	1133.72	1123.56	4%
37	1170.39	1160.36	4%
38	1233.41	1222.85	4%
39	1267.57	1257.81	4%
40	1225.33	1215.34	4%
41	1182.11	1170.64	4%
42	1211.13	1200.88	4%
43	1206.97	1196.2	4%
44	1217.73	1206.83	4%
45	1193.55	1183.15	4%
46	1154.25	1143.2	4%
47	1280.23	1269.03	4%
48	1241.82	1231.23	4%
49	1186.25	1175.52	4%
50	1250.20	1238.83	4%
51	1177.88	1166.85	4%
52	1163.96	1153.81	4%
53	1189.30	1178.42	4%
54	1184.33	1175.00	4%
55	1199.97	-	-
56	1167.17	1157.35	4%
57	1232.45	1223.85	3%
58	1203.62	1193.14	4%
59	1210.42	1200.30	4%
60	1157.78	1147.31	4%
61	1195.74	1185.67	4%
62	1232.33	1222.52	4%
63	1197.83	-	-
64	1276.85	1267.32	3%
65	1186.73	1176.89	4%
66	1169.10	-	-
67	1146.46	-	-
68	1239.54	-	-
69	1217.65	-	-
70	1193.16	-	-
71	1246.82	1234.39	4%
72	1324.75	-	-
73	1243.35	1230.88	4%
74	1275.63	1264.18	4%
75	1168.10	1159.44	3%
76	1145.26	1136.99	3%
77	1190.29	1180.39	3%
78	1261.02	1251.57	3%
79	1176.03	1166.53	3%
80	1214.76	1203.92	4%
81	1241.41	1231.07	4%
82	1204.09	1193.15	4%
83	1266.67	1257.04	4%
84	1149.23	1140.14	3%
85	1251.91	1242.07	3%
86	1244.40	1235.15	3%
87	1182.24	1171.48	4%
88	1178.23	-	-
89	1200.99	1190.37	4%
90	1227.43	1215.71	3%
91	1285.05	1272.77	4%
92	1294.72	1282.35	4%
93	1229.56	1217.40	4%
94	1256.87	1244.46	4%
95	1321.96	1309.07	4%

96	1248.56	1235.42	4%
97	1247.11	1234.97	4%
98	1198.65	1185.99	4%
99	1248.50	-	-
100	1295.01	-	-
101	1222.72	-	-
102	1263.21	-	-
103	1264.64	-	-
104	1252.49	1239.53	4%
105	1338.60	1325.18	4%
106	1250.75	1237.29	4%
107	1280.9	1267.31	3%
108	1279.26	1267.87	4%
109	1124.91	1114.39	4%
110	1268.22	1257.16	4%
111	1291.48	-	-
112	1223.99	1213.52	4%

- Did not record details

Table 33: Summary of % mass loss for different firing temperatures

Firing temperature	Mass (before)	Mass (after)	Loss
600°C	1247.54	1228.88	8%
600°C	1155.57	1136.08	8%
600°C	1210.68	1192.05	8%
600°C	-	-	-
600°C	1164.58	1144.54	8%
600°C	1185.32	1165.85	8%
600°C	1210.74	1191.84	8%
600°C	1114.73	1098.19	8%
600°C	1201.70	1186.94	8%
600°C	1203.35	1185.67	8%
600°C	1178.05	1160.51	9%
600°C	1103.26	1086.61	9%
600°C	-	-	-
600°C	1110.20	1092.21	8%
600°C	-	-	-
600°C	1107.12	1097.74	5%
700°C	1187.15	1167.36	9%
700°C	1152.72	1134.44	8%
700°C	-	-	-
700°C	1136.90	1117.81	8%
700°C	1099.05	1082.42	9%
700°C	1170.45	1150.42	9%
700°C	1165.51	1147.83	7%
700°C	1131.70	1114.28	8%
700°C	1161.81	1144.94	8%
700°C	1182.30	1164.92	9%
700°C	1217.54	1197.55	8%
700°C	1270.53	1249.38	8%
700°C	1192.70	1171.38	9%
700°C	-	-	-
700°C	1137.96	1119.86	8%
700°C	1179.07	1159.00	9%
700°C	1193.18	1173.74	8%
700°C	1168.52	1149.30	8%
800°C	1215.34	-	-

123

800°C	1123.56	1104.01	8%
800°C	1257.81	1237.45	8%
800°C	1222.85	1200.87	9%
800°C	1200.88	1177.02	9%
800°C	1196.20	1172.09	10%
800°C	1182.15	1160.83	9%
800°C	1170.64	1149.13	9%
800°C	1231.23	1206.83	10%
800°C	1269.05	1245.51	9%
800°C	1143.20	1120.75	9%
800°C	1238.83	-	-
800°C	1175.52	1150.48	10%
800°C	-	-	-
900°C	1178.42	1154.72	10%
900°C	1175.00	1153.93	9%
900°C	1166.85	1144.80	9%
900°C	1200.30	1176.97	10%
900°C	1153.81	1131.46	10%
900°C	1193.14	-	-
900°C	1147.31	1120.17	11%
900°C	1223.68	1196.68	12%
900°C	1193.14	1168.08	10%
900°C	1157.35	1133.49	10%
900°C	-	-	-
900°C	1222.52	1202.41	8%
900°C	1185.67	1166.09	8%
900°C	1267.32	1247.99	8%
900°C	1176.89	1157.70	8%
900°C	1184.76	1164.50	8%
900°C	1208.60	1187.59	8%
900°C	1160.98	1139.77	9%
900°C	1138.40	-	-
900°C	1231.47	1209.77	9%
900°C	1234.39	1208.84	9%
900°C	1230.88	1206.22	9%
900°C	1264.18	1238.53	9%
1000°C	1136.99	1116.27	8%
1000°C	1166.53	1144.16	9%
1000°C	1251.57	1227.76	9%
1000°C	1180.39	1160.36	8%
1000°C	1251.57	-	-
1000°C	1231.07	1208.73	9%
1000°C	1257.04	1236.72	8%
1000°C	1203.92	1182.08	8%
1000°C	1140.14	1118.96	8%
1000°C	1193.15	1172.02	8%
1000°C	1190.37	1170.31	8%
1000°C	1242.07	1219.75	8%
1000°C	1235.15	1214.98	8%
1000°C	1171.48	1150.73	8%
1000°C	-	-	-
1000°C	1207.14	-	-
1100°C	1194.13	1167.24	11%
1100°C	1185.70	1158.53	11%
1100°C	1270.30	1244.72	10%
1100°C	1139.45	1114.34	10%
1100°C	1272.77	1240.92	11%
1100°C	1244.46	-	-
1100°C	1215.71	1184.54	11%
1100°C	1282.35	1251.43	11%

124

1100°C	1309.07	1277.54	11%
1100°C	1235.42	1203.45	11%
1100°C	1217.40	1185.99	11%
1100°C	1234.97	-	-
1100°C	1239.53	-	-
1200°C	1267.87	1238.20	11%
1200°C	1267.31	1228.30	12%
1200°C	1114.39	1094.00	9%

- Did not record mass

(a) 600°C	(b) 700°C
(c) 800°C	(d) 900°C
(e) 1000°C	(f) 1100°C
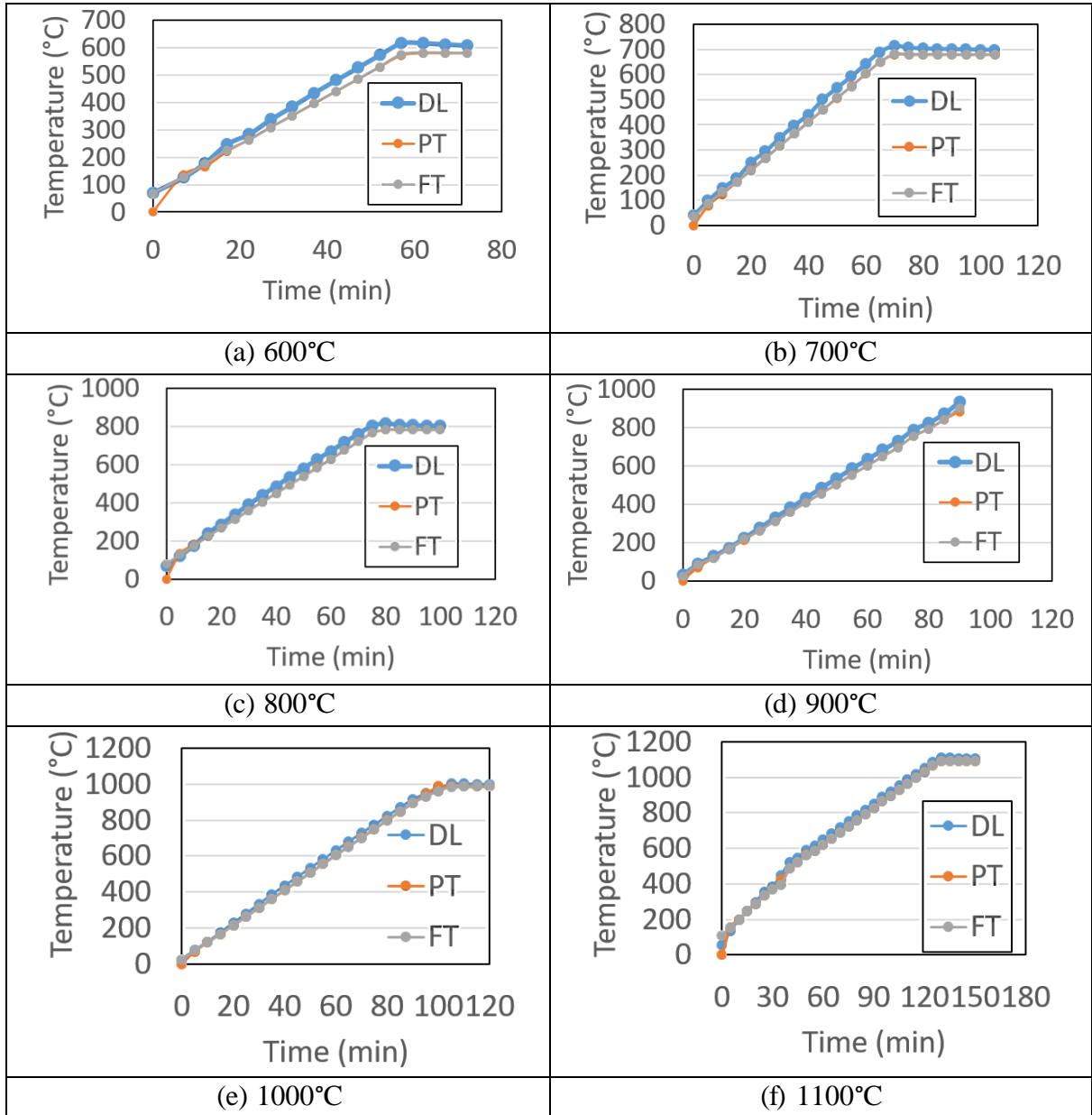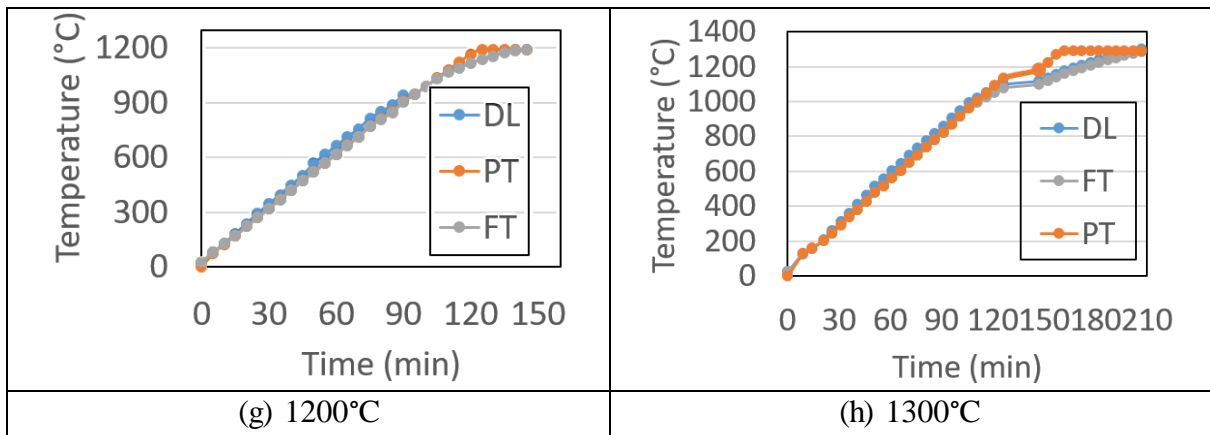
Figure 60: Temperature heating profile for the firing test (only heating up with DL = Data logger temperature, PT = program temperature, and FT = furnace temperature)

APPENDIX C.   METHOD DEVELOPMENT STAGE

(a) Stream 1 (3.5 MPa)	(b) Stream 1 (7.5 MPa)	(c) Stream 1 (10 MPa)
(d) Stream 2 (3.5 MPa)	(e) Stream 2 (7.5 MPa)	(f) Stream 2 (10 MPa)

| (g) Stream 3 (3.5 MPa) | (h) Stream 3 (7.5 MPa) | (i) Stream 3 (10 MPa) |
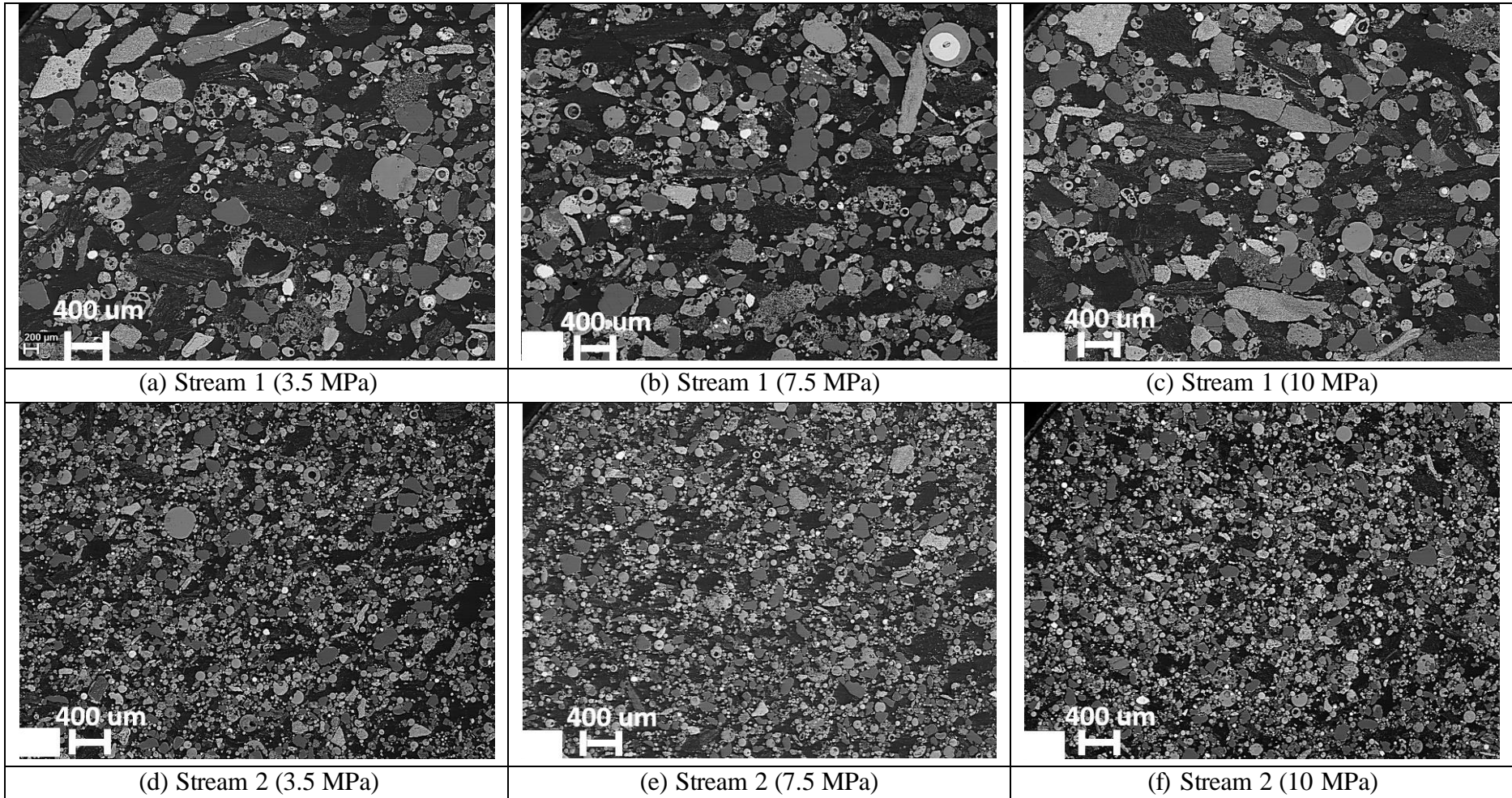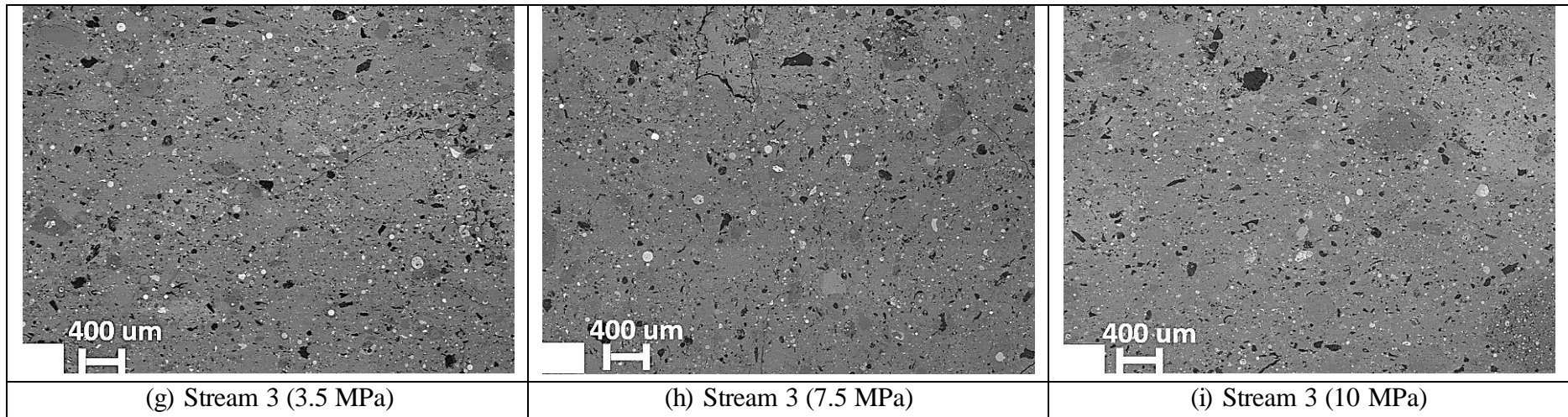
Figure 61: SEM images showing PSD of stream 1 – 3 dust after compressing at different pressures

APPENDIX D.   DETAILED CHARACTERISATION DATA

Table 34: PSD analysis throughout the project for as-sampled stream 1, stream 2, and stream 3 (Data in % unless stated otherwise)

	Stream 1 PSD analysis																	
Run no	*R 1*	*R 2*	*R 3*	*R 4*	*R 5*	*R 6*	*R 7*	*R 8*	*R 9*	*R 10*	*R 11*	*R 12*	*R 13*	*R 14*	*R 15*	*R 16*	*R 17*	*R 18*
Mass before (g)	300.1	500.8	500.5	500.6	501.7	502.1	501.9	500.5	500.4	500.1	500.8	500.9	500.1	500.1	501.4	503.2	502.1	500.0
+1000	20.7	35.1	33.2	33.6	33.5	34.7	33.2	38.0	35.6	32.9	33.6	37.7	22.3	25.8	26.6	35.6	27.6	39.0
+850	4.1	7.0	7.1	6.0	7.4	7.8	5.7	6.3	7.3	6.1	7.7	10.3	5.3	6.6	6.2	6.2	6.4	8.0
+600	15.8	29.7	27.9	25.5	28.2	30.1	25.7	27.8	28.9	28.4	30.5	37.6	29.0	30.0	27.6	28.3	26.0	32.2
+425	30.1	53.9	53.3	48.4	53.0	54.3	51.1	52.4	52.1	53.2	55.0	61.2	55.4	56.0	52.7	53.9	51.6	55.8
+300	62.8	112.0	112.4	106.0	110.6	111.6	110.9	112.4	108.1	109.3	110.6	113.8	114.8	124.5	115.6	111.4	114.6	114.1
+212	68.4	110.3	114.7	117.1	115.4	113.4	117.4	115.5	115.7	114.3	112.7	107.5	118.1	114.9	117.3	116.6	119.5	110.9
+150	59.2	94.5	94.9	100.7	95.3	93.4	97.3	93.4	94.8	94.9	92.3	81.8	95.5	88.0	95.7	93.9	96.4	87.3
+106	23.6	35.7	35.8	38.7	35.6	34.9	36.8	34.2	35.5	36.7	35.2	29.8	36.7	33.8	36.7	35.3	37.0	32.8
+75	9.0	13.2	12.9	14.4	12.6	12.0	13.3	11.9	12.7	13.5	12.6	10.3	13.4	12.1	13.4	12.7	13.5	11.4
+53	2,9	4.3	4.4	4.7	4.2	4.1	4.5	4.0	4.4	4.6	4.1	3.6	4.4	4.3	4.8	4.4	4.7	4.0
+38	1.7	2.5	2.3	2.5	2.5	2.4	2.4	2.3	2.2	2.5	2.4	2.3	2.2	2.3	2.5	2.4	2.5	2.1
-38	1.4	1.6	1.5	1.5	2.2	2.3	2.1	2.2	2.1	1.8	2.3	1.6	1.0	1.8	1.4	1.2	2.1	2.0
Mass after (g)	296.8	499.8	500.4	499.1	500.5	501.0	500.4	500.4	499.4	498.2	499.0	497.5	498.2	500.0	500.2	501.9	501.7	499.5
Loss (g)	3.3	1.0	0.1	1.5	1.2	1.1	1.5	0.1	1.0	1.9	1.8	3.4	1.9	0.0	1.2	1.3	0.4	0.6
Loss (%)	1.1%	0.2%	0.0%	0.3%	0.2%	0.2%	0.3%	0.0%	0.2%	0.4%	0.4%	0.7%	0.4%	0.0%	0.2%	0.3%	0.1%	0.1%
Run no	*R 19*	*R 20*	*R 21*	*R 22*	*R 23*	*R 24*	*R 25*	*R 26*	*R 27*									
Mass before (g)	505.9	500.1	500.6	500.7	503.8	500.5	501.6	500.9	220.4									
+1000	35.6	28.0	31.8	36.9	35.2	34.5	38.9	44.3	18.7									
+850	6.0	5.1	7.1	7.6	7.6	8.5	5.8	9.1	5.3									
+600	28.2	23.6	28.0	33.9	29.0	32.5	33.6	39.0	18.5									
+425	53.0	48.4	52.6	58.8	53.9	58.0	59.3	63.9	27.7									
+300	110.9	105.0	108.7	118.3	114.0	116.0	114.0	113.2	47.4									
+212	118.1	121.6	115.7	110.0	113.9	113.5	112.2	105.9	45.3									
+150	96.2	102.6	96.0	84.1	94.0	87.0	86.8	70.1	35.0									
+106	35.7	40.2	37.3	31.3	34.6	31.8	31.5	28.1	12.9									
+75	12.7	14.6	13.3	11.3	12.5	11.0	10.9	9.5	4.8									
+53	4.2	5.0	4.5	3.9	4.4	3.7	3.8	3.4	1.7									
+38	2.3	2.8	2.5	2.2	2.4	2.1	2.2	2.1	1.2									

129

-38	2.3	0.9	2.2	1.7	1.9	1.6	2.3	2.2	0.9									
Mass after (g)	505.1	497.7	499.6	500.0	503.4	500.3	501.2	490.9	219.3									
Loss (g)	0.8	2.4	1.0	0.7	0.4	0.2	0.4	10.0	1.0									
Loss (%)	0.2%	0.5%	0.2%	0.1%	0.1%	0.0%	0.1%	2.0%	0.5%									

Stream 2 PSD analysis

Run no	R 1	R 2	R 3	R 4	R 5	R 6	R 7	R 8	R 9	R 10	R 11	R 12	R 13	R 14	R 15	R 16	R 17	R 18
Mass before (g)	502.2	505.3	500.2	501.0	500.1	502.7	500.2	503.5	501.7	500.0	500.2	501.1	507.2	502.6	507.9	501.0	501.3	500.7
+1000	0.4	0.2	0.4	0.4	0.2	0.2	0.3	0.2	0.2	0.3	0.3	0.4	0.2	0.5	0.3	0.4	0.5	0.4
+850	0.2	0.2	0.2	0.3	0.3	0.3	0.2	0.3	0.3	0.3	0.4	0.3	0.3	0.4	0.3	0.4	0.3	0.3
+600	1.1	0.9	1.0	1.2	1.0	1.4	1.4	1.7	1.3	1.1	1.9	1.4	1.7	1.6	1.3	1.4	1.6	1.7
+425	3.3	3.6	2.9	3.3	3.0	3.1	3.8	3.6	3.6	3.0	3.7	3.3	3.5	4.2	3.2	3.5	4.0	3.2
+300	14.3	15.1	13.6	14.9	13.7	14.6	15.5	15.6	15.3	14.1	16.5	15.3	15.4	16.6	14.2	15.0	16.5	14.7
+212	41.5	41.3	38.8	41.0	39.2	40.2	41.4	41.7	40.9	40.2	42.3	40.6	45.5	42.5	39.7	40.6	43.1	40.6
+150	88.3	87.3	85.2	86.5	84.9	86.9	87.4	88.2	87.5	86.0	88.0	88.3	82.5	90.7	40.2	86.4	88.4	86.8
+106	101.5	99.6	99.6	102.7	102.5	102.8	114.3	119.4	124.3	105.6	117.9	118.4	110.7	135.2	117.3	115.6	109.0	114.1
+75	105.0	105.0	104.0	102.4	109.7	113.9	110.6	116.9	124.5	116.8	130.4	113.6	130.6	123.7	136.9	133.4	131.7	132.3
+53	73.7	73.2	74.2	70.0	63.8	60.6	51.9	43.4	36.7	54.6	34.5	48.0	38.7	29.0	40.4	37.1	37.8	38.2
+38	47.2	48.3	50.2	49.9	53.5	49.0	50.0	52.6	42.1	53.7	39.1	46.4	44.1	35.7	43.9	41.4	42.2	42.8
-38	22.2	25.0	27.9	25.1	25.3	27.1	20.9	17.2	24.0	22.2	23.9	24.5	24.5	22.0	22.5	21.9	25.3	21.8
Mass after (g)	498.7	499.6	497.8	497.6	497.2	500.1	497.6	500.7	500.8	497.8	499.0	500.5	497.8	502.2	460.2	497.2	500.5	496.9
Loss (g)	3.6	5.7	2.4	3.5	2.9	2.6	2.6	2.8	1.0	2.2	1.2	0.6	9.4	0.4	47.8	3.9	0.9	3.8
Loss (%)	0.7%	1.1%	0.5%	0.7%	0.6%	0.5%	0.5%	0.6%	0.2%	0.4%	0.2%	0.1%	1.9%	0.1%	9.4%	0.8%	0.2%	0.8%

Run no	R 19	R 20	R 21	R 22	R 23	R 24	R 25	R 26
Mass before (g)	500.5	502.3	501.3	503.3	503.4	500.9	500.3	398.6
+1000	0.6	0.4	0.6	0.4	0.4	0.2	0.4	0.5
+850	0.3	0.3	0.3	0.3	0.2	0.4	0.4	0.5
+600	1.5	1.6	1.4	1.7	1.4	2.1	2.2	2.1
+425	4.1	3.6	4.4	3.5	3.7	3.8	4.7	4.0
+300	16.8	15.5	17.5	16.2	15.0	17.4	18.9	16.7
+212	42.5	40.8	43.9	42.2	40.0	43.7	46.2	38.6
+150	94.5	87.7	94.1	100.4	88.3	94.0	108.1	95.3
+106	149.7	136.5	178.0	195.7	163.8	172.8	194.7	161.4
+75	117.4	102.6	93.3	87.4	92.3	83.7	66.2	49.2
+53	22.2	42.5	20.2	15.7	30.4	24.8	16.0	7.7

130

+38	30.0	46.7	30.0	24.6	41.8	35.3	25.4	12.8
-38	19.2	22.7	16.6	14.2	22.2	20.8	16.6	8.5
Mass after (g)	498.7	500.7	500.2	502.3	499.3	498.8	499.9	397.1
Loss (g)	1.7	1.6	1.1	1.0	4.1	2.1	0.4	1.5
Loss (%)	0.3%	0.3%	0.2%	0.2%	0.8%	0.4%	0.1%	0.4%
Stream 3 PSD analysis								
Mass before (g)		**%**						
+ 38	696.1	10.6						
- 38	5887.5	89.4						
Mass after (g)	6583.6	100						

Table 35: Chemical analysis results and specific gravity of as-received dust sample for stream 1, stream 2, and stream 3

No	MnO %	FeO %	Al_2O_3 %	CaO %	MgO %	SiO_2 %	Na_2O %	K_2O %	C %	P_2O_5 %	S %	B %	SG g/cc	ZnO %	Total %
						STREAM 1									
1	24.60	4.24	2.78	9.39	3.86	41.73	0.46	1.30	10.10	0.05	0.54	<0.1	3.00	<0.05	99.04
2	25.10	4.25	2.62	9.41	3.81	42.16	0.47	1.22	9.99	0.05	0.50	<0.1	3.04	<0.05	99.58
3	23.90	4.17	2.61	9.39	3.80	42.16	0.42	1.24	10.10	0.05	0.52	<0.1		<0.05	98.36
4	24.60	4.15	2.71	9.32	3.71	42.16	0.46	1.13	10.60	0.05	0.50	<0.1	3.04	<0.05	99.39
5	25.60	4.16	2.66	9.37	3.83	43.01	0.46	1.18	9.79	0.05	0.53	<0.1	3.04	<0.05	100.65
6	25.83	4.38	2.71	10.10	3.98	41.87	0.49	1.23	9.99	0.06	0.54	<0.1	3.04	<0.05	101.18
7	24.90	4.27	2.66	10.20	3.93	42.16	0.46	1.14	9.87	0.05	0.50	<0.1	3.06	<0.05	100.14
8	25.50	4.33	2.60	9.94	3.87	41.30	0.46	1.19	9.94	0.05	0.56	<0.1	3.05	<0.05	99.75
9	25.70	4.42	2.76	9.96	3.96	41.52	0.43	1.26	10.10	0.06	0.52	<0.1	3.05	<0.05	100.69
10	26.30	4.50	2.77	10.01	3.99	41.30	0.47	1.25	10.00	0.05	0.50	<0.1	3.05	<0.05	101.15
Avg.	25.20	4.29	2.69	9.71	3.87	41.94	0.46	1.22	10.05	0.05	0.52	<0.1	3.04	<0.05	99.99
Stdev.	0.68	0.11	0.06	0.34	0.09	0.49	0.02	0.05	0.21	0.00	0.02	<0.1	0.02		0.89
						STREAM 2									
1	24.95	3.90	3.30	8.48	4.38	42.37	0.48	1.38	8.84	0.05	0.29	<0.1	3.005		98.42
2	25.50	3.98	3.40	9.01	4.47	44.08	0.46	4.31	8.81	0.06	0.30	<0.1	2.98		104.38
3	25.50	3.90	3.29	8.47	4.29	43.44	0.43	4.82	8.95	0.05	0.30	<0.1	2.79		103.44
4	25.70	3.88	3.29	8.41	4.27	45.15	0.44	1.13	8.91	0.06	0.31	<0.1	3.01	0.06	101.62
5	25.20	3.85	3.37	8.50	4.35	44.08	0.28	1.10	8.67	0.05	0.30	<0.1	3.02	0.05	99.81

131

6	27.25	4.20	3.37	9.29	4.62	41.73	0.44	1.67	8.89	0.05	0.30	<0.1	2.98	0.07	101.88
7	26.30	4.09	3.41	9.13	4.67	42.59	0.36	0.99	8.91	0.06	0.30	<0.1	3.03		100.80
8	24.60	3.83	3.16	8.85	4.36	42.80	0.43	1.35	8.81	0.06	0.30	<0.1	3		98.55
9	25.60	3.95	3.32	9.08	4.56	42.37	0.23	2.96	8.45	0.05	0.28	<0.1	2.97		100.85
10	26.00	3.99	3.24	9.24	4.47	42.37	0.43	8.04	8.98	0.05	0.31	<0.1	2.99		107.12
Avg.	25.66	3.96	3.31	8.85	4.44	43.10	0.40	2.77	8.82	0.05	0.30	<0.1	2.98	0.06	101.67
Stdev.	0.70	0.11	0.07	0.33	0.13	1.00	0.08	2.19	0.15	0.01	0.01	<0.1	0.07	0.01	2.56
						STREAM 3									
1	31.30	1.02	2.90	8.06	7.56	34.38	1.71	5.05	4.11	0.05	0.86	<0.1	3.0850	0.27	97.25
2	31.20	1.06	2.85	8.10	7.52	32.31	1.73	4.11	4.09	0.05	0.98	<0.1	3.08	0.24	94.23
3	32.00	1.11	2.93	8.35	7.65	33.81	1.58	3.93	4.06	0.05	0.82	<0.1	3.08	0.26	96.54
4	32.90	1.10	2.88	8.86	7.97	34.24	2.05	4.06	4.07	0.05	0.84	<0.1	3.07	0.26	99.28
5	33.90	1.06	2.95	9.11	8.20	33.81	1.75	4.78	4.11	0.05	0.86	<0.1	3.08	0.25	100.83
6	31.50	1.03	2.86	8.30	7.66	34.38	1.64	4.52	4.03	0.05	0.86	<0.1	3.095	0.26	97.07
7	30.80	1.01	2.98	8.10	7.53	34.45	1.85	4.20	3.98	0.05	0.83	<0.1	3.08	0.26	96.05
8	32.00	1.03	2.89	8.13	7.73	34.24	1.64	3.01	3.99	0.05	0.87	<0.1	3.07	0.26	95.84
9	31.00	0.99	2.81	7.99	7.53	34.03	1.66	3.99	3.94	0.05	0.87	<0.1	3.08	0.26	95.11
10	30.90	1.01	2.79	7.99	7.53	34.67	1.64	3.54	4.07	0.05	0.89	<0.1	3.07	0.26	95.34
Avg.	31.75	1.04	2.88	8.30	7.69	34.03	1.72	4.12	4.04	0.05	0.87	<0.1	3.08	0.26	96.76
Stdev.	0.94	0.04	0.06	0.37	0.22	0.63	0.13	0.56	0.05	0.00	0.04	<0.1	0.01	0.01	1.89

Table 36: Compression strength results for stream 1-3 (Stream 1 and 2 measured in newton's (N), and stream 3 in Kilo newton's (KN))

Stream 1						Stream 2						Stream 3				
Temperature (℃)						Temperature (℃)						Temperature (℃)				
600	700	800	900	1000	1100	600	700	800	900	1000	1100	600	700	800	900	1000
6.40	13.67	24.99	77.98	202.27	2103.29	16.58	27.79	72.22	144.46	656.63	11188	16.28	31.43	26.70	27.58	35.06
5.17	12.21	26.43	82.50	211.87	2190.03	14.17	30.94	76.82	162.29	599.75	7854	17.44	29.02	26.53	30.68	40.57
8.43	13.60	22.86	84.64	250.71	2987.39	16.53	29.12	77.76	141.51	558.09	10556	18.30	32.43	24.43	29.50	31.35
5.68	13.05	22.90	79.44	243.38	2311.02	17.28	31.82	68.49	152.35	703.93	9555	17.95	22.39	24.20	15.80	35.68
5.04	13.89	25.24	81.73	267.29	2581.57	15.13	32.84	71.23	162.75	562.46	11719	17.20	32.78	25.67	38.54	45.02
7.73	15.91	22.11	82.36	273.32	2987.70	14.78	34.80	77.10	149.21	642.34	8855	19.05	27.90	24.11	27.53	43.45
4.64	13.70	22.31	77.08	219.16	2868.00	14.37	36.11	72.57	149.94	641.28	8449	17.11	29.64	30.77	35.39	36.70
5.61	14.46	21.83	81.21	251.42	2502.95	13.35	36.05	74.08	158.66	484.84	8430	17.57	24.35	23.26	28.50	29.91
5.22	14.20	23.85	75.08	215.88	2229.18	16.66	33.79	68.59	151.47	578.46	9675	24.57	25.22	24.38	22.17	37.47

7.23	14.26	21.49	69.61	182.12	1878.36	13.93	31.80	71.92	163.13	649.80	10141	21.64	21.52	22.45	26.63	32.39
5.74	12.95	26.88	90.77	256.50	2944.53	14.13	30.35	72.79	151.34	477.11	11444	20.07	24.15	25.00	26.04	38.34
5.64	14.52	23.49	86.08	244.25	2998.69	16.01	28.25	68.31	150.70	490.55	9464	16.35	22.39	31.10	25.01	32.49
8.40	13.90	24.80	87.94	270.06	2839.03	14.61	33.52	72.72	150.24	567.07	7809	17.04	27.44	22.82	22.11	43.31
5.69	14.06	23.65	88.85	277.10	2276.09	11.95	36.41	72.61	142.02	583.04	12014	15.10	23.88	19.29	25.63	34.28
6.26	15.28	26.35	82.75	231.82	1957.58	11.69	34.06	69.88	156.55	553.89	10776	16.98	23.74	25.82	34.35	40.38
7.12	12.82	21.01	74.25	235.83	2131.98	12.88	33.94	68.93	153.66	711.07	10215	17.88	30.08	20.39	26.27	46.06
6.08	15.07	20.48	85.59	267.27	1949.09	16.88	32.10	73.02	156.23	603.2	11438	20.70	18.91	20.36	28.77	48.96
4.49	13.85	27.87	73.30	228.66	3204.75	11.30	33.15	75.33	158.89	712.30	10245	19.73	28.81	19.85	16.11	39.21
8.13	14.01	23.63	76.89	205.84	2506.12	13.07	36.35	69.78	156.37	478.13	10998	20.30	25.28	29.39	20.74	38.10
8.57	12.44	23.74	69.26	220.43	2404.48	14.31	29.46	71.71	156.13	737.62	9441	18.02	25.84	29.46	18.33	44.67
5.59	15.47	23.50	70.53	251.06	2126.90	14.61	35.03	67.06	154.10	643.34	10966	22.95	31.92	19.60	22.01	36.09
6.79	15.19	24.80	85.49	193.29	2551.67	14.76	30.69	73.50	158.66	605.31	12112	19.22	26.29	27.40	24.92	35.79
8.26	12.77	22.79	89.33	192.35	2817.48	15.16	32.03	70.23	158.71	526.26	11022	15.40	27.03	23.95	21.83	42.70
7.40	14.88	26.83	69.70	192.18	2064.19	13.74	29.05	78.40	159.07	714.27	11819	16.83	23.39	20.26	33.66	40.38
7.44	16.14	23.62	67.70	215.38	2343.14	15.10	34.83	75.21	141.50	660.46	12881	15.91	26.19	19.54	27.60	44.24
7.16	15.74	24.08	69.34	218.02	2854.33	16.64	28.98	72.82	139.20	457.22	10418	16.61	34.27	23.42	24.55	36.49
7.02	14.80	21.53	70.39	199.53	3199.93	17.11	28.02	77.82	145.04	690.38	9654	18.50	22.96	26.74	38.37	42.89
8.30	14.57	23.71	90.77	225.58	2304.82	17.08	28.25	70.16	138.27	761.11	10446	-	26.94	22.66	29.50	44.76
7.83	16.06	23.60	81.30	229.95	1912.14	16.64	33.01	66.61	159.08	517.39	10053	-	22.87	23.53	29.01	35.00
8.98	13.47	26.01	86.63	214.84	2154.05	17.91	30.15	72.49	138.25	713.96	9795	-	33.21	23.22	32.52	38.51
7.18	12.77	20.29	63.00	229.74	3047.44	18.16	31.56	75.13	153.07	672.21	12342	-	33.01	20.22	22.72	33.32
6.84	12.17	25.06	70.56	255.59	3004.96	13.91	32.41	70.62	137.61	624.24	8333	-	29.93	17.03	24.40	38.48
5.62	14.02	20.50	81.79	207.32	2683.44	16.36	31.10	74.96	145.21	621.59	10631	-	28.73	26.10	42.00	34.60
5.85	14.94	19.94	64.64	207.33	2471.32	18.11	33.09	73.19	147.86	526.25	9671	-	24.51	27.39	37.77	31.53
5.96	14.48	22.99	75.71	187.62	2762.16	16.63	28.29	67.49	147.25	564.07	9190	-	26.48	25.30	19.46	38.67
7.05	15.83	22.44	77.35	205.55	2476.34	13.39	29.83	76.27	148.29	558.60	10419	-	28.75	27.44	32.85	36.54
7.87	15.35	25.19	72.46	244.35	3278.35	13.91	31.90	71.68	137.34	526.77	8770	-	16.50	23.84	25.58	33.54
6.47	13.65	21.28	69.42	175.77	2672.56	15.20	29.16	75.20	139.45	634.12	10787	-	22.93	24.09	26.67	38.90
6.06	13.74	24.14	69.72	194.00	2527.94	14.43	33.44	70.88	138.43	691.42	11060	-	28.42	25.14	26.01	37.16
6.79	14.48	23.11	84.97	195.25	2054.55	14.26	35.10	71.46	151.59	540.39	10849	-	25.72	26.74	25.64	39.05

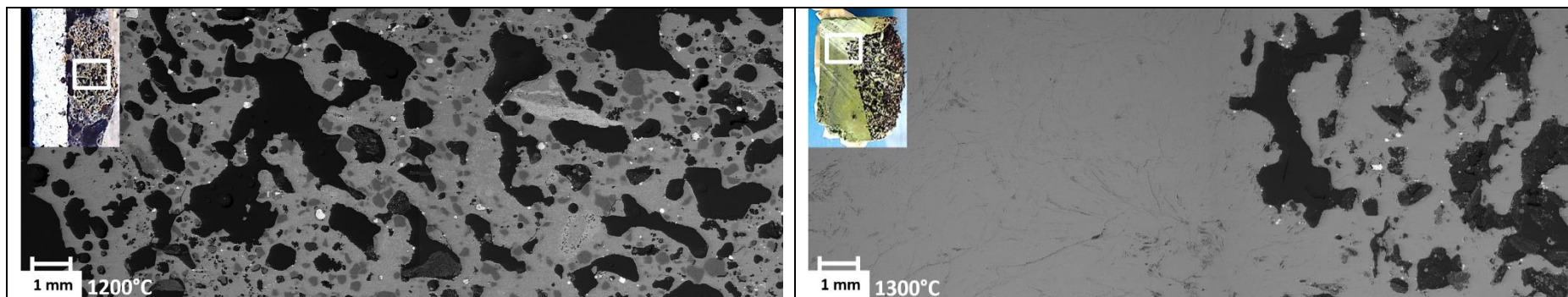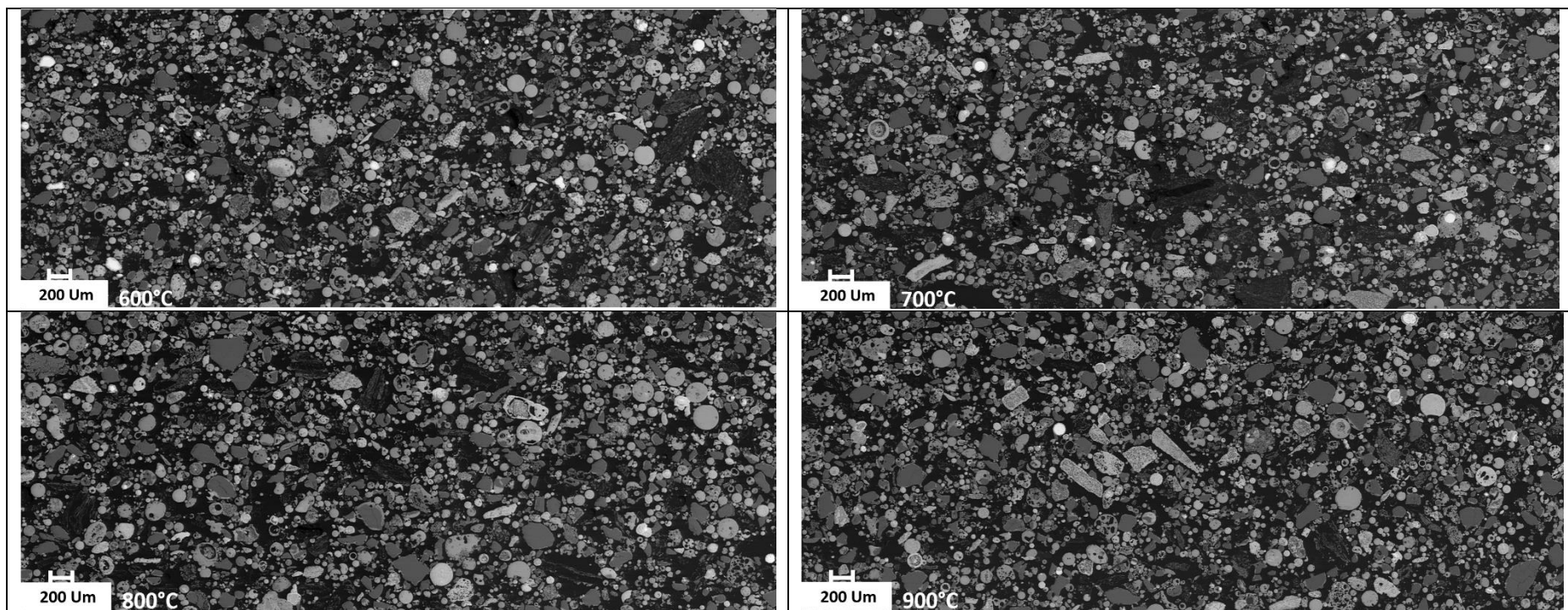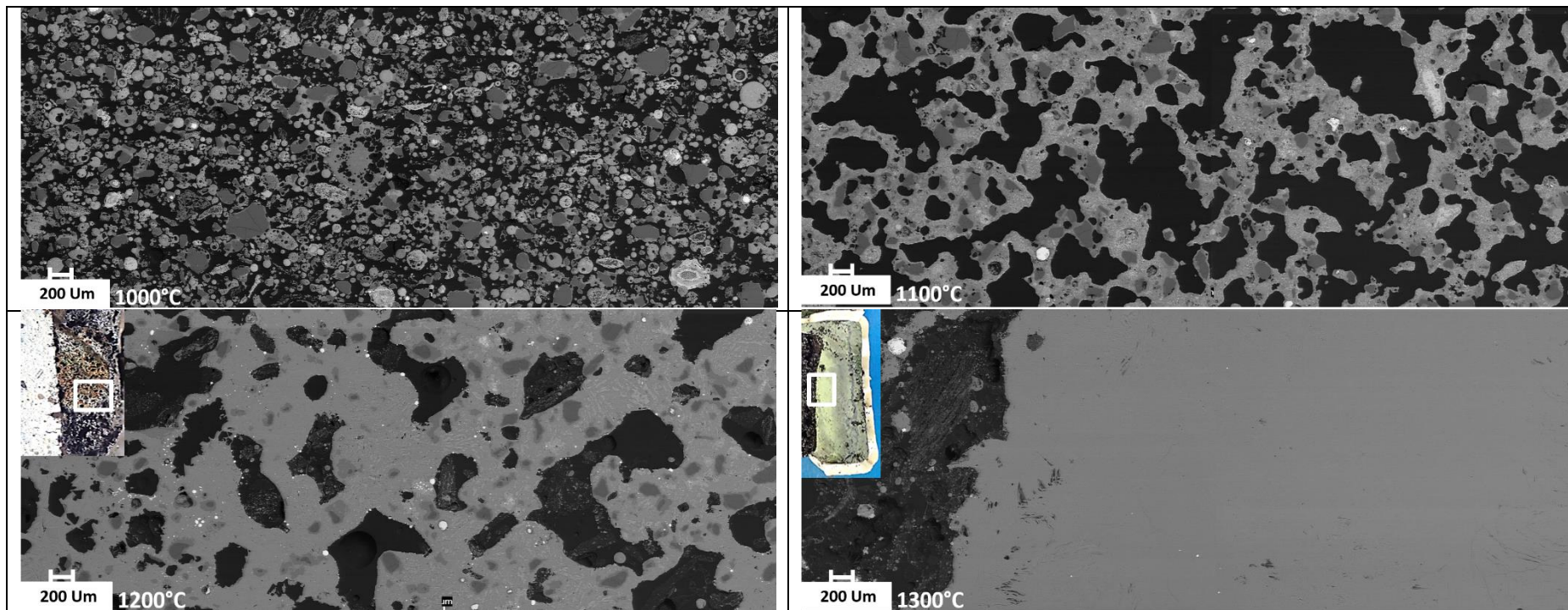- Dimensionally unsuitable (not included in the calculation)
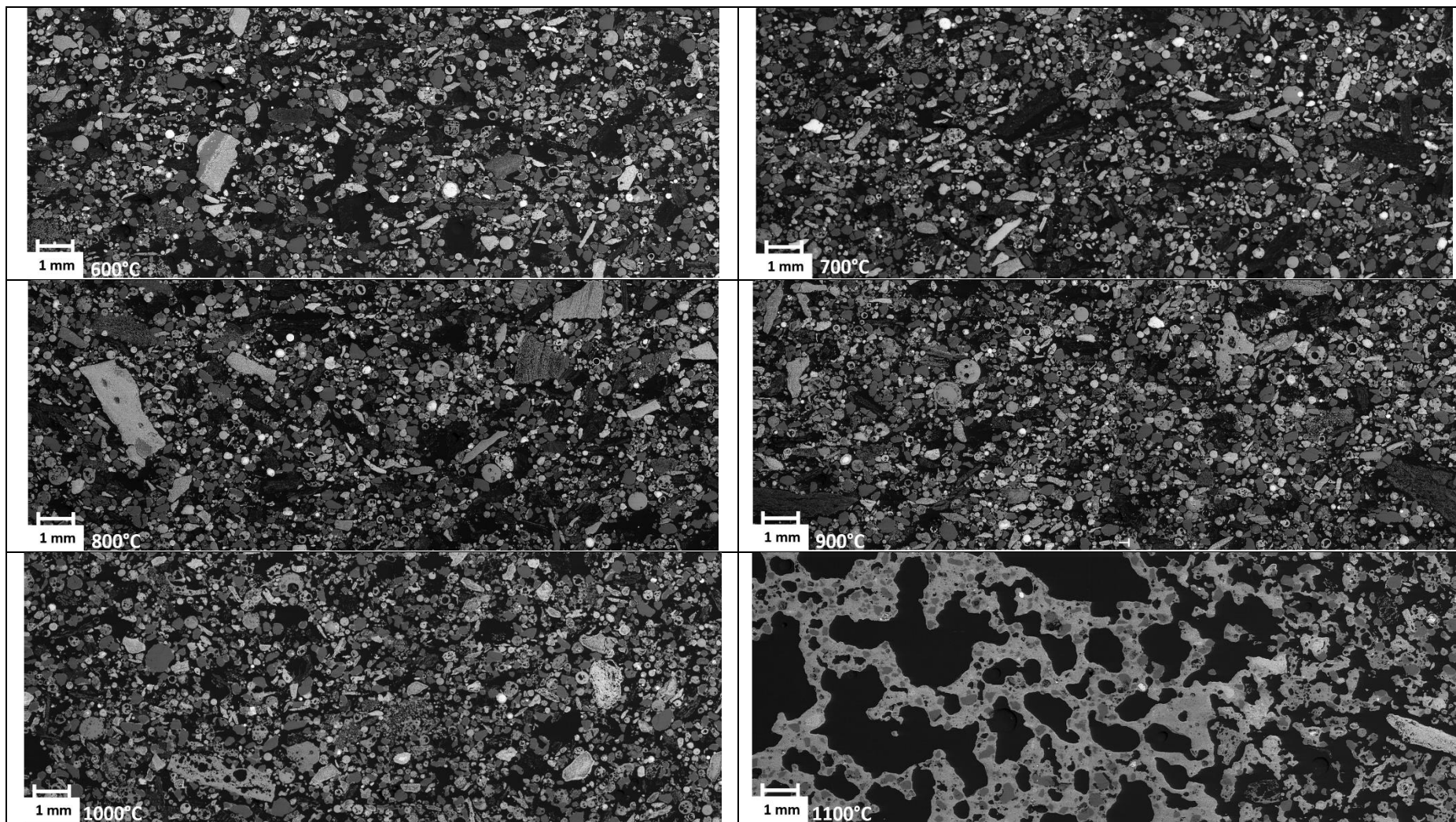
Figure 62: Overview SEM images for stream 1 dust fired at 600-1300°C

135

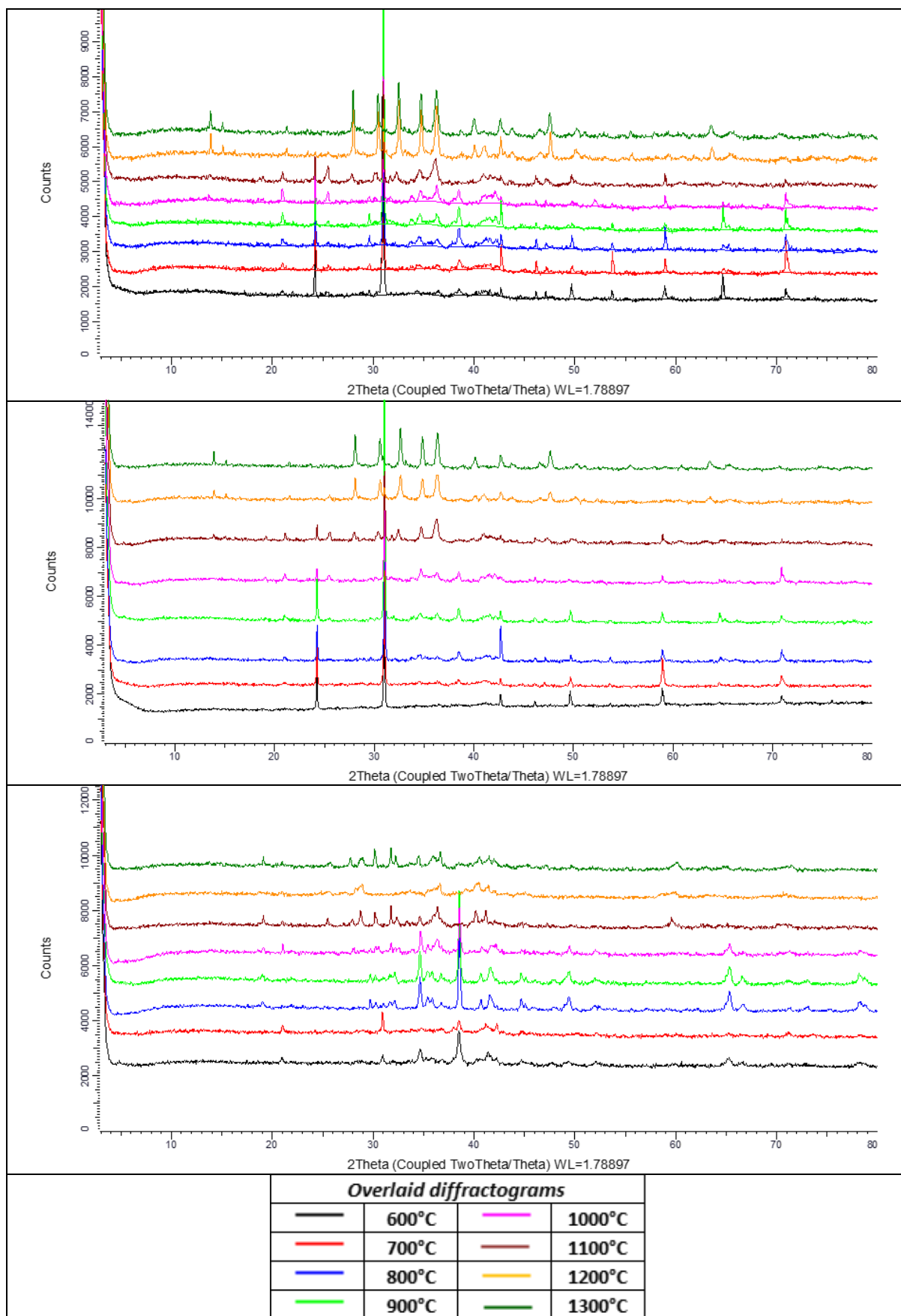*Figure 63: Overview SEM images for stream 2 dust fired at 600-1300°C*

Figure 64: XRD overlaid diffractograms showing phase counts for fired samples with top: stream 1, middle: stream 2, and bottom stream 3